Development of Modelling Techniques for Pulsed Pressure Chemical Vapour Deposition (PP-CVD)

Hadley M. Cave B.E.(Hons)

A thesis presented for the degree of
Doctor of Philosophy
in
Mechanical Engineering
at the
University of Canterbury
Christchurch, New Zealand
31 January 2008

To Mum and Dad,

Who never denied anything for their children's education.

This thesis is their achievement.

Table of Contents

Acknowledgements

"Difficult times have helped me to understand better than before, how infinitely rich and beautiful life is in every way, and that so many things that one goes worrying about are of no importance whatsoever."
-Isak Dinesen

The last year has been, for the most part, my *annus horribilis* in which I experienced some of the greatest trials of my life so far. However, during the difficult times I did learn the value of family, friends and supervisors who value their students as people and not just research machines. They got me through the most difficult period of my life so far and motivated me to continue my work and finish this thesis at a time when the cards seemed stacked against me.

A thesis maybe a work of science and research, but it is a deeply personal document. It represents years of dedication, emotion and even sacrifice. Those who have helped contribute to this thesis have made a lasting impression on my life and consciousness. I will endeavour to express my thanks, however inadequately, in these acknowledgements.

Firstly I would like to thank my supervisors: Assoc. Prof. Susan Krumdieck, Dr. Mark Jermy and Prof. Chong-sin Wu. They all have contributed so much in their own unique ways to the project and I think their personalities show through in different aspects of this thesis. I think the best summary I can give of them, is the answer I gave when a friend asked me to tell them about my supervisors: "When Dr. Jermy says 'Jump!', I say 'How high?'. When Dr. Krumdieck says 'Jump!', I say 'Which way?' and when Prof. Wu says 'Jump!', I don't say anything, I just jump as high as possible and prepare to jump again immediately upon landing". However, the best quality about all of my supervisors is that I regard them all as friends who care about the welfare of their students and whose advice is always valued and useful.

Perhaps the most important person in helping me complete this work has been Dr. Kun-Chang (K.-C.) Tseng (National Space Organisation, Hsinchu, Taiwan). K.-C. has dedicated weeks of his time to helping me, in modifying the PDSC code and in running simulations. At times we have frustrated and exhausted each other, but ultimately his dedication, friendship and knowledge have been an inspiration to me.

To the students in the Prof. Wu's group at the National Chiao-Tung University (NCTU) I owe enormous appreciation. I have been truly humbled by their friendship and good-will in helping me with both my research and my integration into Taiwanese life. Every member of the group receives my profound thanks, but I must particularly acknowledge Chiei-Tsai (C.-T.) Hong. C.-T. epitomises the Taiwanese spirit and he can take significant credit for keeping me alive during my early days in Taiwan. His friendship and help will never be forgotten.

So much of the experimental work would not have been possible without the knowledge, advice and hard work of Dr. Maxim Lebedev whose sense of humour and ability to make advanced deposition equipment from objects swept from the workshop floor (literally on several occasions) was always a tonic.

I have also received generous advice and support from a number of overseas academics. Dr. Charles Lilley, formerly at the University of Melbourne, was always happy to lend advice. The immensely talented Dr. Matthew Smith, now at NCTU, gave no nonsense advice which was appreciated and valued. I was also honoured to receive the support of Prof. Graeme Bird, pioneer of DSMC, who made alterations to his excellent DS2V software to assist my initial modelling work.

To my good friends at the University of Canterbury: Jake Frye, Shannon Page, Jerry Chang, Kerry Mulligan, Laurens de la Ossa, Andy Hamm, Jaclyn Moore, Lionel Rogers, Laurent Pasticier, Montira Watcharasukarn, Vilailuck Sirwongrungson, Callum Spence, Jordan Gilmore, Nicolas Buchmann, Wei Hua Ho and Gabrielle Attanasi; I thank you for making the last three years so enjoyable. A special mention goes to my Taiwanese friends: Mike Dahl, Ru-Juan Chao and in particular my old air force friend Ben Hall.

To my beautiful girlfriend, Ai-tse (Ashley) Sun: thanks for your support, love and kindness. You gave me purpose when I didn't have any. Always remember we are stronger together.

Finally, to my family, thank you for your unwavering support and belief that I would eventually finish this thing! Mum, Dad, Vanessa and Rowan: thank you for being there with your love and comfort when I needed you. You will always have my gratitude.

Contributions of Others

The majority of the work in this thesis is my own, however several others have contributed to the testing of the unsteady PDSC and DREAM code developed in this thesis. This is primarily a reflection of the different approach to research in Taiwan. I feel it is appropriate to delineate where this work is entirely my own, and where others have made a substantial contribution.

- Section 2.3.2: Dr. Maxim Lebedev (formerly University of Canterbury) and I jointly carried out the deposition of diamond films and carbon nano-structures. The SEM images were produced by Dr. Lebedev.

- Chapter 6: Dr. Kun-Chang Tseng (National Space Organisation, Taiwan) lent considerable assistance in the programming of the unsteady PDSC modules and the DREAM code which I developed. The simulations of shock tube flow (section 6.3.2) and benchmarking tests (section 6.4.2.2) were carried out jointly.

- Section 6.4.2.1: Sheng-Fan Hsien (Masters student, National Chiao Tung University, Taiwan) carried out the simulations of driven cavity flow under my supervision.

- Section 6.6.1: Wei-Cheng Hong (Masters student, National Chiao Tung University, Taiwan) carried out the simulations of unsteady Couette flow under my supervision.

- Chapters 7: Tsung-Han Lin (Masters student, National Chiao Tung University, Taiwan) carried out the simulations to obtain the Navier-Stokes inlet conditions for the PP-CVD reactor simulations

- Additionally, several of the diagrams in the thesis were produced by my supervisor, Dr. Susan Krumdieck, and have been reproduced directly in my thesis. This is noted below the diagrams concerned.

Abstract

In this thesis, a numerical and theoretical investigation of the Pulsed Pressure Chemical Vapour Deposition (PP-CVD) progress is presented. This process is a novel method for the deposition of thin films of materials from either liquid or gaseous precursors. PP-CVD operates in an unsteady manner whereby timed pulsed of the precursor are injected into a continuously evacuated reactor volume.

A non-dimensional parameter indicating the extent of continuum breakdown under strong temporal gradients is developed. Experimental measurements, supplemented by basic continuum simulations, reveal that spatio-temporal breakdown of the continuum condition occurs within the reactor volume. This means that the use of continuum equation based solvers for modelling the flow field is inappropriate. In this thesis, appropriate methods are developed for modelling unsteady non-continuum flows, centred on the particle-based Direct Simulation Monte Carlo (DSMC) method.

As a first step, a basic particle tracking method and single processor DSMC code are used to investigate the physical mechanisms for the high precursor conversion efficiency and deposition uniformity observed in experimental reactors. This investigation reveals that at soon after the completion of the PP-CVD injection phase, the precursor particles have an approximately uniform distribution within the reactor volume. The particles then simply diffuse to the substrate during the pump-down phase, during which the rate of diffusion greatly exceeds the rate at which particles can be removed from the reactor. Higher precursor conversion efficiency was found to correlate with smaller size carrier gas molecules and moderate reactor peak pressure.

An unsteady sampling routine for a general parallel DSMC method called PDSC, allowing the simulation of time-dependent flow problems in the near continuum range, is then developed in detail. Nearest neighbour collision routines are also implemented and verified for this code. A post-processing procedure called DSMC Rapid Ensemble Averaging Method (DREAM) is developed to improve the statistical scatter in the results while minimising both memory and simulation time. This method builds an ensemble average of repeated runs over small number of sampling intervals prior to the sampling point of interest by restarting the flow using either

a Maxwellian distribution based on macroscopic properties for near equilibrium flows (DREAM-I) or output instantaneous particle data obtained by the original unsteady sampling of PDSC for strongly non-equilibrium flows (DREAM-II). The method is validated by simulating shock tube flow and the development of simple Couette flow. Unsteady PDSC is found to accurately predict the flow field in both cases with significantly reduced run-times over single processor code and DREAM greatly reduces the statistical scatter in the results while maintaining accurate particle velocity distributions. Verification simulations are conducted involving the interaction of shocks over wedges and a benchmark study against other DSMC code is conducted.

The unsteady PDSC routines are then used to simulate the PP-CVD injection phase. These simulations reveal the complex flow phenomena present during this stage. The initial expansion is highly unsteady; however a quasi-steady jet structure forms within the reactor after this initial stage. The simulations give additional evidence that the collapse of the jet at the end of the injection phase results in an approximately uniform distribution of precursor throughout the reactor volume.

Advanced modelling methods and the future work required for development of the PP-CVD method are then proposed. These methods will allow all configurations of reactor to be modelled while reducing the computational expense of the simulations.

List of Publications

Journal Papers in Publication

H.M. Cave, K.-C. Tseng, J.-S. Wu, M.C. Jermy, J.-C. Huang and S.P. Krumdieck. Implementation of Unsteady Sampling Procedures for the Parallel Direct Simulation Monte Carlo Method. *J. Comp. Phys.* (in press, 2008).

H.M. Cave, S.P. Krumdieck and M.C. Jermy, Development of a model for high precursor conversion efficiency pulsed-pressure chemical vapor deposition (PP-CVD) processing, *Chem. Eng. J.* 135, 120-128 (2008).

S.P. Krumdieck, **H.M. Cave**, S. Baluti, M. Jermy and A. Peled, Expansion Transport Regime in Pulsed-Pressure Chemical Vapor Deposition, *Chem. Eng. Sci.* 62 (2007) 6121-6128 (2007).

Journal Papers in Review and Preparation

H.M. Cave, K.-C. Tseng, J.-S. Wu, M.C. Jermy and J.-P Yu, The Improved Direct Simulation Monte Carlo (DSMC) Rapid Ensemble Averaging Method (DREAM-II) for Simulating Highly Non-Equilibrium Unsteady Rarefied Gas Flows, *J. Comp. Phys.* (in review 2008).

K-.C. Tseng, **H.M. Cave**, T.-C. Kuo, M.C. Jermy and J.-S. Wu, Implementation of the Transient Adaptive Sub-Cell Module for the Parallel DSMC Code, *J. Comp. Phys.* (in final preparation 2008).

M.R. Smith, **H.M. Cave**, Y.-S. Chen, M.C. Jermy and J.-S. Wu, Quiet Direct Simulation of Eulerian Fluids Using Second Order Schemes, *J. Comp. Phys.* (in final preparation 2008).

Refereed Conference Papers

H.M. Cave, K.-C. Tseng, J.-S. Wu, M.C. Jermy, Y.-Y Lian, S.P. Krumdieck, T.-C. Kuo and M.-Z. Wu. Modelling Unsteady Processes with the Direct Simulation Monte Carlo Technique. In Proc. of 16th Australasian Fluid Mechanics Conference, Gold Coast, Australia (2007).

H.M. Cave, J.-C. Huang, J.-S. Wu, S.P. Krumdieck, K.-C. Tseng, M.C. Jermy, M. Lebedev, K.-W. Cheng and Y.-S. Chen. Flow Field Modelling of Pulsed Pressure Chemical Vapour Deposition. In Proc. of 16th European Symposium on Chemical Vapour Deposition, Den Haag, The Netherlands (2007).

Other Publications and Presentations

J.-S. Wu, K.-C. Tseng, **H.M. Cave**, Y.-Y. Lian, J.-P. Yu, Y.-S. Chen, M.C. Jermy and S.P. Krumdieck. Developing a General-Purpose Parallelized Direct Simulation Monte Carlo Code (PDSC) Using Unstructured Grid: A Progress Report. Presentation at DSMC: Theory, Methods and Applications Workshop, Sante Fe, New Mexico (2007).

K.-C. Tseng, T.-C. Kuo, **H.M. Cave** and J.-S. Wu. Development of Unsteady-Flow Module for the Parallel DSMC Code. Presentation at the 14th National Computational Fluid Dynamics Conference, Nantou County, Taiwan (2007).

J.-S. Wu, K.-C. Tseng, Y.-Y. Lian, **H.M. Cave** and U.-M. Lee. PDSC User's Manual, National Chiao Tung University (Hsinchu, Taiwan, 2007).

H.M. Cave, S.P. Krumdieck and M. Jermy. Simulations of Reactor Efficiency for Pulsed Pressure Chemical Vapor Deposition (PP-CVD), In Proc. of the 25th International on Rarefied Gas Dynamics, St. Petersburg, Russia (2006).

1. Introduction

1.1 Thin Film Technology, Materials and Applications

Thin film materials are used in an enormous variety of applications and can be found in a vast array of modern manufactured products. In fact thin film materials have a longer history than one might suppose: the art of beating gold into a decorative "leaf" with thicknesses on the order of 1μm was practiced by the ancient Egyptians as long ago as 1500 B.C. [1]. Modern thin films are used for far more than purely aesthetic applications. The modification of a surface with a thin film is carried out to add some property which the base material would not otherwise possess. For example, a ceramic (metal oxide) film may be applied to a metallic substrate to protect the metal from high temperature environments or chemical attack. Thin films can be used to modify a variety of surface properties, including:

- optical (e.g. anti-reflective coatings, compact disc manufacturing)
- mechanical (e.g. hardness coatings, wear resistant films)
- electronic (e.g. semiconductors, conduction pathways)
- magnetic (e.g. hard disc manufacturing)
- thermal (e.g. thermal barrier coatings)
- chemical (e.g. corrosion protection, diffusion barriers)

A variety of materials can be deposited including metallic materials, ceramics, semi-conducting materials and polymers. New technologies, such as fuel cells and nano-scale devices, along with increasingly sophisticated electronic, optical, bio-medical and mechanical devices, continue to require new types of thin film materials and set new standards in required film purity, conformity and microstructural control [2]. These increasingly stringent material requirements necessitate advances in thin film deposition technology. Furthermore, the substrates upon which the films are deposited place additional demands on deposition technologies including the requirement to deposit over non-planar surfaces and complex shapes.

1.2 Deposition Technologies

The techniques used to deposit thin film materials can be categorised into three basic types of process [3]:

- physical vapour deposition
- liquid-phase chemical processes
- gas-phase chemical processes

Physical Vapour Deposition (PVD) processes are so named since no chemical reactions occur during the deposition, with the processes relying purely on physical phenomenon such as evaporation and condensation. These processes include evaporative and glow-discharge processing. In evaporative processes, the source material is evaporated and then condenses to a solid film on the substrate. The source material, which is usually metallic, can be evaporated in a number of ways: by resistive heating, exposure to an electron or ion beam, by radiation or by lasers.

Glow discharge processes evolved from sputtering. Here a target material is bombarded with a glow discharge plasma causing atoms from the target to be ejected into the gas phase. These atoms are out of thermodynamic equilibrium and so tend to deposit on any surface they come into contact with, including the reactor components and the substrate.

PVD generally results in a deposited film with the same composition as the source material and has the advantage of low substrate temperatures. It is used most commonly for integrated circuit processing and optical coating deposition on glass.

Liquid phase chemical processes involve the deposition of a film via chemical reaction in the liquid phase. Generally the substrate is immersed in or sprayed with a solution and a chemical reaction is induced in the liquid resulting in the deposition of a solid film on the substrate. Examples of these processes include electroplating, sol-gel processes and anodising.

In gas phase processes, generally referred to as Chemical Vapour Deposition (CVD), materials are transported to the deposition surface in the gas phase with the thin film being deposited on the substrate by the reaction of a compound or compounds on or near that surface. Other characteristics of the process are used to further categorise CVD, for example

the pressure regime in which the reactor operates enables the process to be classified as atmospheric pressure CVD (APCVD), low pressure CVD (LPCVD) or ultra-high vacuum CVD (UHVCVD). Usually heat is used to initiate the chemical reaction(s) resulting in the film deposition, however variations to this include chemical activation by exposure to a plasma or microwave radiation.

The development of metal-organic precursors, which have organic ligands attached to the metallic atoms, have resulted in a proliferation of metal-organic CVD (MOCVD) techniques which essentially involve the thermal decomposition of the precursor at or near the substrate thus depositing the desired solid metallic or ceramic coating. These processes have significant environmental advantages over the traditionally used halogenated compounds. A variation of MOCVD is atomic layer deposition (ALD), in which deposition is controlled to the atomic level by the use of self-limiting surface reactions.

An excellent review of CVD and related technologies is presented by Crowell [4].

1.3 Research Motivation: Pulsed Pressure Chemical Vapour Deposition

Pulsed Pressure Chemical Vapour Deposition (PP-CVD) was developed by Versteeg *et al.* [5] at Cornell University in Ithaca (NY), U.S.A. as a potential method of producing high uniformity thin films. In PP-CVD the precursor is injected into a continuously evacuated reactor volume in timed pulses, resulting in a time-variant reactor pressure. The precursor can either be liquid which is injected as an aerosol via an ultrasonic nozzle, or a gas which is injected from a high pressure source volume via an orifice. The process has a wide range of operating parameters, which can be easily controlled. Figure 1-1 shows a schematic of a typical gas-fed PP-CVD reactor showing the components in the system which are divided into injection, reactor, exhaust and control sub-systems.

The patent for PP-CVD is currently held by Sonotek Corporation in Milton (NY), U.S.A., however development of the PP-CVD process has been largely conducted by the group led by Krumdieck at the University of Canterbury in Christchurch, New Zealand. The experimental results conducted on prototype PP-CVD reactors indicate that the process is capable of producing highly uniform and conformal coatings at high deposition rates and very high precursor conversion efficiencies, while affording a high degree of microstructural control through varying the reactor operating parameters.

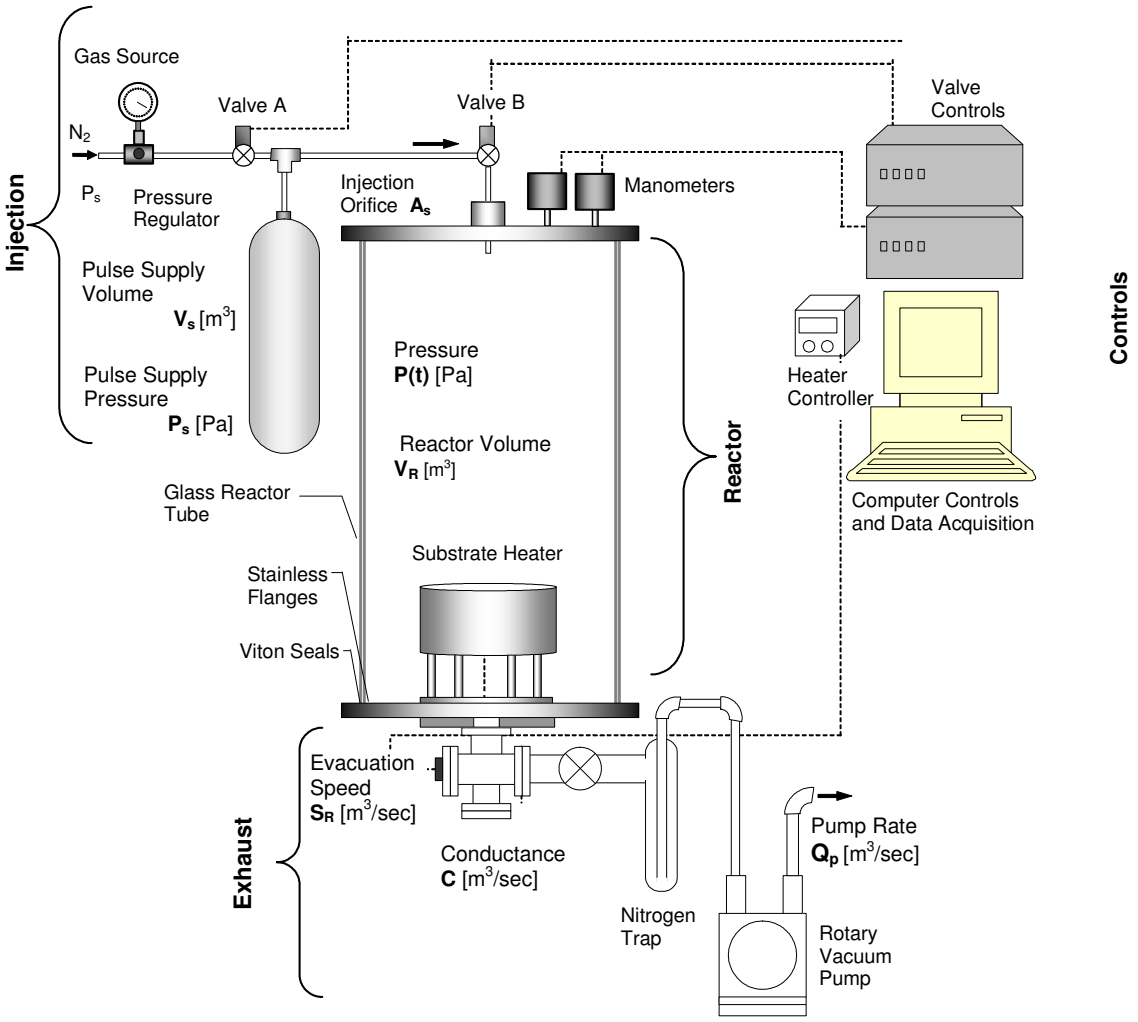

Figure 1.1. Schematic diagram of a typical PP-CVD reactor showing the primary design subsystems for control of injection, reactor, and exhaust [diagram courtesy of S.P. Krumdieck].

The potential of the PP-CVD process as an industrial deposition technology has initiated research into the process itself and into materials which can be deposited by the process. The physical mechanisms behind the PP-CVD process must be understood in order to effectively predict the performance for different reactor/deposition material configurations so that the process can be developed for specific industrial applications. The relationship between the time-dependent flow field and the material deposition process is needed for further development of the technology. The requirement to understand the PP-CVD flow field is the motivation behind this research.

1.4 Research Objectives

The goal for the PP-CVD research group is to develop a complete model of the Pulsed Pressure Chemical Vapour Deposition (PP-CVD) process from the flow field to the deposition kinetics, to develop deposition processes for new materials and to prepare reactor designs for industrial deployment.

Experimental investigations have already been carried which have identified the non-dimensional operating parameters for the PP-CVD process. However, theoretical treatment of the process from first principles and numerical model studies are required to reveal details important to reactor design and process control.

The objectives of the current research are thus:

- to develop simulation tools to model the flow field during the injection and pump-down phases
- to numerically investigate the PP-CVD flow field
- to investigate the physical mechanisms in the PP-CVD process which lead to the high reactor efficiency and excellent deposition uniformity observed experimentally.

Successful completion of these objectives will provide the basis for a simulation and experimental programme which can be utilised to further develop the PP-CVD process.

1.5 Thesis Organisation

Chapter 2 starts with an overall description of the CVD and provides the terminology required to understand the process. The role of the process flow regime in CVD reactors is discussed. This section focuses on the two most important parameters required to describe the flow processes: the Knudsen number and the Reynold's number. Pulsed Pressure Chemical Vapour Deposition (PP-CVD) is then described in detail and the state of knowledge on this process is presented. Firstly, the origins of PP-CVD are outlined. The results of material deposition experiments are then presented, including films from metal-organic precursors, diamond-like films and carbon nano-structures. An overview of the flow processes in PP-CVD is then given and seminal reactor models presented. The chapter concludes with a discussion of the experimental investigations carried out on the PP-CVD flow field to date.

Chapter 3 presents background information on the basics of flow dynamics and modelling. The historical background of gas kinetic theory is outlined, and then particle collision dynamics are discussed. This leads to a discussion on the development of the kinetic theory of gases and the Boltzmann equation. The continuum assumption leading to the Navier-Stokes equations via a Chapman-Enskog expansion is then outlined and the approximate collision terms leading to model Boltzmann equations, in particular the Bhatnagar-Gross-Krook (BGK) approximation, are then reviewed. The requirement for a particle based modelling method is then presented, and the Direct Simulation Monte Carlo (DSMC) is then introduced. The basic DSMC procedures and collision models are outlined, and advanced methods including parallel and hybrid implementations are reviewed.

Chapter 4 presents a conceptual approach for the flow dynamics of PP-CVD and discusses potential modelling methods. Here the important distinction between the injection and pump-down phases of PP-CVD is detailed and important process terminology is introduced. The validity of the continuum assumption during the injection phase is then analysed using a spatial-temporal continuum breakdown parameter. The results of experimental investigations show that when the PP-CVD flow field is most uniform, there are significant regions of the flow field under-going continuum breakdown during the injection phase. The influence of breakdown within the reactor is also investigated using a simple computational fluid dynamics (CFD) approach. The selection of an appropriate modelling methodology is then presented.

The next 4 chapters of the thesis are devoted to the development and implementation of modelling techniques for PP-CVD. Chapter 5 presents the results of basic single-processor DSMC simulations of representative PP-CVD reactors. Commercially available DSMC code is used to generate the flow field of a background carrier gas, and a particle tracking model is used to trace representative precursor particles through this flow field. The development of this simple particle tracking model is discussed in detail, and a number of validation studies are presented. These simulations allow an understanding to be developed of the physical mechanisms leading to high reactor efficiency and deposition uniformity. The limitations of this study are then discussed in detail.

Chapter 6 presents the development of a parallel-DSMC (PDSC) code to enable the simulation of PP-CVD processes at a greater range of operating pressures. PDSC is first

introduced and the existing features of this code are then outlined. The requirement for an unsteady sampling technique, transient sub-cells and a method of reducing the statistical scatter in the results is introduced. For each of these a method is developed, implemented into PDSC and validation studies conducted. These include a benchmark test comparing PDSC to other contemporary DSMC code. The chapter concludes with several application case studies including the development of Couette flow and the interaction of shocks on two-dimensional wedges. These simulations demonstrate the capacity of PDSC to model unsteady near-continuum processes with acceptably fast run-times and serve as further verification of the method.

In chapter 7 the unsteady PDSC code is applied to a test case cylindrical PP-CVD reactor. In these simulations, a basic coupled Navier-Stokes/DSMC method is used allowing a significant reduction in the computational expense of using PDSC alone. Two cases are modelled using different supply pressures and the limitations of the technique are discussed.

In chapters 8 and 9, suggested future work is presented. Chapter 9 focuses on the continued development of modelling tools suitable for PP-CVD. Extensions to the DSMC scheme and PDSC are proposed. Several other promising schemes are also proposed, including hybrid methods with continuum solvers and a novel Model Boltzmann Equation (MBE) scheme utilising the Conservation Element/Solution Element (CE/SE) approach. Chapter 10 includes a discussion on the reactor development process, the required experimental validation of the present work and the requirement to extend the work to liquid fed PP-CVD reactors. Finally the concept of plasma assisted PP-CVD is introduced.

Please also note that references are listed at the end of individual chapters.

References

[1] M. Ohring, Materials Science of Thin Films: Deposition and Structure (Academic Press, San Diego 2002).

[2] K.K. Schuegraf (ed.), Handbook of thin-film deposition processes and techniques : principles, methods, equipment, and applications (Noyes Publications, Park Ridge, N.J., 1988).

[3] K. Seshan (ed.), Handbook of thin-film deposition processes and techniques : principles, methods, equipment and applications (Noyes Publications, Norwich, N.Y., 2002).

[4] J.E. Crowell, Chemical methods of thing film deposition: Chemical vapor deposition, atomic layer deposition and related technologies, *J. Vac. Sci. Technol. A.* 21(5), S88-S95 (2003).

[5] V.A. Versteeg, T.A. Avedisian and R.Raj, Method and Apparatus for CVD using Liquid Delivery System with Ultrasonic Nozzle US Patent No: 5 451 260, September 19, 1995 Sono-Tek Corp. licensee (1995).

2. Physical Processes in PP-CVD

2.1 CVD Chemistry and Physics: A Process Overview

The generalised physical and chemical processes involved in CVD are illustrated schematically in figure 2.1. The reactants are delivered into the reactor volume by the delivery system (1), are transported to the surface (2), diffuse through any concentration gradient which may be present (3), are then adsorbed onto the surface (4), nucleate (6), undergo surface diffusion and are incorporated into the crystal lattice (7). Reaction products then desorb and diffuse away from the substrate (8) and are transported out of the reactor in the exhaust (10). In certain systems, all or part of the precursor decomposition reaction may occur in the gas phase rather (9) than on the substrate surface (5).

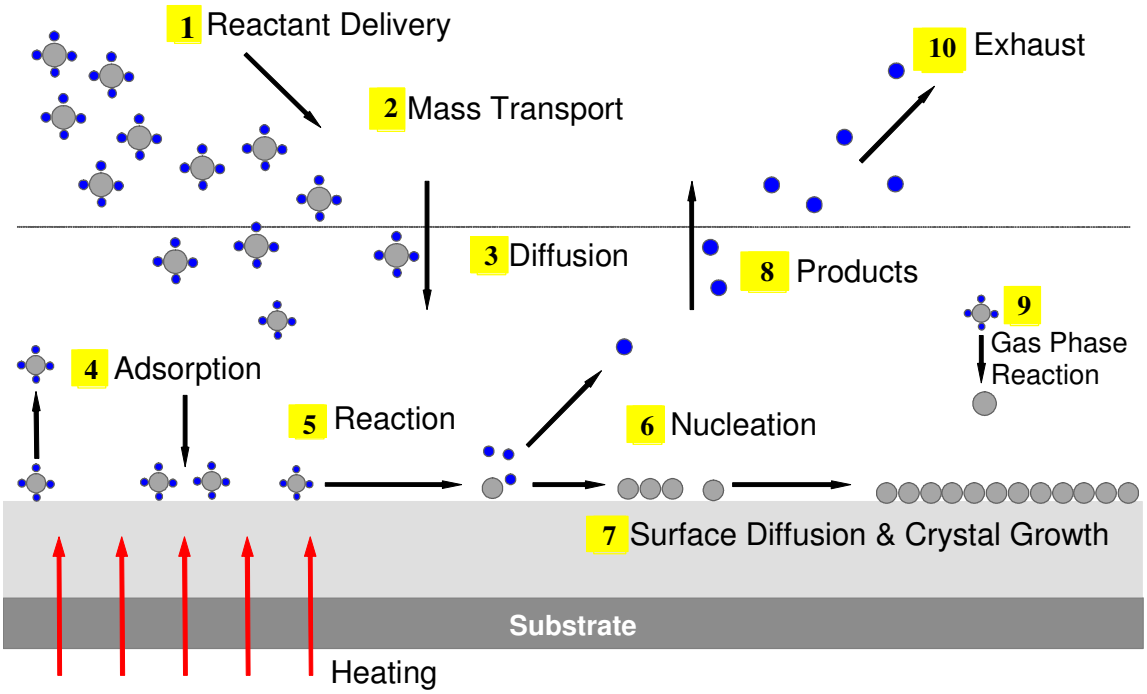

Figure 2.1. Mass transport and surface kinetics in a typical CVD process [diagram courtesy of S.P. Krumdieck].

The overall process can be broken down into two parts: (a) the mass transport of the reactants to and products away from the substrate; and (b) the surface processes. Typically, amongst the steps shown in figure 2.1, there will be a rate limiting step, which is the slowest step in the entire CVD process, and this will control the overall deposition rate. The control types can be broken down into three categories [1]:

1. Type I Mass Transport - here the transport of reactants to, or of products away, from the deposition zone is the rate limiting step. In other words, the main gas flow limits the deposition rate.

2. Type II Mass Transport - the diffusional or convective mass transport between the main gas flow and the substrate is the rate limiting step.

3. Kinetic Control - the surface kinetics limit the speed of the process. These steps include the reactant adsorption, chemical reactions and the surface migration/lattice incorporation.

The modelling of each of the steps in figure 2.1 is an important step in the research into and the design of CVD reactors. For any particular application, the desired film can only be produced by an appropriate set of conditions at the substrate. These deposition conditions can be controlled by manipulation of the process control parameters such as temperature, reactor pressure and mass flow rate [2]. Furthermore, understanding each process enables the rate limiting step to be readily determined, which has direct consequences on precursor conversion efficiency, deposition rate and film microstructure. This in turn enables reactors to be optimised for specific deposition applications. Interestingly, the design of many CVD reactors is made by trial-and-error or rule-of-thumb processes – an expensive and time-consuming task.

2.2 CVD Flow Classification

As mentioned above, the mass transport of precursor through the CVD reactor and to the substrate is an important step in understanding the process. Consequently, modelling the flow through the reactor is a critical step in reactor design and optimisation. This is particularly true when a reactor is being developed for a new process, or operates in a fundamentally different manner from established CVD technology. Hitchman and Jensen's diagram of CVD modelling complexity [3] shows that with 3D transport phenomena and complex chemistry, geometric complexity of the reactor is inevitable in an actual CVD process. This means that the design of a reactor for a particular application is often unique and, in many cases, un-scalable.

Because of the large variety of CVD reactor configurations, the flow within the reactor may encompass one or several flow regimes from laminar or turbulent viscous flow, transition flow, rarefied flow or molecular flow. Two dimensionless parameters which are important in distinguishing between CVD flow regimes are the Reynolds (Re) and the Knudsen (Kn) numbers:

$$\mathrm{Re} = \frac{\rho V L}{\mu} = \frac{V L}{\nu} \tag{2-1}$$

$$Kn = \frac{\lambda}{L} \tag{2-2}$$

where ρ is the fluid density, V is the flow velocity, L is a characteristic dimension, μ is the viscosity, ν is the kinematic viscosity and λ is the mean free path.

The Reynolds number expresses the ratio of inertial to viscous forces and thus gives the relative significance of those forces within the flow. Laminar flow occurs when the viscous forces are dominant (i.e. Reynolds number is low) and the flow field appears smooth. Turbulent flow occurs when inertia forces are dominant (i.e. at high Reynolds number) and the flow is characterised by the presence of highly random eddies and fluctuations. The transition between the two regimes is not immediate, but occurs gradually [4].

The Knudsen number gives the ratio of molecular mean free path (the distance between intermolecular collisions) to some characteristic flow dimension and expresses the relative level of rarefaction of the flow. In flows with a low Knudsen number, the gas density is sufficiently high that effects at the molecular level can be ignored and the flow can be treated as a mathematical (and physical) continuum for modelling purposes [5]. In these cases, the flow can be represented by a continuum model such as the Navier-Stokes equations, which will be discussed in more detail in section 3.4. However, as the Knudsen number becomes large, effects at the molecular level become significant and the continuum models become invalid. In such cases statistical mechanics must be considered, as will be discussed in section 3.3.

In general, both the Reynolds and Knudsen numbers are based on some characteristic flow dimension (i.e. the diameter of the pipe for internal flow, the diameter of the orifice of a jet etc), however this can be misleading. Generally, the Navier-Stokes equations are assumed to be valid when the Knudsen number is less than approximately 0.1, however locally within the

flow field the value may be much greater than this. For this reason, it is useful to define a local Knudsen number. Here the local mean free path is compared to the scale length of any macroscopic gradient Q which can be density, temperature, pressure or velocity [6]:

$$Kn_Q = \frac{\lambda}{L} \qquad \text{where} \qquad L = \frac{Q}{\left| \partial Q / \partial x \right|} \tag{2-2a}$$

In regions where flow gradients are large, for example in shock structures, the local Knudsen number may be large enough for the continuum assumption to be invalid. Where this occurs, the use of continuum equations to model the entire flow field would be inappropriate, even though the overall Knudsen number based on some characteristic flow dimension may be quite small. In other words, continuum breakdown may have occurred locally within the flow field and so caution must be exercised when choosing an appropriate flow modelling technique for a particular CVD process.

CVD reactors are generally classified depending on their operating pressure. Atmospheric pressure CVD (AP-CVD) reactors operate in the continuum flow regime at close to atmospheric pressure. In processes which are mass transport limited (as opposed to kinetically limited), the rate of deposition in AP-CVD reactors tends to be diffusion limited (mass transport type II control) since diffusivity decreases with increasing pressure. Because film growth is limited by the diffusion of reactant and products through the boundary layer to the substrate, reactors must be designed to ensure that no regions of the deposition surface suffer reactant depletion with consequent poor deposition uniformity [7]. Methods used to overcome this include susceptor tilt, shower-head type precursor inlets and rotating susceptors. Further complicating the flow dynamics in these reactors is the presence of temperature gradients resulting in buoyancy driven flows. Deposition on non-planar substrates in LP-CVD reactors is very difficult due to the strong influence of a non-planar surface on the complexity of the boundary layer. The result is that AP-CVD reactors generally have great geometric complexity and often can only be used for a unique combination of reactant, substrate shape and material. Hitchman and Jensen provide an excellent summary of the complex transport phenomena present in reactors operating within the viscous flow regime [3].

Low pressure CVD (LP-CVD) was developed in the 1970s to overcome some of the difficulties associated with the well-established AP-CVD process. By the reduction of the

reactor pressure, the diffusivity can be increased dramatically, meaning diffusion is no longer the rate limiting process. The result of this was reduced process cost over AP-CVD due to some simplifications in reactor design [8], however because of the reduced reactor pressure it is necessary to increase the reactant concentration to maintain deposition rates comparable to AP-CVD. The enhanced diffusivity of the reactants means that planar substrates can be positioned normal to the flow and at close intervals and this increased substrate "stacking" means LP-CVD reactors have high throughputs compared to AP-CVD [7]. Furthermore LP-CVD tends to have better film quality and uniformity, along with reduced film contamination, compared to AP-CVD.

Ultra-high vacuum CVD (UHV-CVD) reactors operate at pressures typically below 0.001 torr (~0.1Pa), and were developed as a solution to the problems of auto-doping in high temperature silicon epitaxy [7]. Such low pressures are outside of the continuum flow regime, so these reactors operate in the rarefied flow regime. UHV-CVD reactors are able to produce films of very high purity, however because of the high vacuum the molecular impingement rate of molecules on the substrate is so low that deposition rate is very slow.

The way in which the deposition reaction is activated also affects the flow field and is used to further characterise the reactors. Often, heat is used to initiate the reaction. Hot wall reactors, in which the entire reactor volume is heated in an oven, provide good temperature uniformity however result in deposition on surfaces other than the substrate, particle contamination and poor precursor conversion efficiency. Cold wall reactors, in which only the substrate is heated, alleviate some of these problems and generally have lower construction costs, however providing uniform substrate heating is challenging. Plasma systems also can be used to initiate deposition and require lower substrate temperatures, however these systems are generally high cost.

Interested readers should refer to the review of CVD reactors and precursor delivery technology by Krumdieck, for a highly readable background on contemporary CVD system design [2].

2.3 Pulsed Pressure Chemical Vapour Deposition

2.3.1 PP-CVD Process Overview

As mentioned in section 1.3, the process of interest in this thesis is the Pulsed Pressure Chemical Vapour Deposition (PP-CVD) reactor proposed by Versteeg *et al.* [9] and further developed by the group led by Krumdieck. In this process a gaseous precursor is injected through an orifice or a liquid metal-organic precursor is introduced via an ultrasonic nozzle into a continuously evacuated reactor volume. The introduction of the precursor is not carried out continuously, but in timed pulses followed by a pump-down period. This results in the characteristic pulsed-pressure profile shown in figure 2.2, along with a schematic of a simple gas fed PP-CVD reactor.

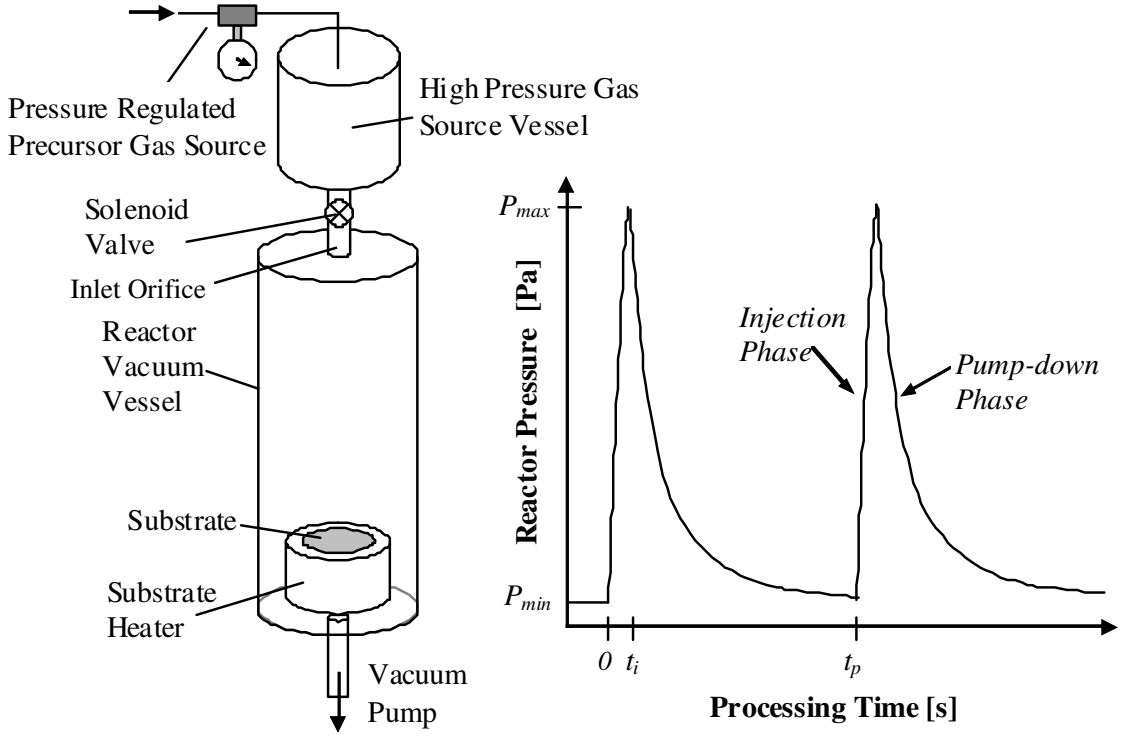

Figure 2.2. Pulsed Pressure Chemical Vapour Deposition (PP-CVD) reactor schematic and reactor pressure over several pulse cycles [diagram courtesy of S.P. Krumdieck].

During the injection phase of the process ($0 < t < t_i$) a solenoid valve is opened which releases the precursor from the high pressure source vessel into the reactor volume which is at the initial reactor pressure P_{min}. When the valve closes at $t = t_i$ the reactor is at its maximum pressure of P_{max}. During the pump-down period ($t_i < t < t_p$) the reactor is evacuated by the vacuum pump. This cycle is repeated continuously throughout the deposition process.

With reference to figure 2.1, we note that in conventional steady-state CVD processes, every step in the deposition process is happening simultaneously. In PP-CVD, these processes occur in series over each individual pulse. Firstly the precursor is introduced into the reactor and then it is transported to the reaction surface, where it undergoes the deposition reaction. The reaction products are then transported away from the surface. Although these individual processes may overlap, they do not happen simultaneously over the entire length of the pulse cycle.

It has been demonstrated experimentally by Krumdieck and Raj [10] that even at relatively high processing pressures the deposition rate is a function of the reaction temperature T (proportional to $1/T$), equivalent to what would be expected for steady flow CVD reactors. Thus, at low temperatures the growth rate follows an exponential Arrhenius type behaviour, indicating that here reaction kinetics are the controlling process. With increased temperature, the growth rate becomes constant (proportional to T) indicating the reaction speed is limited by the reactant supply rate rather than the rate of diffusion to the substrate. In contrast, in steady flow CVD reactors the deposition rate in the diffusion controlled regime is a function of T^2 since the diffusivity increases with the square of temperature. Krumdieck and Raj postulated that the non-steady state flow field in PP-CVD means that diffusion does not limit the rate of deposition.

2.3.2 Deposition by PP-CVD

Thin film deposition by PP-CVD has already been reported for a wide variety of materials from both liquid and gas precursors. The earliest depositions using the technique were carried out by Xie and Raj [11] who deposited lithium tantalate ($LiTaO_3$) on sapphire from a liquid metalorganic precursor of lithium tantalate hexa-*t*-butoxide. Lithium tantalate is an optical film which can be used to manufacture blue light emitters when integrated with semiconductor diodes. Soon after, the technique was used by Versteeg *et al.* to deposit titanium dioxide (TiO_2 or titania) on sapphire from titanium tetra isoproxide (TTIP), also a liquid metalorganic precursor [12]. Titania films have a wide range of applications including thermal barrier coatings, optical coatings, semiconductors, as a photocatalyst in solar cells and even as a coating to promote osseointegration between bone and medical implants.

Titania deposition experiments were also carried out by Krumdieck *et al.* [10,13-16], with increased emphasis on characterising and modelling both the deposition process and the

reactor itself. These studies showed that by varying substrate temperature and precursor concentration, PP-CVD is capable of producing a wide range of microstructures. The group also reported high precursor conversion efficiency and good deposition uniformity. Figure 2.3 shows optical and scanning electron microscope (SEM) images of titania films deposited by PP-CVD.

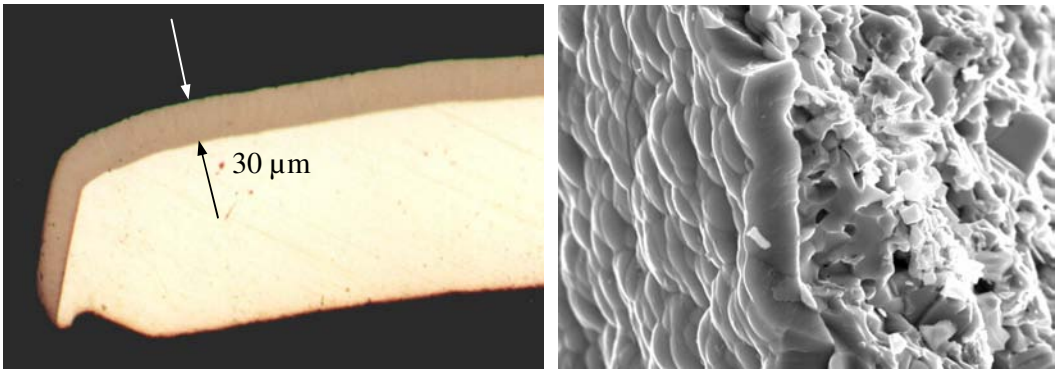

Figure 2.3. Cross sectional optical micrograph (left) and SEM image (right) of titania films deposited on nickel from TTIP precursor by PP-CVD [10].

Deposition of yttria-stabilised zirconia (YSZ) films by PP-CVD have also been carried out by Krumdieck *et al.* [17,18]. The YSZ films were deposited onto solid oxide fuel cell electrodes to act as an electrolyte layer. PP-CVD was found to be a viable method for the manufacture of the electrolyte layers due to its high efficiency and low reactor/metal-organic precursor cost. Figure 2.4 shows an SEM image of a YSZ layer as deposited on the porous solid oxide fuel cell electrode

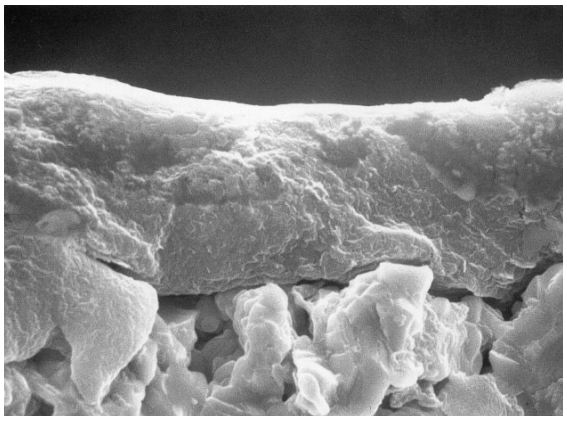

Figure 2.4. SEM image of a YSZ electrolyte layer deposited on the electrode of a sold oxide fuel cell by PP-CVD [18].

Ongoing research includes the deposition of titania onto patterned silicon substrates by Siriwongrungson *et al.* [19]. Such conformal films on patterned substrates have potential applications in photovoltaic devices and anti-stick coatings for moulds for nano-imprint lithography processes. The conformality of the films was assessed on a statistically and found to exceed 80%. Figure 2.5 shows a titania film on a patterned silicon substrate produced using PP-CVD.

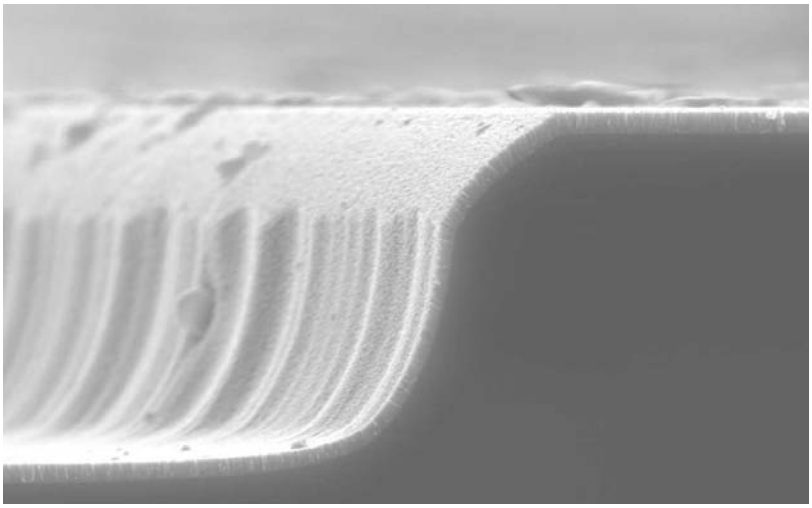

Figure 2.5. Titania film deposited on a patterned silicon substrate using PP-CVD showing high film conformality and thickness uniformity [19].

Work at the University of California at Irvine in collaboration with the University of Canterbury is also being conducted using PP-CVD. Here PP-CVD is used to deposit films of

zirconia and various analysis techniques are used to attempt to build a model of film growth. The results are compared to similar films deposited using a sol-gel technique.

As part of the research presented in this thesis, depositions were also made from gaseous precursors. The PP-CVD process is ideally suited to gas deposition and most experimental work investigating the flow field to date has been carried out assuming a gas-supplied system (see section 2.3.5). Unfortunately most gaseous precursors for thin film manufacture are highly dangerous due to their toxicity and/or pyrophoric properties (for example, the deposition of silicon from silane gas) [20]. For safety reasons, experimental depositions from methane were conducted. A dilute mixture of methane in hydrogen can be used to manufacture both diamond films and carbon nano-structures by CVD. Diamond films have a vast array of engineering applications due to their remarkable material properties including extremely high mechanical hardness, thermal conductivity, electrical resistivity and corrosion resistance; along with low compressibility and thermal expansion. Diamond films also can be doped to become semiconductors, have very high optical transparency and high wear resistance [21]. Diamond films can be used for applications as diverse as tool coatings, speaker diaphragms, window coating and heat sinks in a global market estimated to be worth over $US1 billion and rapidly rising [22]. Carbon nanostructures also have remarkable properties and a vast number of potential applications. For example, carbon nano-tubes were first discovered by Wiles and Abrahamson at the University of Canterbury in 1978 [23], however their true potential was realised much later. They have very high strength, unique electrical properties and conduct heat very readily, with many potential applications [24, 25].

There are several processes for manufacturing diamond films. Most commonly a plasma is generated using either a microwave generator or a DC arc. A dilute mixture of methane (CH_4) in hydrogen (H_2) is introduced which dissociates within the plasma to form reactive species which then deposit on a heated substrate. An alternative, and simple, method is hot filament or hot wire CVD in which a hot wire is placed just above the substrate. This wire, typically made from tungsten or tantalum, is maintained at approximately 2200ºC to dissociate the precursor which then deposits on the substrate which is heated to approximately 800ºC. The mechanism for deposition is complex and involves a multi-stage process consisting of deposition and etching by atomic hydrogen. Detailed reviews of diamond deposition CVD and the deposition mechanism can be found in the review by May [21].

In the hot wire PP-CVD experiments, a small modification was made to the basic reactor configuration shown in figure 2.2 by placing a tungsten wire array above the substrate. This was heated to approximately 2000ºC by applying an electric current to the wire. A silicon substrate was heated to approximately 600ºC and a mixture of methane in hydrogen was pulsed into the reactor. The concentration of methane was varied between 1 and 5 vol% and the pulse pressure range was maintained between 30Pa and 800Pa with a pulse time of 20s. It was found that concentrations of methane of around 5vol% resulted in the production of nanofibres, whereas lower concentrations produced diamond films. Figure 2.6 shows SEM images of a variety of the nano-fibres and diamond films produced using this technique. Work is ongoing to further develop this process, overcome technical difficulties and characterise the materials produced.

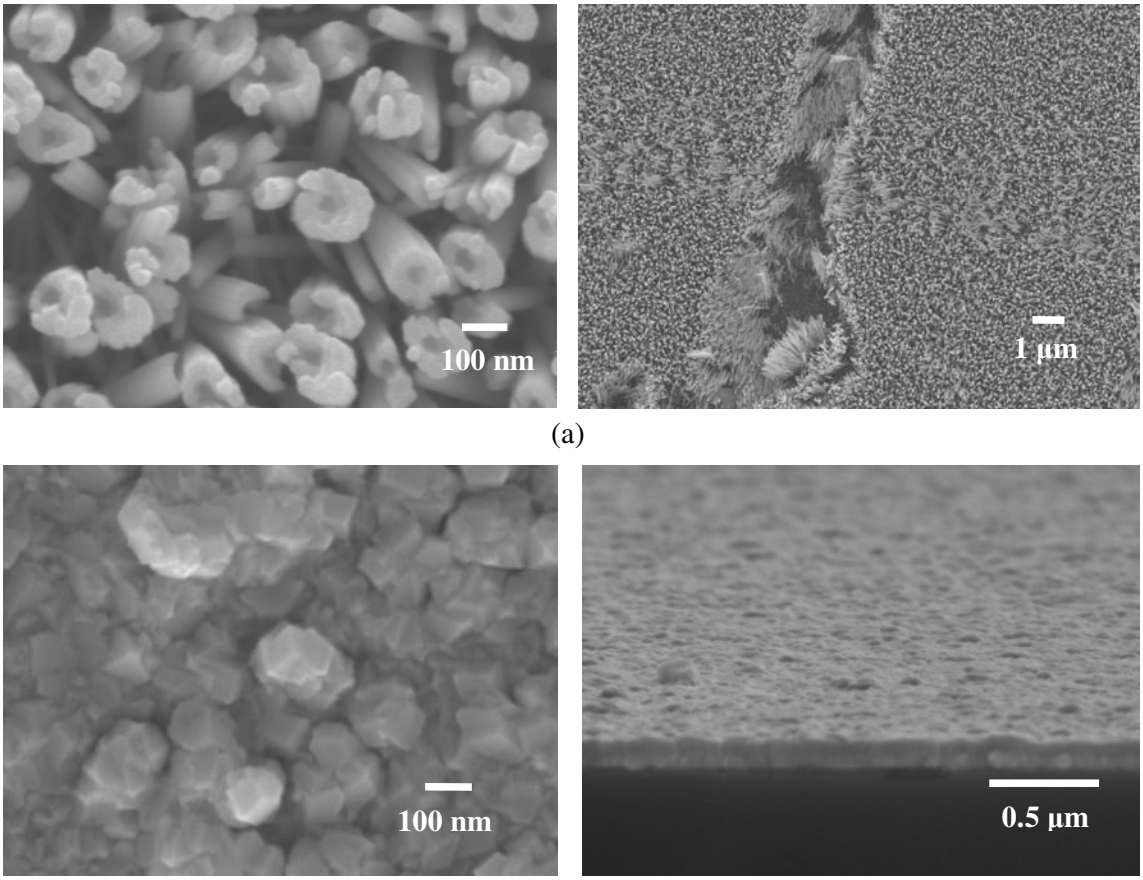

Figure 2.6. a) Carbon nano-fibres and b) diamond films deposited by hot wire PP-CVD.

Already a wide variety of materials have been produced from both liquid and gaseous precursors using basic experimental PP-CVD reactors. Further research will no doubt yield new possibilities in this area and expand the range of PP-CVD's material deposition utility.

2.3.3 PP-CVD Flow Regime

As can be seen from figure 2.2, the PP-CVD process consists of an injection phase followed by a pump-down phase. These two phases are repeated continuously throughout the deposition process. During the injection phase, a solenoid valve opens releasing the high pressure precursor gas through an orifice and into the low pressure reactor volume. The injection phase is typically very short, on the order of 0.1s. The high pressure differential between the inlet and the reactor volume means the precursor gas expands rapidly as an under-expanded jet. During the pump-down phase the solenoid valve between the precursor supply volume and the reactor is closed and the reactor is evacuated by the vacuum pump. This process is longer, on the order of 40s.

A consequence of this unique operating regime is that the process gases tend to be in a continuous state of overall expansion. First the gases expand rapidly as a jet from the inlet nozzle during the injection phase, and then more slowly as the reactor is evacuated by the vacuum pump. As will be shown in section 4.1, during this process the gas flow within the reactor cannot be modelled by continuum equations.

2.3.4 Process Models

The first basic model of the flow within the pulsed pressure CVD reactor was presented by Krumdieck [16] as part of her deposition kinetics model. Here the flow was simply assumed to be well mixed plug flow which fills the reactor volume above the substrate instantaneously with a homogeneous mixture of precursor vapour at the start of each pulse cycle. The pressure immediately above the substrate was then assumed to drop during the pump down phase by:

$$P(t) = P_{\min} + (P_{\max} - P_{\min})\exp\left(-\frac{t}{\tau_P}\right) \tag{2-3}$$

where τ_P is the experimentally determined pump-down time constant.

The bulk vapour temperature in the λ-layer, a layer above the substrate one mean free path in height, was assumed to be spatially uniform and vary with time according to:

$$T_v(t) = T_0 + \left(\frac{T_P - T_0}{t_P} \right) t \tag{2-4}$$

where T_0 is the bulk vapour temperature at the start of the pump-down phase and T_P is the temperature at the end of the pump-down phase. This basic model, when combined with a kinetic model film growth rate, was found to fit experimental data for titania deposition reasonably well.

More recent studies [26] have been dedicated solely to investigating the molecular flux within the reactor and are summarised here. The number of molecules within a reactor of volume V_R and temperature T_R at time t is given by the ideal gas law:

$$n(t) = \frac{P(t) V_R N_A}{R_0 T_R(t)} \tag{2-5}$$

The reactor is continuously being evacuated by a vacuum system with a volume displacement rate S_P and a conductance C, at a rate of Q_P given by:

$$Q_P = \frac{S_P C}{S_P + C} \tag{2-6}$$

A mass balance on the reactor, which has a negligible leak rate and a minimum number of molecules n_{min} at the end of the pump down cycle, is given by:

$$n_L dt - \frac{Q_P}{V_R} \left[n(t) - n_{\min} \right] dt = d\left[n(t) - n_{\min} \right] \tag{2-7}$$

By integrating this equation over the entire pulse a dimensionless reactor pressure $P^*(t)$ can be defined as:

$$P^*(t) = \frac{P(t) - P_{\min}}{P_{\max} - P_{\min}} = \exp\left(-\frac{t}{\tau_R} \right) \tag{2-8}$$

where the reactor time constant $\tau_R = \frac{V_R}{Q_P}$ and $P_{\max} = P_s \left(\frac{V_s}{V_R} \right) \left(\frac{T_R}{T_s} \right) + P_{\min}$. Here P_S, V_S and T_S are the pressure, volume and temperature of the precursor supply volume respectively. Baluti

found [27] that the maximum and minimum pressures are repeated continuously throughout the deposition process if the pump-down time $t_P \geq 4\tau_R$.

Assuming that the Maxwell-Boltzmann relation applies, the mean free path is given by [28]:

$$\lambda = \frac{1}{\sqrt{2}\pi n \xi^2} = \frac{kT}{\sqrt{2}\pi \xi^2 P} \tag{2-9}$$

The incidence rate of molecules striking an elemental area of internal reactor surface is (molecular flux):

$$\phi = \left(\frac{n}{2\pi^{1/2}} \right) \sqrt{\frac{2kT}{m}} \tag{2-10}$$

And for a reactor having an internal surface area A and volume V, the important ratio of intermolecular to molecule-wall collisions can be shown from the above definitions to be:

$$\frac{X}{N} = \frac{4\sqrt{2}\pi n \xi^2 V}{A} \tag{2-11}$$

Equation (2-11) can thus be modified to give the ratio of intermolecular collisions X to the number of molecule-wall collisions for this time-variant flow:

$$\frac{X}{N}(t) = \frac{4\sqrt{2}\pi n(t) \xi^2 V_R}{A_R} = \frac{4\sqrt{2}\pi \xi^2 N_A V_R}{R_0 T_R A_R} P(t) \tag{2-12}$$

The molecular flux from equation (2-10) can also be modified to assume a time-variant form:

$$\phi(t) = \left(\frac{n(t)}{2\pi^{1/2}} \right) \sqrt{\frac{2kT_R}{m}} = \frac{P(t) N_A}{\sqrt{2\pi n R_0 T_R}} \tag{2-13}$$

By combining equations (2-8) and (2-13) and integrating them over one pulse cycle we obtain the total flux per unit area per pulse cycle as being:

$$J_P = \left[\frac{N_A}{\sqrt{2\pi n R_0 T}} \right] \left[P_{\min} t_P + \tau (P_{\max} - P_{\min}) \left(1 - e^{-t_P/\tau} \right) \right] \tag{2-14}$$

This allows the definition of a pulsed non-dimensional molecular flux or exposure J_P^*:

$$J_P^* = \frac{J_P - J_{\min}}{J_{\max} - J_{\min}} = \frac{\tau}{t_P}\left(1 - e^{-t_P/\tau}\right) \quad \text{where} \quad J_P = \phi\, t_P \tag{2-15}$$

2.3.5 Experimental Investigation of PP-CVD Flow Field

A number of strategies have been explored to investigate the PP-CVD flow field experimentally. The highly unsteady nature of the flow makes most standard experimental techniques, such as Schlieren imaging and smoke visualisation, extremely difficult if not impossible. One method of investigating the flow field was to measure the convective uniformity throughout the reactor volume using a naphthalene sublimation technique adapted from the method of Souza-Mendes [29] by Krumdieck *et al.* [26, 30] and Baluti [27].

In this naphthalene sublimation technique, it was reasoned that the relative convective conditions at different positions in the reactor could be assessed through evaporation of solid naphthalene, and that the flow phenomena that drives evaporation would be the same as for deposition. In the experiments, 10mm diameter cylinders of naphthalene were cast and suspended by fine wires in the reactor as shown figure 2.7. These cylinders were sized so that there was minimal flow shadowing from upstream cylinders on those downstream during steady flow as verified by CFD modelling [27]. A cylindrical glass reactor 530 mm high and 210 mm in diameter was used with a nitrogen source gas pressure P_S of 350 kPa. The reactor pressure was measured through connections near the gas inlet using MKS capacitance manometers.

Specific sublimation rate depends strongly the rate of transport of vapour away from the naphthalene cylinders i.e. the local flow velocity. With this measurement strategy, the cumulative effect of convection over a number of pulses could be compared at different locations. However, because evaporation rate is highly sensitive to pressure and temperature as well as convection, the absolute value of sublimation rate between tests at different processing conditions cannot be meaningfully compared. Rather, the relative sublimation rate between points in the reactor for any given set of conditions is the relevant measurement.

A number of experiments were carried out on both pulsed and steady flow reactors of the same geometric configurations. In these experiments, the specific sublimation rate for each of

the six samples was calculated as the weight loss divided by the cylinder surface area. The pulsed tests were of 20 minutes duration, comprising an initial two minute pump-down and 30 pulse cycles. The naphthalene sublimation measurement error was calculated to be less than ±2%. The test was calibrated by running a 20 minute sublimation test with the reactor at vacuum conditions (e.g. no pulsing gas). The specific sublimation rate is strongly dependent on the temperature, however only the relative sublimation rate between cylinders is necessary to illustrate the convective uniformity of the flow.

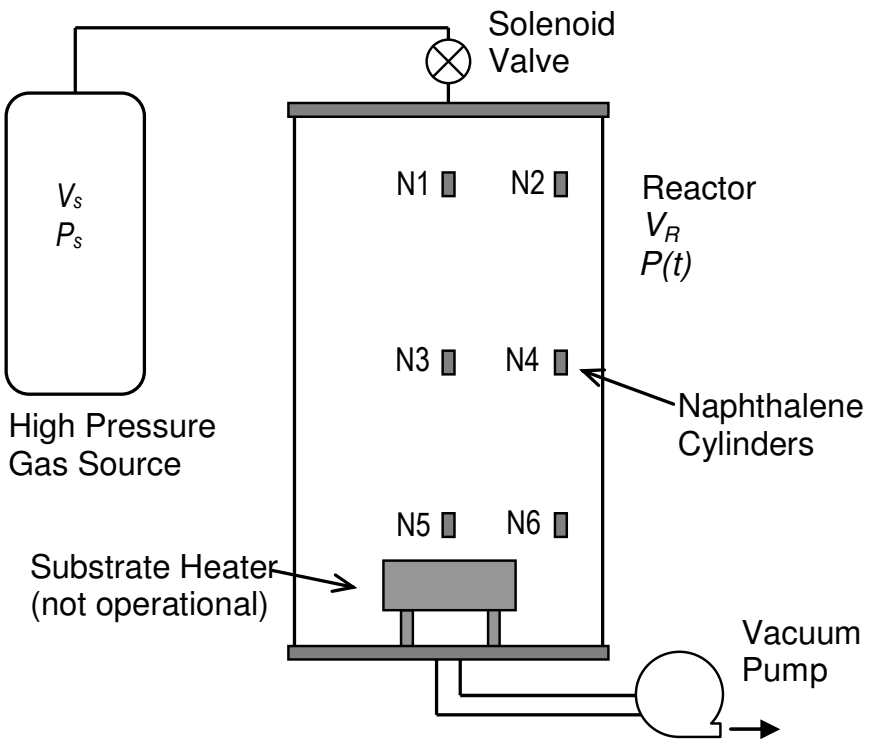

Figure 2.7. Reactor configuration and relative naphthalene cylinder positions used in convective flow field uniformity experiments [diagram courtesy of S.P. Krumdieck].

Figure 2.8 shows the sublimation rates of the cylinders for several relatively high pressure steady flow experiments. Here naphthalene cylinders N1 and N3 exhibit high rates of sublimation as they are within the region of influence of the expanding jet, resulting in poor convective field uniformity.

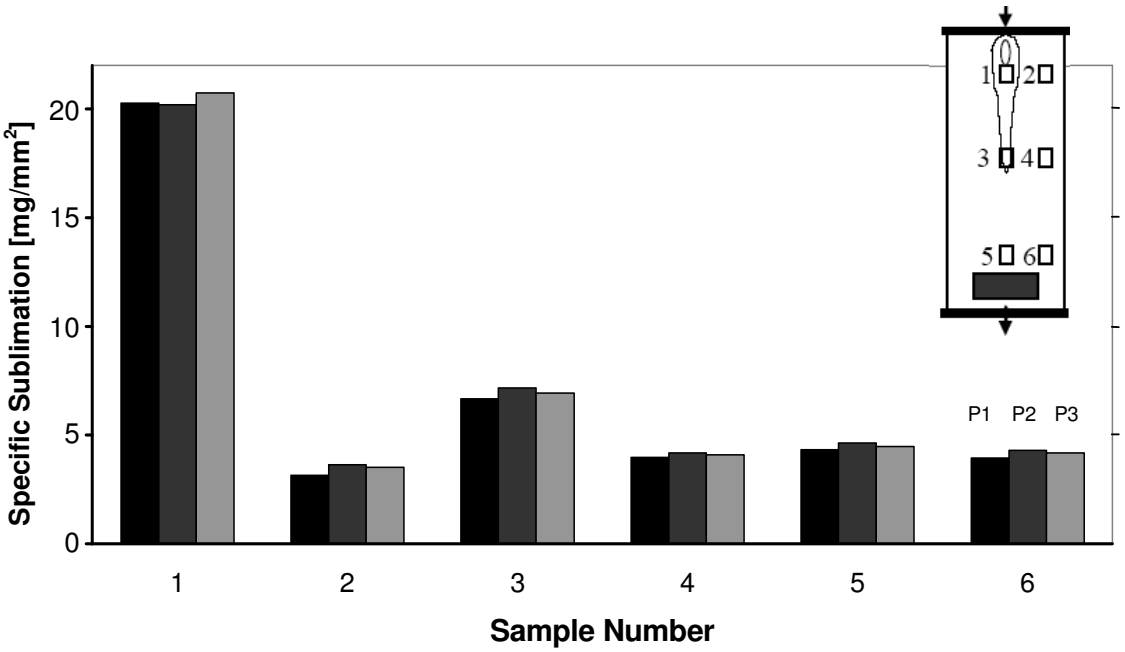

Figure 2.8. Naphthalene specific sublimation results for steady nitrogen gas flow over a range of reactor pressures (P_1 = 3080Pa, P_2 = 2618Pa, P_3 = 2000Pa). Inset shows the approximate structure of a steady gas jet along with the relative locations of the naphthalene cylinders [30].

Figure 2.9 shows the specific sublimation rates of the cylinders, measured over a range of injection times between 0.5 and 4 seconds, and at steady flow conditions in the same pressure range as the pulsed experiments. In each case, the experiment was repeated twice. The short injection time experiments in figure 2.9a) and figure 2.9(b) are observed to have much more uniform evaporation rates at different reactor locations than the longer injection time experiments. Figure 2.9(f) shows the highly variant sublimation conditions created by steady flow conditions, even at the low reactor pressure of 100 Pa.

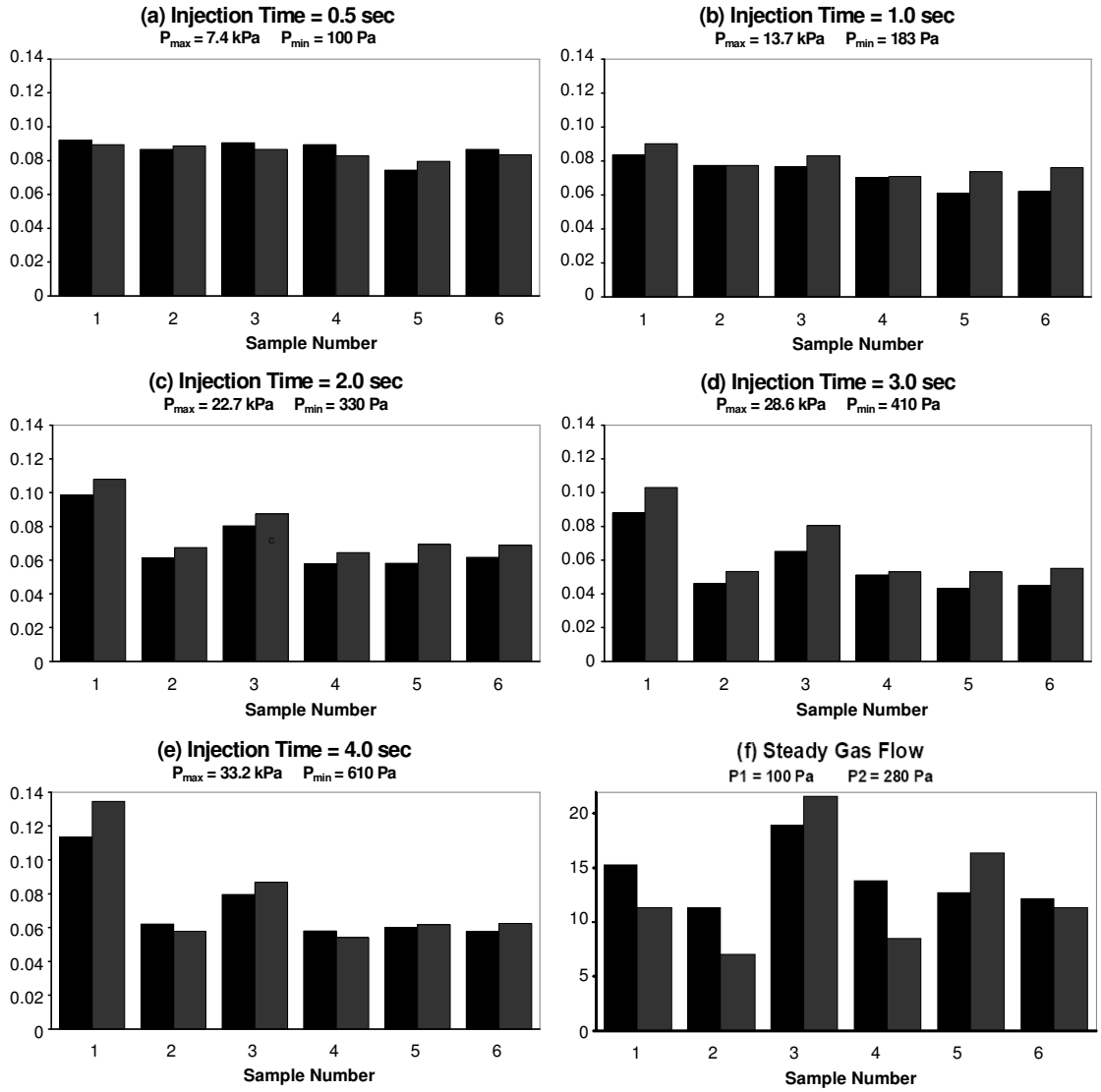

Figure 2.9. Naphthalene sublimation rates [mg/mm^2] for (a-e) pulsed PP-CVD reactors with different injection times and (f) a steady flow reactor [30].

To obtain a quantitative value for the uniformity of the convective flow field uniformity U, a statistical measure was used to take into account both the specific sublimation rate of each cylinder $\dot{S}$ and the average sublimation rate $\overline{\dot{S}}$ thus allowing a quantitative measure of flow field uniformity to be achieved by comparing the relative sublimation rates of each naphthalene cylinder:

$$U = 1 - \frac{\sum_{i=1}^{M} \left| \dot{S}_i - \overline{\dot{S}} \right|}{\sum_{i=1}^{M} \dot{S}_i} \tag{2-16}$$

The convective uniformity was measured for more than fifty experiments with three different reactor volumes and a range of different injection and exhaust parameters. The pulse cycle timing relation $t_P \geq 4\tau_R$ was verified for all cases. When the pulse timing is at least four times the reactor pump-down time constant, then the system operates in a stable, repeatable manner, and the uniformity throughout the reactor is very high, consistently above 0.95. In addition, if the top 1/4 of the reactor volume is exempted from the uniformity measure, and left to act as an expansion zone, then the uniformity of the remainder of the reactor volume is above 0.9 for t_p/τ_R as low as 3.

Figure 2.10 shows the uniformity results for experiments of 30 minute duration in two different size reactors at a wide range of peak pressures. All experiments resulted in excellent uniformity ($U > 0.95$) for the shortest possible injection times and pulse times at least $4\tau_R$. The data indicate that uniformity greater than 0.95 can be achieved for $t_p/t_i \geq 20$ for the small reactor and $t_p/t_i \geq 40$ for the large reactor. Both reactors had the same pump and exhaust system, but different injection supply volume and orifice area. In both cases, the range for high uniformity is characterized by a very rapid injection phase and return of the reactor pressure to P_{min} during each cycle.

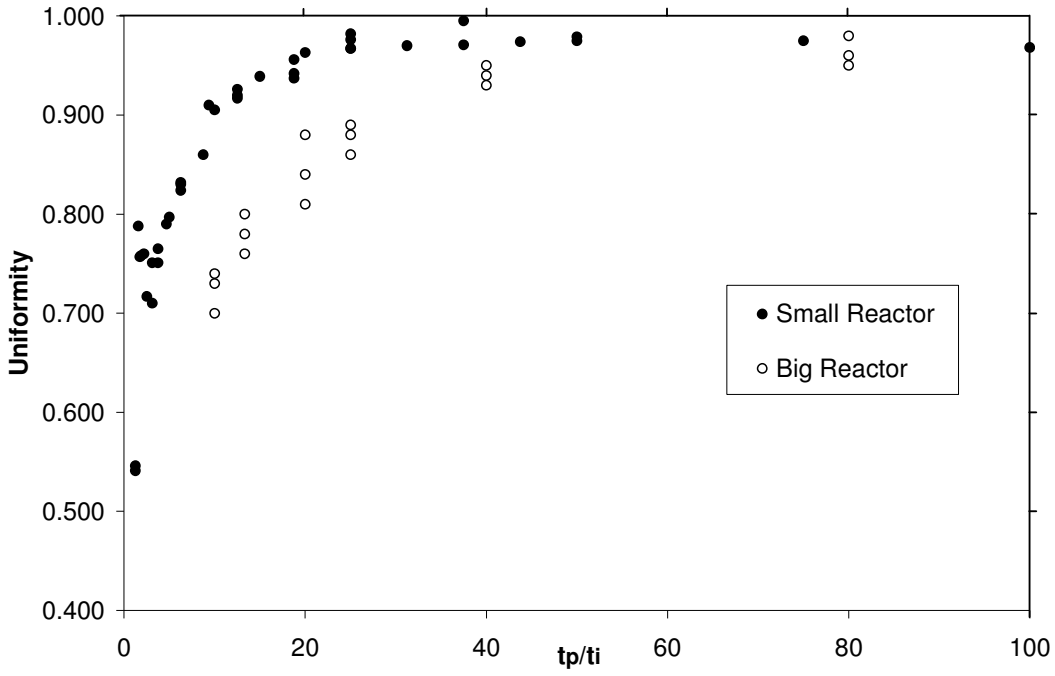

Figure 2.10. Empirical relationship for uniformity in both large and small PP-CVD reactors, both with the same vacuum pump and exhaust configuration [30].

The results of the uniformity experiments show that to obtain high flow field uniformity, and thus good deposition uniformity, it is necessary to operate the reactor in a stable, repeatable manner and to minimise the injection time.

References

[1] C.E. Morosanu, Thin Films by Chemical Vapour Deposition (Elsevier, Amsterdam, 1990).

[2] S. Krumdieck, "Chapter 2. CVD Reactors and Delivery Systems Technology", to appear in: Chemical Vapour Deposition: Precursors and Processes, Eds: A. Jones and M. L. Hitchman (Royal Society of Chemistry Publishing, Cambridge, 2008).

[3] M.L. Hitchman and K.F. Jensen, Chemical Vapor Deposition: Principles and Applications (Academic Press, London, 1993).

[4] H. Schlichting and K Gersten, Boundary-Layer Theory (Springer-Verlag, New York, 2003).

[5] G.A. Bird, Molecular Gas Dynamics and the Direct Simulation of Gas Flows (Clarendon Press, Oxford, 1994).

[6] E.S. Oran, C.K. Oh, and B.Z. Cybyk, Direct Simulation Monte Carlo: Recent Advances and Applications, *Annu. Rev. Fluid Mech.* 30, 403-441 (1998).

[7] M. Ohring, Materials Science of Thin Films: Deposition and Structure (Academic Press, San Diego 2002).

[8] K.K. Schuegraf (ed.), Handbook of thin-film deposition processes and techniques : principles, methods, equipment, and applications (Noyes Publications, Park Ridge, N.J., 1988).

[9] V.A. Versteeg, T.A. Avedisian and R.Raj, Method and Apparatus for CVD using Liquid Delivery System with Ultrasonic Nozzle US Patent No: 5 451 260, September 19, 1995 Sono-Tek Corp. licensee (1995).

[10] S.P. Krumdieck and R. Raj, Experimental Characterization and Modeling of Pulsed MOCVD with Ultrasonic Atomization of Liquid Precursor, *Chem. Vap. Deposition* 7(2), 85-90 (2001).

[11] H. Xie and R. Raj, Epitaxial $LiTaO_3$ thin film by pulsed metalorganic chemical vapor deposition from a single precursor, *Appl. Phys. Lett.* 63(23), 3146-3148 (1993).

[12] V.A. Versteeg, C.T. Avedisian and R. Raj, Metalorganic chemical vapor deposition by pulsed liquid injection using an ultrasonic nozzle : titanium dioxide on sapphire from titanium(IV) isopropoxide, *J. Am. Ceram. Soc.* 78(10), 2763-2768 (1995).

[13] S.P. Krumdieck, Experimental Characterization and Modeling for the Growth Rate of Oxide Coatings from Liquid Solutions of Metalorganic Precursors by Ultrasonic Pulsed Injection in a Cold Wall Low Pressure Reactor, PhD Thesis, University of Colorado (1999).

[14] S.P. Krumdieck and R. Raj, Conversion Efficiency of Alkoxide Precursor to Oxide Films Grown by an Ultrasonic-Assisted, Pulsed Liquid Injection, Metalorganic Chemical Vapor Deposition (Pulsed-CVD) Process, *J. Am. Ceram. Soc.* 82(6), 1605-1607 (1999).

[15] S.P. Krumdieck, Kinetic Model of Low Pressure Film Deposition from Single Precursor Vapor in a Well-Mixed, Cold-Wall Reactor, *Acta Mater.* 49, 583-588 (2001).

[16] S.P. Krumdieck and R. Raj, Growth Rate and Morphology for Ceramic Films by Pulsed-MOCVD, *Surf. Coat. Technol.* 141, 7-14 (2001).

[17] S.P. Krumdieck, O. Sbaizero, A. Bullert and R. Raj, Solid Yttria-Stabilized Zirconia Films by Pulsed Chemical Vapor Deposition from Metal-organic Precursors, *J. Am. Ceram. Soc.* 85(11), 2873-2875 (2002).

[18] S.P. Krumdieck, O. Sbaizero, A. Bullert and R. Raj, YSZ layers by pulsed-MOCVD on solid oxide fuel cell electrodes, *Surf. Coat. Technol.* 167, 226-233 (2003).

[19] V. Siriwongrungson, M.M. Alkaisi, S.P. Krumdieck, Step Coverage of Thin Titania Films on Patterned Silicon Substrate by Pulsed-Pressure MOCVD, 16th European Conference of Chemical Vapor Deposition, Deen Haag (The Netherlands), 16-21 September 2007.

[20] J. K. Holt, M. Swiatek, D. G. Goodwin , R. P. Muller, W. A. Goddard, III and Harry A. Atwater, Gas phase and surface kinetic processes in polycrystalline silicon hot-wire chemical vapor deposition, *Thin Solid Films* 395, 29-35 (2001).

[21] P.W. May, Diamond thin films: a 21st-century material, *Phil. Trans. R. Soc. Lond. A* 356, 473-495 (2000).

[22] A.A.R. Elshabini-Riad and F.D. Barlow, Thin film technology handbook (McGraw-Hill, New York, 1998).

[23] P.G. Wiles and J. Abrahamson, Carbon fibre layers on arc electrodes - I. Their properties and cool-down behaviour. *Carbon*, 16, 341-349 (1978).

[24] P.J.F. Harris, Carbon nanotube composites, *Int. Mater. Rev.* 49(2), 31-43 (2004).

[25] M. Daenen, R.D. de Fouw, B. Hamers, P.G.A. Janssen, K. Schouteden and M.A.J. Veld, The Wondrous World of Carbon Nanotubes: a review of current carbon nanotube technologies, Eindhoven University of Technology Report (2003).

[26] S.P. Krumdieck, J.-Y. Lee, and H. Raatz, Uniform molecular flux in a vertical reactor with pulsed transition regime gas flow, *J. Electrochem. Soc.* 8, 179-185 (2003).

[27] S.I. Baluti, Experimental characterization of flow dynamics of pulsed-chemical vapour deposition, ME Thesis, University of Canterbury (2005).

[28] A. Roth, Vacuum Technology (North-Holland, Amsterdam, 1990).

[29] P.R. Souza-Mendes, The naphthalene sublimation technique *Exp. Therm. Fluid Sci.*, 4, 510-523 (1991).

[30] S.P. Krumdieck, H.M. Cave, S. Baluti, M. Jermy and A. Peled, Expansion Transport Regime in Pulsed-Pressure Chemical Vapor Deposition, *Chem. Eng. Sci.* 62(22), 6121-6128 (2007).

3. Flow Dynamics and Modelling

3.1 Overview

The study of fluid flow phenomena has its roots in the methods of hydrostatics, the study of stationary fluids, which was developed by the ancient Greeks and Romans. Hydrostatics essentially uses engineering approximations to fit known experimental data and enables relatively accurate calculations of large scale phenomena.

The more complex field of hydrodynamics is based on rigorous theory and was developed from the work of mathematicians in the 1700s, although it was the development of boundary layer theory by Ludwig Prandtl in the early 20th century which enabled hydrodynamic theory to be applied practically. In hydrodynamics the conservation equations for mass, momentum and energy are applied to determine the nature of a liquid or gas flow field. Empirical relationships are required to describe some of the internal properties of the fluid such as the viscosity and diffusivity. Dimensional analysis and empirical studies are in turn used to develop drag, pressure drop, heat and mass transport correlations. Numerical methods were developed in the later half of the 20th century allowing the flow around complex geometries to be studied by dividing the flow field into a large number of elements and applying the conservation equations to these elements. The availability of inexpensive and efficient digital computers has seen these computational fluid dynamics (CFD) techniques find a wide variety of applications.

Despite the power of hydrodynamics in the study of many flow problems, the inherent assumptions of a continuum and the reliance on empirical coefficients mean that in many situations, such as high speed, high energy or low density gas flows, the classical hydrodynamics approach cannot be used. In these flows the rate of intermolecular collisions at a particular position may be so low that equilibrium conditions cannot be re-established before the particles are convected downstream. In such a case “continuum breakdown” can be said to have occurred and the true nature of the gas must be considered: the fact that it is comprised of an enormous number of discrete molecular particles rather than a continuous substance and that the interaction of these particles on the microscopic level is what causes the gas to behave as it does on the macroscopic level. This way of looking at gas flow is

known as gas kinetic theory and was developed primarily from the work of Ludwig Boltzmann during the 1870s.

As discussed in section 2.2, during some vacuum processes the continuum assumption in hydrodynamics becomes invalid. For this reason it is necessary to study the flow processes in PP-CVD starting from the fundamentals of gas kinetic theory. In this chapter particle collision and gas kinetic theory is described, the relationship to hydrodynamics is investigated and the methods for solving practical flow problems from this theory are discussed.

3.2 Particle-Particle Collision Dynamics

Rarefied gas dynamics is primarily concerned with collisions between two particles (collisions simultaneously involving three or more particles occur so infrequently they can be ignored) and the dynamics of these collisions is fundamental in both stochastic and numerical modelling of rarefied flows. The reason particle-particle collision dynamics are so important is that it is via the collision mechanism that equilibrium is established and macroscopic flow properties propagate through the flow field.

In classical binary elastic collisions between two particles (having masses m_1 and m_2 with pre- and post-collision velocities of $\boldsymbol{v}_1$ and $\boldsymbol{v}_2$ and $\boldsymbol{v}_1^*$ and $\boldsymbol{v}_2^*$ respectively) both momentum and energy will be conserved such that:

$$m_1\boldsymbol{v}_1 + m_2\boldsymbol{v}_2 = m_1\boldsymbol{v}_1^* + m_2\boldsymbol{v}_2^* = (m_1 + m_2)\boldsymbol{v}_m \tag{3-1}$$

$$m_1\boldsymbol{v}_1^2 + m_2\boldsymbol{v}_2^2 = m_1\boldsymbol{v}_1^{*2} + m_2\boldsymbol{v}_2^{*2} \tag{3-2}$$

where $\boldsymbol{v}_m$ is the centre of mass velocity.

Noting that the magnitude of the relative velocity is unchanged by the collision ($\|\boldsymbol{v}_r^*\| = \|\boldsymbol{v}_r\|$) we can obtain useful expressions for the post collision velocities of any such collision in the centre of mass coordinate system in terms of relative velocities pre- ($\boldsymbol{v}_r = \boldsymbol{v}_1 - \boldsymbol{v}_2$) and post-collision ($\boldsymbol{v}_r^* = \boldsymbol{v}_1^* - \boldsymbol{v}_2^*$), as:

$$\boldsymbol{v}_1^* = \boldsymbol{v}_m + \frac{m_2}{m_1 + m_2}\boldsymbol{v}_r^* \qquad \text{and} \qquad \boldsymbol{v}_2^* = \boldsymbol{v}_m - \frac{m_1}{m_1 + m_2}\boldsymbol{v}_r^* \tag{3-3}$$

To fully define the collision event for spherically symmetric molecules we also need to calculate the change in direction of the particles during the collision. In the collision plane, this change of direction can be represented by a distance of closest approach between the initial particle directories b and a deflection angle χ as shown in figure 3.1.

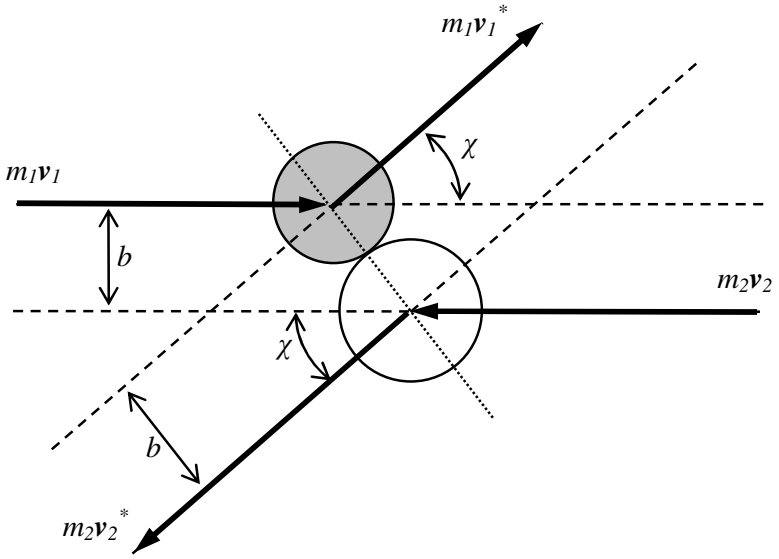

Figure 3.1. Collision parameters in the plane of the collision

For practical purposes, we need to determine the new components of velocity relative to some convenient reference plane which is at an angle ε to the collision plane as shown in figure 3.2.

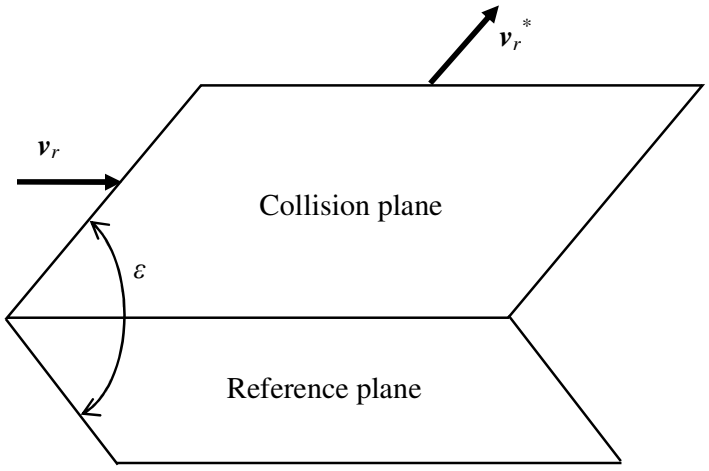

Figure 3.2. Relationship between the collision and reference planes

This enables the definition of the relative velocities of the particles after collision in the coordinate system of the reference plane (here the *x, y, z* coordinate system) as [1]:

$$\boldsymbol{v}_r^* = \begin{pmatrix} u_r^* \\ v_r^* \\ w_r^* \end{pmatrix} = \begin{pmatrix} u_r \cos\chi + \sqrt{v_r^2 + w_r^2}\,\sin\chi\sin\varepsilon \\ v_r \cos\chi + \dfrac{\sin\chi(\|\boldsymbol{v}_r\| w_r \cos\varepsilon - u_r v_r \sin\varepsilon)}{\sqrt{v_r^2 + w_r^2}} \\ w_r \cos\chi - \dfrac{\sin\chi(\|\boldsymbol{v}_r\| v_r \cos\varepsilon + u_r w_r \sin\varepsilon)}{\sqrt{v_r^2 + w_r^2}} \end{pmatrix} \tag{3-4}$$

The functional relationship between the deflection angle χ, the magnitude of the relative velocity between the particles $\|\boldsymbol{v}_r\|$ and the distance of closest approach b is related to the intermolecular potentials between the particles during the collision event. The range over which these intermolecular forces act is generally described using a total collision cross section σ_T. This cross section is defined by Liboff [2] by considering a uniform beam of particles having intensity I (in particles/(m^{2}s)) incident on a particle acting as a scatterer and located at the origin of figure 3.3. Particles from the beam which collide on the collision plane at an angle between ε and $\varepsilon+d\varepsilon$, and have deflection angles between χ and $\chi+d\chi$ and a distance of closest approach between b and $b+db$ will be deflected into an element $d\Omega = \sin\chi d\chi d\varepsilon$ of the unit sphere surrounding the origin. The number deflected into $d\Omega$ is given by $I\sigma(\Omega)d\Omega$ where σ is the differential collision cross section which is effectively a proportionality factor which gives the probability of this type of collision occurring. Note that the number of particles scattering into $d\Omega$ is the same that passed through the annular area $bdbd\varepsilon$ such that $I\sigma d\Omega = Ibdbd\varepsilon$ such that:

$$\sigma = \frac{bdbd\varepsilon}{d\Omega} = \frac{b}{\sin\chi}\frac{db}{d\chi} \tag{3-5}$$

By integrating over the unit sphere the total collision cross section can also be obtained by:

$$\sigma_T = \int_0^{4\pi} \sigma d\Omega \tag{3-6}$$

A number of models have been developed for the relationship between the translational energy, distance of closest approach and the scattering angle to help describe these collision events. Many of these models are phenomenological in nature, as complete data usually does not exist to describe these relationships. The dynamics for collisions which involve energy

exchange between the translational and internal energies (including rotational, vibrational and electronic modes) are more complex as these collisions are inelastic. Collision models will be discussed in more detail in section 3.6.3.

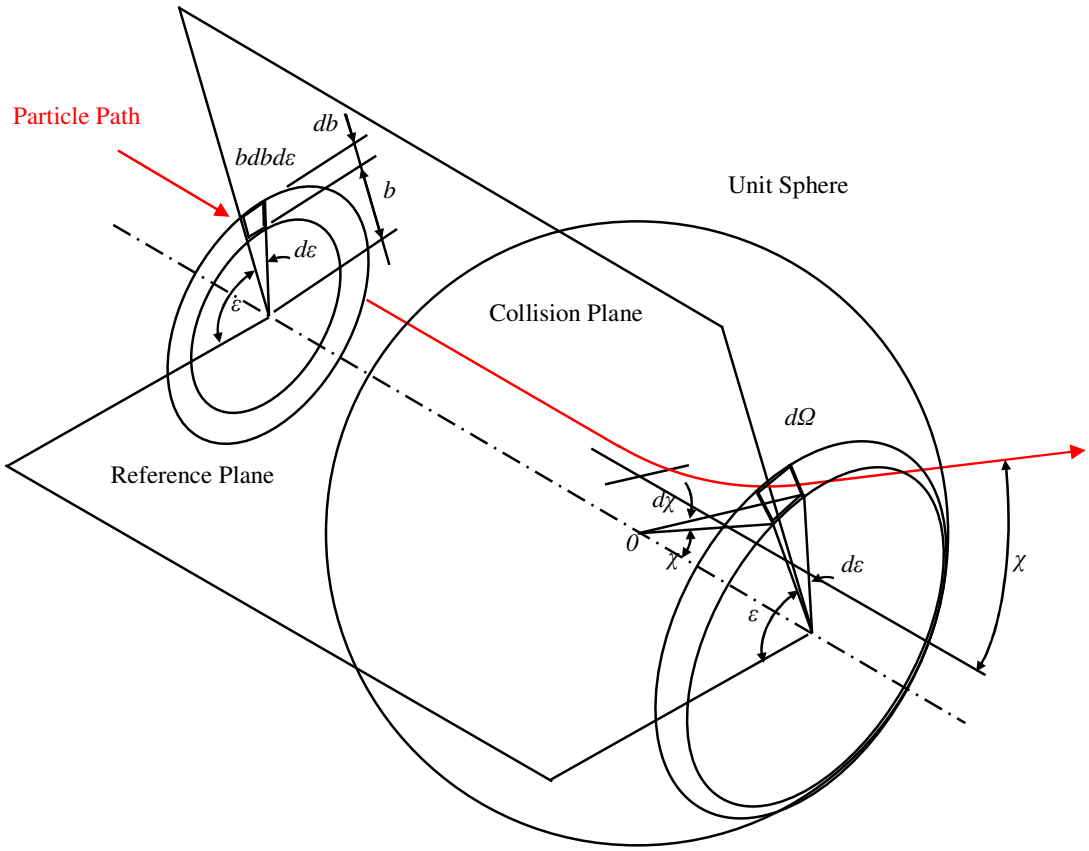

Figure 3.3. Diagram for derivation of the collision cross section.

3.3 The Boltzmann Equation

Rarefied gas theory is a development of the kinetic theory of gases, which examines the behaviour of gases from the molecular approach, rather than the macroscopic approach of classical thermodynamics. The theory stems from a statistical analysis of two particle (binary) collisions between molecules in a gas [1,3,4]. The theory recognises that a gas is composed of a huge number of individual particles (even if it is highly rarefied) so it is, by necessity, based on a statistical description of the position and velocity of the particles.

As shown in figure 3.4, any particular gas particle can be described by its position in physical space (described by a vector $\boldsymbol{r}$) and velocity in velocity space (described by the vector $\boldsymbol{v}$) at a particular time t. The physical and velocity space together make up the "phase space" for the particle.

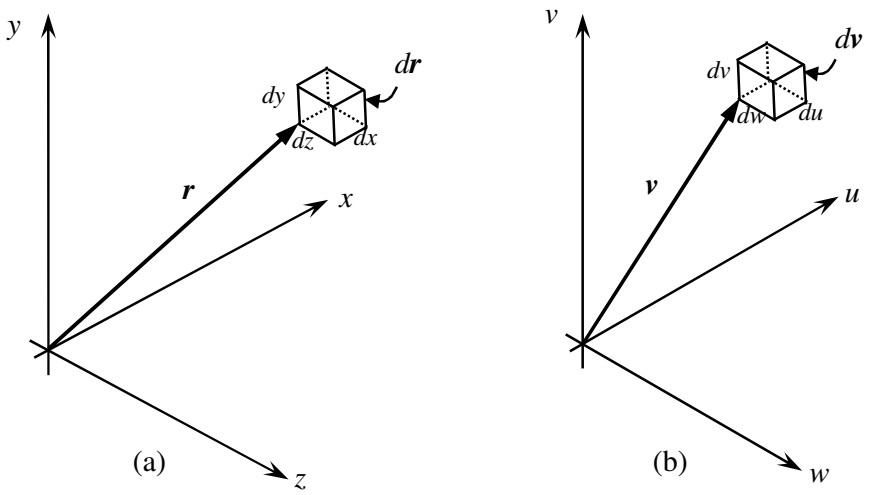

Figure 3.4. The a) physical and b) velocity space components which make up the phase space for a single particle.

The ensemble of particles in the system allows us to define a phase space distribution function for that system $F(\boldsymbol{r}, \boldsymbol{v}, t)$ which characterises the number of particles dN in the volume element of phase space $dxdydzdudvdw = d\boldsymbol{r}d\boldsymbol{v}$:

$$dN = F(\boldsymbol{r},\boldsymbol{v},t)d\boldsymbol{r}d\boldsymbol{v} \tag{3-7}$$

The phase space distribution function can then be normalised against the local number density $n(\boldsymbol{r}, t)$:

$$f(\boldsymbol{r},\boldsymbol{v},t) = \frac{F(\boldsymbol{r},\boldsymbol{v},t)}{n(\boldsymbol{r},t)} \tag{3-8}$$

It is obvious that if we know the position and velocity of every particle in a particular gas flow, then we know everything there is to know about the flow at that instant of time. The same is true if we know the phase space distribution function at every point in the gas, since

by taking moments of the distribution function we can obtain the macroscopic properties [1,3]. These moments essentially represent the average of some property Q over velocity space:

$$\overline{Q}(\boldsymbol{r},t) = \int_{-\infty}^{\infty}\int\int Q(\boldsymbol{v},t) f(\boldsymbol{r},\boldsymbol{v},t) d\boldsymbol{v} \tag{3-9}$$

For example, the first three moments of the distribution function give values for the number density n, the components of the macroscopic flow velocity u_i and the gas temperature T which are, respectively [5]:

$$n(\boldsymbol{r},t) = \int_{-\infty}^{\infty}\int\int f(\boldsymbol{r},\boldsymbol{v},t) d\boldsymbol{v} \tag{3-10a}$$

$$nu_i(\boldsymbol{r},t) = \int_{-\infty}^{\infty}\int\int v_i f(\boldsymbol{r},\boldsymbol{v},t) d\boldsymbol{v} \tag{3-10b}$$

$$\frac{3}{2} nRT(\boldsymbol{r},t) = \int_{-\infty}^{\infty}\int\int \frac{1}{2}\left[v - u(r,t)\right]^2 f(\boldsymbol{r},\boldsymbol{v},t) d\boldsymbol{v} \tag{3-10c}$$

Higher order moments can also be used to define gas pressure p, stress tensor τ_{ij} and the heat flux vector $\boldsymbol{q}$.

To determine the phase space distribution function for anything but a stationary equilibrium flow is non-trivial because the number of particles in the element $d\boldsymbol{r}d\boldsymbol{v}$ will change as:

i) molecules move out of the physical space element $d\boldsymbol{r}$ due to their molecular velocities

ii) molecules are accelerated out of the velocity space element $d\boldsymbol{v}$ by some external force

iii) collisions between molecules, and the consequent exchange of energy, cause the molecules to be scattered out of the velocity space element $d\boldsymbol{v}$

Each of the above mechanisms is represented by a term in the Boltzmann equation which essentially describes the evolution of the phase space distribution function. If no collisions

occur (i.e. in free molecular flow) then this probability density function would remain constant. That is, under some external force $\boldsymbol{F}_{ext}$:

$$F\left(\boldsymbol{r}+\boldsymbol{v}dt,\boldsymbol{v}+\frac{\boldsymbol{F}_{ext}}{m}dt,t+dt\right)=F(\boldsymbol{r},\boldsymbol{v},t) \tag{3-11}$$

However, collisions will occur if another molecule moves within the collision cross section of another and these collisions will cause the probability density function to change with time such that the equality of equation (3-11) no longer holds:

$$\left[F\left(\boldsymbol{r}+\boldsymbol{v}dt,\boldsymbol{v}+\frac{\boldsymbol{F}_{ext}}{m}dt,t+dt\right)-F(\boldsymbol{r},\boldsymbol{v},t)\right]=\frac{\delta F(\boldsymbol{r},\boldsymbol{v},t)}{\delta t}d\boldsymbol{r}d\boldsymbol{v}dt \tag{3-12}$$

or

$$\frac{\partial F}{\partial t}+\boldsymbol{v}\cdot\frac{\partial F}{\partial \boldsymbol{r}}+\frac{\boldsymbol{F}_{ext}}{m}\cdot\frac{\partial F}{\partial \boldsymbol{v}}=\left[\frac{\delta F}{\delta t}\right]_{colls} \tag{3-12a}$$

The term on the right of equation (3-12a) is commonly called the "collision term" and represents the change in the phase space distribution function due to the scattering of particles into $(\delta F/\delta t)^{+}$ and out of $(\delta F/\delta t)^{-}$ the phase space element $d\boldsymbol{r}d\boldsymbol{v}$ due to collision events such that:

$$\frac{\delta F}{\delta t}=\left(\frac{\delta F}{\delta t}\right)^{+}-\left(\frac{\delta F}{\delta t}\right)^{-} \tag{3-13}$$

To evaluate the collision term it is necessary to assume that only binary collisions occur, that there is "molecular chaos" (i.e. the position and velocity of colliding molecules are statistically independent of each other) and that any external forces have no influence on the collision rate.

First we consider the scattering of a particle which has a velocity in the range $(\boldsymbol{v}, \boldsymbol{v}+d\boldsymbol{v})$ out of the phase space element $d\boldsymbol{r}d\boldsymbol{v}$ because of a collision with another particle having a velocity in the range $(\boldsymbol{v}_1, \boldsymbol{v}_1+d\boldsymbol{v}_1)$. This collision will produce post collision velocities for the particles in the ranges of $(\boldsymbol{v}^*, \boldsymbol{v}^*+d\boldsymbol{v}^*)$ and $(\boldsymbol{v}^*_1, \boldsymbol{v}^*_1+d\boldsymbol{v}^*_1)$ respectively (we will denote this type of collision as a $\boldsymbol{v}, \boldsymbol{v}_1 \rightarrow \boldsymbol{v}^*, \boldsymbol{v}^*_1$ class collision). It can be shown [1] that the number of collisions of this class per unit time in the element is:

$$FF_1 v_r \sigma d\Omega d\boldsymbol{v}_1 d\boldsymbol{v} d\boldsymbol{r} \tag{3-14}$$

The "inverse" class of collision $\boldsymbol{v}^*$, $\boldsymbol{v}^*_1 \rightarrow \boldsymbol{v}$, $\boldsymbol{v}_1$ leads to a similar expression for the scattering of particles into the space element, such that the combined rate of change of the number of particles in the phase space element $d\boldsymbol{r}d\boldsymbol{v}$ is:

$$(F^* F_1^* - FF_1) v_r \sigma d\Omega d\boldsymbol{v}_1 d\boldsymbol{v} d\boldsymbol{r} \tag{3-15}$$

Integration of this expression over the entire collision cross section and the whole of the velocity space for $\boldsymbol{v}_1$, then substitution into equation (3-12a) leads to the Boltzmann equation:

$$\frac{\partial F}{\partial t} + \boldsymbol{v} \cdot \frac{\partial F}{\partial \boldsymbol{r}} + \frac{\boldsymbol{F}_{ext}}{m} \cdot \frac{\partial F}{\partial \boldsymbol{v}} = \int_{-\infty}^{\infty} \int_{0}^{4\pi} \left(F^* F_1^* - FF_1 \right) v_r \sigma d\Omega d\boldsymbol{v}_1 \tag{3-16}$$

Equation (3-16) is in essence a conservation equation. The terms on the left hand side represent respectively i) the change in the number of particles in an element of phase space $d\boldsymbol{r}d\boldsymbol{v}$ with time, ii) the convection of particles into and out of the physical space element $d\boldsymbol{r}$, and iii) the acceleration of particles into and out of the velocity space element $d\boldsymbol{v}$ by external forces. The term on the right hand side represents the scattering of particles into and out of the velocity space $d\boldsymbol{v}$ due to collisions.

For a gas at equilibrium the velocities of individual gas molecules are distributed according to the equilibrium distribution $F_0(\boldsymbol{r},\boldsymbol{v})$. This is the solution of the stationary Boltzmann equation for a gas moving with bulk velocity $\boldsymbol{v}_0$, and can be derived from the Boltzmann H-theorem [4] as:

$$F_0(\boldsymbol{r},\boldsymbol{v},t) = \left[\frac{n(\boldsymbol{r})m}{2\pi kT(\boldsymbol{r})} \right]^{3/2} \exp\left\{ \frac{-m[\boldsymbol{v} - \boldsymbol{v}_0(\boldsymbol{r})]^2}{2kT(\boldsymbol{r})} \right\} \tag{3-17}$$

3.4 The Chapman-Enskog Expansion and the Navier-Stokes Equations

The three basic hydrodynamic, or continuum, equations governing viscous convective flow in the continuum regime are the continuity equation (conservation of mass), the conservation of momentum and the conservation of energy (derived from the first law of thermodynamics). The derivation of these expressions can be found in any elementary text on fluid mechanics, with a good example being the text by White [6]. These equations are often referred to as the Navier-Stokes equations and are given below in vector notation:

$$\frac{\partial \rho}{\partial t} + div \rho \boldsymbol{u} = 0 \tag{3-18a}$$

$$\rho \frac{D\boldsymbol{u}}{Dt} = \rho \boldsymbol{g} + \nabla \cdot \tau_{ij}^{'} - \nabla p \tag{3-18b}$$

$$\rho \frac{Dh}{Dt} = \frac{Dp}{Dt} + div(k \nabla T) + \tau_{ij}^{'} \frac{\partial u_i}{\partial x_j} \tag{3-18c}$$

where ρ is fluid density, $\boldsymbol{u}$ is the velocity vector, p is pressure, $\boldsymbol{g}$ is the acceleration due to gravity vector, h is enthalpy, T is temperature, k is the conduction coefficient and where, for a Newtonian fluid, the viscous stresses are $\tau_{ij}^{'} = \mu\left(\frac{\partial u_i}{\partial x_j} + \frac{\partial u_j}{\partial x_i}\right) + \delta_{ij} \lambda div \boldsymbol{u}$

The Navier-Stokes equations can also be obtained as a solution to the Boltzmann equation via a first order Chapman-Enskog expansion. This technique approximates the normalised phase space distribution function (see equation (3-8)) by a power series expansion:

$$f \approx f_0 (1 + \Theta_1 + \Theta_2 + ...) \tag{3-19}$$

In equation (3-19) the Θ parameters represent perturbations from the equilibrium phase space distribution function f_0. By substituting only the first two terms of the power series $f_0 (1+ \Theta_1)$ into equation (3-16), the Navier-Stokes equations can be obtained via the method detailed in Chapman and Cowling [7]. This solution helps us highlight a very important point: *the Navier-Stokes equations are only valid for flows with only small departures from thermodynamic equilibrium*. Thus, when flows are encountered with regions significantly departed from equilibrium, such as in a shock layer, then "continuum breakdown" can be said to have occurred. Furthermore, non-linear terms for the shear stress and heat transfer arise within these regions of high property gradients. The Burnett equations, resulting from a

higher order Chapman-Enskog expansion have the potential to resolve these non-linear terms, but are far more difficult to solve numerically than the Navier-Stokes equations [1]. Continuum breakdown and methods for detecting it will be discussed in more detail in section 4.1.2.

Another form of the continuum equations are the inviscid Euler equations. These are equivalent to the Navier-Stokes equations however they have zero viscosity and heat conductions terms. These equations are applicable in regions in which viscosity can be considered to have negligible effects which precludes their use in regions of the flow with significant flow gradients, such as boundary layers.

3.5 Approximate Collision Terms and Model Equations

Solution of the Boltzmann equation for all but the simplest situations is extremely difficult mathematically, if not impossible. A numerical approach using similar techniques to conventional computational fluid dynamics (CFD) methods can be adopted, however there is a large computational expense involved in evaluating the collision term in equation (3-16).

One method of making the Boltzmann equation more mathematically tractable is by replacing the collision term on the right of equation (3-16) with an approximate term. These simplified equations are collectively known as the model Boltzmann equations (MBEs). A number of MBEs have been proposed, including the Fokker-Planck approximation [4], higher order Chapman-Enskog expansions, the ellipsoidal model by Holway [8] and the integro-differential model of Lebowitz *et al.* [9], however by far the most widely known model is the Bhatnagar-Gross-Krook (BGK) equation [10] which was independently developed by Welander [11] at about the same time. In the BGK method, the collision term is replaced by a term which recognises that collisions of frequency υ will tend to move the local velocity distribution function towards equilibrium. The BGK version of the Boltzmann equation is thus:

$$\frac{\partial F}{\partial t} + \boldsymbol{v} \cdot \frac{\partial F}{\partial \boldsymbol{r}} + \frac{\boldsymbol{F}_{ext}}{m} \cdot \frac{\partial F}{\partial \boldsymbol{v}} = \upsilon\left(F_0 - F\right) \tag{3-20}$$

The lower order moments of equation (3-20) are the same as the full Boltzmann equation, however the third order moments of the equation such as the shear stress tensor and the heat

flux vector are incorrect. Solutions of the equation also give a Prandtl number (ratio of momentum to thermal diffusivity) of one, which is unrealistic, so an alternative higher order approach has been suggested by Shakov where the equilibrium distribution term F_0 in equation (3-20) is replaced by [12]:

$$F^+ = F_0\left[1+(1-\mathrm{Pr})\boldsymbol{v}\cdot\boldsymbol{q}\left(\frac{c^2}{RT}-5\right)/(5pRT)\right] \tag{3-21}$$

These simple MBEs have been shown to be effective ways of modelling rarefied flow problems across a variety of applications when solved using an appropriate numerical method. One such method is the finite difference scheme proposed by Yang and Huang [13].

The difficulty inherent in any MBE method is the requirement to discretise the system in both physical and velocity space, which results in a large computational expense and memory requirement. For example, a three-dimensional unsteady problem in physical space is also three dimensional in velocity space meaning each grid point in physical space needs to be described by seven independent variables (including time). An additional limitation lies in the fact that finite limits must be placed on velocity space which is theoretically limitless in extent. These limits must be chosen judiciously to ensure that a negligible number of particles have velocities outside their range, which makes the method unsuitable for hypersonic (high Mach number) or high temperature flows.

3.6 The Direct Simulation Monte Carlo (DSMC) Technique

3.6.1 Overview

An alternative approach to the solution of the Boltzmann equation (or MBEs) is the use of methods which recognise that the gas is comprised of a large number of particles which can be simulated by appropriate modelling of their ballistic and collision behaviour. The obvious approach is to model every particle in the system deterministically such that every particle movement and collision would occur as it does in the real system. This approach, known as the molecular dynamics (MD) method, was first proposed by Alder and Wainwright [14] and has the advantage that it remains valid for dense gases and liquids where binary collisions cannot be assumed. Unfortunately, the computational expense involved in modelling even

very small systems using MD is enormous because typical number densities, even for very dilute gases, are still measured in hundreds of millions of particles per cubic meter.

Stochastic methods, in which only a relatively small number of particles representative of the whole system are modelled, have been developed in an attempt to overcome the computational expense of MD simulations. The first such method was developed by Haviland and Lavin [15] and is known as the test particle Monte Carlo method. Here a large number of test particles are tracked individually through the flow field until a representation of the flow field is built up. This method works well for collisionless flows; however for flows with a significant number of intermolecular collisions the method requires that there is a quite detailed knowledge of the flow field in advance. This flow field can be refined iteratively using data from the test particles, however the requirement for a detailed knowledge of the flow field prior to computation is a major disadvantage.

The method which has become the gold standard for stochastic flow field simulation (and, it could be argued, for rarefied gas flow simulation) is the Direct Simulation Monte Carlo (DSMC) method developed by Bird in the 1960s [16]. In this method the ballistic motion of the particles and their collisions are decoupled by moving the particles over a time step which is smaller than their mean collision time, indexing the particles to within a grid having dimensions which are smaller than the mean free path and then choosing collision partners from within this grid. Bird [17] has shown that the DSMC method essentially provides a statistical solution to the Boltzmann equation and Wagner [18] proved mathematically that DSMC does provide a solution to the Boltzmann equation as the number of simulated particles approaches the number in the actual system.

The DSMC method was first used by Bird to model the relaxation of a non-equilibrium gas towards the equilibrium distribution [16] and since that time has been used in an wide array of applications including CVD reactor modelling [19], hypersonic flight simulations [20], supersonic jet studies [21,22], microfluidic simulations [23] and in the modelling of molecular pumps [24]. The method has grown increasingly sophisticated and powerful as improved algorithms, intermolecular collision models, gas-phase chemistry and boundary conditions have been developed and implemented.

The method has several advantages over other numerical approaches in that no iterative procedure is required for convergence to a final solution, there are no numerical instabilities and complex effects, such as non-equilibrium chemistry, can be added without changing the overall computational procedure [25]. The disadvantage of the method is that it becomes very computationally expensive for flows approaching the continuum regime, especially for unsteady cases where an ensemble average of separate runs is usually made.

Extensive details of the DSMC method can be found in the monograph by Bird [1] and further information can be found in the reviews by Bird [26,27], Alexander and Garcia [28], Oran *et al.* [29] and Ivanov and Gimelshein [30]. This section will outline the basic procedures of the method.

3.6.2 Basic DSMC Procedures

Figure 3.5 shows the typical steps undergone in a DSMC simulation. After setting up the simulation domain and boundaries, and populating these with particles at the initial conditions, the DSMC procedure undergoes a number of iterative steps. Firstly particles are moved ballistically through a time step Δt which must be smaller than the mean collision time Δt_c. Appropriate boundary conditions are applied if the particle interacts with a boundary during this time step. Secondly, the particles are indexed within a grid which consists of cells with sides which must be smaller than the mean free path of the molecules. Finally, collisions between the molecules within each cell are generated on a probabilistic basis and the post-collision velocities of each particle are upgraded accordingly. The cells also serve a second purpose in that flow properties are sampled by taking the mean value of the particles properties within the cell (for example, the mean velocity of the particles represents the local flow velocity and the number of simulated particles within the cell determines the local gas density). In some implementations of DSMC, the cells for generating collisions ("collision cells") are different from those used for determined the macroscopic properties ("sampling cells"), although usually there is some dependence between the two cell types.

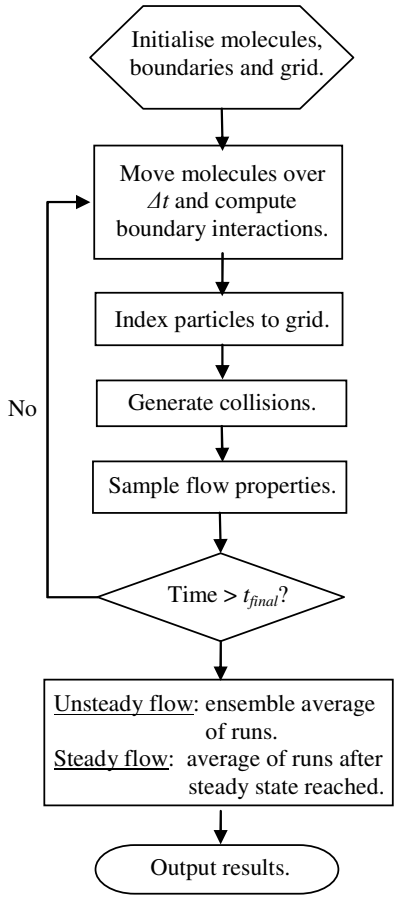

Figure 3.5. Steps in a DSMC simulation process.

The accuracy of the DSMC simulation depends on the methods used to model the physical processes within the simulation, in particular the simulation of collision events between particles and the interaction of particles with boundaries such as solid surfaces. Statistical considerations concerning the sampling of flow properties from a limited number of simulated particles are also important. The size of the time step Δt over which particle movement and collisions are decoupled needs to be set to a period which is less than the mean collision time Δt_c and generally $\Delta t \leq \Delta t_c / 5$ is recommended [25]. Equally, the dimensions of the sampling cell are important. Generally these dimensions must be on the order of $\lambda / 3$ so that the local gradients of macroscopic properties can be accurately resolved by the simulation and so that the particles chosen for collision are not widely separated.

An additional requirement of the method is that there are sufficient simulated particles per sampling cell such that a statistically acceptable determination of macroscopic flow properties in the cell can be made. Generally the number of particles per cell should be maintained at approximately twenty [25]. In most DSMC procedures, the sampling cells are additionally

divided into a number of sub-cells, containing two or three particles, and collision partners are selected from within these sub-cells to ensure that intermolecular collisions only happen between closely spaced particles. This method has been shown to help maintain flow vorticity information within the simulations without greatly increasing computer storage requirements or computational time [1]. Some DSMC programs, like Bird's DS2V, deploy sub-cells transiently by generating these one cell at a time during the collision routine [25].

More recent implementations of DSMC utilise "virtual sub-cells", which were first introduced by LeBeau [31], as an alternative to, or in conjunction with, sub-cells. Here the distance from the first collision partner to all other particles within the sampling cell is calculated, and the nearest particle is chosen for collision. This has been shown to be faster than employing transient sub-cells for sampling cells containing a small number of particles (for DS2V this value has been found to be approximately 35 particles per cell) [32].

One problem with employing sub-cells or virtual sub-cells to ensure nearest neighbour collisions in DSMC is that two collision partners are likely to collide with each other consecutively. Clearly this situation is physically impossible, since particles which collide will then be moving away from each other, so will not collide again before they collide with another particle or surface. This situation has been found to incur an error in some sampled properties and so is forbidden in most DSMC algorithms employing nearest neighbour collisions [25].

Recently Bird has been promoting the concept of "merit of collision" to determine the quality of a DSMC simulation [25,32,33]. Here the ratio of the mean collision spacing (the mean distance between two particles selected for collision) and the mean free path (*mcs/mfp*) is determined. The smaller the value of this ratio, the higher the quality of the simulation since, as is physically evident, *mcs/mfp* tends to zero in a real gas system.

The requirements for time step size, sampling cell dimensions and number of particles per cell set the computational requirements for the DSMC simulation of a particular problem. Higher density flows, which have a lower mean collision time and smaller mean free path, are therefore more computationally expensive. Additionally, unsteady flows require an ensemble average of separate runs to reduce the statistical scatter in the results which further increases the computational expense. This will be discussed in more detail in section 6.3.1.

During the movement step, where particles are moved ballistically over the time step Δt, each particle moves (assuming there is no external force field acting on the particle) from position $\boldsymbol{r}$ to $\boldsymbol{r}'$:

$$\boldsymbol{r}'(x', y', z') = \boldsymbol{r}(x, y, z) + \boldsymbol{v}(u, v, w)\Delta t \tag{3-22}$$

In axisymmetric simulations (with spatial coordinates r, θ & z and velocity components v_r, v_θ & v_z), the positions and velocities of the particles are projected onto the zero-azimuth plane. Bird gives the new radial particle positions and radial and circumferential velocities as [1]:

$$r' = \sqrt{\left(r + v_r \Delta t\right)^2 + \left(v_\theta \Delta t\right)^2} \tag{3-23a}$$

$$v_r' = \frac{\left[v_r\left(r + v_r \Delta t\right)^2 + v_\theta^2 \Delta t\right]}{r'} \tag{3-23b}$$

$$v_\theta' = \frac{\left[v_\theta\left(r + v_r \Delta t\right) - v_r v_\theta \Delta t\right]}{r'} \tag{3-23c}$$

During this movement step, the interaction of particles with any flow boundaries they encounter is also computed. These boundary conditions can include specular or diffuse reflection from a wall, entry or exit via a stream boundary, periodic boundary conditions or an interface with a vacuum. Details on detecting when a particle intersects with a surface and the application of these boundary conditions can be found in Bird [1]. Guo and Liaw also give a review of boundary conditions for the method [34].

In axisymmetric simulations the positions of particles are projected onto the zero-azimuth plane after every time step using equations (3-23), however simulated particles at a large radius are projected from a much greater volume of flow, and so are representative of a greater number of real particles than those close to the axis. This can be corrected by the employment of radial weighting factors which define the number of real particles each simulated particle represents, as a function of its radius. As a particle moves radially it must therefore be duplicated or deleted so that the number of real particles it represents remains approximately constant. Generally duplicated particles are held in a "buffer" and released after a random amount of time to prevent the physically unrealistic circumstances of having

two identical particles in a cell [1], however this may prove problematic for unsteady simulations.

Weighting factors are also required for multi-species DSMC simulations where the concentration of one species is very low. In order to maintain adequate numbers of particles of the trace species for acceptable statistical sampling, these species must be weighted so that each species is represented by a similar number of simulated particles, however complexity is added to the collisional procedures so that the overall flow momentum and energy can be conserved [1]. Procedures for implementation of these species weighting factors have been proposed Boyd [35] and this conservative weighting scheme (CWS) has been utilised by Wu *et al.* to investigate its potential for modelling CVD processes [36]. This will be discussed in more detail in section 8.2.2.

Following a procedure to index particles to cells depending on their position, particle collisions are generated. Most modern DSMC code uses the efficient "no time counter" (NTC) scheme to select collision pairs within each sampling cell (or sub-cell) [28]. The number of collisions which should occur in a sampling cell N_{coll} is dependent on the number of particles in the cell N_c, the number of real particles each simulated particle represents N_R, the average relative velocity between particles in the cell $\|v_r\|$, the collision cross section σ_T and the cell volume V_C:

$$N_{coll} = \frac{N_c^2 \sigma_T \|v_r\| N_R \Delta t}{2V_C} \tag{3-24}$$

Determination of the average relative velocity in the cell $\|v_r\|$ induces unnecessary computational expense, however by assigning an arbitrary maximum relative velocity $v_{r,max}$ an acceptance-rejection method for choosing collision partners from a set of N_{cand} candidate collision pairs can be employed. Here two potential collision partners having velocity $\boldsymbol{v}_1$ and $\boldsymbol{v}_2$ respectively are selected randomly and a collision is generated if:

$$\frac{|\boldsymbol{v}_1 - \boldsymbol{v}_2|}{v_{r,\max}} > Rand \tag{3-25}$$

where *Rand* is a uniformly distributed random number between 0 and 1, which is usually produced using a pseudo random number generator in the DSMC algorithm.

The number of candidate pairs is selected by:

$$N_{cand} = \frac{N_c^2 \sigma_T v_{r,\max} N_R \Delta t}{2V_C} \tag{3-26}$$

Noting that $N_{coll} / N_{cand} = \|v_r\| / v_{r,max}$ we can see that applying equation (3-25) to N_{cand} collision partners from equation (3-26) will select the same number of collision partners, on average, as required by equation (3-24). This procedure reduces the computational expense of the simulations and can readily be modified to gas mixtures [1]. The determination of the total collision cross section σ_T depends on the collision model being used, and will be discussed in greater detail in section 3.6.3.

3.6.3 Collision Models for the DSMC Method

As mentioned in section 3.2, to fully describe a collision event between two particles a relationship between the magnitude of the particle velocity $\|\boldsymbol{v}\|$, the distance of closest approach b and the scattering angle χ must be determined. The simplest of these models is the hard sphere model where the molecular diameter remains independent of particle velocity and is constant. Two hard sphere molecules will collide when $b \leq d_{12}$ where d_{12} is the mean collision cross section of the collision partners. It follows that $b = d_{12}\cos(\frac{1}{2}\chi)$ and the total collision cross section from equation (3-6) is: $\sigma_T = \pi d_{12}^2$.

A disadvantage of the simple hard sphere model is that the collision cross section is also a function of the translational energy (and hence the magnitude of velocity) of the particle. Consequently the hard sphere model gives an incorrect relationship between the viscosity coefficient and temperature for typical gases. The variable hard sphere (VHS) model, in which the hard sphere diameter becomes a function of the magnitude of the relative velocity of the collision partners $\|\boldsymbol{v}_r\|$ and the temperature exponent of the coefficient of viscosity ω, was formulated to correct this problem [37]. In the VHS model the particle momentum cross section σ_M and the total collision cross section are equivalent, however this leads to discrepancies in simulating flows where diffusion is important. This led to the development of the variable soft sphere (VSS) model by Koura and Matsumoto [38].

In the VSS model, the momentum cross section is related to the total collision cross section by:

$$\sigma_M = \frac{2}{(\alpha+1)}\sigma_T \tag{3-27}$$

where α is the VSS scattering parameter, a function of the Schmidt number which gives the ratio of viscosity to diffusion.

The total collision cross section for the VSS model is given by [1]:

$$\sigma_T = \pi d^2 \qquad \text{where} \quad d = d_{ref}\sqrt{\frac{\left(2kT_{ref}/m_r c_r^2\right)^{\omega-0.5}}{\Gamma(2.5-\omega)}} \tag{3-28}$$

where d_{ref} is the reference molecular diameter at temperature T_{ref}, k is Boltzmann's constant, Γ represents the gamma function and m_r is the reduced mass of the collision partners.

Using equation (3-28) to calculate the collision diameter d, the deflection angle can be determined by [1]:

$$\chi = 2\cos^{-1}\left[\left(\frac{b}{d}\right)^{1/\alpha}\right] \tag{3-29}$$

Polyatomic molecules also have internal degrees of freedom. Consequently energy can be stored in the rotational and vibrational modes, and during collisions this internal energy can be exchanged with the translational mode. The collisions between polyatomic molecules must therefore be regarded as inelastic. A number of phenomenological approaches for dealing with energy exchange between the degrees of freedom have been developed, the most widely known being the Larsen-Borgnakke model [39]. Here energy is exchanged between the internal and translational modes during a fraction of the total number of collisions, which controls the relaxation of the modes toward thermodynamic equilibrium. The procedures for the Larsen-Borgnakke model are detailed in the monograph by Bird [1]. An excellent review of modelling molecules with internal energy can also be found in the thesis by Lilley [40].

3.6.4 Parallel and Hybrid Implementations of the DSMC Method

As mentioned, the DSMC method becomes increasingly computationally expensive as the density of the gas increases and when unsteady simulations are conducted. The computational capacity of the DSMC method can be increased by either parallelising or hybridising the code.

In the parallel DSMC method the computational load of the simulations is shared over multiple computer processors. The DSMC method is ideally suited to parallelisation since the simulated particles move independently during the ballistic movement stage of the simulations, with the coupling only happening during the collision stage. The implementation of parallel DSMC schemes requires careful balancing of the computational load across the processors and often the computational speed-up over single processor calculations is often limited by unbalanced loads and communication between processors.

During the past two decades, a number of parallel-DSMC schemes have been implemented and reported in the literature [41-44]. These schemes utilized either structured or unstructured meshes and mostly static domain decomposition. Here message passing is used to transfer molecules between processors and for simulation synchronisation, however the computational speed-up due to parallelisation is limited by load imbalance and the cost of communication between the processors. These limitations necessitate sizing the problem carefully to the number of processors. Several recent implementations of parallel-DSMC include those by the groups led by Boyd [45], Ivanov [46], LeBeau [47] and Wu [48-51].

Boyd's code, named MONACO, utilizes unstructured grids so that objects with complex geometry can be handled relatively readily, and static domain decomposition for the distribution of computational load. The method has been used to model flow around a planetary probe using 100 million particles and 400 IBM-SP2 processors. Ivanov's code, named SMILE, arranges the cells into "clusters" which are in turn divided among the processors using scalable dynamic domain decomposition. The code employs a simple but effective method of indexing particles to the grid, which reduces the computational time, and determines the direction and amount of workload transfer using the concept of heat diffusion. LeBeau has developed the DSMC Analysis Code (DAC) which uses a two-level embedded Cartesian grid, which is uncoupled from the surface geometry, to discretize the computational domain. The code has been used to study the flow over a sphere using 128 processors with 90% parallel efficiency.

The parallel DSMC algorithm developed by the Wu group will be discussed in more detail in section 6.2. An excellent review of parallel methods can be found in a paper by Wu and Tseng [50].

An alternative method proposed for increasing the computational capabilities of DSMC is by coupling it to a continuum solver. These hybrid methods take advantage of the fact that significant regions of the flow may be able to be accurately solved using a numerical continuum method, such as the finite element solution of the Navier-Stokes equations. In this technique, non-continuum regions are detected through the use of a continuum breakdown parameter (see section 4.1.2) and the flow field in these regions is computed using DSMC, while continuum flow regions are solved using appropriate numerical methods.

A major challenge for hybrid methods lies in the coupling between the two computational techniques. Flow information needs to be passed accurately and efficiently from one scheme to the other. The earliest approaches utilised uncoupled schemes in which flow field information was passed from the continuum solution to the DSMC region, but not vice-versa [52-54]. More sophisticated hybrid techniques employ methods so that information is regularly exchanged between the two types of solvers. There has been a large volume of studies in the literature concerning these strongly coupled hybrid continuum-DSMC methods, most notably from by Sun *et al.* [55], Duttweiler *et al.* [56], Wijesinghe *et al.* [57] and, more recently, Wu *et al.* [58]. An interesting example is the paper by Roveda *et al.* [59] who use an Euler solver in the continuum region to reduce computational expense, and use this method to investigate unsteady slit flow.

A further technique worthy of mention is the particle-only hybrid schemes recently proposed by Macrossan [60-62]. Here a particle method is used everywhere in the flow, however the method for calculating collisions in the continuum regions is changed to the Equilibrium Particle Simulation Method (EPSM) proposed by Pullin [63] in which particle velocities are updated by re-assigning velocities chosen at random from the equilibrium Maxwell-Boltzmann distribution, while conserving the total momentum and energy of the particles in the cell. This saves computational expense over pure DSMC simulations, in which the collision routines somewhat inefficiently exchange one equilibrium state for another in the continuum regions, and avoids the complex coupling procedures of other hybrid continuum/DSMC methods. Several refinements for the method have been suggested, such as the True Direction Equilibrium Flux Method (TDEFM) proposed by Macrossan *et al.* [P64], which does not utilize particles but determines the flux of properties between all cells.

References

[1] G.A. Bird, Molecular Gas Dynamics and the Direct Simulation of Gas Flows (Clarendon Press, Oxford, 1994).

[2] R.L. Liboff, Kinetic theory: classical, quantum, and relativistic descriptions (Wiley, New York, 1998).

[3] C. Cercignani, Rarefied Gas Dynamics: From Basic Concepts to Actual Calculations (Cambridge University Press, Cambridge, 2000).

[4] T.I. Gombosi, Gaskinetic theory (Cambridge University Press, Cambridge, 1994).

[5] J.-Y. Yang, J.-C. Huang and L. Tsuei, Numerical solutions of the nonlinear model Boltzmann equations, *Proc. R. Soc. Lond. A.* 448, 55-80 (1995).

[6] F.M. White, Fluid mechanics (McGraw-Hill, Boston, MA, 1999).

[7] S. Chapman and T.G. Cowling, The mathematical theory of non-uniform gases: an account of the kinetic theory of viscosity, thermal conduction and diffusion in gases (Cambridge University Press, Cambridge, 1970).

[8] L. Holway Jr., New statistical models for kinetic theory, methods of construction, *Phys. Fluids* 9, 1658-1673 (1966).

[9] J. L. Lebowitz, H. L. Frisch and E. Helfand, Nonequilibrium distribution functions in a fluid, *Phys. Fluids* 3, 325-338 (1960).

[10] P.L. Bhatnagar, E.P. Gross and M. Krook, A model collision process in gases. I. Small amplitude processes in charge and neutral one-component system, *Phys. Rev.* 94, 511-525 (1954).

[11] P. Welander, On the temperature jump in a rarefied gas, *Ark. Fys.* 7, 507-553 (1954).

[12] E.M. Shakov, Approximate kinetic equations in rarefied gas theory, *Fluid Dynamics* 3, 112-115 (1968).

[13] J.-Y. Yang and J.-C. Huang, Rarefied Flow Computations Using Nonlinear Model Boltzmann Equations, J. *Comp. Phys.*, 120(2), 323-339 (1995).

[14] B.J. Alder and T. E. Wainwright, Studies in Molecular Dynamics. I. General Method, *J. Chem. Phys.* 31(2), 459-466 (1959).

[15] J.K. Haviland and M.L. Lavin, Applications of the Monte Carlo method to heat transfer in a rarefied gas, *Phys. Fluids* 5, 1399-1405 (1962).

[16] G.A. Bird, Approach to translational equilibrium in a rigid sphere gas, *Phys. Fluids* 6, 1518-1519 (1963).

[17] G.A. Bird, Direct Simulations of the Boltzmann Equation, *Phys. Fluids* 13, 2676-2681 (1970).

[18] W. Wagner, A convergence proof for Bird's direct simulation Monte Carlo method for the Boltzmann equation, *J. Stat. Phys.* 66, 1011-1044 (1992).

[19] D.G. Coronell and K.F. Jensen, Analysis of Transition Regime Flows in Low Pressure Chemical Vapor Deposition Reactors Using the Direct Simulation Monte Carlo Method, *J. Electrochem. Soc.* 8, 2264-2273 (1992).

[20] G. J. LeBeau and F. E. Lumpkin III, Application highlights of the DSMC Analysis Code (DAC) software for simulating rarefied flows, *Comput. Meth. Appl. Mech. Eng.* 191(6), 595-609 (2001).

[21] I.D. Boyd, Y. Jafry and J.V. Beukel, Particle simulations of helium microthruster flows, *J. Spacecraft Rockets* 31(2), 271-277 (1994).

[22] K. Teshima and M. Usami, DSMC simulation of axisymmetric supersonic free jets, *Comp. Fluid Dyn. J.* 10, 525-530 (2001).

[23] G.E. Karniadakis and A. Beskok, Micro flows: fundamentals and simulation (Springer, New York, 2002).

[24] M.-K. Kwon and Y.-K. Hwang, A Study on the Pumping Performance of a Molecular Drag Pump in the Rarefied Gas Flow, in Proc. of 25th International Symposium on Rarefied Gas Dynamics, St. Petersburg, Russia (2006).

[25] G.A. Bird, The DS2V Program User's Guide, GAB Consulting Pty Ltd (2005).

[26] G.A. Bird, Monte Carlo Simulation of Gas Flows, *Annu. Rev. Fluid Mech.* 10, 11-31 (1978).

[27] G.A. Bird, Direct Simulation of Gas Flows at the Molecular Level, *Comm. Appl. Num. Meth.* 4, 165-172 (1998).

[28] F. Alexander and A. Garcia, Direct Simulation Monte Carlo, *Comput. Phys.* 11 588-593 (1997).

[29] E.S. Oran, C.K. Oh and B.Z. Cybyk Direct Simulation Monte Carlo: Recent Advances and Applications, *Annu. Rev. Fluid Mech.* 30, 403-441 (1998).

[30] M. S. Ivanov and S. F. Gimelshein, Computational Hypersonic Rarefied Flows, *Annu. Rev. Fluid Mech.* 30, 469-505 (1998).

[31] G.J. LeBeau, K.A. Jacikas and F.E. Lumpkin, Virtual sub-cells for the Direct Simulation Monte Carlo Method, 41st AIAA Aerospace Sciences Meeting & Exhibit, Reno (NV) (2003).

[32] G.A. Bird, The DS2V/3V Program Suite for DSMC Calculations, in Proc. of 24th International Symposium on Rarefied Gas Dynamics, Bari, Italy (2004).

[33] G.A. Bird, Sophisticated Versus Simple DSMC, in Proc. of 25th International Symposium on Rarefied Gas Dynamics, St. Petersburg, Russia (2006).

[34] K. L. Guo and G. S. Liaw, A Review: Boundary conditions for the DSMC method, 35th AIAA Thermophysics Conference, Anaheim, CA (2001).

[35] I.D. Boyd, Conservative species weighting scheme for the direct simulation Monte Carlo method, *J. Thermophys. Heat Tran.* 10(4), 579-585 (1996).

[36] J.-S. Wu, W.-J. Hsiao, Y.-Y. Lian and K.-C. Tseng, Assessment of conservative weighting scheme in simulating chemical vapour deposition with trace species, *Int. J. Numer. Meth.* 43, 93-114 (2003).

[37] G.A. Bird, Monte-Carlo simulation in an engineering context, in Proc. of 12th International Symposium on Rarefied gas dynamics, Charlottesville, VA (1981).

[38] K. Koura and H. Matsumoto, Variable soft-sphere molecular model for inverse-power or Lennard-Jones potential, *Phys. Fluids A* 3, 2459-2465 (1991).

[39] C. Borgnakke and P.S. Larsen, Statistical collision model for Monte Carlo simulation of polyatomic gas mixtures. *J. Comput. Phys.* 18, 405-420 (1975).

[40] C.R. Lilley, A macroscopic chemistry method for the direct simulation of non-equilibrium gas flows, PhD thesis, University of Queensland (2005).

[41] T.R. Furlani and J.A. Lordi, Implementation of the direct simulation Monte Carlo method for an exhaust plume flowfield in a parallel computing environment, AIAA Paper 88-2736 (1988).

[42] Y. Matsumoto and T. Tokumasu, Parallel computing of diatomic molecular rarefied gas flows, *Parallel Comput*. 23 1249-1260 (1997).

[43] R.P. Nance, R.G. Wilmoth, D. Moon, H.A. Hassan and J. Saltz, Parallel solution of three-dimensional flow over a finite flat plate, AIAA Paper 94-0219 (1994).

[44] M. Ota and T. Tanaka, On speedup of parallel processing using domain decomposition technique for direct simulation Monte Carlo method, *JSME (B)* 57(540) 2696-2701 (1991).

[45] S. Dietrich and I. Boyd, Scalar and parallel optimized implementation of the direct simulation Monte Carlo method. *J. Comput. Phys.* 126, 328-342 (1996).

[46] M. Ivanov, G. Markelov, S. Taylor and J. Watts, Parallel DSMC strategies for 3D computations, in Proc. Parallel CFD96, Capri, Italy (1996).

[47] G.J. LeBeau, A parallel implementation of the direct simulation Monte Carlo method, *Comp. Meth. Appl. Mech. Engrs*. 174, 319-337 (1999).

[48] J.-S. Wu and Y.-Y. Lian, Parallel three-dimensional direct simulation Monte Carlo method and its applications, *Comput. Fluid* 32(8), 1133-1160 (2003).

[49] J.-S. Wu, K.-C. Tseng and F.Y. Wu, Parallel three-dimensional DSMC method using mesh refinement and variable time-step scheme, *Comput. Phys. Comm.* 162, 166-187 (2004).

[50] J.-S. Wu and K.-C. Tseng, Parallel DSMC method using dynamic domain decomposition, *Int. J. Numer. Meth. Eng.* 63, 37-76 (2005).

[51] J.-S. Wu, S.-Y. Chou, U.-M. Lee, Y.-L. Shao, and Y.-Y. Lian, Parallel DSMC simulation of a single under-expanded free orifice jet from transition to near-continuum regime, *J. Fluid Eng.* 127 1161-1170 (2005).

[52] D.C. Wadsworth and D.A. Erwin, One-dimensional hybrid continuum/particle simulation approach for rarefied hypersonic flows, in Proc. of 5th Joint Thermophysics and Heat Transfer Conference, Seattle, WA (1990).

[53] F.E. Lumpkin, S.M. Fitzgerald, G.J. LeBeau, G.N. Markelov, and M.S. Ivanov, Study of 3D rarefied flow on a flat plate in the wake of a cylinder, in Proc. of 33rd AIAA Thermophysics Conference, Norfolk, VA (1999).

[54] D.B. Hash and H.A. Hassan, A decoupled DSMC/Navier-Stokes analysis of a transitional flow experiment, in Proc. of 34th Aerospace Sciences Meeting and Exhibit, Reno, NV (1996).

[55] Q. Sun, I.D. Boyd, and G.V. Candler, A hybrid continuum/particle approach for modelling subsonic rarefied gas flows. *J. Comput. Phys.* 194, 256-277 (2004).

[56] C.R. Duttweiler, D. Baganoff, W.J.A Feiereisen, Hybrid Navier-Stokes/Particle Method for Simulating Rarefied Flow, American Physical Society Division of Fluid Dynamics Meeting (1997).

[57] H.S. Wijesinghe, R.D. Hornung, A.L. Garcia and N.G. Hadjiconstantiou, Three-dimensional hybrid continuum-atomistic simulations for multiscale hydrodynamics, *J. Fluids Eng*. 126(5), 768-777 (2004).

[58] J.-S. Wu, Y.-Y. Lian, G. Cheng, R.P. Koomullil and K.-C. Tseng, Development and verification of a coupled DSMC-NS scheme using unstructured mesh, *J. Comp. Phys.* 219(2), 579-607 (2006).

[59] R. Roveda, D.B. Goldstein and P.L. Varghese, Hybrid Euler/Direct Simulation Monte Carlo Calculation of Unsteady Slit Flow, *J. Spacecraft Rockets* 37(6), 753-760 (2000).

[60] M.N. Macrossan (2001) A Particle-Only Hybrid Method for Near-Continuum Flows, in Proc. of 22nd International Symposium on Rarefied Gas Dynamics, 388-395, Sydney, Australia (2001).

[61] M.N. Macrossan, μ-DSMC: A general viscosity method for rarefied flows, *J. Comput. Phys*., 185, 612-627 (2003).

[62] M.N. Macrossan, υ-DSMC: A fast simulation method for rarefied flows, *J. Comp. Phys.*, 173, 600-619 (2001).

[63] D.I. Pullin, Direct simulation methods for compressible ideal gas flow, *J. Comput. Phys.* 34, 231-144 (1980).

[64] M.N. Macrossan, M.R. Smith, M.V. Metchnik and P.A. Pinto, True Direction Equilibrium Flux Method applications on rectangular 2D meshes, in Proc. of 25th International Symposium on Rarefied Gas Dynamics, St. Petersburg, Russia (2006).

4. PP-CVD Flow Field Modelling

4.1. Modelling Considerations

4.1.1. The Injection and Pump-down Phases

As mentioned in section 2.3.1, the PP-CVD process consists of a series of regular injection and pump down phases. During the injection phase, precursor is released into the reactor from a high pressure source vessel. During the pump-down (or evacuation) phase, the inlet jet collapses and the reactor is partially evacuated by a vacuum pump to a base pressure P_{min}. It was shown experimentally in previous work (see section 2.3.5) that minimising the injection time and having a relatively long pump-down time results in a highly uniform convective flow field within the reactor. During the injection and pump-down phases, the gas within the reactor experiences a continuous state of overall expansion, but each phase is clearly a physically different processes. The injection phase is an extremely rapid (approximately 0.1s), whereas the pump-down phase occurs relatively slowly (approximately 40s).

During the injection phase, gas is released from a high pressure source volume through an orifice into the reactor. For a pressure ratio between the source and the quiescent atmosphere (in this case the reactor volume) of more than 10, a highly under-expanded jet will form [1]. In PP-CVD this ratio is at least three orders of magnitude, so it is expected that an unsteady under-expanded jet will form during this phase, and collapse as the inlet orifice closes at the start of the pump-down phase

The structure of a steady under-expanded jet exhausting into a constant pressure quiescent atmosphere is shown in figure 4.1. When the choked flow condition is satisfied at the orifice, a Prandtl-Meyer expansion fan is formed and these expansion waves reflect from the jet boundary as compression waves. The interaction of these waves forms a barrel-shaped incident shock surrounding the jet core. In the highly under-expanded case, a shock normal to the direction of the flow, commonly called a Mach disk, is formed which separates a highly supersonic region upstream from a subsonic region downstream [2]. This structure may be repeated in series, forming Mach diamonds which generally decrease in size in the downstream direction.

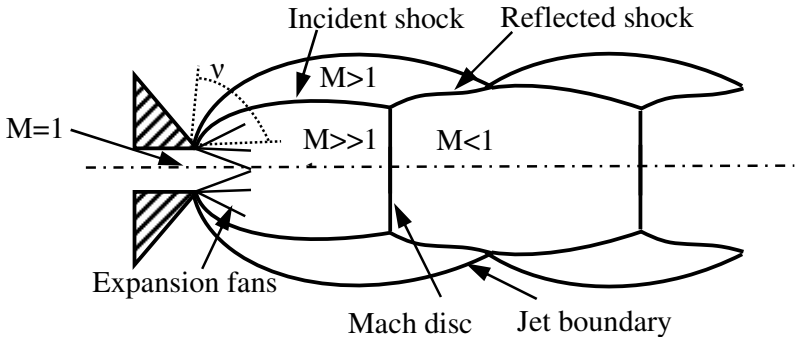

Figure 4.1. Schematic of the structure of a steady highly under-expanded jet

Computational fluid dynamics (CFD) software has been used to model under-expanded jets [3,4] however there are only limited CFD studies of highly under-expanded jets. The presence of strong discontinuities, such as shocks, tends to lead to solver instability during calculation and a further difficulty is the presence of a wide range of flow conditions including continuum regions near the jet inlet, rarefied regions far downstream and significant breakdown of thermodynamic equilibrium in the shocks and expansion fans. Some effort has been made to overcome these difficulties, for example Mate *et al.* [5] used the quasi-gas dynamic (QGD) method, which is less sensitive to computational instabilities under strong property gradients, in an attempt to overcome solver instability for steady supersonic jets of CO_2.

Hybrid methods, combining continuum solvers and the particle based Direct Simulation Monte Carlo (DSMC) approach have been used where the flow transitions between the continuum and rarefied regimes. These generally involve uncoupled methods where the CFD solution simply provides a boundary condition to the region modelled using DSMC [6,7]. The authors of these papers indicate that they have confidence that CFD can reasonably predict the conditions for the breakdown of continuum behaviour even though the solution of the Navier-Stokes equations via CFD does not give an accurate representation of the flow downstream of the continuum region. Stand-alone DSMC simulations have also been used to study low density jet expansions [8,9] and other studies compare CFD and DSMC simulations for steady expansions under various conditions [10,11].

The literature concerning the unsteady expansion of jets into a constant-pressure quiescent atmosphere is considerably more limited. Unsteady jet structure development is particularly

important during the start up of propulsion systems and during the PP-CVD injection phase. Chang [12] has used the space-time conservation element/solution element (CE/SE) based Navier-Stokes solver (see section 9.4.2) to model unsteady-state jet flows, noting that the development of the shock structure gives the appearance of a travelling vortex ring. Roveda *et al.* [13] have used a coupled hybrid method to model the unsteady development of a jet issuing from a two-dimensional slit in a domain containing regions of continuum, rarefied and transition flows, however they relied on a continuum breakdown definition which did not take into account temporal effects. No research could be found in the literature documenting the unsteady expansion of an under-expanded jet into a confined volume in which the pressure constantly rises, as is the case in PP-CVD.

4.1.2. PP-CVD Flow Regime and Continuum Breakdown

As discussed in section 3.4, the continuum approach to gas dynamics assumes that:

- the molecular velocity distribution is only slightly perturbed from the equilibrium Maxwell-Boltzmann distribution,
- the molecular velocity distribution is characterized by a single translational temperature,
- there are sufficient molecules within the region of interest such that macroscopic quantities may be defined by the average of the molecular quantities.

Under certain flow conditions, these assumptions no longer remain valid and continuum breakdown occurs. In hypersonic flows, which include under-expanded jet flow, the reason for continuum breakdown is that the number of intermolecular collisions within the gas is insufficient to maintain the equilibrium molecular velocity distribution because the scale lengths of macroscopic property changes are of the same order as the mean free path. It is reasonable to suppose that during the PP-CVD injection phase, which is a rapidly expanding flow in which a strongly under-expanded jet is likely to form, continuum breakdown will occur.

In vacuum systems the transition from continuum to molecular flow is normally characterized by the operating pressure [14]. Bird proposed a semi-empirical Lagrangian “freezing” parameter for assessing continuum breakdown based on the divergence of the kinetic temperature components [15]:

$$P_f = \frac{1}{f}\frac{D(\ln \rho)}{Dt} \tag{4-1}$$

where f is the collision frequency, ρ is the fluid density, and D/Dt represents the substantial derivative. Breakdown occurs for $P_f > 0.04$ in steady expanding flows.

Boyd *et al.* [16] and Wang and Boyd [17] extended upon this idea by modifying the parameter to allow gradients based on other fluid properties to be considered. The limitations in flow around stagnation points in equation (4-1) were noted, and a breakdown parameter for steady flows based on a gradient-length Knudsen number was proposed:

$$Kn_Q = \frac{\lambda}{Q}|\nabla Q| \tag{4-2}$$

where λ represents the mean free path, Q some flow property such as density, velocity magnitude or translational temperature, and ∇ is the gradient operator.

Although Bird's parameter does not preclude unsteady expansion, the work within the literature primarily concerns steady-state expansion. Roveda *et. al.* modelled unsteady flow through a slit, but used a steady form of P_f and Kn_Q to identify continuum breakdown [13].

During the steady expansion of a gas, continuum breakdown will occur as the mean free path of the gas becomes large relative to the scale length of property gradients within the flow. In an unsteady expansion, local flow properties will vary with time and position. During a very rapid expansion the mean free path may change at a rate of the same order as the collision frequency, hence the time-rate of expansion will have an important affect on continuum breakdown. Figure 4.2 illustrates the conceptual difference between steady continuum flow, steady molecular flow, and the motion of molecules when a high pressure gas is suddenly released into an evacuated chamber. The chamber experiences rapid filling and rapid pressure rise, while the injected gas jet experiences rapid expansion. This sudden expansion leads to an exponential increase in mean free path, and a corresponding drop in the rate of intermolecular collisions.

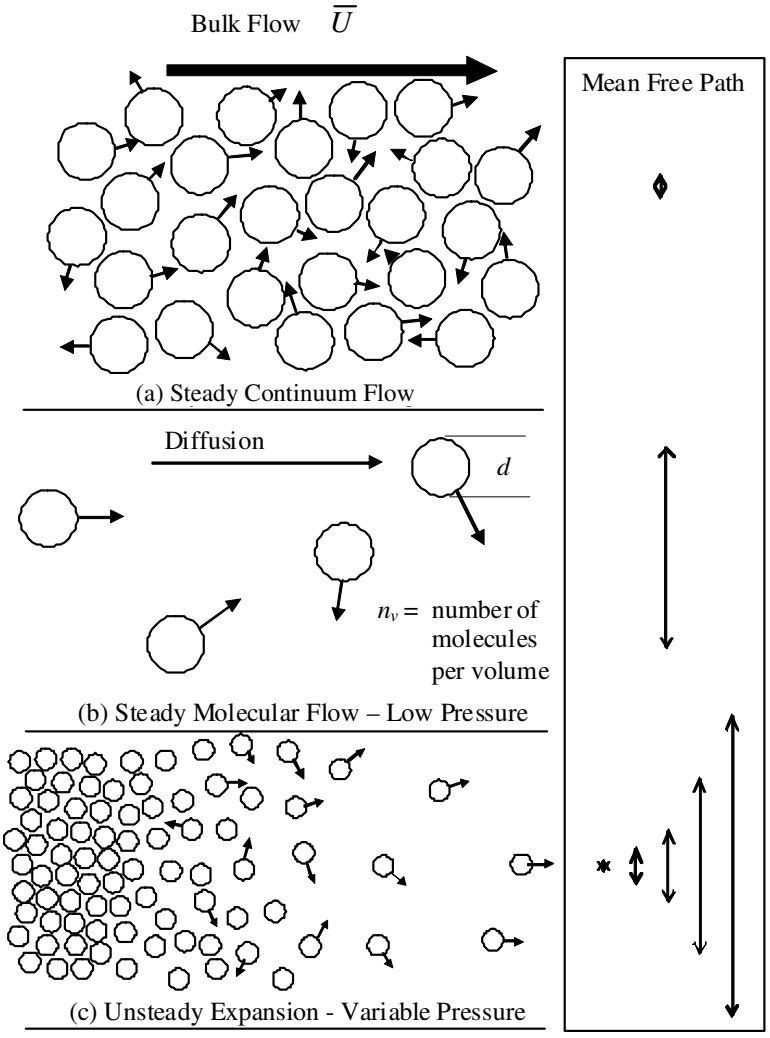

Figure 4.2. Schematic illustrating the requirement for a continuum breakdown parameter which accounts for temporal effects and the difference between a) steady continuum flow, b) molecular flow and c) and unsteady expansion flow [diagram courtesy of S.P. Krumdieck].

An alternative breakdown parameter based on the time dependent mean free path evolution in an expanding gas is proposed, which is also discussed in the paper by Krumdieck *et al.* [18]:

$$B = \frac{1}{f\lambda}\left|\frac{D\lambda}{Dt}\right| = \frac{1}{v_{av}}\left|\frac{D\lambda}{Dt}\right| \tag{4-3}$$

where v_{av} is the local average molecular velocity.

In equation (4-3) expansion effects dominate the transport behaviour when the spatio-temporal change of mean free path becomes significant compared to the local average molecular velocity. When the rate of expansion is rapid enough, the rate of mass transport

due to expansion throughout a volume will be greater than the rate at which intermolecular equilibrium is established. The continuum assumption will not then be valid even at molecular densities (e.g. pressure ranges) which would result in continuum behaviour under steady conditions. The parameter was developed from the above observations, however it can also be constructed from Bird's freezing parameter (equation (4-1)), by replacing density with mean free path as the local gas property of interest and normalizing by mean free path to non-dimensionalise the equation.

Equation (4-3) can be further broken into spatial and temporal components by separating the time-dependent terms:

$$B = B_{spat} + B_{temp} \quad \text{with: } B_{temp} = \frac{1}{v_{av}}\left|\frac{d\lambda}{dt}\right| \qquad B_{spat} = \frac{1}{v_{av}}\left|\bar{u}\cdot\nabla\lambda\right| \tag{4-4}$$

where $\bar{u}$ is the velocity vector for the bulk flow of the expanding gas at a given point.

The relative influence of temporal breakdown on the reactor flow can be illustrated by assuming a Maxwell-Boltzmann distribution of molecular velocities in equation (4-3) and a uniform temperature throughout the flow. The average molecular velocity over the region, $\bar{v}_{av}$, can then be compared to the rate of change of the average value of the mean free path $\bar{\lambda}$ over that region such that:

$$\bar{B}_{temp} = \frac{1}{\bar{v}_{av}}\left|\frac{d\bar{\lambda}}{dt}\right| \tag{4-5}$$

Equation (4-5) enables reactor pressure measurements to be used to determine when there are substantial regions of the flow where time-dependent continuum breakdown is significant without the requirement for using simulation methods to determine the value of the breakdown parameter at particular points in the flow field.

Figure 4.3 shows equation (4-5), as determined by the reactor pressure, for a 0.5s and a 4.0s injection time.

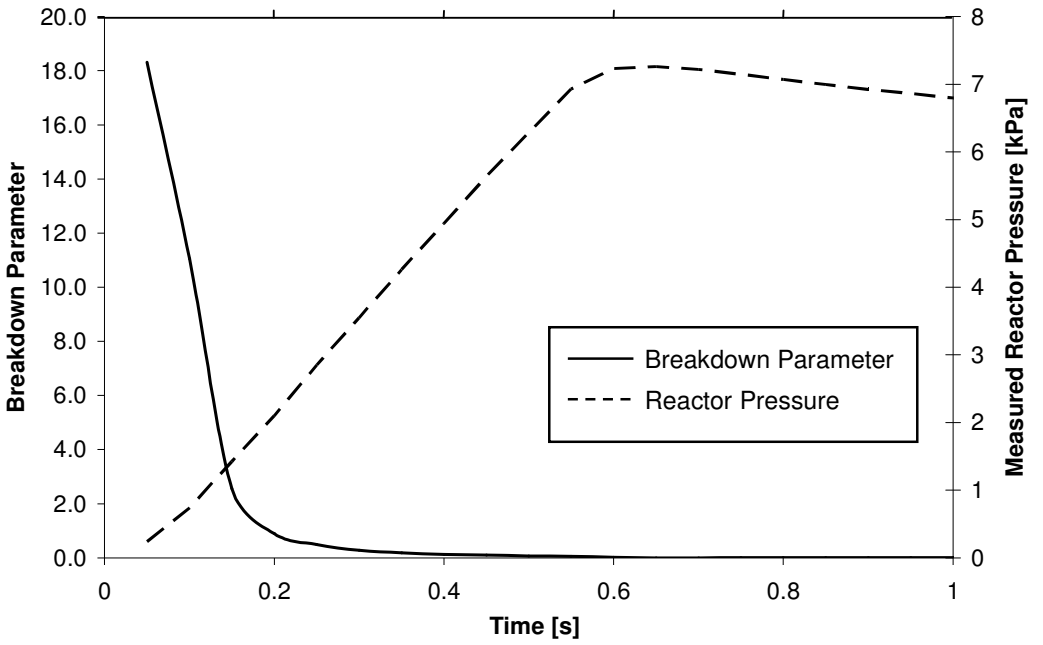

(a)

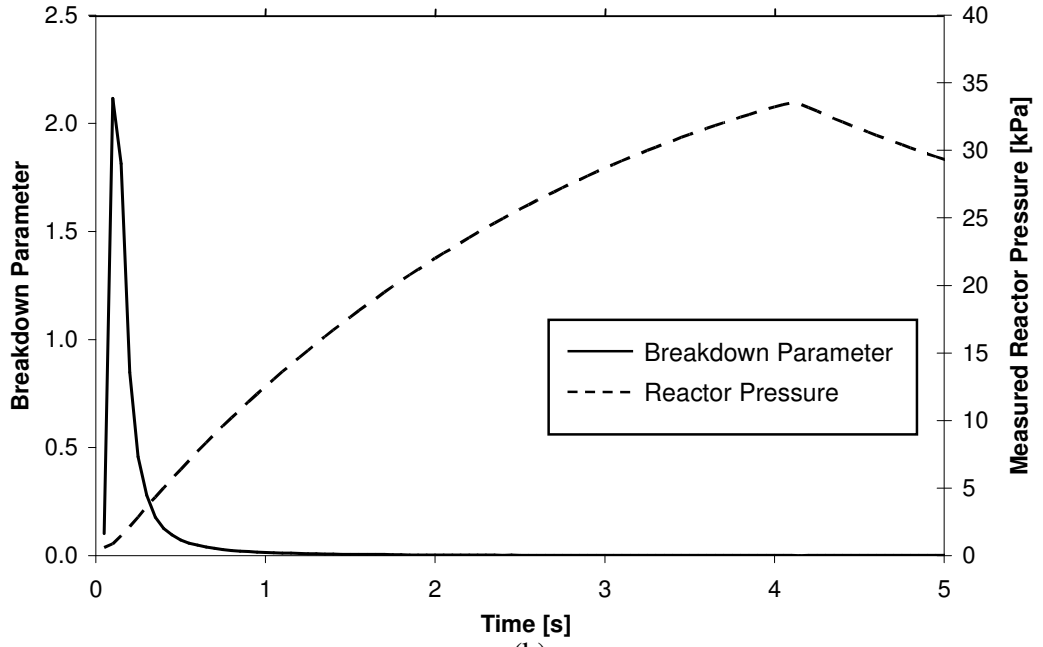

(b)

Figure 4.3. The relative influence of temporal continuum breakdown determined by reactor pressure and equation (4-5) in PP-CVD reactors with a) a short (0.5s) injection time and b) a long (4.0s) injection time [18].

In figure 4.3a, the reactor pressure and breakdown parameter is shown during the short injection time of 0.5s. Here there is a very sharp rise in reactor pressure of around 7kPa in 0.5s, coupled with a sharp rise in the breakdown parameter which remains significant during most of the injection phase ($\overline{B}_{temp} \approx 0.07$ at $t = t_i$). This indicates there are likely to be significant regions of the flow undergoing time-dependent continuum breakdown during this process.

Figure 4.3b shows the reactor pressure and breakdown parameter over the longer injection time of 4s. During the initial expansion the breakdown parameter is significant, however as the expansion progresses, the time-dependent continuum breakdown effectively ceases within the flow ($\overline{B}_{temp} \approx 6.64 \times 10^{-4}$ at $t = t_i$). This indicates that throughout a large proportion of the injection phase, there is unlikely to be continuum breakdown due to temporal effects (however, this does not preclude breakdown due to high spatial gradients of flow properties).

Although the above method is somewhat crude, it illustrates that continuum breakdown due to temporal effects is significant during the PP-CVD process. Krumdieck *et al.* [18] proposed that when a PP-CVD reactor is operated with $B > B_{crit}$ during the injection phase, then expansion effects will dominate the mass transport processes within the reactor. They additionally proposed that when $B < 0$ during the pump-down phase of the pulse cycle, the quiescent gas in the reactor volume experiences expansion mass transport with increasing diffusion-driven molecular motion as the pressure drops back to the minimum pressure. The results of this study are consistent with the experimental findings of section 2.3.5 in that highly rapid injection phases and relatively slow pump-down processes are required to give high convective uniformity, and thus uniform deposition, within a PP-CVD reactor.

4.1.3. Validity of the Continuum Equations

The method discussed above allows the relative influence of time-dependent continuum for a given reactor configuration to be determined. However, within the reactor flow field there will be regions in which the spatial-temporal gradients of the flow properties are very high, and other regions where these gradients are low. The presence of localised high property gradients in which equations (4.1)-(4.3) show the continuum assumptions to be invalid, demonstrate that simulating the flow using continuum equations, such as the Navier-Stokes equations, is inappropriate.

To investigate the influence of non-continuum regions in the flow, computational fluid dynamics (CFD) software was used. Although using the Navier-Stokes equations to investigate the presence of non-continuum phenomena seems counter-intuitive, CFD actually is able to predict continuum breakdown quite well, as demonstrated by Glass [7] and Sun *et al.* [6]. By determining the breakdown values for equation (4-3) using a CFD simulation, a qualitative understanding of continuum breakdown in the flow field can be obtained, even if numerical dissipation due to the presence of these regions means that quantitative values spatially and temporally downstream in the flow field cannot accurately be determined.

To this end, a simulation of the preliminary part of the PP-CVD injection phase was conducted using the commercial CFD package Fluent version 6.2. For the purposes of the simulation, the reactor gas supply pressure is assumed to remain constant during the injection process, and the exhaust of gas from the reactor is assumed to have negligible flow rate compared to the inlet (thus no outlet boundary condition is implemented). PP-CVD processing typically involves precursor injection times of less than one second in duration and, as these simulations were intended to study the injection phase only, the maximum simulated time was one second. Firstly, the development of the unsteady jet was investigated by tracking the position of the Mach 1 contour. The post processing code was then used to assess the value of equation (4-3) at a position within the expansion front along the jet's central axis. Equation (4-3) was also resolved into temporal and spatial components to illustrate the changing contribution each component makes to the total value of the breakdown parameter with time.

The two-dimensional axisymmetric computational domain consists of a supply volume which is held at a constant static pressure P_S, a supply tube of diameter d and length l, and an enclosed reactor volume of diameter D and length L with an initial pressure of P_i. An unstructured mesh was used in the reactor and supply volumes, with a structured mesh in the supply tube where alignment of the flow with the quadratic cells could be guaranteed. An initial grid size of 13,388 cells was used, with the mesh being refined within the vicinity of the supply tube. Figure 4.4 shows the grid in the region of the supply tube. The grid was iteratively refined based on Mach number gradients throughout the solution process to ensure the shock structures were resolved with sufficient detail to determine the breakdown value.

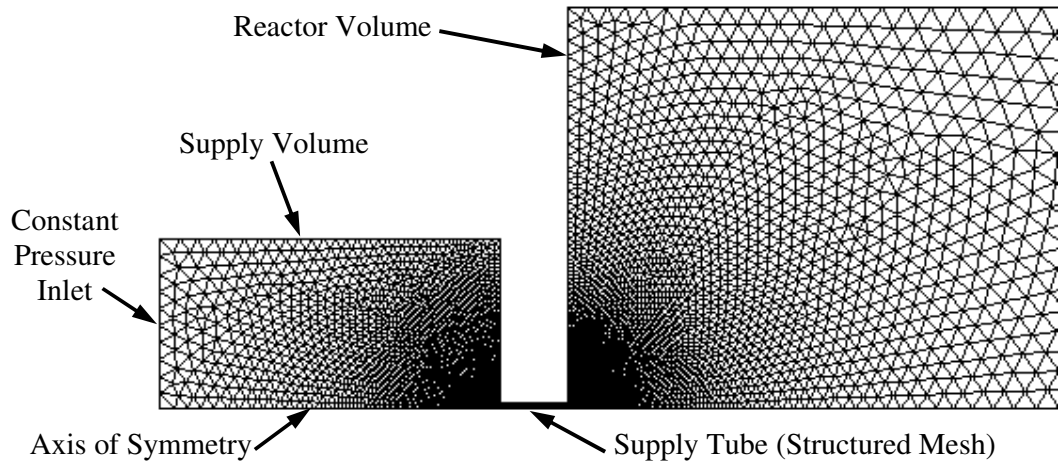

Figure 4.4. Grid detail for the simulation of a PP-CVD reactor using CFD

The parameters used in the simulations are listed in table 4.1. The pressure values and dimensions were chosen as being typical reactor parameters for the experimental PP-CVD uniformity studies being conducted at the time of these simulations.

Table 4.1. Simulation parameters for CFD study of PP-CVD injection phase

Parameter	**Value**
Supply pressure, P_S	350 kPa
Initial reactor pressure, P_i	100 Pa
Gas	Nitrogen, N_2
Gas temperature, T	300 K
Jet inlet diameter, d	2 mm
Supply tube length, l	10 mm
Reactor diameter, D	118 mm
Reactor length, L	400 mm
Time step, t	1 - 100 μs

The segregated solver available in Fluent® was utilized, using first-order temporal and spatial discretisation. Time steps of 1μs were used to ensure convergence during the initial expansion, with this value being increased to 10-100μs as the flow developed. The convergence criteria was taken to be when residuals were of the order $O(10^{-4})$ for the

continuity equation, momentum equations and the turbulence models; and $O(10^{-6})$ for the energy equation. The Reynolds number based on the inlet conditions is approximately 55,000 which necessitates the use of a turbulence model to close the Navier-Stokes governing equations. The model chosen was the renormalization group theory (RNG) k-ε model, which has been the model of choice for other under-expanded jet simulations [1,11,20].

A verification study was conducted by comparing the results obtained using the PP-CVD reactor grid with simulations replicated from Woodmansee *et al.* [1], who used a Fluent model with a structured grid to simulate a steady under-expanded jet. They conducted a grid independence study and compared their results to experimental data obtained using an anti-Stokes Raman scattering (CARS) technique. The PP-CVD reactor geometry was modified slightly by replacing the reactor walls with far field boundary conditions at P = 0.98atm and T = 294K; and replacing the inlet with a slightly convergent nozzle with d = 5mm conforming to the nozzle used by Woodmansee *et al.* [1], otherwise the fundamental structure and type of grid was preserved. A jet of air with P_S = 6.05atm and T_S = 296K was expanded unsteadily through the nozzle until the steady state was reached. The results of this study are illustrated in Figure 4.5 which compares the variation of density along the jet's central axis for both grids to the experimental data obtained by Woodmansee *et al.* [1]. Both simulations show reasonable agreement with the experimental data and the predicted axial position of the Mach disk occurs at approximately 1.5d in both cases. The results of this validation study indicate that the present simulation method is appropriate for modeling an under-expanded jet, that the results have reasonable physical accuracy and that grid independence has been achieved in the region of the Mach disc.

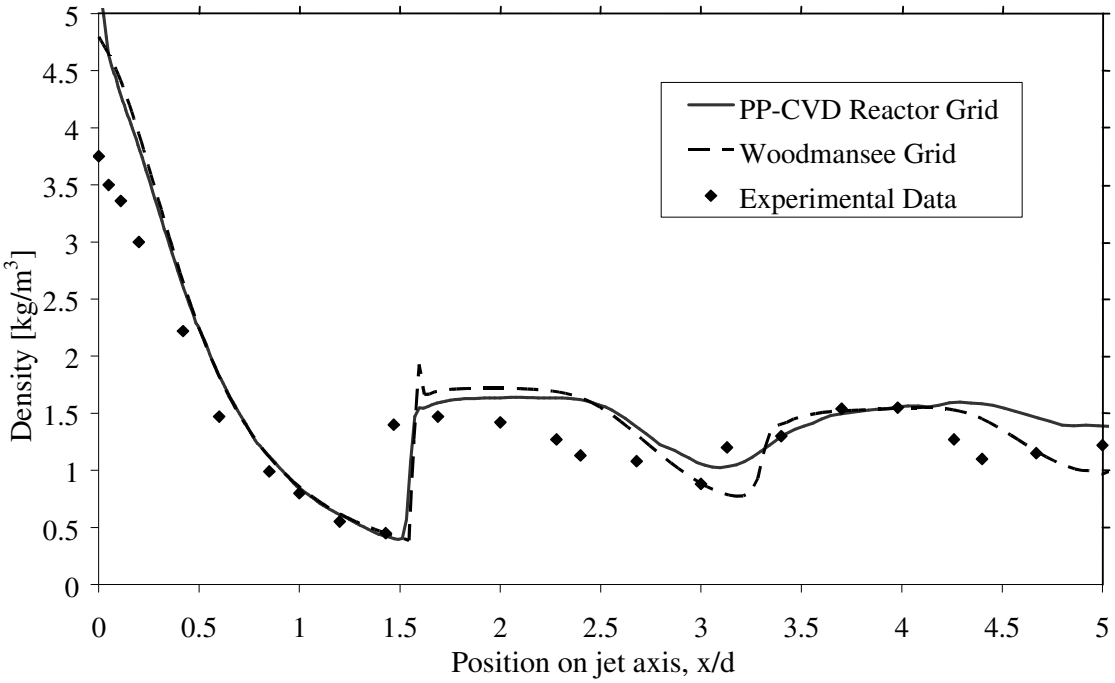

Figure 4.5. Comparison of the predicted axial variation of density along the axis of a steady under-expanded jet from CFD simulations with the experimental data obtained by Woodmansee *et. al.* [1].

Figure 4.6 shows the development of the total value of the breakdown parameter B in the expansion front as determined from equation (4-3), along with illustrations of the Mach 1 contour indicating the size of the jet structure as the flow develops. During the initial transient, the region enclosed by the sonic expansion front increases in both the axial and radial directions. By 1ms, two distinct shock regions are discernable: the Mach disk normal to the flow direction, and the barrel shock extending downstream from the Mach disk; both of which are enclosed by the Mach 1 contour. As the static pressure within the reactor continues to rise, the highly supersonic region contracts and the features of a quasi-steady under-expanded jet such as the Mach disk and barrel shock become clearly visible.

The value of the breakdown parameter initially increases with the expanding shock region and then decreases as the jet contracts. During the initial expansion, the peak velocities in the region immediately upstream of the shock front become very large (in this case, approximately Mach 11.3 at 1ms). This tends to increase the spatial terms in the breakdown parameter. As the jet contracts and begins to tend towards a quasi-steady state, the peak velocities gradually reduce causing the total value of B to decrease. As the expansion

continues, the position of the Mach disc tends asymptotically towards a steady value, as does the value of *B*.

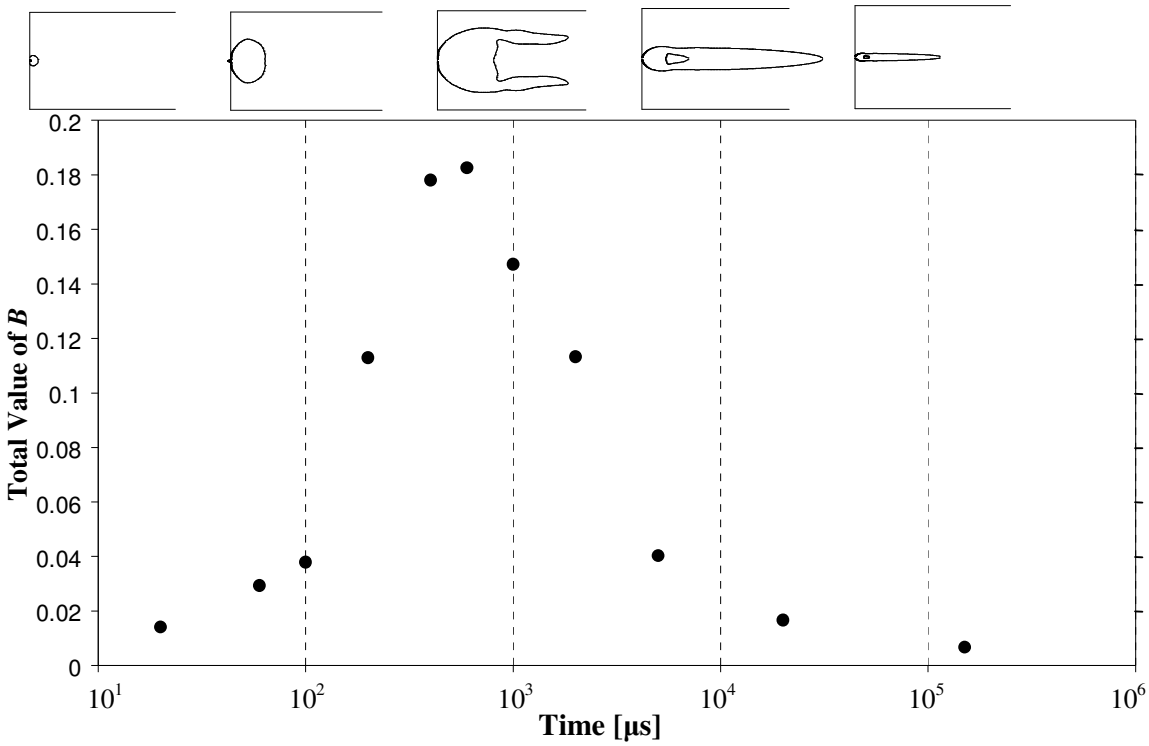

Figure 4.6. The relationship between the total value of the breakdown parameter *B* in an unsteady under-expanded jet and the size of the unsteady jet as illustrated by the position of the Mach 1 contour.

Resolution of the total value of *B* into its spatial and temporal components, as per equation (4-4), is shown in Figure 4.7. Early in the expansion, the time-dependent components of the breakdown parameter contribute considerably to its total value, however by later in the expansion the importance of time dependent terms becomes negligible. The reasons for this are twofold: firstly, the speed at which the expansion front advances decreases with time meaning the $d\lambda/dt$ term in equation (4-4) decreases and, secondly, the gas behind the expansion front accelerates increasing the *u* and *v* velocity component terms in equation (3-4) and thus increasing the spatial breakdown components.

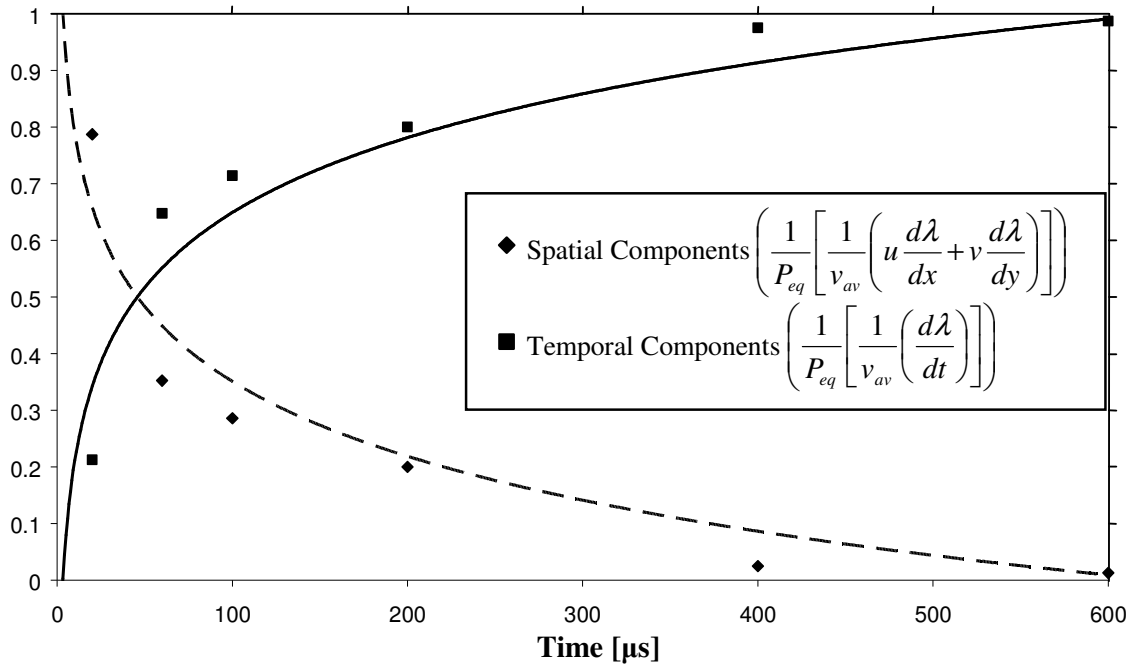

Figure 4.7. The contribution of spatial and temporal components to the total value of the breakdown parameter *B*.

The unsteady continuum breakdown parameter in equation (4-3) predicts a significant degree of continuum breakdown during the PP-CVD injection phase. Figure 4.7 shows that during the early expansion transient a significant proportion of the breakdown predicted is due to temporal effects. As the flow develops, temporal effects become less significant; however there are still substantial regions of continuum breakdown due to the steep property gradients within the shock structure. The parameter appears to be an efficient method of capturing continuum breakdown in unsteady expansions. During the early part of the expansion, the parameter shows the strong influence of time-dependent breakdown and as the jet develops and the influence of time dependent terms diminishes, the parameter is able to predict space-dependent continuum breakdown.

Although the solution of the flow field using CFD has limitations, the method does produce a qualitative description of the evolution of an unsteady jet expanding into a confined volume. Further, despite the inaccuracies of simulating this flow with the Navier-Stokes equations, this CFD study predicts the existence of regions of continuum breakdown within the flow field which require a non-continuum method to accurately resolve.

4.2. Selection of an Appropriate Modelling Technique for PP-CVD

Section 4.1 shows that a method for simulating PP-CVD requires a technique capable of capturing both time-dependent and non-continuum effects accurately. Recent simulations by T.-H. Lin (National Chiao Tung University, Hsinchu, Taiwan) using the UNIC-UNS Navier-Stokes solver indicate that at initial reactor pressures above approximately 1000Pa, the Navier-Stokes equations are able to capture the flow field accurately, however at lower pressures the results have unrealistic values for the gas temperature (on the order of 10,000K) providing a further indication that the continuum equations are invalid (details to be published in Lin's masters thesis). At lower reactor pressures, the use of continuum equations alone to solve the flow field is precluded due to continuum breakdown. This means the options for modelling the PP-CVD flow field are a method which solves the Boltzmann equation or model Boltzmann equation, a particle based approach or some hybrid continuum/non-continuum approach.

As mentioned in section 3.5, the complexity of the non-linear integral collision term means the full Boltzmann equation is extremely difficult to solve for all but the most basic of situations. For this reason, the model Boltzmann equation (MBE) has been developed (see section 3.5). There are several difficulties with using an MBE based solver for PP-CVD. The first is due to the wide range of flow velocities in the PP-CVD flow field, which ranges from stationary gas to hypersonic flow. This would require a large range on the limits for discretisation in the velocity domain which would greatly increase the computational expense of the simulations. The second problem is that the method is presently restricted to a simple model of collision dynamics which is likely to ultimately preclude modelling the complex metal-organic precursors used in some PP-CVD applications.

The use of some kind of hybrid continuum/Boltzmann-based non-continuum solver is equally problematic for the reasons listed above and because very few solvers of this type have been developed. One such solver is the Unified Flow Solver (UFS) developed by Kolobov *et al.* [20] which uses a direct numerical solver for the Boltzmann transport equation coupled with a kinetic scheme (usually an Euler solver). However the case studies presented for the UFS solver show that the computational expense of using it to solve a PP-CVD flow field would be unfeasibly high [21]. The possibility for the development of alternative schemes is discussed in chapter 9.

A further issue with any differential equation based (as opposed to particle-based) approach is that the methods do not provide output information on the behaviour of individual particles, which would be useful for future integration of the flow field model with a Monte Carlo based surface film growth model.

The most widely used particle-based method is the Direct Simulation Monte Carlo (DSMC) method discussed in section 3.6. This method tracks a large number of simulated particles which each represent a number of real particles through the computational domain by decoupling the intermolecular collisions with the ballistic transport of particles. The method is well established and accurate for rarefied to continuum flows and, most importantly, is inherently non-steady (even though the vast majority of DSMC studies in the literature concern steady flows). DSMC is able to incorporate a variety of phenomenological collision models which were discussed in section 3.6.3. The parameters for these collision models can be determined by experiment or from using quantum chemistry based models [22]. Furthermore, DSMC does not suffer from any numerical instability or convergence issues. Reducing the statistical scatter in the results requires increasing the number of the simulated particles which in turn increases the computational time.

DSMC is the most appropriate method for an initial investigation of the PP-CVD flow field for the reasons listed above. It has the added advantage of being readily incorporated into a Monte Carlo based surface deposition model. Furthermore, the computational expense and accuracy of the basic DSMC algorithm can be improved by parallelisation (see chapter 6) and by incorporating it into advanced solvers such as hybrid continuum/particle solvers (see chapter 9).

References

[1] M.A. Woodmansee, V. Iyer, J.C. Dutton and R.P. Lucht, Nonintrusive Pressure and Temperature Measurements in an Underexpanded Sonic Jet Flowfield, *AIAA J.* 42(6), 1170-1180 (2004).

[2] S. Crist, P.M. Sherman and D.R. Glass, Study of the highly underexpanded sonic jet, *AIAA J.* 4(1), 68-41 (1966).

[3] P. Birkby and G.J. Page, Numerical predictions of turbulent underexpanded sonic jets using a pressure-based methodology, *P. I. Mech. Eng. G-J. Aer.* 215(3), 165-173 (2001).

[4] L. Keysar and D. Degani, Numerical Investigation of Axisymmetric Compressible Turbulent Jets, in Proc. of 42nd AIAA Aerospace Sciences Meeting and Exhibit, Reno (NV) (2004).

[5] B. Mate, I.R. Graur, T. Elizarova, I. Chirokov, G. Tejeda, J.M. Fernandez and S. Montero, Experimental and numerical investigation of an axisymmetric supersonic jet *J. Fluid Mech.* 426, 177-197 (2001).

[6] Q. Sun, I.D. Boyd and K.E. Tatum, Particle simulation of gas expansion and condensation in supersonic jets, in Proc. of 37th AIAA Thermophysics Conference, Portland (OR) (2004).

[7] C.E. Glass, A Parametric Study of Jet Interactions With Rarefied Flow, in Proc of 21st International Symposium on Rarefied Gas Dynamics, Marseille, France (1998).

[8] I.D. Boyd, Y. Jafry and J.V. Beukel, Particle simulations of helium microthruster flows, *J. Spacecraft Rockets* 31(2), 271-277 (1994).

[9] K. Teshima and M. Usami, DSMC simulation of axisymmetric supersonic free jets, *Comp. Fluid Dyn. J.* 10, 525-530 (2001).

[10] I.D. Boyd, P.F. Penko, D.L. Meissner and K.J. DeWitt, Experimental and numerical investigations of low-density nozzle and plume flows of nitrogen, *AIAA J.* 30(10), 2453-2461 (1992).

[11] S.E. Selezneva, M.I. Boulos, M.C.M. van de Sanden, R. Engeln and D.C. Schram, Stationary supersonic plasma expansion: continuum fluid mechanics versus direct simulation Monte Carlo method, *J. Phys. D Appl. Phys.* 35, 1362-1372 (2002).

[12] I.S. Chang, Unsteady-state underexpanded jet flows, in Proc. of 38th AIAA/ASME/SAE/ASEE Joint Propulsion Conference and Exhibit, Indianapolis (IN) (2002).

[13] R. Roveda, D.B. Goldstein and P.L. Varghese, Hybrid Euler/Direct Simulation Monte Carlo Calculation of Unsteady Slit Flow, *J. Spacecraft Rockets* 37(6), 753-760 (2000).

[14] A. Roth, Vacuum Technology (North-Holland, Amsterdam, 1990).

[15] G.A. Bird, Breakdown of translational and rotational equilibrium in gaseous expansions, *AIAA J.*, 8(11), 1997-2003 (1970).

[16] I.D. Boyd, G. Chen and G.V. Candler, Predicting failure of the continuum fluid equations in transitional hypersonic flows, *Phys. Fluids*, 7(1), 210-219 (1995).

[17] W.-L. Wang and I.D. Boyd, Predicting continuum breakdown in hypersonic viscous flows, *Phys. Fluids* 15(1), 91-100 (2003).

[18] S.P. Krumdieck, H.M. Cave, S. Baluti, M. Jermy and A. Peled, Expansion Transport Regime in Pulsed-Pressure Chemical Vapor Deposition, *Chem. Eng. Sci.* 62(22), 6121-6128 (2007).

[19] L. Keysar and D. Degani, Numerical Investigation of Axisymmetric Compressible Turbulent Jets, in Proc. of 42nd AIAA Aerospace Sciences Meeting and Exhibit, Reno, NV (2004).

[20] V.I. Kolobov, S.A. Bayyuk, R.R. Arslanbekov, V.V. Aristov, A.A. Frolova and S.A. Zabelok, Construction of a unified continuum/kinetic solver for aerodynamic problems, *J. Spacecraft Rockets* 42(4), 598-606 (2005).

[21] V. Aristov and V. Kolobov, Lecture notes from the Workshop on Direct Boltzmann Equation Solver and Its Applications, Hsinchu, Taiwan (2007).

[22] J.-S. Wu and Y.-L. Hsu, Derivation of Variable Soft Sphere Model Parameters in Direct-Simulation Monte Carlo Method Using Quantum Chemistry Computation, *Jpn. J. Appl. Phys.* 42, 7574-7575 (2003).

5. Understanding PP-CVD Efficiency and Deposition Uniformity: A Basic DSMC Approach

5.1 Introduction

In chapter 4, it was shown that there are significant regions in the PP-CVD flow field for which the Navier-Stokes equations are invalid, due localised breakdown of the continuum assumption resulting from the high spatial-temporal gradients of flow properties compared to the mean free path. Methods of dealing with such flows have been discussed in depth in chapter 3 and the Direct Simulation Monte Carlo (DSMC) technique was shown in section 4.2 to be an appropriate method for modelling this kind of rarefied flow.

In this chapter the DSMC method is used to model the expansion of the carrier gas into a representative PP-CVD reactor. A model is then developed for tracking the dilute precursor species through the carrier gas flow field, and the information from this model is used to determine the reactor efficiency and deposition uniformity. The computational expense of the DSMC technique in the relatively dense and unsteady PP-CVD flow field means that single-processor codes cannot be used to model realistic reactors within acceptable time frames; however it does enable the physical mechanisms behind reactor efficiency and uniformity to be investigated. Results are presented for some representative reactor cases and these are used to explain the operating principles of PP-CVD. Simulations of steady flow reactors operating with similar inlet pressures are also conducted, as a point of comparison.

5.2. DSMC Flow Field Modelling

5.2.1 Method

The DSMC code used to generate the unsteady PP-CVD flow field was Bird's DS2V code [1]. This programme is designed to run on a single processor, however it incorporates a number of sophisticated features such as nearest neighbour collisions, adaptive sampling cell structure and an adaptive variable time step. Bird has shown in simulations of hypersonic flow past a circular cylinder that these sophisticated features enable the code to produce similar results to parallel-DSMC methods utilising far more simulation particles and requiring considerably more computational time [2].

Despite the sophisticated features in the DS2V code, there are still limitations on the computational capacity of the code imposed by the requirements on sampling cell size, number of simulation particles per cell and time step, as discussed in section 3.6.2. The very high pressure at the inlet of approximately 100 kPa requires cell size dimensions on the order of 10 nm due to the very small mean free path in this region. These tiny cell dimensions near the orifice, the small mean collision time (and subsequent small simulation time step) and the extra sampling required due to the unsteady nature of the flow make the computational expense, in terms of both memory and calculation time, massive even given the lower pressures downstream of the inlet. For this reason, a pure DSMC simulation can only be used to simulate a representative reactor with a relatively low inlet pressure. Additionally, a large inlet orifice is used to increase the mass flow rate and thus reduce the simulation time. Despite the limitations imposed by the DSMC method, the simulations are expected to be a useful tool in explaining the physical mechanisms behind reactor efficiency and deposition uniformity.

Table 5.1 shows the simulation parameters used in the DSMC flow field calculations while figure 5.1 shows the set up of the PP-CVD geometry and boundary conditions for the simulations. The flow field parameters are set to ensure the parameters discussed in section 2.3 of $t_P \geq 4\tau_R$ and $t_P/t_i >> 1$ are maintained.

Table 5.1. PP-CVD reactor parameters for DSMC flow field simulations.

Parameter		Value	Parameter	Value
Reactor length	L	0.2 m	Cell type	Unstructured
Reactor radius	r	0.05 m	Simulation type	Axisymmetric
Substrate radius	r_{sub}	0.0375 m	Radial weighting factors	Yes
Inlet orifice radius	r_i	0.005 m	Wall type	Diffusely reflecting
Inlet supply pressure	P_S	100 & 1000 Pa	Carrier gas	Helium
Inlet supply temperature	T_S	293 K	Molecular model	VSS
Reactor wall temperature	T_W	300 K	Simulated particles	Maximum 4 million
Substrate temperature	T_{sub}	800 K	Indexing type	Normal
Reactor Initial Pressure	P_{min}	1 Pa	Sampling	Unsteady
Reactor Final Pressure	P_{max}	~10 Pa		
Reactor Evacuation Rate	V'_{out}	0.05 m^3/s		

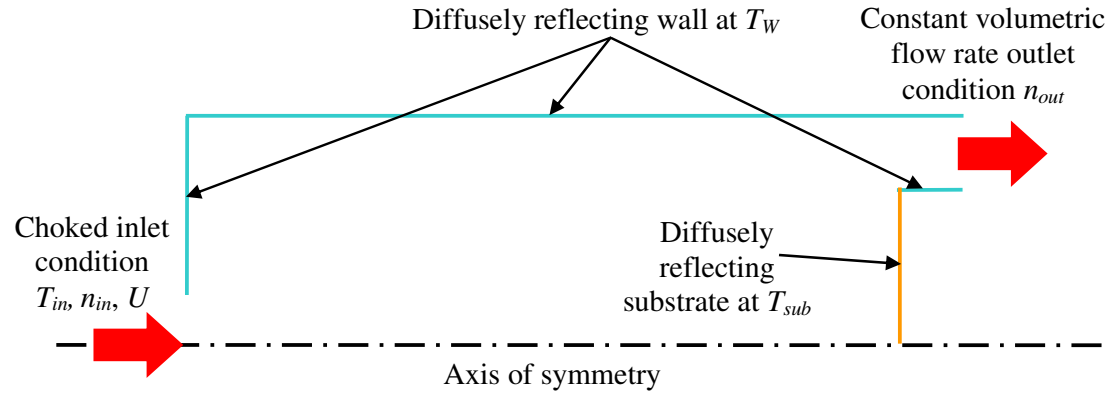

Figure 5.1. Typical DSMC grid for PP-CVD flow field simulations.

The inlet conditions for the jet were determined from the choked flow condition. Choked flow occurs when [3]:

$$\frac{P_S}{P_R} \geq \left(\frac{k+1}{2}\right)^{\frac{k}{k-1}} \tag{5-1}$$

where k is the specific heat ratio for the carrier gas and P_R is the reactor pressure. For helium k = 5/3, so we require P_S / $P_R \geq 2.05$. Thus the maximum reactor pressures to maintain choked flow for supply pressures of 100 Pa and 1000 Pa are 48.8 Pa and 488 Pa respectively. Here the maximum reactor pressure is P_{max} ~ 10 Pa, so the choked flow condition can be assumed at all times.

For an orifice which is choked, the inlet conditions are related only to the upstream conditions and are independent of downstream conditions. The inlet temperature, pressure and velocity can be determined by:

$$\frac{P_S}{P_{in}} = \left(1 + \frac{k-1}{2} M^2\right)^{k/k-1} \tag{5-2a}$$

$$\frac{T_S}{T_{in}} = 1 + \frac{k-1}{2} M^2 \tag{5-2b}$$

$$U = M\sqrt{kRT_{in}} \tag{5-2c}$$

where M is the Mach number of the flow (=1.00 for a choked nozzle) and R is the specific gas constant (=2077 J/(kgK) for helium).

For the 100 Pa supply case, equations (5-2) give P_{in} = 48.7 Pa, T_{in} = 220 K and U = 873 m/s hence, from ideal gas considerations, the inlet number density n_{in} = 1.604 x 10^{22} m^{-3}. Similarly, for the 1000 Pa supply case n_{in} = 1.604 x 10^{23} m^{-3}.

The constant volumetric flow rate outlet boundary condition can be approximated by calculating the number flux to the surface under equilibrium conditions. The number flux N' per unit area A is [4]:

$$N' = \frac{1}{4} n v_{av} A \tag{5-3}$$

where v_{av} is the average velocity in the Maxwell-Boltzmann equilibrium distribution (equation (3-17)):

$$v_{av} = \frac{2}{\sqrt{\pi}} \sqrt{\frac{2kT}{m}} \tag{5-4}$$

The mass flux of particles we wish to remove from the reactor m' is:

$$m' = \rho \dot{V} = nm\dot{V} \tag{5-5}$$

The fraction of particles we want to remove from the reactor x is thus:

$$x = \frac{n\cancel{m}\dot{V}}{\cancel{m}N'} = \frac{4\cancel{n}\dot{V}}{\cancel{n}v_{av}A} = \frac{4\dot{V}}{v_{av}A} \tag{5-6}$$

If we assume an outlet temperature of 293K, then from equations (5-4) and (5-6) we can determine the fraction to remove to maintain the outlet boundary conditions given in table 5.1 to be x = 0.0467. Thus, to implement the outlet boundary condition, 4.67% of simulated molecules which strike the boundary are removed from the flow. The validity of this boundary condition will be discussed in section 5.2.2.

5.2.2 Flow Field Results and Discussion

Figures 5.2 and 5.3 show contours of Mach number at different stages during and immediately after the injection phase for the P_S = 100 Pa and P_S = 1000 Pa cases respectively. In each case a smoothing algorithm has been used along the plot axis of symmetry to reduce the statistical scatter mentioned in section 3.6.2.

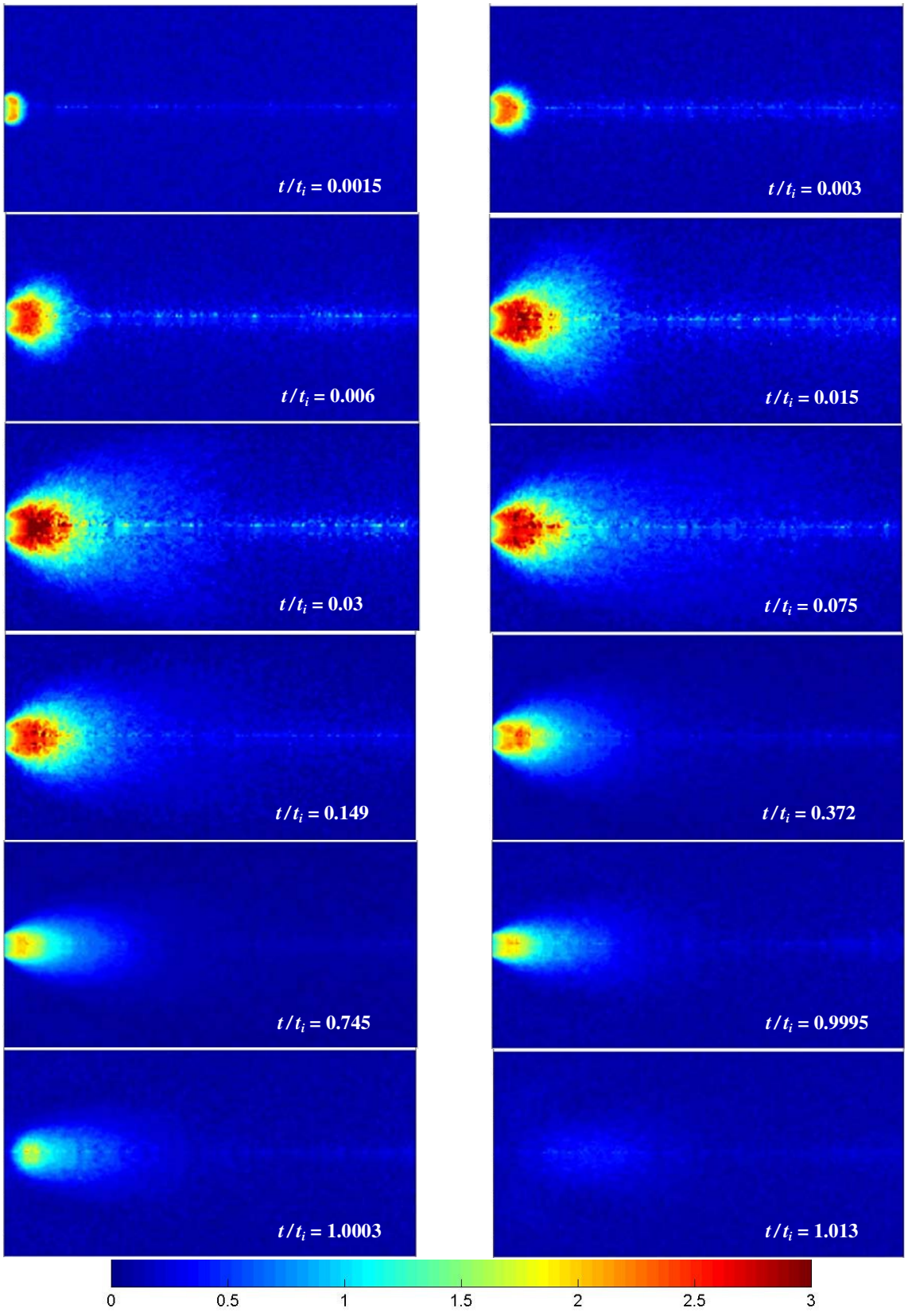

Figure 5.2. Contours of Mach number calculated using DSMC for the unsteady jet expansion during a PP-CVD process with $P_S / P_{min} = 100$.

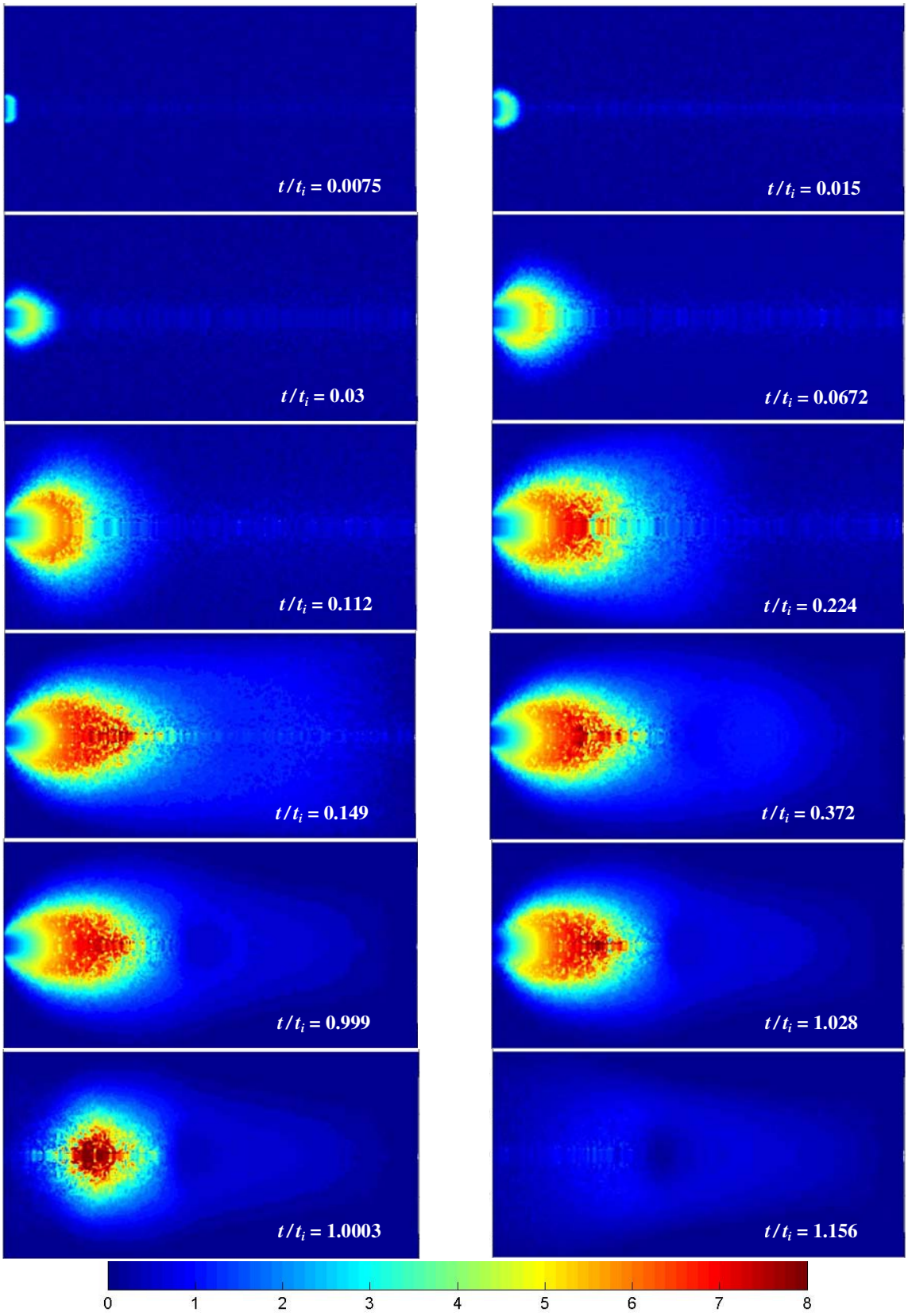

Figure 5.3. Contours of Mach number calculated using DSMC for the unsteady jet expansion during a PP-CVD process with P_S / P_{min} = 1000.

Both figures 5.2 and 5.3 indicate a highly unsteady expansion during the early part of the injection phase. The region of highly supersonic flow upstream of the Mach disc expands rapidly before the jet reaches a quasi-steady state and slowly contracts as the ambient pressure in the reactor rises (this is particularly noticeable in figure 5.2). After the inlet orifice closes at $t = t_i$, the jet structure collapses resulting in an approximately uniform flow field by $t = 2t_i$. Both figures show quite a high degree of statistical scatter, which could not be avoided due without a massive increase in the computational expense of the calculations.

To assess the validity of the outlet boundary condition discussed in section 5.2.1, a comparison was made between the average reactor pressure predicted by the DSMC simulations during the pump-down phase and the analytical result from equation (5-6). From equation (2-8), the pump-down time constant for the reactor described in table 5.1 is τ_R = 0.03142s. Figure 5.4 compares the analytical result using equation (2-8) to the average pressure data predicted for the P_S = 100 Pa case using DSMC.

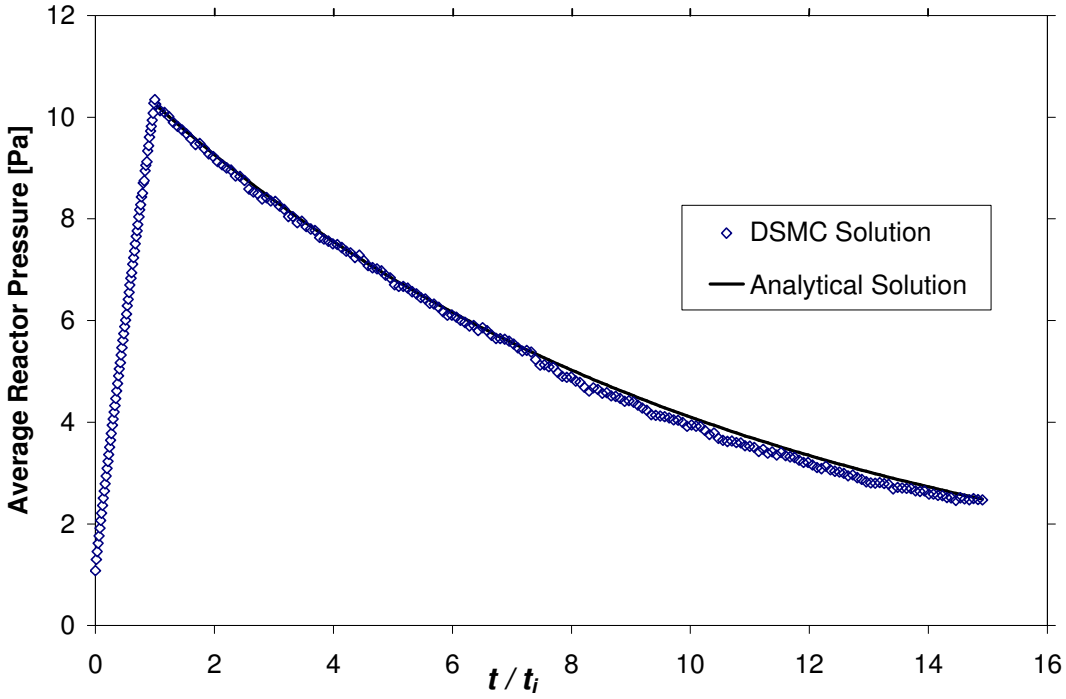

Figure 5.4. Comparison of analytical and DSMC pump-down data to assess the validity of the DSMC outlet boundary condition.

Figure 5.4 shows that the average reactor pressure predicted by the analytical model and the DSMC solution are very similar. From this it can be concluded that the outlet boundary

condition for the DSMC model, expressed by equation 5.6, is a good approximation of actual reactor conditions.

A number of steady flow reactors with the same geometry were also simulated as a point of comparison. These reactors also had the same supply pressure as their PP-CVD counterparts. The steady reactor pressure P_R was adjusted by varying the reactor evacuation rate $\dot{V}_{out}$. Figure 5.5 shows contours of Mach number for several examples of steady flow reactors simulated using DS2V.

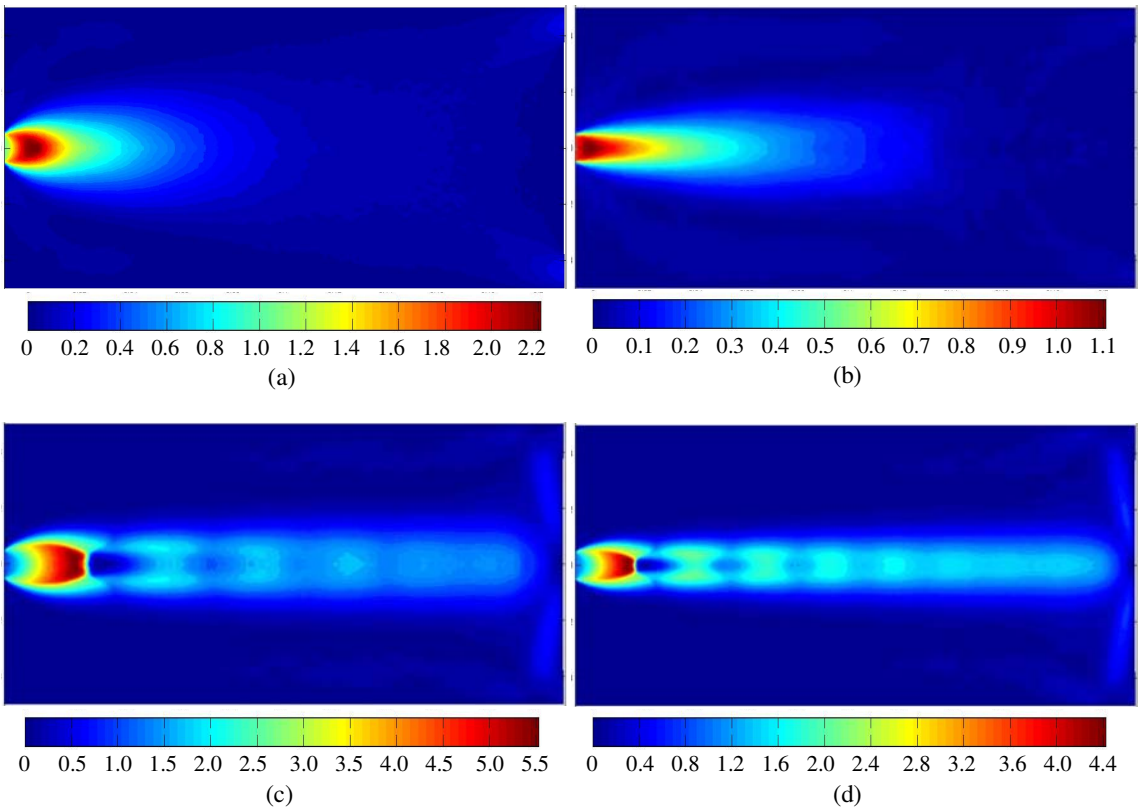

Figure 5.5. Contours of Mach number calculated using DSMC for the steady jet expansion during a steady CVD process with a) P_S = 100 Pa & P_R = 9.5 Pa, b) P_S = 100 Pa & P_R = 41 Pa, c) P_S = 1000 Pa & P_R = 59 Pa and d) P_S = 1000 Pa & P_R = 104 Pa.

The flow fields shown in figure 5.5 exhibit the typical structure of steady under-expanded jets which were discussed in section 4.1.1 including the Mach disc, the incident and reflected shocks, the stand-off shock near the substrate and the shock cell structure. This features are particularly evident in the P_S = 1000 Pa cases where the degree of under-expansion is higher.

5.3. Particle Tracking Model

5.3.1. Model Development

As mentioned in section 3.6.2, species weighting factors are often required to ensure adequate statistical sampling of the concentrations of any trace species present in the flow field. This is the case in PP-CVD where low concentrations of precursor ($\leq$ 5 mol%) are diluted in the carrier gas stream. The DS2V code does not include procedures for species weighting factors and simulating the presence of such species without these procedures would be prohibitively computationally expensive. A technique used to overcome a similar problem is the stochastic biatomic collision theory (BCT) method developed by Groves to model the Directed Vapour Deposition (DVD) of copper [5]. Here the paths of a large number of reactant molecules are tracked individually through a steady background gas field generated using DSMC. The technique assumes the concentration of reactant molecules is low enough that there is negligible interaction between them and utilises a complex method for the determination of vapour atom mean free path and collision dynamics, which is suitable for the high vapour molecule energies of the system.

The reactor efficiency model used in this thesis was loosely based on the BCT method, however mean free path calculations and the interaction of molecules during collision events were simulated using the variable soft sphere (VSS) model (see section 3.6.3). In this way the movement of the test particles through the reactor volume was decoupled from collision events in much the same way as the DSMC method, while allowing the use of readily available collision parameters, such as those listed in the monograph by Bird [6].

The algorithm at the core of the model, known as the Pulsed Injection Efficiency Simulation (or "PIES") model, is illustrated in figure 5.6. Here N_{parts} represents the number of test particles tracked for each simulation run. Another model was implemented for steady flow simulations, as shown in figure 5.7. Additional information about the PIES model is given in the paper by Cave *et al.* [7].

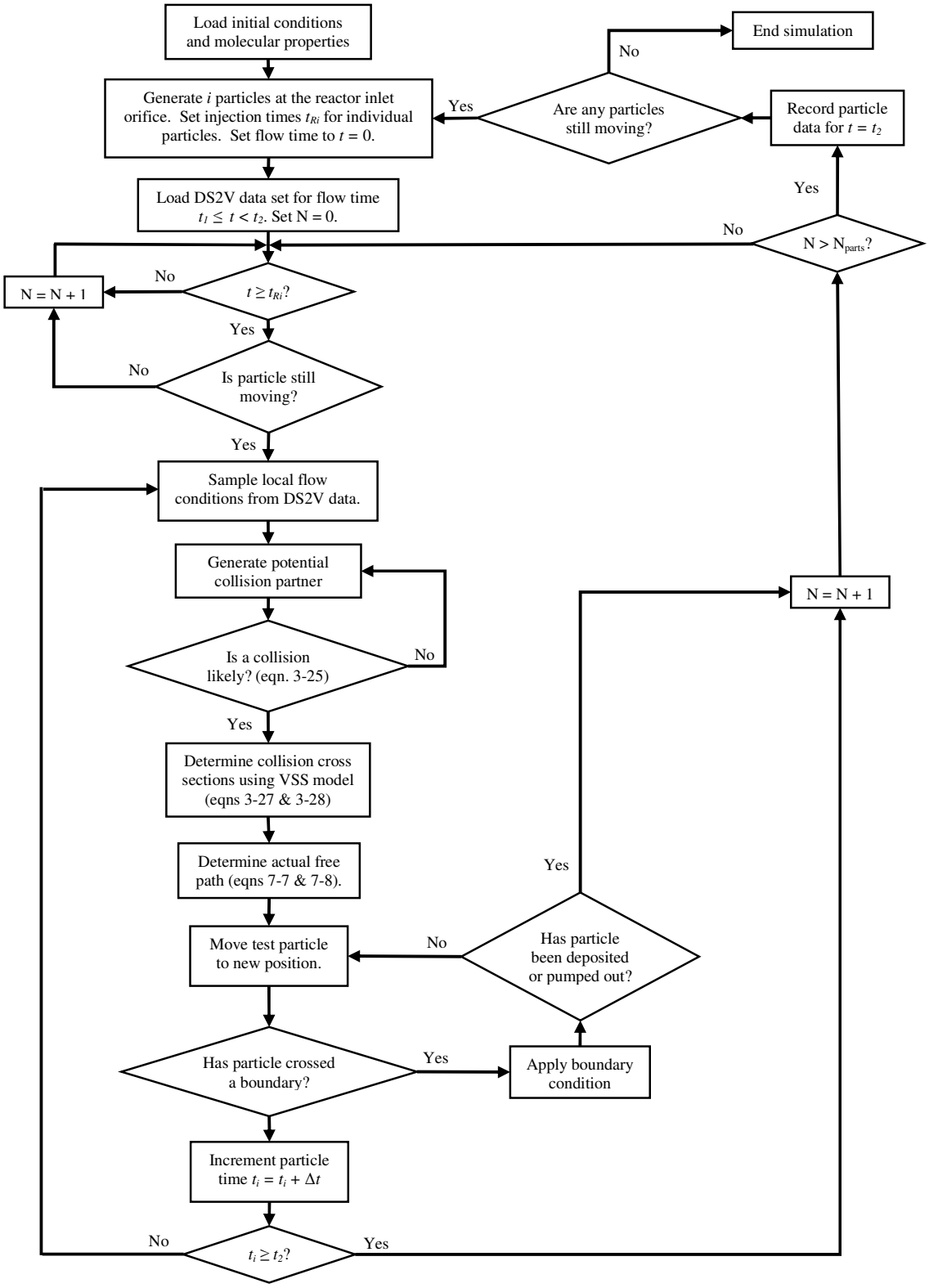

Figure 5.6. Unsteady flow "PIES" reactor efficiency model computational flow diagram.

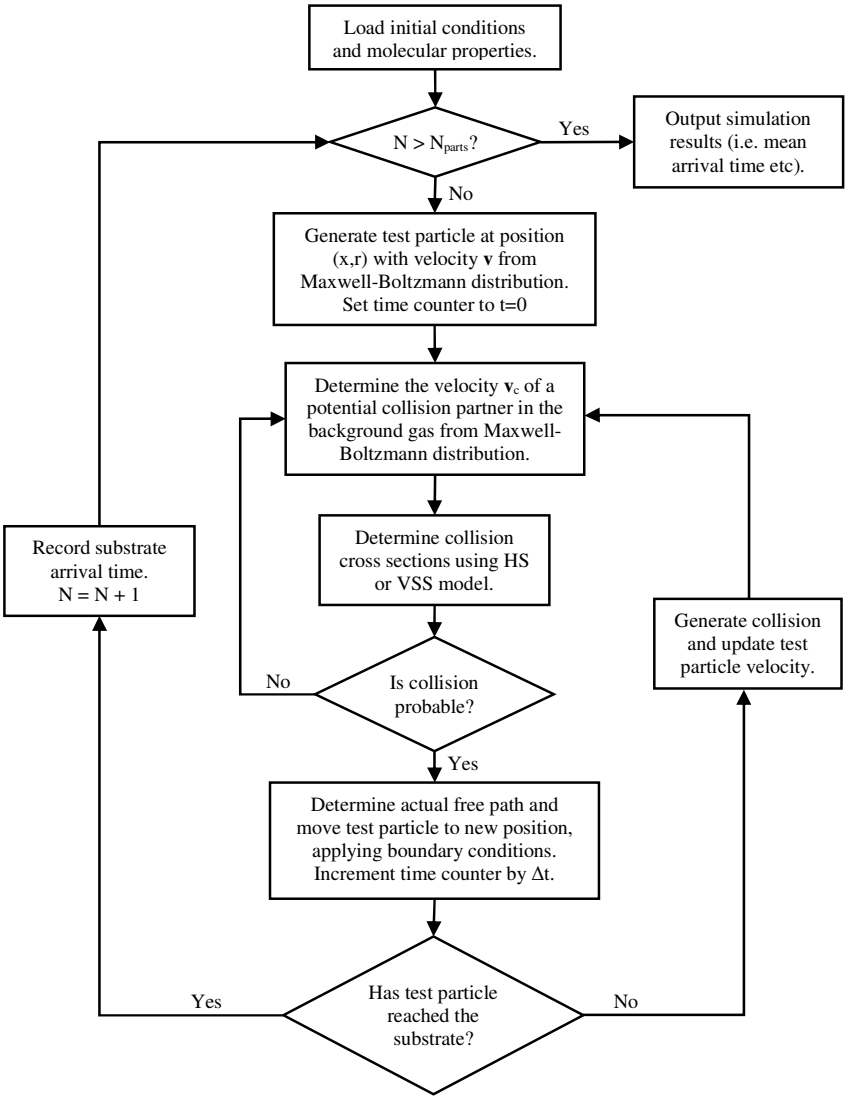

Figure 5.7. Steady flow "PIES" reactor efficiency model computational flow diagram.

The main difference between the unsteady and steady flow implementations of the PIES model, as illustrated in figures 5.6 and 5.7 respectively, is that in the steady version each particle is simulated in series whereas in the unsteady version the particles are simulated in parallel. This saves the computational expense associated with loading the DS2V flow field data at each time step as the unsteady calculation progresses.

In the PIES model it was assumed collisions were elastic. At each time step the local flow conditions were sampled from the DS2V flow field data. A potential collision partner for each particle was generated, with its velocity components being chosen at random from equation (3-17) at the local gas temperature, and the macroscopic flow field velocities were

added to this. Collision properties were calculated using equations (3-27) to (3-29) and the acceptance/rejection method of equation (3-25) was used to determine if a collision should be generated. The transport mean free path was calculated using the momentum collision cross section from equation (3-27) and reference [8]:

$$\lambda_m(t) = \frac{RT}{\sqrt{2}P(t)N_A\sigma_M} \tag{5-7}$$

The actual free path λ_a of a molecule is distributed about the mean value given in equation (5-7) with the probability of a particle travelling at least a distance x before a collision being e^{-x/λ_m}, hence the probability of a collision occurring between x and $x+dx$ is [5]:

$$\frac{1}{\lambda_m} e^{-x/\lambda_m} dx \tag{5-8}$$

The particle was then moved using equation (3-22) and equations (3-23) applied for axisymmetric cases. The collision itself was then generated by random selection of appropriate deflection and azimuth angles, along with expressions for the conservation of momentum and energy (equations (3-3) and (3-4)). In this way the position of the collision and the collision event itself are effectively decoupled.

Where particles were incident with a boundary (other than the substrate and the pump outlet) they were diffusely reflected. In diffuse reflection the particle is assumed to come into complete thermal equilibrium with the wall and is then ejected from the wall with a velocity sampled from the half-range Maxwellian distribution and in a random direction. Thus the velocity of the particle after impact is independent of its initial velocity, reflecting the fact that gases tend to come into rapid thermal equilibrium with any surface they impinge upon and that these surfaces tend to be very rough at the molecular scale. In these simulations it was assumed that no particles were absorbed by any surface other than the substrate.

The choked flow inlet boundary condition for particles was determined by adding the choked velocity from equation (5-2c) to a particle velocity sampled from equation (3-17). The pump outlet boundary condition was implemented by absorbing a fraction x of particles incident on the boundary and diffusely reflecting all others. All particles incident upon the substrate were absorbed, with the position and time of impact being recorded.

The code for the unsteady and steady PIES model was implemented in MATLAB™ version 6.5. The standard pseudorandom number generator in MATLAB "rand" was used to generate the required random variables and was started in a different state for each run. The "rand" function has been shown to have a period, which is the number of random numbers generated before the sequence is repeated, of almost 2^{1430} [9].

5.3.2. Model Verification

In order to test the procedures employed in the code, a series of four validation studies were carried out. These were designed to test the simulated rate of diffusion of the precursor particles in the reactor and the collision procedures employed for molecular interactions. Here MATLAB™ code using identical procedures to the PIES model was developed to assess the velocity persistence and random walk distance in an ideal gas to assess the diffusion rates predicted by the model. The VSS collision procedures were tested using basic DSMC code to measure the unsteady self diffusion of argon and the PIES model was used in an unsteady 2D slit flow to verify that precursor particles were following the flow correctly.

5.3.2.1 Velocity Persistence in an Equilibrium Gas

After a collision of particles of masses m_1 and m_2 in the vapour phase, the collision partners can be expected to maintain a component of their velocity in the pre-collision direction. The ratio of this post-collision component to the pre-collision velocity is known as the velocity persistence ratio which has a mean value for hard sphere particles of [10]:

$$\varpi_{12} = \frac{1}{2} M_1 + \frac{1}{2} M_1^2 M_2^{-1/2} \ln\left[\frac{\left(M_2^{1/2} + 1\right)}{M_1^{1/2}}\right] \quad \text{where} \quad M_1 = \frac{m_1}{m_1 + m_2} \;\&\; M_1 = \frac{m_2}{m_1 + m_2} \qquad (5\text{-}9)$$

For molecules of the same size $\varpi_{12} = 0.406$, while when $m_1 >> m_2$, $\varpi_{12} \to 1$ and the heavy particles move almost ballistically; and when $m_1 << m_2$, $\varpi_{12} \to 0$ and the light particles move as if they were undergoing random walk.

To validate the reactor efficiency code, the algorithm was used to calculate the persistence ratio for the movement of various noble gas particles through a uniform and stationary field of other noble gas particles. This was done by determining the magnitude of the projection of the post-collision velocity vector $\boldsymbol{v}_2$ onto the unit vector of the pre-collision velocity vector $\boldsymbol{v}_1$,

and comparing this to the magnitude of the pre-collision vector $\|\boldsymbol{v}_1\|$. The results were averaged over a large number of collisions N:

$$\varpi_{12,simulated} = \frac{1}{N}\sum_{i=1}^{N}\frac{\boldsymbol{v}_1 \bullet \boldsymbol{v}_2}{\|\boldsymbol{v}_1\|^2} \tag{5-10}$$

The simulated results with N = 10,000 in equation (5-10), utilising both hard sphere and VSS models, were compared to theoretical values obtained from equation (5-9) and are shown in figure 5.8. Because statistical error is of the order of $1/\sqrt{N}$ the error in these calculations is approximately 1%.

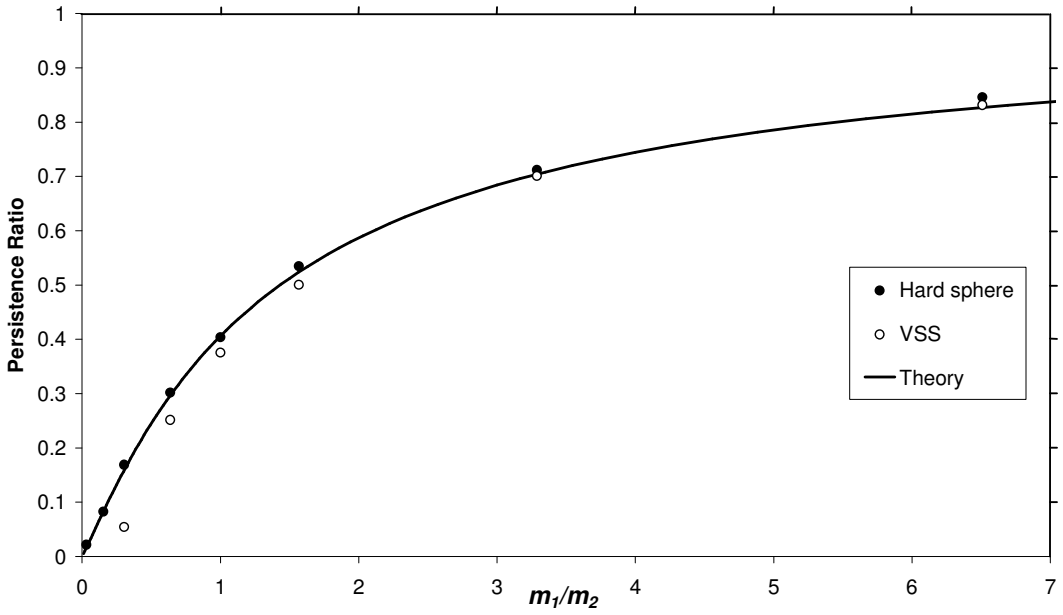

Figure 5.8. Code validation study comparing molecular persistence ratio predicted using the hard sphere and VSS collision models to theoretical values.

The hard sphere values show good agreement with the theoretical curve from equation (5-9) which itself assumes hard sphere collisions. This indicates that the algorithm is performing correctly since the persistence ratios computed by the algorithm and those from hard sphere theory are almost identical. The VSS model deviates significantly from the theoretical values especially when the ratio m_1/m_2 is small. This does not indicate a problem with the algorithm, but rather illustrates the limitations of the hard sphere model in real gas simulations. The VSS model can reproduce experimentally measured values of the diffusion coefficient [6] and consequently will produce more accurate values of the persistence ratio than can be produced by the hard sphere model or predicated from hard sphere theory.

5.3.2.2 Comparison with Pure Random Walk

A further check was carried out by comparing the average straight line distance travelled by small particles in a field of large particles (i.e. as m_1/m_2 becomes very small) to the distance predicted by pure random walk. Pure random walk occurs when the direction of movement after a collision has no relation to the pre-collision direction (i.e. $\varpi_{12} = 0$) and corresponds to the movement of a particle undergoing surface diffusion. The average straight line distance d travelled from the origin for a particle undergoing random walk is equivalent to the standard deviation of the Gaussian distribution, centred about the origin, of the distance travelled by a large number of particles, thus $d = \lambda\sqrt{n}$, where n is the number of steps taken by the particles and λ is the mean step distance [11].

Figure 5.9 shows a comparison of the average straight line distance travelled by 1000 helium atoms in a uniform stationary field of xenon at 10Pa (for which $\varpi_{12} = 0.0159$) to the distance predicted by random walk, where n is the number of collision events and λ is the mean free path. Deviation between the two lines is due in part to the slight velocity persistence of the simulated system and in the small statistical error in the simulations.

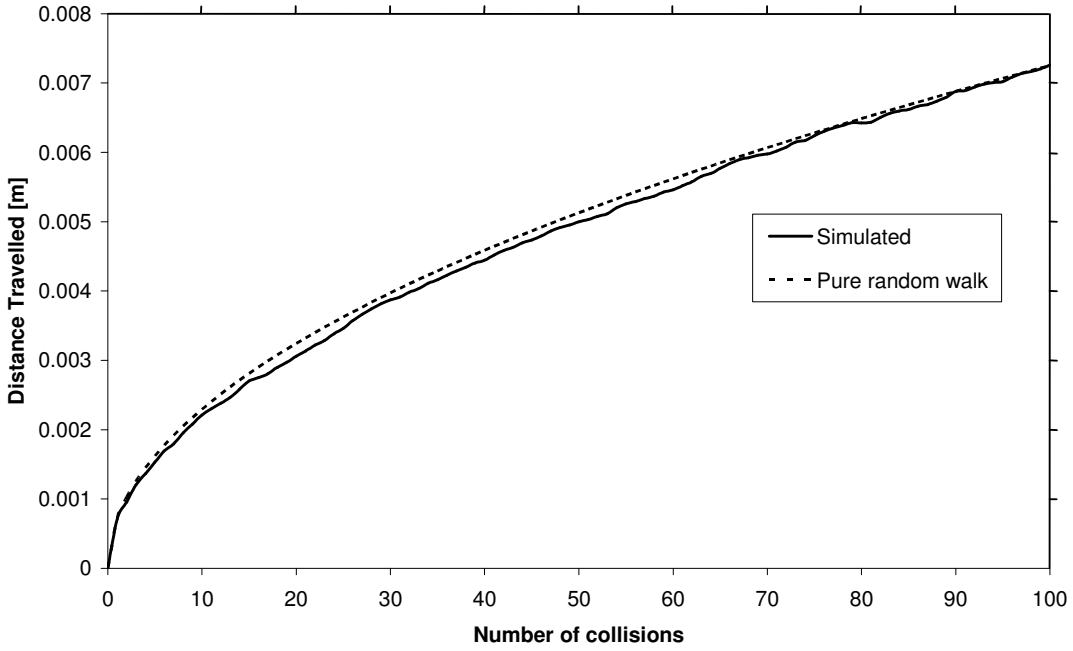

Figure 5.9. Code validation study comparing the average straight line distance travelled by helium atoms in a stationary uniform field of xenon molecules at 10 Pa.

5.3.2.3 Unsteady Self Diffusion

To validate the procedures for the VSS collision model, DSMC code was developed in MATLAB to measure the unsteady (i.e. time dependent) self diffusion of argon with a number density of 1.4 x 10^{20} m^{-3} and a temperature of 273K. The analytical solution for one dimensional transient diffusion into a semi-infinite region is analogous to the transient heat conduction into a semi-infinite solid with constant surface temperature such that the density of species A, $\rho_A(x,t)$, is [12]:

$$\frac{\rho_A(x,t)}{\rho_{A,0}} = \frac{1}{2}\left[1 - erf\left(\frac{x}{2\sqrt{D_{AA}t}}\right)\right] \tag{5-11}$$

where $\rho_{A,0}$ is the initial density of species A, x is the position from the initial separation interface of the two species, D_{AA} is the self-diffusion coefficient and *erf(…)* represents the error function.

It should be noted that due to the requirement of species equilibrium at $x = 0$, the density ratio $\rho_A(0,t)/\rho_{A,0} = 0.5$ for all values of time $t > 0$ in a manner equivalent to the thermal equilibrium requirement of the analogous heat transfer problem.

The simulations utilised 100,000 test particles on a 1 x 0.01 m two-dimensional grid with periodic boundary conditions in the y-direction. An ensemble average was taken to reduce statistical error in the sampling. Figure 5.10 compares the results of these simulations with the predicted values from equation (5-11) using the value for self diffusion calculated by Bird of D_{AA} = 2.95 m^2/s [6]. The results show agreement between the simulations and the theoretical values within the statistical scatter of the sampling and confirm the validity of the VSS collision procedures.

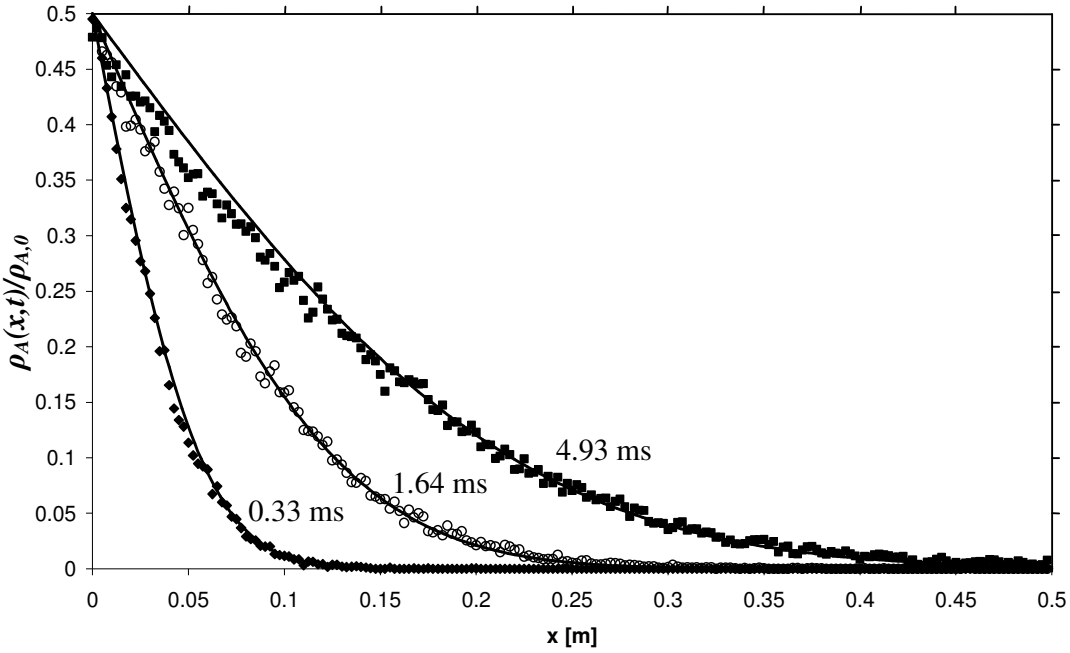

Figure 5.10. Validations of VSS collision procedure by DSMC simulations of transient self-diffusion of argon.

5.3.2.4 Two-Dimensional Slit Flow

To test how well the particles generated using the PIES model "adhered" to the flow generated using DSMC, helium molecules were tracked through a helium two-dimensional slit flow. It was reasoned that if the PIES code was performing correctly, the contours of macroscopic properties sampled from the DSMC flow field files and those generated by the PIES model would be very similar. A two-dimensional flow situation was chosen to avoid having to apply weighting factors to particles based on their radial positions. The grid configuration used was identical to that in figure 5.1, except with two dimensional rather than axisymmetric procedures employed in the DS2V calculations. 500,000 particles of helium were tracked through the first 50μs of the flow, and then the macroscopic flow properties generated from the DS2V and PIES data were plotted, as shown in figure 5.11.

The results show that the helium particles being tracked by the PIES model "adhered" well to the DS2V generated helium flow field. Contours of number density and velocities components were very similar from both methods. The slight lag in velocities from the PIES generated data is thought to be due to the time-averaged unsteady sampling employed in the DS2V code compared to the instantaneous sampling for the PIES method, however as the source code for DS2V is unavailable, this cannot be verified.

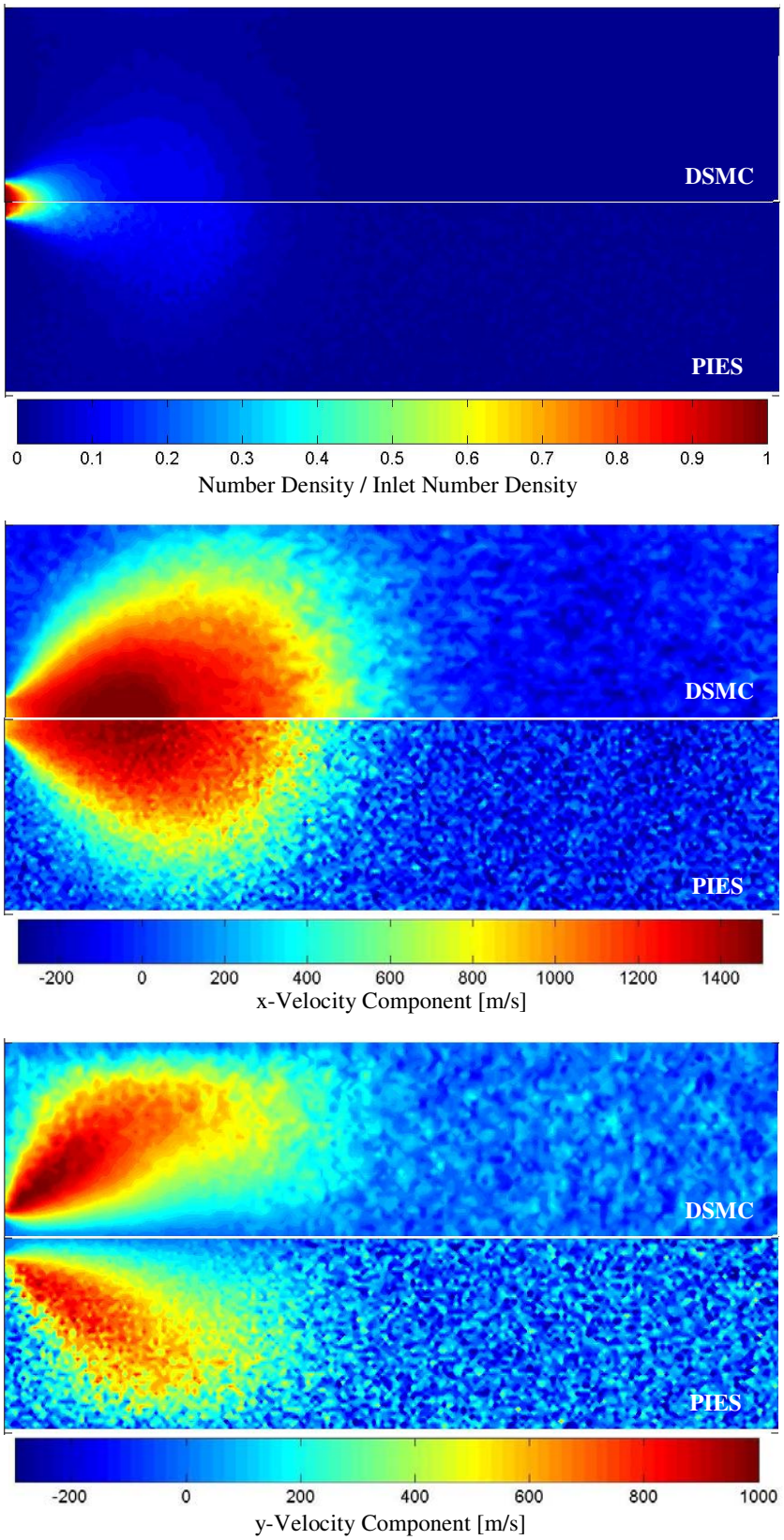

Figure 5.11. Comparison of relative number density, x-velocity component and y-velocity component for helium 2D slit flow generated using the DS2V code and the PIES model.

The results of the various verification studies confirm that the computational procedures employed in the PIES code will result in realistic diffusion rates of precursor molecules through the background flow field and gives confidence in the validity of the reactor efficiency simulation results.

5.4 Results and Discussion

5.4.1. Deposition Time Scale Simulations

The PIES model was used to investigate the process of precursor diffusion from a well mixed gas to a substrate that consumes the precursor component. This numerical investigation aims to determine the time scale for the diffusion of the precursor to the substrate from the start of the pump-down phase. It is reasoned, that if the diffusion and deposition processes are much faster than the pump-down process, then it is possible that high precursor conversion efficiency can be achieved.

The investigation was based around noble gas molecules as a model for the precursor-carrier gas system because noble gases have known collision parameters and only translational degrees of freedom. The model system was necessary because very limited data is available for the collision behaviour of the actual precursor or the solvent molecules used in typical PP-CVD processes. Of the data which is available, Tatsuda *et al.* estimate the hard sphere diameter of TTIP as 12Å [13] and Rubio *et al.* estimate the hard sphere diameter of toluene as 5.72Å [14]. This data was used in the study, however the limitations of the hard sphere model mentioned in section 3.6.3 should be noted.

In these simulations, reactor pressures more typical of actual experimental PP-CVD processes were used, as shown in table 5.2. This simulations are less computationally expensive than the DSMC-PIES simulations described in sections 5.2 and 5.4.2, however the background gas during the pump-down phase is assumed to have no bulk velocity and to be everywhere uniform throughout the reactor volume (i.e. have no property gradients) with the gas pressure throughout the reactor volume being determined at from equation (2-3). These assumptions are physically impossible in a volume which is being evacuated, however it is hoped that these simulations will bridge the gap between the more accurate DSMC-PIES simulations which are unable to model actual PP-CVD processes and the experimental data showing high uniformity and reactor efficiency. It will be shown that these assumptions hold over the time

scale required for the vast majority of precursor molecules to be consumed by the substrate. Furthermore, the rate of pump-down in this PP-CVD process is approximately 3 m^3/h which translates to a bulk flow velocity of approximately 0.3 m/s through the reactor cross section: several orders of magnitude less than the molecular velocities experienced in the flow.

Table 5.2. Simulation parameters for deposition time scale simulations

Parameter		Value
Reactor length	L	0.185 m
Reactor radius	r	0.03 m
Substrate radius	r_{sub}	0.0225 m
Reactor peak pressure	P_{max}	1, 10, 100, 1000 Pa
Reactor minimum pressure	P_{min}	0 Pa
Pump-down constant	τ_R	2.65 s
Wall and background gas temperature	T	293 K
Noble gases studied (VSS model*)		He, Ne, Ar, Kr, Xe
Real precursor / solvent pairs studied (HS model)		TTIP / Toluene

*VSS parameters were obtained from the monograph by Bird [6]

Figure 5.12 gives a schematic representation of the modelling process with the PP-CVD reactor geometry shown in figure 5.12a. As illustrated in figure 5.12b, the precursor molecule is spawned at a random point in the reactor and moves ballistically, undergoing collisions with solvent molecules, until it impacts the substrate and is deposited upon it. The pressure, and thus the number of solvent molecules, in the reactor decreases with time causing an increase in the precursor (mean) free path λ, as shown in figure 5.12c. Precursor particles which strike the reactor's walls are assumed to be diffusely reflected with complete thermal accommodation. Because the reactor is axially symmetric, the computational expense of the simulations can be greatly reduced by projecting the path of the precursor molecules onto the zero-azimuth plane.

Simulations were conducted to assess the effect of reactor peak pressure, solvent gas type and precursor molecule type on the residence time of particles within the reactor. The time taken for 95% of the precursor molecules within the reactor volume to reach the substrate $t_{95\%}$ was chosen as a suitable measure of this residence time. Figure 5.13 shows the $t_{95\%}$ values for different precursor-solvent gas pairs for a reactor with P_{max} = 10 Pa.

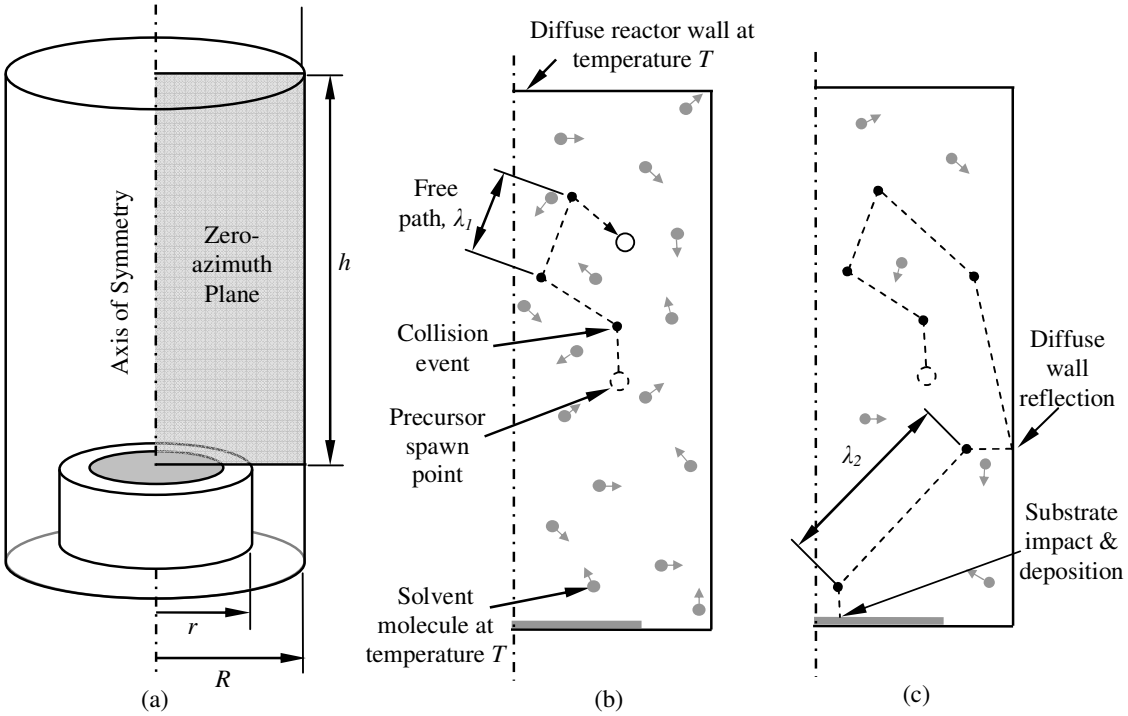

Figure 5.12. a) PP-CVD reactor geometry showing zero-azimuth axisymmetric plane and precursor particle tracking schematic at b) time t_1 and c) time t_2 where $t_2 > t_1$.

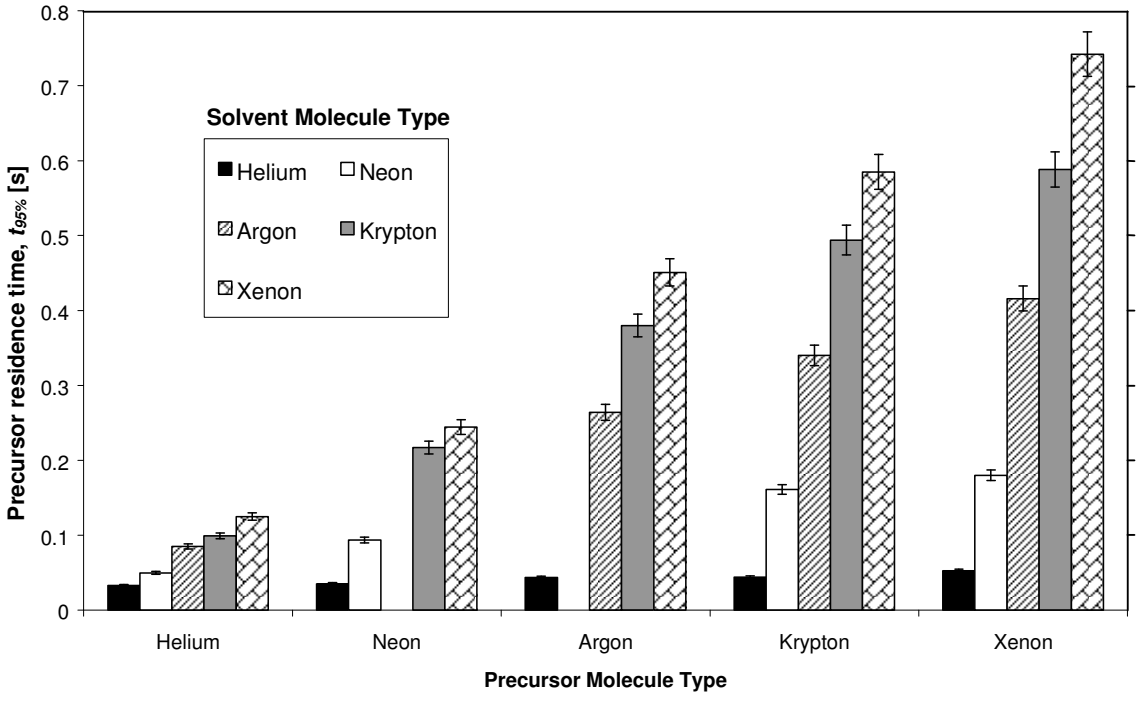

Figure 5.13. Precursor residence time $t_{95\%}$ for different precursor-solvent combinations with P_{max} = 10 Pa.

The same data is presented in figure 5.14 showing an approximately logarithmic relationship between the precursor to solvent gas mass ratio and residence time when the data is grouped by solvent molecule type. Here mr is the mass of the solvent gas relative to the mass of helium. Included on this plot is the data point for the toluene-TTIP hard sphere system.

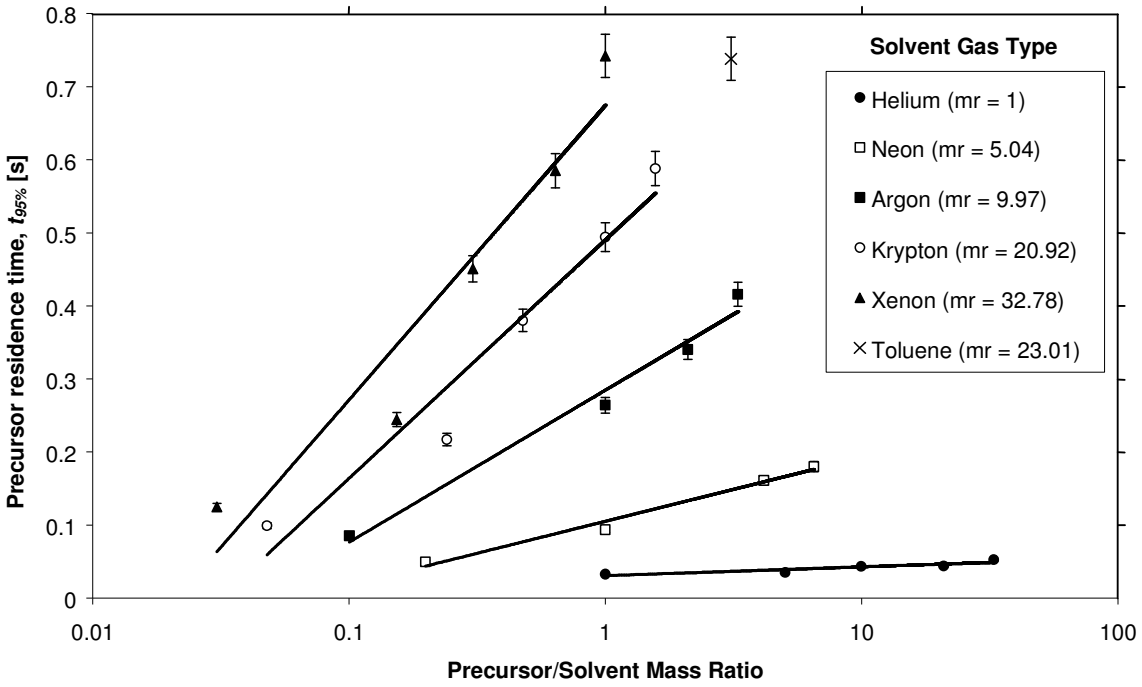

Figure 5.14. Precursor residence time $t_{95\%}$ for different precursor-solvent combinations with P_{max} = 10 Pa (logarithmic scale).

The effect of reactor peak pressure on precursor residence time was studied by simulating the pump-down phase for several precursor-solvent combinations including the hard sphere TTIP-toluene combination, Xe-Ar (which has a similar precursor to solvent mass ratio as TTIP-toluene) and, as a point of comparison, Ar-He. Simulations we not carried out for peak pressures exceeding 1000 Pa due to the large computational expense required. The larger magnitude of the error on the higher pressure values is a consequence of a smaller sample size due to the large computational expense. The results of this study are illustrated in figure 5.14.

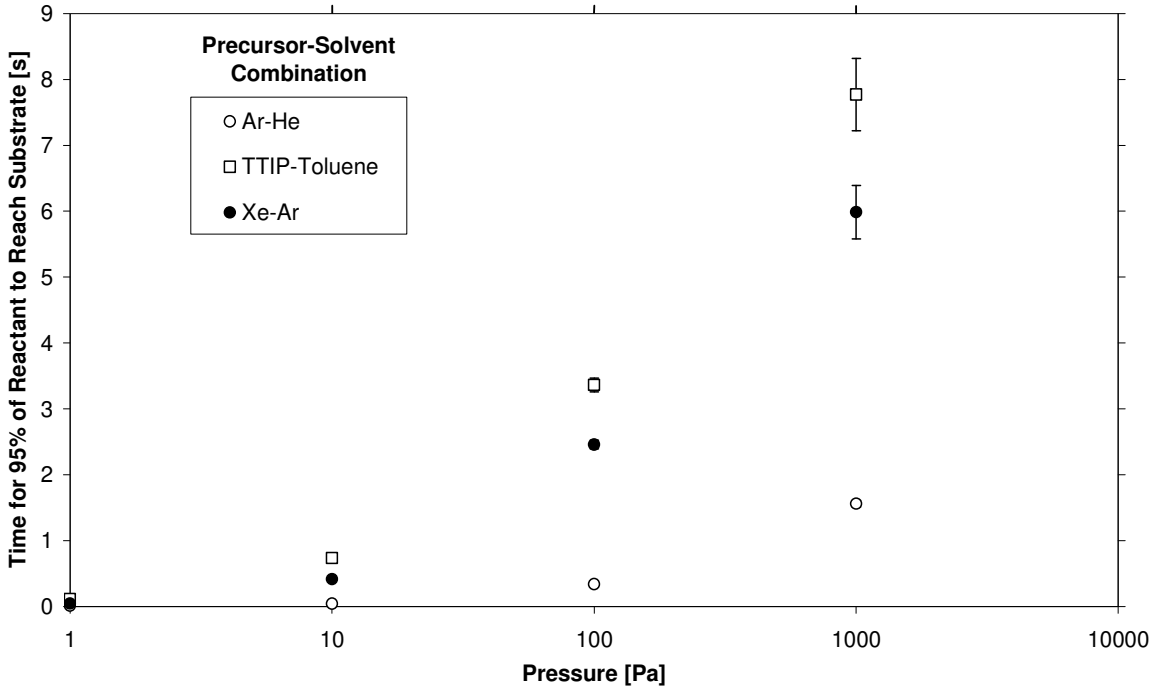

Figure 5.15. Precursor residence time $t_{95\%}$ for different reactor peak pressures P_{max} (logarithmic scale).

The results can be compared to reactor pump-down time t_P to gain an appreciation of the processes leading to the observed high precursor conversion efficiencies in PP-CVD. As shown in section 2.3.4, typically PP-CVD reactors operate with a pulse period $t_P \geq 4\tau$ and $t_P >> t_i$ to ensure that both mass flux uniformity is high after the injection phase and the reactor pressure does not climb over a period of several pulses. For the reactor studied in these simulations the reactor pump-down time $t_P = 10.6$ seconds.

From figures 5.12 and 5.13 we see that in every case residence time $t_{95\%} << 10.6$s for $P_{max} = 10$ Pa. Because the time for diffusion of precursor particles to the substrate is much less than the pump-down time we can expect very high efficiencies for a reactor operating in this regime. The relationship between the different precursor-solvent combinations in these figures reveals that the mass ratio of the precursor to the solvent along with the relative mass of the solvent both have large effects on the precursor residence time. Lighter solvent molecules result in a decrease in precursor residence time as does a decrease in precursor size relative to the size of the solvent.

The reasons for these relationships can be readily understood by examining equation (5-7). As the collision cross section of the collision partners increases, the free-path of the molecules within the gas decreases. Larger molecules undergo more scattering events and, coupled with the fact that their molecular speed is lower than smaller molecules at the same temperature, their residence time increases, as would be expected from diffusion relationships. Clearly the lesson here is that solvents should be chosen with as low a molecular weight as possible for the PP-CVD process. Similar results have been reported for Jet Vapour Deposition (JVD), in which a helium carrier gas stream is employed to deposit gold vapour [15], and in Directed Vapour Deposition (DVD) [5].

From figure 5.15 it can be seen that the arrival rate for the precursor at the substrate is highly dependent on reactor peak pressure. As P_{max} increases so that the residence time $t_{95\%}$ approaches t_P we can expect a corresponding drop in reactor efficiency. This result is as would be expected from diffusion relationships, however it should be kept in mind that the decreasing reactor pressure throughout the pump-down phase given by equation means that precursor residence time will be significantly lower than for a reactor which operates at steady pressures.

It has been shown that when the precursor residence time $t_{95\%} << t_P$ we can expect high reactor efficiencies. When this condition is satisfied, convective effects within the reactor due to bulk flow are minimal and precursor particles diffuse to the surface due to random molecular walk. Random walk is a very rapid process in stationary gases at the relatively low pressures in the pump-down phase of PP-CVD and consequently high precursor conversion efficiencies are achieved.

The study confirms that the physical mechanisms for high efficiencies in PP-CVD reactors occur when the rate of precursor diffusion, adsorption onto the substrate and thermal decomposition are faster than the reactor pump-down rate. The study also shows that to achieve high efficiencies solvents of minimal molecular size should be employed and confirms that high reactor peak pressures will result in a decrease in precursor conversion efficiency.

5.4.2. Efficiency and Uniformity Simulations

Efficiency and uniformity simulations were conducted by tracking precursor particles through both the injection and pump-down phase. The DSMC flow fields generated using DS2V, as discussed in section 5.2.2, were used as the input to the unsteady PIES model described in section 5.3.1. In each case approximately 10,000 precursor particles were tracked through the carrier gas field until they impacted the substrate or were removed from the reactor by the vacuum pump (this boundary condition was implemented in the same way as in section 5.2.1). In every case, the particles were tracked in three-dimensions (projection onto the zero-azimuth plane was not used). Figure 5.16 shows the three-dimensional positions for argon precursor particles at different stages during, and immediately after, the injection phase, for the P_S = 100Pa case.

Figure 5.16 shows the precursor particles are rapidly dispersed by the injection phase. During the injection phase, convection is significant especially near the jet inlet, however by approximately $t = 2t_i$ the convection field has died away and the precursor particles, which have not already been deposited, have become evenly dispersed throughout the reactor volume.

The uniformity of the flow field during the injection phase was calculated by dividing the reactor volume into M interrogation volumes and counting the number of precursor particles n in each volume. A modified version of equation (2-16) was then used to calculate the flow field uniformity:

$$U = 1 - \frac{\sum_{i=1}^{M} \left| n_i - \overline{n} \right|}{\sum_{i=1}^{M} n_i} \tag{5-12}$$

The flow field uniformity throughout during, and immediately after, the injection phase was calculated using equation (5-12) and the results for the two supply pressure cases are shown in figure 5.17. In order to compare the results to the naphthalene sublimation results discussed in section 2.3.5, these calculations were made with no deposition on the substrate. However it should be noted that the DSMC flow fields from section 5.2.2 were used in these calculations, so substrate temperature was set at 800K, unlike in the experimental investigations in which the substrate heater is not turned on.

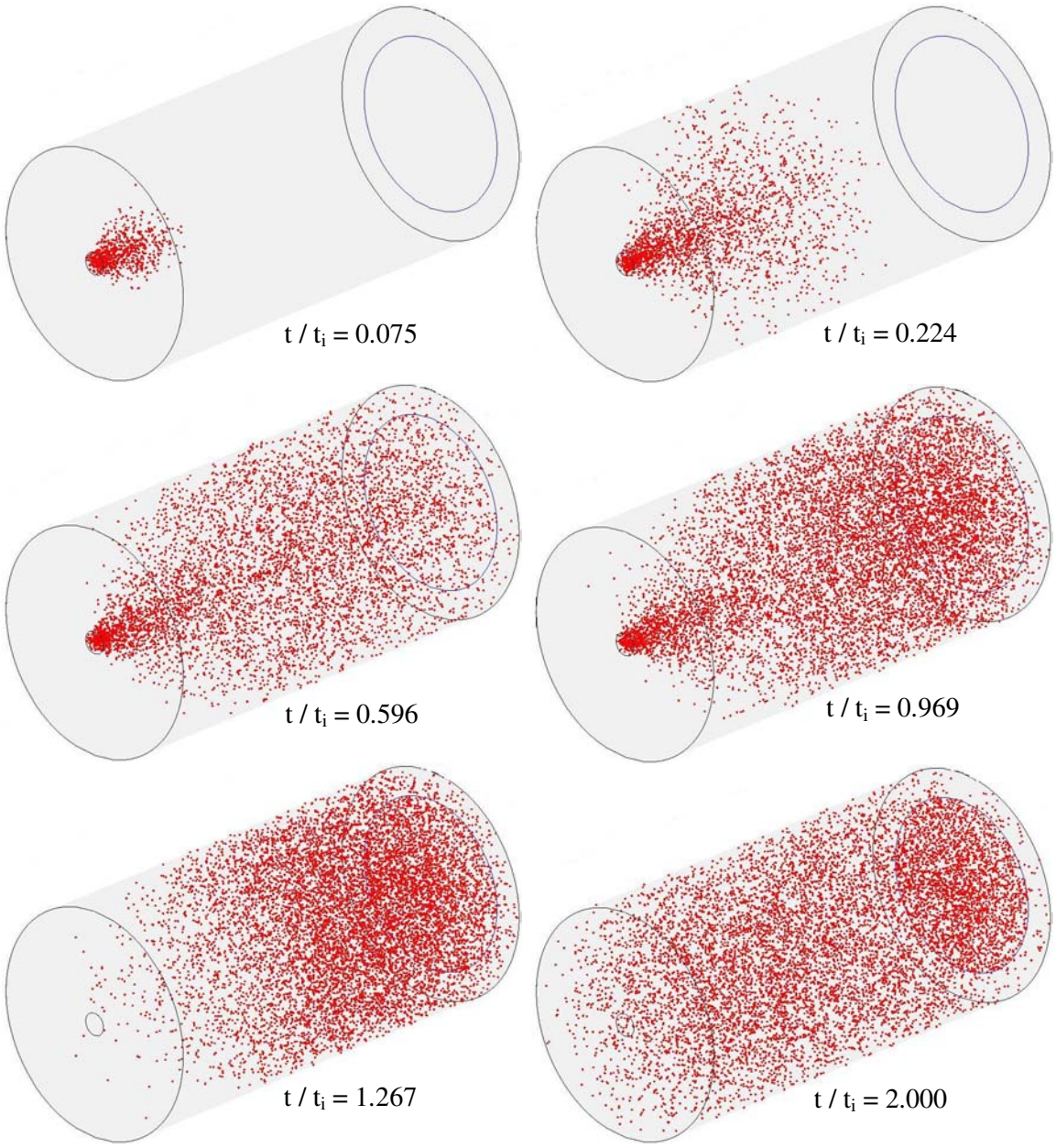

Figure 5.16. Argon "precursor" particle positions at different values of t / t_i for the P_S = 1000 Pa case.

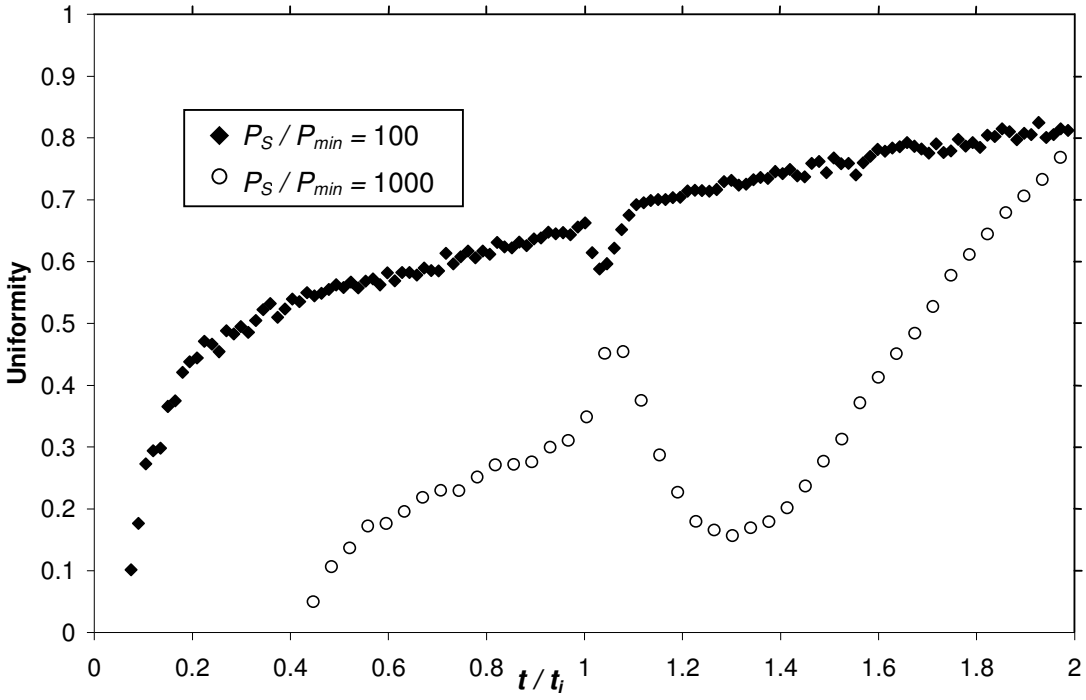

Figure 5.17. Flow field uniformity during, and immediately after, the injection phase.

Figure 5.17 shows that during the initial part of the injection phase, the uniformity is very poor because all of the particles in the reactor are near the inlet orifice (in fact at $t = 0$, equation (5-12) gives the uniformity as $U = -\infty$ since all of the particles are outside the reactor volume). The uniformity climbs throughout the injection phase, however there is a drop in uniformity immediately after $t = t_i$ because the high momentum of the jet means the particles just ejected from the nozzle are carried out of the interrogation volumes in the upper part of the reactor. This is more pronounced in the $P_S = 1000$ Pa case due to the higher momentum of the carrier gas jet. After this initial drop, the uniformity climbs rapidly as the convective effects in the reactor dissipate and diffusion begins to dominate particle movement. By $t = 2t_i$ the flow field uniformity has reached approximately 80%.

The steady flow PIES code was also used to track precursor particles through the steady flow fields shown in figure 5.5. Figure 5.18 shows some typical examples of particle tracks through these flow fields (in each case the particle track has been projected onto the zero-azimuth plane). These results show that precursor particles tend to get entrained in the jet and convected toward the substrate, particularly for the highly under-expanded cases.

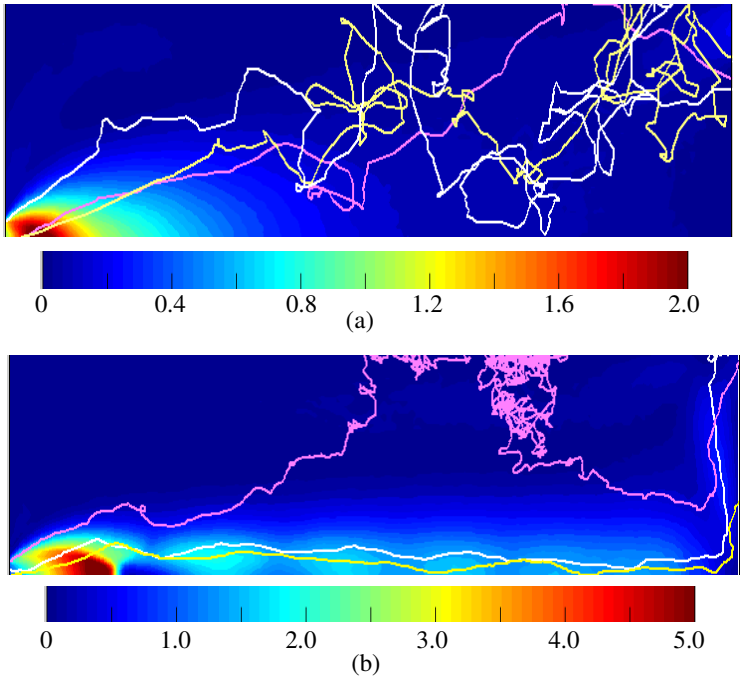

Figure 5.18. Mach number contours and typical argon "precursor" particle paths in steady flow reactors with a) P_S = 100 Pa & P_R = 9.5 Pa and b) P_S = 1000 Pa & P_R = 59 Pa.

Deposition uniformity for both pulsed and steady cases was assessed by recording deposition time and position on the substrate. A modified version of equation (2-16) was used to determine the uniformity by the number of particles impacting per unit area N' over M annular sampling areas:

$$U = \left(1 - \frac{\sum_{i=1}^{M} \left| N_i' - \overline{N}' \right|}{\sum_{i=1}^{M} N'} \right) \bullet 100\% \tag{5-13}$$

Reactor efficiency was calculated by comparing the number of particles deposited on substrate N_{dep} to the number removed by the vacuum pump N_{rem}:

$$\eta = \left(\frac{N_{dep}}{N_{dep} + N_{rem}} \right) \bullet 100\% \tag{5-14}$$

Table 5.3 shows the reactor efficiency calculated using equation (5-14), deposition uniformity calculated using equation (5-13) and percentage deposition before $t = t_i$ for the two pulsed cases and the steady cases from figure 5.18 for a range of "precursor" types.

Table 5.3. Reactor efficiencies, deposition uniformities and percentage of reactant deposited with $t \leq t_i$ for a range of pulsed and steady reactor configurations

Reactor Type	Supply Pressure	Steady Pressure	Precursor Type	Efficiency	Deposited at $t < t_i$	Deposition Uniformity
Pulsed	100 Pa	--	He	94.5 %	22.3 %	89.8 %
			Ar	96.5 %	26.3 %	94.6 %
			Xe	96.9 %	34.7 %	92.0 %
Pulsed	1000 Pa	--	He	93.8 %	7.6 %	88.9 %
			Ar	96.1 %	13.5 %	95.4 %
			Xe	97.2 %	18.1 %	86.1 %
Steady	100 Pa	9.5 Pa	He	53.4 %	--	89.1 %
			Ar	54.3 %	--	90.2 %
			Xe	57.5 %	--	91.5 %
Steady	1000 Pa	59 Pa	He	36.3 %	--	63.5 %
			Ar	37.7%	--	56.5 %
			Xe	55.9 %	--	32.5 %
			Xe	52.9 %	--	18.0 %

The efficiency and deposition uniformity results for all steady flow reactors are summarised in figures 5.19 and 5.20 respectively.

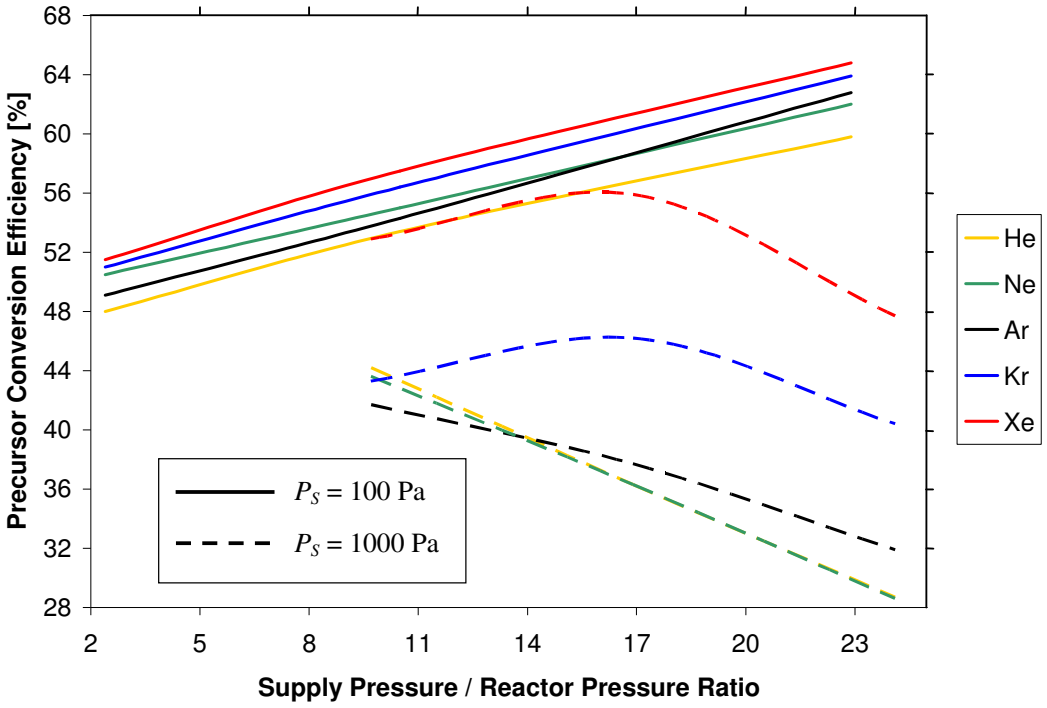

Figure 5.19. Reactor efficiencies for steady flow reactors simulated using the DSMC-PIES model.

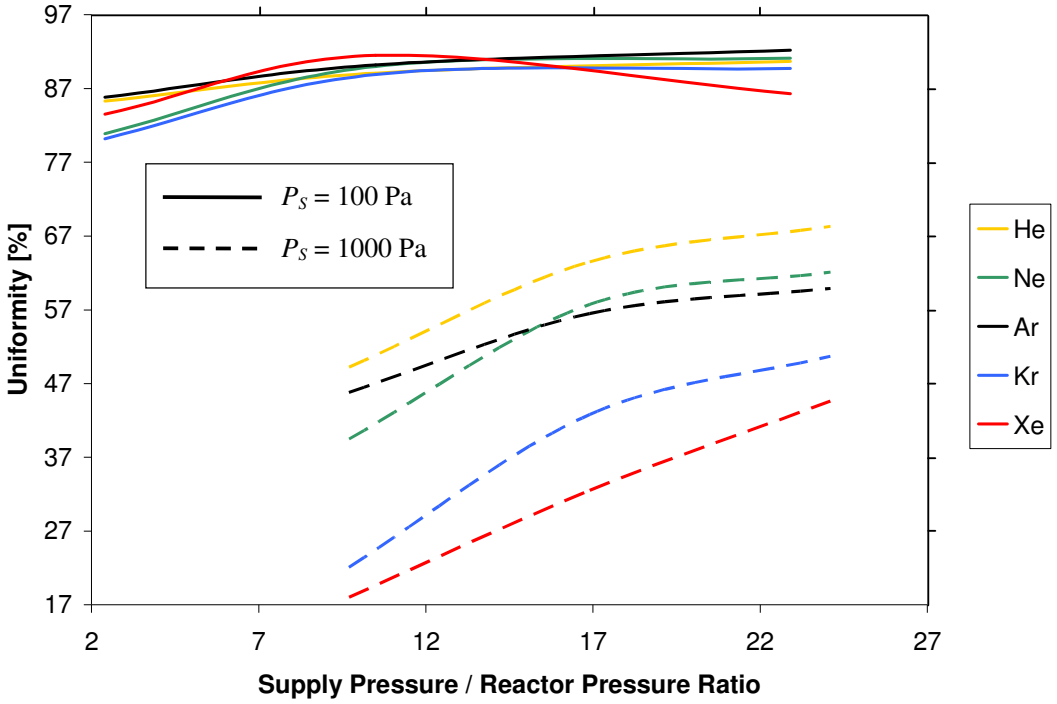

Figure 5.20. Deposition uniformity for steady flow reactors simulated using the DSMC-PIES model.

The above results illustrate some general trends. In both cases efficiency and deposition uniformity was high for the pulsed reactors. There was a slight increase in reactor efficiency for heavier precursors, probably due to the heavier particles retaining their momentum in the axial direction to a greater extent. For the same reason, the heavier particles were more likely to be deposited during the injection phase. For steady reactors, deposition uniformity was comparable to the pulsed cases but only when the jet structure had dispersed well above the substrate. Where the jet impacted upon the substrate, uniformity was very poor. Lighter particles tended to have better uniformity as these particles were able to diffuse more rapidly through the stand-off shock above the substrate. In every steady reactor case, reactor efficiency was inferior to the pulsed reactors, especially when the jet structure impacted on the substrate.

Figure 5.21 shows the impact positions for argon "precursor" particles on the substrate for the pulsed reactors with P_S = 100 Pa and P_S = 1000 Pa. Also shown is the deposition profile calculated by recording the impact frequency on different sampling annuli. The deposition profile is compared to the idea (100% efficiency, 100% uniformity) case. Figure 5.22 shows similar plots for the steady cases from figure 5.18.

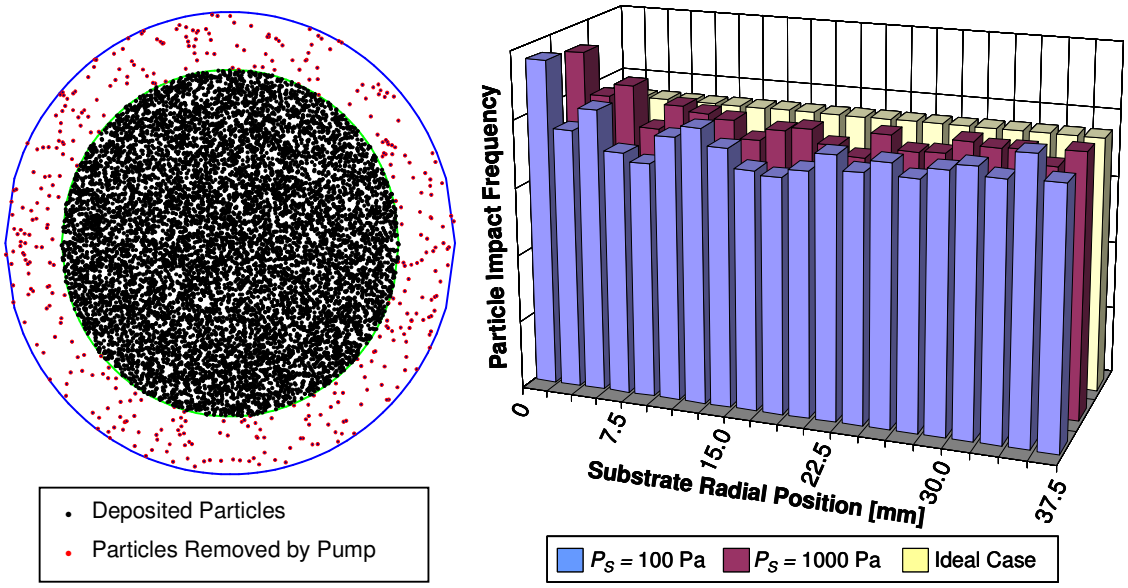

(a) (b)

Figure 5.21. a) Substrate deposition positions for the P_S =1000 Pa case and b) deposition profiles for pulsed reactors compared to the ideal case.

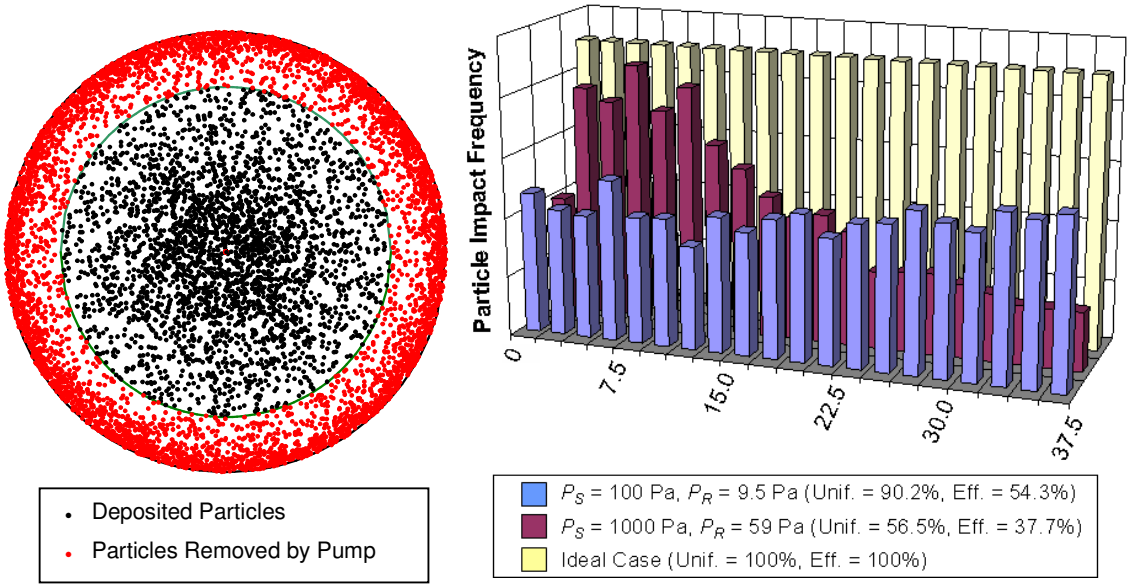

(a) (b)

Figure 5.22. a) Substrate deposition positions for the P_S =1000 Pa, P_R=59 Pa case and b) deposition profiles for several steady reactors compared to the ideal case.

The above figures further confirm the results that in steady flow reactors convective effects are high and precursor particles must diffuse in a direction which is generally normal to the bulk flow direction in order to reach the deposition surface. Consequently convective effects move large quantities of the precursor out of the reactor before the molecules can diffuse to the deposition surface resulting in low precursor conversion efficiencies. Additionally these convective effects mean precursor concentration immediately above the substrate is non-constant resulting in highly non-uniform deposition profiles.

5.5. Conclusions

The results of DSMC/PIES simulations of representative PP-CVD reactors give an insight into the physical mechanisms resulting in high precursor conversion efficiencies and deposition uniformity in the process.

During the injection phase, a fraction of the particles arrive at the substrate because of the significant axial momentum imparted by the expansion process. Heaver precursor particles are scattered less by collisions with the carrier gas particles hence the fraction arriving during the injection phase is proportional to the precursor mass. This accounts for the increase in reactor efficiency as the precursor particles increase in mass. Longer injection times also increase the fraction of particles arriving at the substrate during the injection phase.

After the jet structure collapses at the conclusion of the injection phase there is negligible bulk flow in the reactor volume and the precursor particles move to the substrate primarily via random molecular walk. The rate at which this diffusion process occurs is considerably higher than the rate at which particles can be removed from the reactor by the vacuum pump resulting in high precursor conversion efficiencies.

The uniform distribution of precursor particles at the end of the injection phase and the lack of significant bulk flow structures within the reactor also account for the high film deposition uniformity. Since precursor particles move to the substrate via random walk, there are no regions of high precursor concentration near the substrate and the resultant film profile is consequently of uniform thickness. It is expected that long injection times would decrease the uniformity of the films due to the development of quasi-steady bulk flow structures within the reactor. Heavier precursor particles would exacerbate this because of their high axial

momentum and low scattering during the injection phase which the simulations demonstrated to some extent. This effect was offset by the slightly higher deposition rates towards the edge of the substrate due to the influence of the pump outlet, so the results are not entirely conclusive.

The results clearly illustrate potential advantages over steady flow reactors. In the steady flow case, bulk flow effects are always significant and consequently a large proportion of precursor particles are convected out of the reactor volume before they can diffuse to the deposition surface. Deposition uniformity was found to be poor especially when the steady jet structure impinged upon the substrate. The high momentum of heavy particles close to the jet's axis resulted in a film which was thicker towards the centre of the substrate and thin toward the substrate edges where precursor particles had to diffuse in a direction approximately normal to the bulk flow direction to reach the deposition surface. Steady flow reactors with jet structures which had dispersed well above the substrate had film uniformities equivalent to PP-CVD reactors, however precursor conversion efficiency was always inferior.

The limitations in the modelling method have not permitted the simulation of actual PP-CVD reactor systems meaning there is no corresponding experimental data at the same reactor pressures to directly validate the results. However the results are consistent with experimental studies, discussed in section 2.3.5, which show uniform deposition can be achieved when the injection time is as short as possible (to evenly distribute precursor particles in the reactor) and pump-down times should be relatively long (so that reactor bulk flow is negligible) [16]. Additionally, the predicted efficiencies are consistent with those achieved experimentally.

The use of a simple DSMC and particle tracking model enables the physical processes governing PP-CVD deposition uniformity and conformity to be further investigated and understood. The simulations form a stepping stone to the more challenging problem of investigating reactors with high inlet pressures, which will be discussed in chapter 7.

References

[1] G.A. Bird, The DS2V Program User's Guide, G.A.B. Consulting Pty Ltd (2005).

[2] G.A. Bird, Sophisticated Versus Simple DSMC, in Proc. of 25th International Symposium on Rarefied Gas Dynamics, St. Petersburg, Russia (2006).

[3] J.D. Anderson, Modern Compressible Flow: With Historical Perspective (McGraw-Hill, New York, 1990).

[4] A. Roth, Vacuum Technology (North-Holland, Amsterdam, 1990).

[5] J.F. Groves, Directed Vapor Deposition, PhD Thesis, University of Virginia (1998).

[6] G.A. Bird, Molecular Gas Dynamics and the Direct Simulation of Gas Flows (Clarendon Press, Oxford, 1994).

[7] H.M. Cave, S.P. Krumdieck and M.C. Jermy, Development of a model for high precursor conversion efficiency pulsed-pressure chemical vapor deposition (PP-CVD) processing, *Chem. Eng. J.* 135, 120-128 (2008).

[8] E.W. McDaniel, Collision phenomena in ionized gases (Wiley, New York, 1964).

[9] C. Moler, Random thoughts, Matlab News and Notes (Fall, 1995).

[10] S. Chapman and T.G. Cowling, The mathematical theory of non-uniform gases: an account of the kinetic theory of viscosity, thermal conduction and diffusion in gases (Cambridge University Press, Cambridge, 1970).

[11] D.L. Smith, Thin-film Deposition: Principles and Practice (McGraw-Hill, New York, 1995).

[12] F.P. Incropera and D.P. DeWitt, Fundamentals of heat and mass transfer (Wiley, New York, 2001).

[13] N. Tatsuda, Y. Fukushima and H. Wakayama, Penetration of Titanium Tetraisopropoxide into Mesoporous Silica Using Supercritical Carbon Dioxide, *Chem. Mater.* 16, 1799-1805 (2004).

[14] J.E.F. Rubio, V.G. Baonza, M. Taravillo, J. Nunez and M. Caceres, A dynamic light scattering study of the hypersonic relaxation in liquid toluene, *J. Chem. Phys.* 115(10), 4681-4688 (2001).

[15] B. L. Halpern and J. J. Schmitt, Multiple jets and moving substrates: Jet Vapor Deposition of multicomponent thin films, *J. Vac. Sci. Tech. A* 12(4), 1623-1627 (1994).

[16] S.P. Krumdieck, H.M. Cave, S. Baluti, M. Jermy and A. Peled, Expansion Transport Regime in Pulsed-Pressure Chemical Vapor Deposition, *Chem. Eng. Sci.* 62(22), 6121-6128 (2007).

6. Development of Unsteady Parallel DSMC Techniques

6.1. Introduction

In chapter 5, the DSMC method along with a precursor particle tracking code were used to provide an insight into the physical mechanisms leading to high precursor conversion efficiency and deposition uniformity in the PP-CVD process. The computational limitations of this technique which prevented the simulation of actual systems were discussed. The method was limited to low reactor pressures and the results had relatively high statistical scatter preventing the simulation of existing experimental PP-CVD reactors.

One method of increasing the capacity of the DSMC technique is to parallelise the code such that the computational load is shared across a number of computer processors. DSMC is particularly suitable for parallel processing because over a time step the particles move independently of each other with coupling between them only occurring during the collision step. In this chapter a parallel DSMC method is discussed, the existing steady flow code is modified for unsteady sampling, various improvements are made to the code and a number of validation simulations are carried out. This code will be used in chapter 7 for the simulation of PP-CVD reactors at realistic operating pressures.

6.2. Parallel DSMC (PDSC) Code

The DSMC algorithm is readily parallelised through decomposition of the physical domain into groups of cells which are then distributed amongst the parallel processors. Each processor executes the DSMC algorithm in serial for all particles and cells in its own domain. Parallel communication between processors is required when particles cross the domain boundaries requiring particles to be transferred between processors. To achieve high parallel efficiency it is necessary to minimise the communication between processors whilst maintaining a balance between the computational load on each processor. In the present study, we have adapted the previously developed Parallel DSMC Code (PDSC) which has been described in detail in the papers by Wu *et al.* [1-7] and will only be outlined briefly here.

In PDSC, a two-dimensional, axisymmetric or three-dimensional structured or unstructured mesh of the physical flow domain is first generated using an appropriate commercial code.

The DSMC algorithm discussed in section 3.6 is implemented on this mesh using a particle ray-tracing technique, which takes advantage of the cell connectivity information provided by the mesh data and is able to handle complex boundary geometry. PDSC utilises the multi-level graph partitioning tool ParMETIS to decompose the computational domain and distribute the structured or unstructured cells amongst the processors. A stop-at-rise (SAR) algorithm [8] is used to determine when to dynamically repartition and re-distribute the computational load between processors based on the value of a degradation function which compares the computational cost of repartition to the idle time for each processor. The transfer of particle data between the processors uses the standard Fortran Message Passing Interface (MPI) libraries and only occurs when particles strike the inter-processor boundaries and after all other particles on each processor have been moved, thus minimising communication between processors and maximising the parallel speed-up. During calculation, the mesh can be iteratively refined using the h-refinement technique whereby local grid points are added to improve the cell distribution according to the solution based on some adaptation criteria (for example, flow field density). Cell quality control is used to maintain the integrity of the mesh during this process.

Figure 6.1 shows the important features of PDSC. Special features include pressure boundary treatment, a spatial variable time-step scheme, adaptive mesh refinement, the implementation of a conservative weighting scheme to efficiently deal with gas flows with trace species [5] and the gas phase chemistry for simulating chemical reactions in reactive flows. These features have been developed to enhance the computational efficiency, flexibility and utility of PDSC.

The PDSC code described above has been extensively tested and its procedures verified in numerous two- and three-dimensional studies including supersonic corner flow [1], sonic orifice expanding flow [1], hypersonic flow over a sphere [1-3], spiral drag groove pump simulations [1,2], twin jet interaction [2,3], high speed driven cavity flow [3], hypersonic flow over a cylinder [3] and compression ramp flow [3].

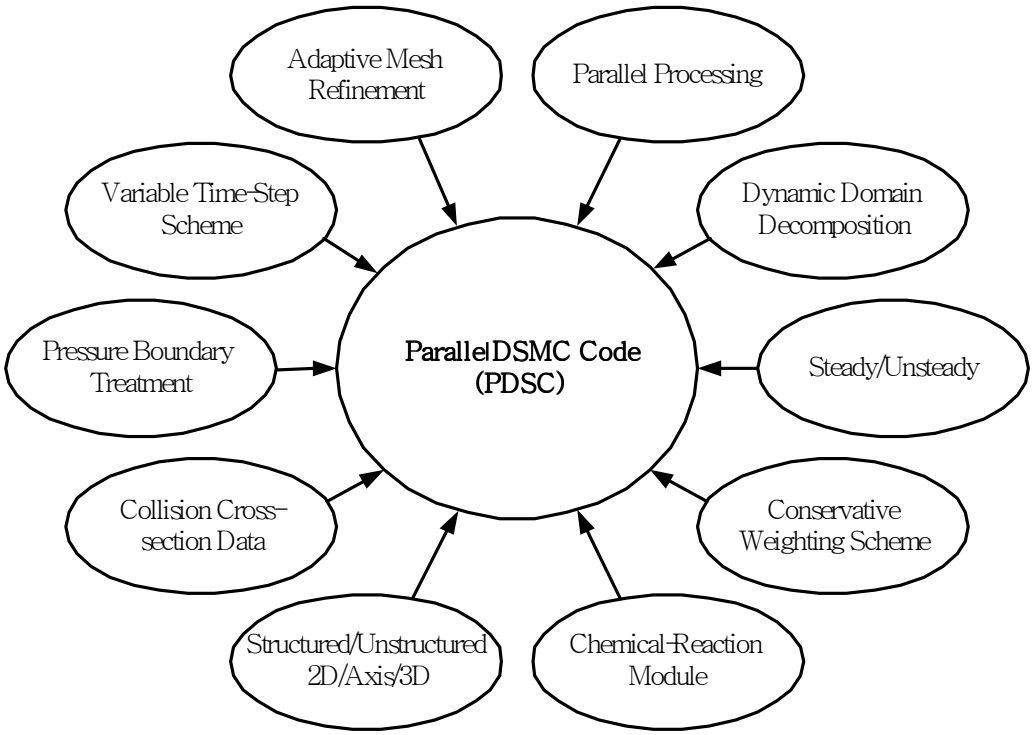

Figure 6.1. Features of PDSC [diagram courtesy of J.-S. Wu]

6.3. Unsteady Sampling for PDSC

6.3.1 Method

The PDSC code described in the previous section has been designed specifically for simulating steady flows, using the sampling method illustrated in figure 6.2a. However in the PP-CVD flow field a significant proportion of the injection phase is highly unsteady (and the remainder can be termed "quasi-steady", at best). For this reason, the PDSC code was modified for unsteady sampling.

There are two possible methods for unsteady sampling, the differences between which are illustrated in figure 6.2. The first, which will be termed "ensemble averaging" and is shown in figure 6.2b, requires multiple simulation runs. During each run, the flow field is sampled at the appropriate sampling time and the samples at this time are averaged over the runs to provide the flow field output. This method is very accurate, however it is extremely computationally expensive because a large number of runs are required to reduce the

statistical scatter to an acceptably low level and a large amount of memory is required to record the sampling data for each simulation.

The second unsteady sampling method, which will be termed "time-averaging" and is shown in figure 6.2c, averages a number of time steps over an interval centred on the sampling time. This method only requires one simulation run, however it suffers a potential disadvantage in that the results will be "smeared" over the time over which samples are taken. This occurs because the particles will propagate downstream during the sampling interval, resulting in a broadening of any areas with large macroscopic gradients, such as shocks, if the sampling interval is too long. Hence the sample time must be sufficiently short to minimize time "smearing" and yet long enough to obtain a good statistical sample. This method of time averaging has been used previously by Auld to model shock tube flow [9] and is the method used in Bird's DS2V code.

The time-averaging method was implemented into PDSC. In order to set the flow time step, it was reasoned that the flow could not travel more than one mean free path during the sampling period so as to prevent the flow field "smearing". Generally this requirment was set by examining the free stream flow conditions. A technique called the temporal variable time step (TVTS) method was used to reduce the simulation time by increasing the size of the time step between sampling intervals. The code has an option for the user to choose specific output flow times or for output at regular intervals. Figure 6.3 shows the flow chart of the parallel DSMC method for *np* processors with the unsteady sampling procedures implemented. Here M is the output matrix for sampling interval M. Most parts of the procedure are the same as the steady simulation procedure except the sampling data must be reset after completing each simulation interval.

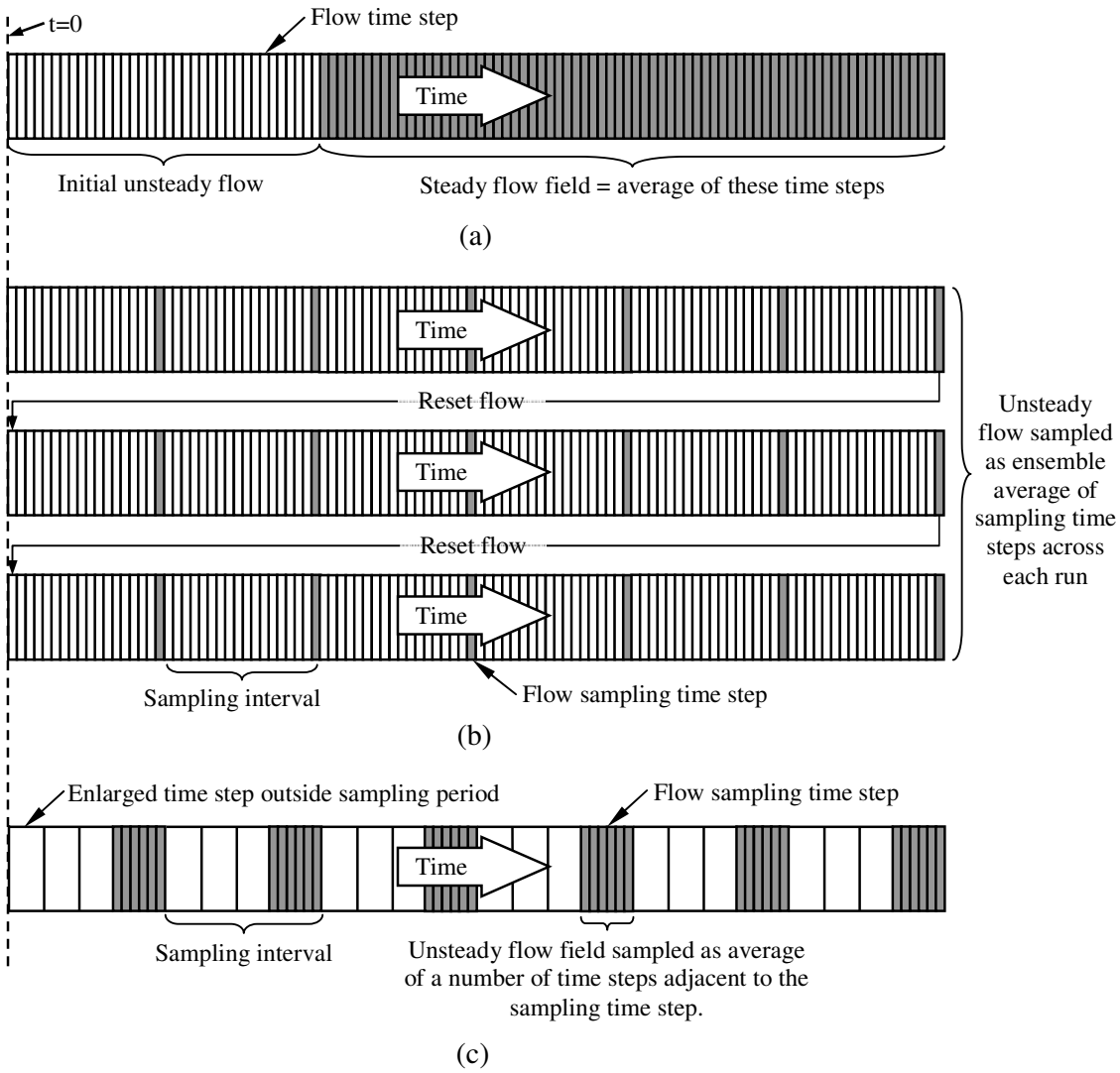

Figure 6.2. Sampling methods in DSMC including a) steady sampling, b) unsteady ensemble averaging and c) unsteady time averaging.

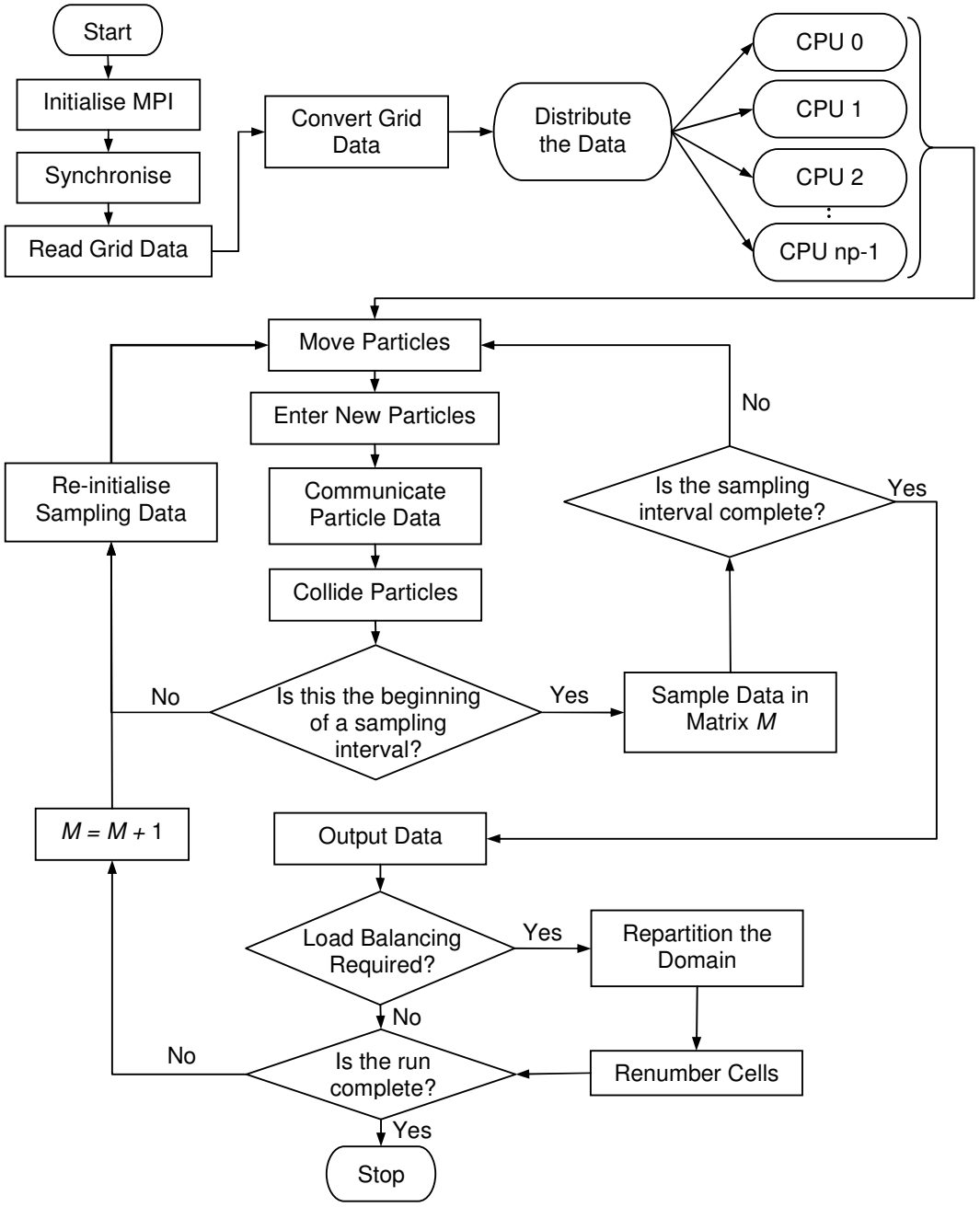

Figure 6.3. Simplified flow chart of the unsteady parallel DSMC method

6.3.2. Model Validation – Shock Tube Flow

As a validation of the unsteady sampling techniques employed in the PDSC code, a test problem of shock tube flow was used. Shock tubes are devices in which a shock wave is created by bursting a diaphragm separating a high pressure "driver" gas from a low pressure "driven" gas. These devices are used to investigate a wide variety of physical phenomena including shock structures and high temperature gas reactions. Shock tubes have enabled the study of many practical problems which cannot be studied in conventional wind tunnels such as space vehicle re-entry problems and ballistic missile aerodynamics [10-12]

The structure of the flow within a typical shock tube is shown in figure 6.4. Here the structure is divided into four distinct regions: (1) the undisturbed low pressure gas at the initial pressure p_1 and temperature T_1, (2) the gas behind the shock front travelling at constant velocity u_P, (3) the gas behind the contact surface between the driving and driven gases and (4) the undisturbed high pressure gas at the initial pressure p_4 and temperature T_4. Regions (1) and (2) are separated by a normal shock which moves into the undisturbed driven gas, while regions (3) and (4) are separated by an expansion fan.

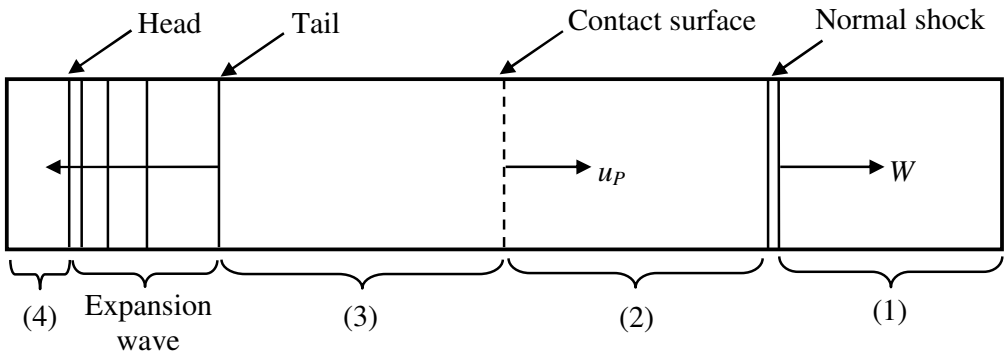

Figure 6.4. Flow structure in a shock tube

The Riemann continuum solution for a shock tube allows the properties of the flow structure to be investigated [10]. After the diaphragm bursts, a normal shock propagates into the low pressure region at a supersonic speed given by:

$$W = a_1\sqrt{\frac{k+1}{2k}\left(\frac{p_2}{p_1}-1\right)+1} \tag{6-1}$$

where a_1 is the speed of sound in the undisturbed driven gas.

The shock strength, which is the ratio of the pressures upstream and downstream of the shock, is related to the ratio of the undisturbed pressures in regions (1) and (4) by:

$$\frac{p_4}{p_1}=\frac{p_2}{p_1}\left[1-\frac{(k-1)\left(a_1/a_4\right)\left(p_2/p_1-1\right)}{\sqrt{2k\left\{2k+(k+1)\left(p_2/p_1-1\right)\right\}}}\right]^{-2k/(k-1)} \tag{6-2}$$

Solution of equation (6-2) allows the temperature and density ratios across the shock to also be determined using:

$$\frac{T_2}{T_1}=\frac{p_2}{p_1}\left(\frac{\frac{k+1}{k-1}+\frac{p_2}{p_1}}{1+\frac{k+1}{k-1}\frac{p_2}{p_1}}\right) \tag{6-3a}$$

$$\frac{\rho_2}{\rho_1}=\frac{1+\frac{k+1}{k-1}\left(\frac{p_2}{p_1}\right)}{\frac{k+1}{k-1}+\frac{p_2}{p_1}} \tag{6-3b}$$

The contact surface between the two gases moves in the direction of the normal shock. Entropy and density are discontinuous across this surface however pressure and velocity remain constant. The contact surface moves with a velocity given by:

$$u_P=\frac{a_1}{k}\left(\frac{p_2}{p_1}-1\right)\sqrt{\frac{\frac{2k}{k+1}}{\frac{p_2}{p_1}+\frac{k-1}{k+1}}} \tag{6-4}$$

As the shock wave moves into the driven gas an expansion wave (or fan) moves into the driving gas. The head of the fan moves at the speed of sound in the undisturbed driving gas a_4, while the tail of the fan moves at the relative speed of sound in region 3 $u_P - a_3$. The strength of the expansion fan along with the density and temperature across it can be calculated from:

$$\frac{p_3}{p_4}=\left(\frac{p_3}{p_1}\right)\left(\frac{p_1}{p_4}\right)=\left(\frac{p_2}{p_1}\right)\left(\frac{p_1}{p_4}\right)=\left(\frac{\rho_3}{\rho_4}\right)^k=\left(\frac{T_3}{T_4}\right)^{k/(k-1)} \tag{6-5}$$

Since this expansion process is isentropic, the flow properties change gradually throughout the fan, hence the flow velocity, speed of sound, temperature, density and pressure in this region are given by:

$$u(x) = \frac{2}{k+1}\left(a_4 + \frac{x}{t}\right) \tag{6-6a}$$

$$\frac{a(x)}{a_4} = 1 - \frac{k-1}{2}\left(\frac{u}{a_4}\right) \tag{6-6b}$$

$$\frac{p(x)}{p_4} = \left[1 - \frac{k-1}{2}\left(\frac{u(x)}{a_4}\right)\right]^{2k/(k-1)} \tag{6-6c}$$

$$\frac{T(x)}{T_4} = \left[1 - \frac{k-1}{2}\left(\frac{u(x)}{a_4}\right)\right]^{2} \tag{6-6d}$$

$$\frac{\rho(x)}{\rho_4} = \left[1 - \frac{k-1}{2}\left(\frac{u(x)}{a_4}\right)\right]^{2/(k-1)} \tag{6-6e}$$

where x is measured relative to the head of the expansion fan.

More details on the derivation of equations (6-1) to (6-6e) can be found in the monograph by Anderson [10]. By solving these expressions, the properties of the shock tube flow structure can readily be obtained. The positions of each of the features in figure 6.4 at any time before the normal shock impinges on the end wall of the shock tube can be determined from:

Expansion fan head: $x_4 = x_0 - a_4 t$ (6-7a)

Expansion fan tail: $x_3 = x_0 - (a_3 - u_P)t$ (6-7b)

Contact surface: $x_2 = x_0 + u_P t$ (6-7c)

Normal shock: $x_1 = x_0 + Wt$ (6-7d)

where x_0 is the initial position of the diaphragm separating the driven and driving gases.

In a shock tube of finite length, the incident shock will reflect from the end wall. It can be shown that the Mach number of the reflected shock M_R is related to the Mach number of the incident shock M_S by [10]:

$$\frac{M_R}{M_R^2 - 1} = \frac{M_S}{M_S^2 - 1}\sqrt{1 + \frac{2(k-1)}{(k+1)^2}\left(M_S^2 - 1\right)\left(k + \frac{1}{M_S^2}\right)} \tag{6-8}$$

where $M_S = W / a_1$ and $M_R = (W_R + u_P) / a_1$.

There is already some work in the literature in which shock tube flow has been investigated by DSMC and hybrid methods. Auld presents the results for pure DSMC simulations and finds the method is suitable for predicting unsteady flow properties, despite a large level of statistical scatter [9]. Roveda *et al.* [13] used their adaptive discrete velocity (ADV) Euler-DSMC hybrid scheme and compared their results with a pure DSMC calculation. Likewise, Smith [14] used a hybrid method using the Equilibrium Particle Simulation Method (EPSM) and Equilibrium Flux Method (EFM) which he compared to pure DSMC results.

To validate the PDSC code, simulations were conducted on a two-dimensional shock tube of length 0.1m and width 0.0125m with argon as the working gas. The upper and lower walls were implemented as specular walls to preserve the one-dimensional nature of the flow, while the end walls were simulated as diffuse walls at 300K. The initial conditions of the flow were p_4 = 100Pa, p_1 = 10Pa and $T_4 = T_1$ = 300K. Both PDSC and DS2V were used to solve the flow field and the solutions compared with the analytical solution discussed above. Additionally as a further point of comparison, custom one-dimensional ensemble-averaging code called HDSMC was written in MATLAB™ using the same flow conditions but with a cell size set to approximately one-third of the average mean free path, as recommended by Bird [15]. The conditions for the PDSC run were selected to attempt to preserve the simulation conditions from the DS2V run, the details for which are outlined in table 6.1. Both the DS2V and HDSMC were simulated on a single processor Intel Pentium IV 3.2GhZ (Hyper-threading enabled) with 1.0GB of RAM, whereas PDSC was implemented on a PC cluster system of ten Athlon XP2100s, each with 512MB of RAM.

Table 6.1. Shock tube simulations using PDSC and DS2V

Solver	DS2V	PDSC	HDSMC
Number of Sampling Cells	21,675	80,000	2,000
Number of Collision Cells	~65,981	80,000	2,000
Number of Simulated Molecules	2,081,284	2,200,000	50,000
Time Step	Variable	9.15×10^{-8}s	9.15×10^{-8}s
Number of Time Steps Averaged Per Sample	30	30	N/A
Number of Simulations in the Ensemble Average	N/A	N/A	50
Run Time (hours per second of simulated flow)	~24,150 hrs/sec	~2,449 hrs/sec	~579,235 hrs/sec

Figure 6.5 shows the pressure, density and temperature profiles in the shock tube at 27.45μs for the PDSC, DS2V and HDSMC simulations along with the Riemann continuum solution. In this figure the normal shock, expansion fan and contact surface are all clearly visible in all the results. All three methods capture the flow profile accurately with the positions and general structure of each flow feature comparing well with the continuum solution. As would be expected the sharp continuum solution is not followed exactly since it does not include viscous effects. The PDSC results show similar scatter to the DS2V solution; however the PDSC solution does not exhibit the "spikes" in the temperature profile predicted by DS2V, which can be seen more clearly in figure 6.6. Additionally, parallelisation means PDSC runs approximately ten times faster than DS2V.

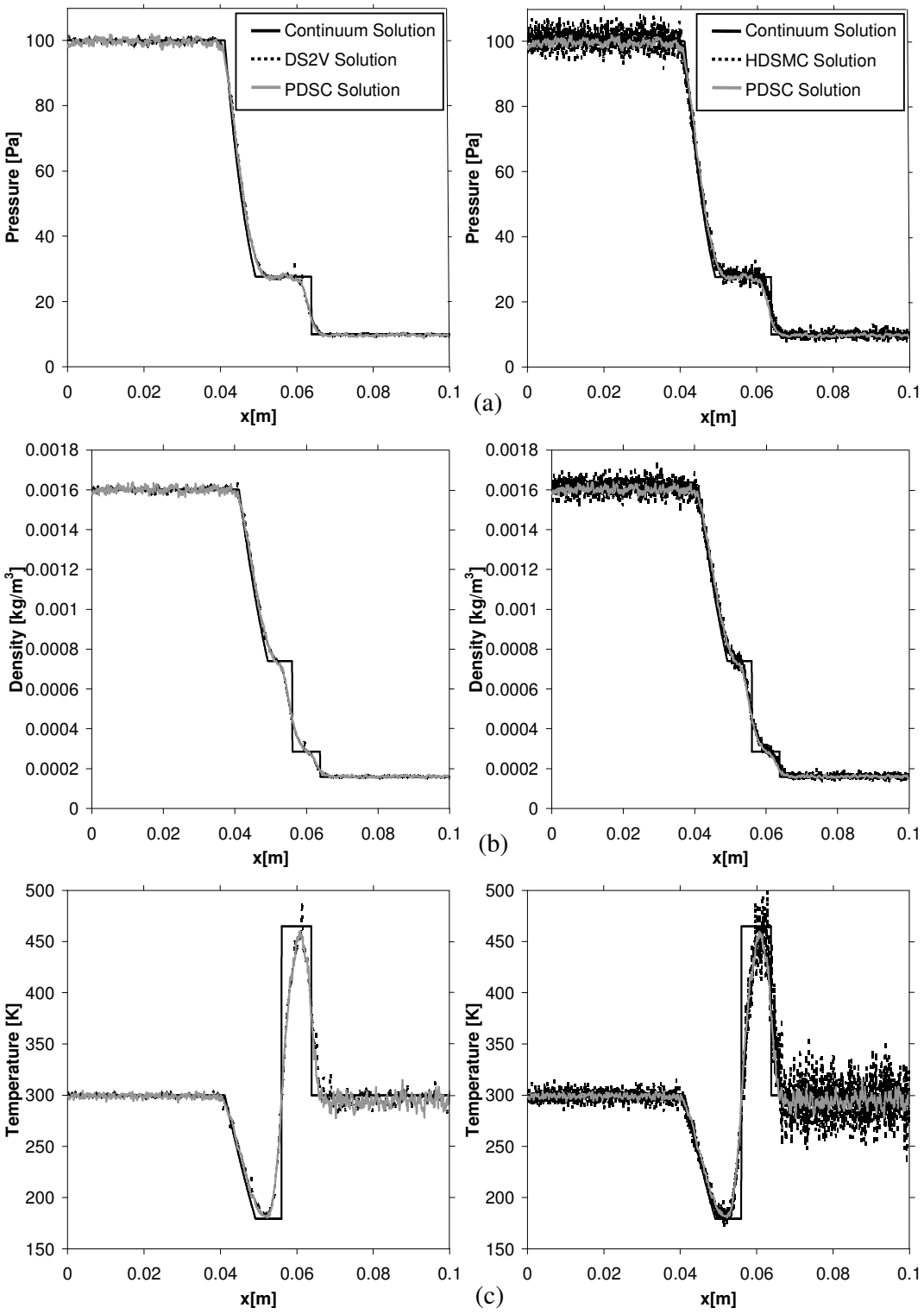

Figure 6.5. Shock tube flow field profiles of a) pressure, b) density and c) temperature at 27.45μs generated using PDSC (both sides), DS2V (left) and HDSMC (right).

From equation (6-1) the velocity of the incident shock is 500.8 m/s, hence at 99.8μs, the normal shock reaches the end of the shock tube and reflects from it. Figure 6.6 shows the evolution of the shock tube density profile both before and after the incident shock impinges on the end of the tube. Note that the high computational expense for HDSMC prevented results being obtained for this figure. Both methods predict equivalent flow profiles, with equivalent amounts of statistical scatter. At 27.5μs and 76.9μs, the incident shock can be seen advancing toward the right hand end of the shock tube. After the shock has been reflected from the wall there is a sharp rise in density as the reflected shock begins to travel to the left. This reflected shock interacts with the advancing contact surface, creating the peak in density visible at 175.7μs. At the left hand end of the tube, the expansion fan also reflects from the solid wall, creating the reduction in density visible at 175.7μs.

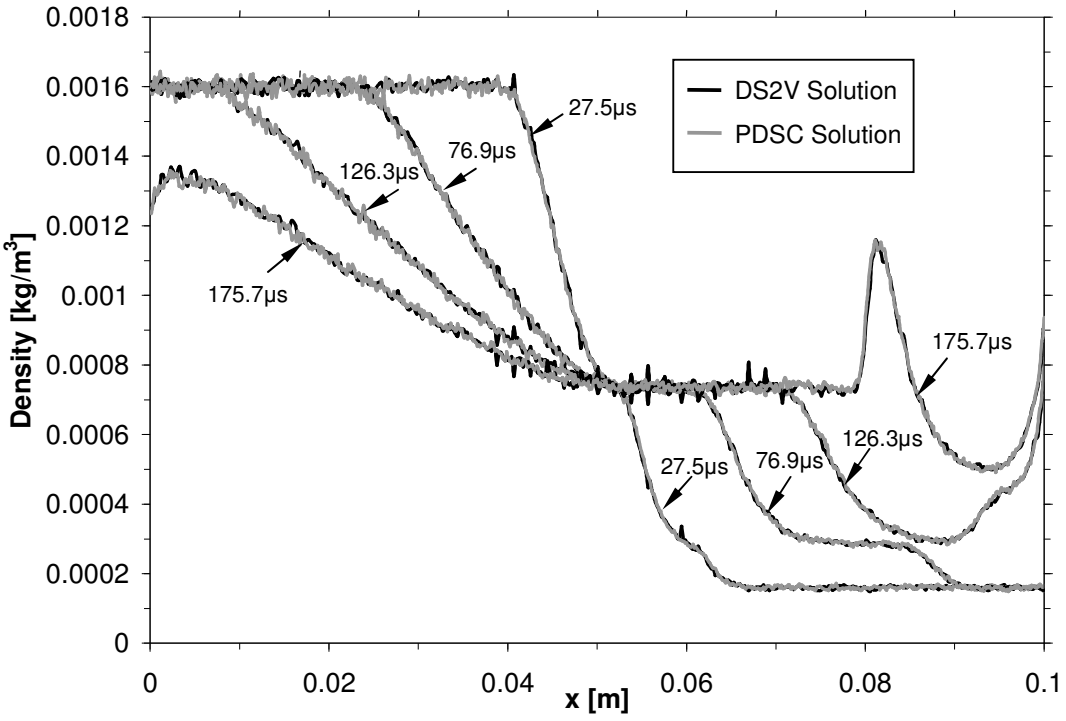

Figure 6.6. Evolution of flow structure in the shock tube as predicted by PDSC and DS2V

From equation (6-8) the reflected shock speed, W_R, is 241.4 m/s. Figure 6.7 also shows profiles of pressure, density and temperature as predicted by DS2V and PDSC at 219.6μs, along with the expected position of the reflected shock for the continuum, inviscid solution. The difference in the results predicted by DSMC and the continuum solution can again be accounted for by viscous effects.

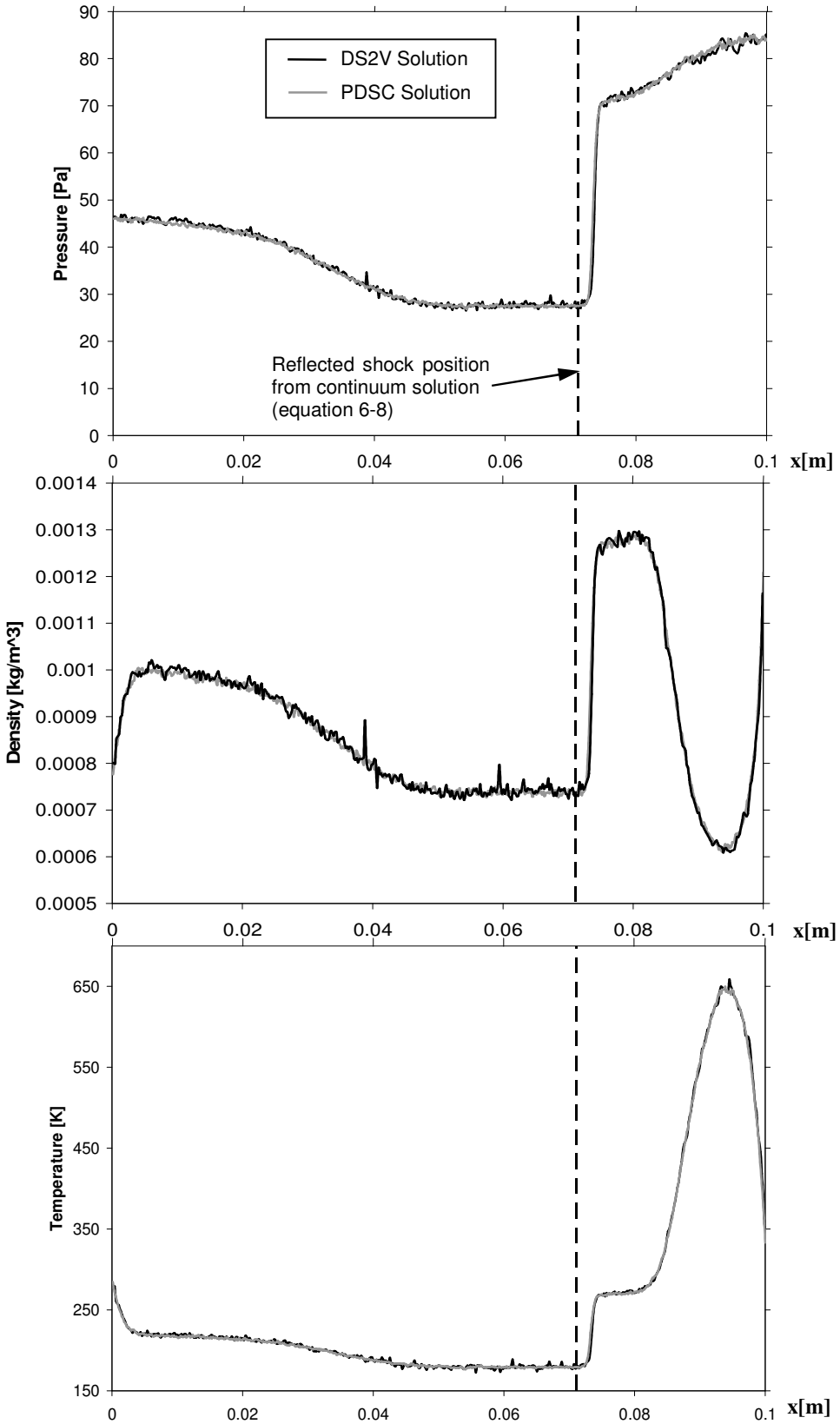

Figure 6.7. Profiles of a) pressure, b) density and c) temperature for shock tube flow as predicted by DS2V and PDSC at 219.6μs

In the above results, each of the methods captures the expected flow structure. The PDSC solution shows slightly reduced statistical scatter in the results compared to DS2V and considerably reduced scatter over HDSMC. Additionally, parallelisation means PDSC runs approximately ten times faster than DS2V. The utilisation of TVTS, which was not employed here, would result in further increases in the speed of PDSC. These results confirm that the unsteady sampling routines used in PDSC have been implemented correctly since the results compare well with the continuum solution and are almost identical with the results obtained from the established DS2V code. Additionally it can be concluded from table 6.1 that the computation time for the PDSC method is superior to the other two methods (the disadvantages of ensemble averaging are readily apparent from this table). This will allow simulations of higher accuracy and/or greater flow density to be carried out relatively readily.

The sensitivity of the PDSC solution to the number of particles simulated and the cell size was also investigated. Figure 6.8 shows the temperature profile at 27.45μs (which is statistically the most sensitive measurement) for a range of average number of particles per cell. It can be seen from these results that the flow profile is insensitive to the number of simulated particles however, as would be expected, the statistical uncertainty increases as the number of particle is reduced, in particular in the driven gas where the number of particle per collision cells is below the average. Since the computational expense of the simulations is proportional to the number of simulated particles, it is necessary to minimise the number of particles while maintaining a sufficient number to preserve statistical accuracy. From figure 6.8 it can be concluded that approximately 25 particles per sampling cell should be maintained for accurate PDSC simulations.

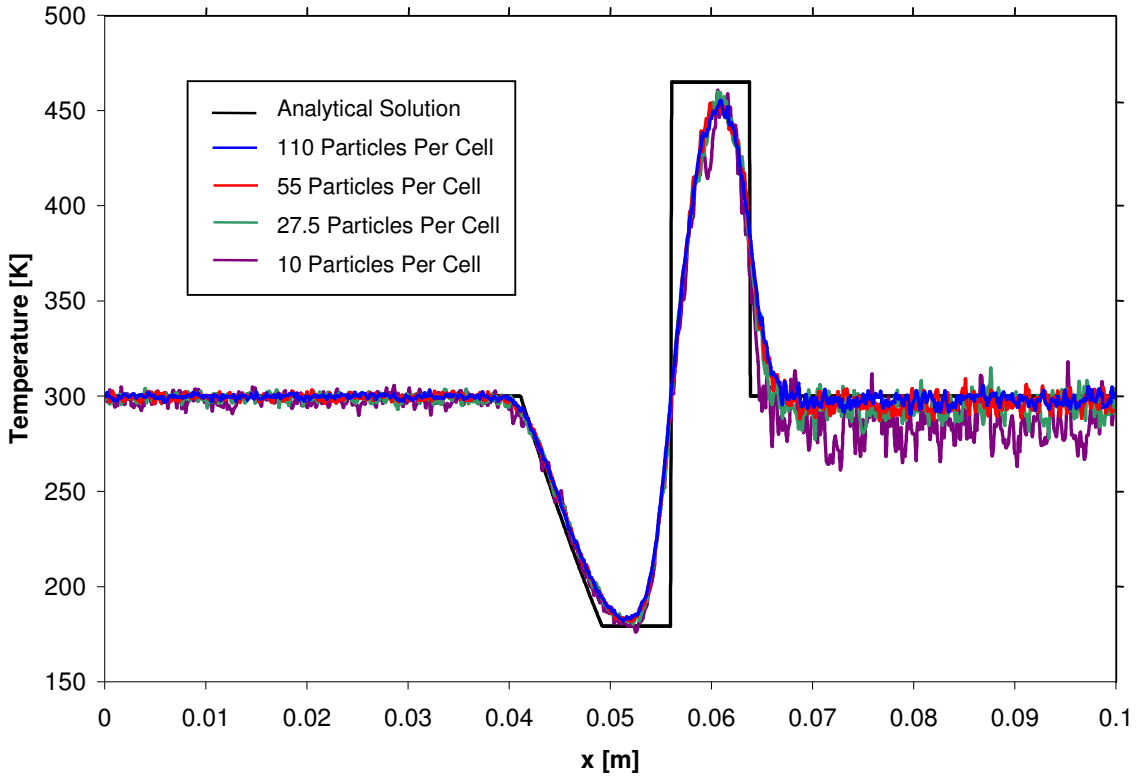

Figure 6.8. Temperature profile at 27.45μs illustrating the sensitivity of the solution to the average number of particle per collision cell.

Figure 6.9 shows the temperature profile at 27.45μs for a range of total number of sampling cells. Here an average of 27.5 particles per sampling cell was used to set the total number of sampling cells. The ratio of the cell size to the initial mean free path in the driving section of the tube, *R*, is also given. It can be seen that the cell size has a strong influence on the statistical scatter in the results, especially in the regions where the number of simulated particles is low. In this simulation accurate results can be maintained for quite a large cell size compared to the mean free path since the scale length macroscopic flow gradients are relatively large, however Bird has shown that in flows with large flow gradients the cell size should be kept to approximately one-third of the local mean free path [15]. This may become at issue within the jet in PP-CVD where the flow gradients can be large, hence some care will be required when setting up the grid for PP-CVD flow simulations

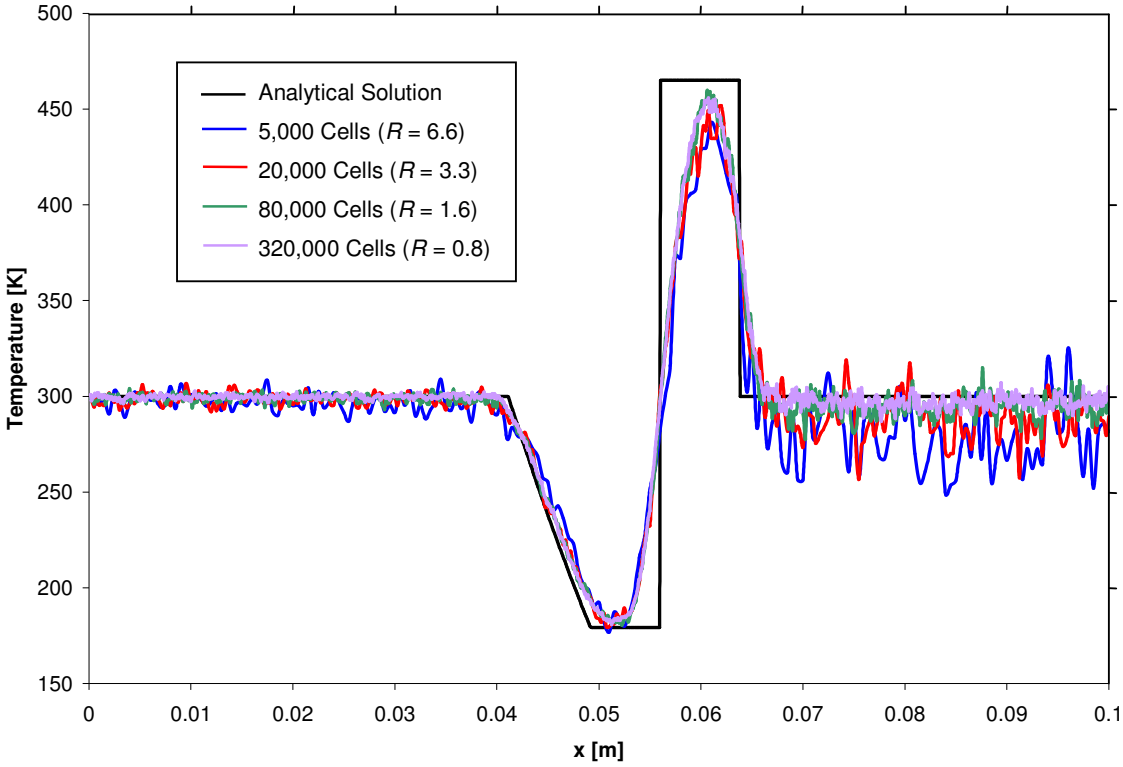

Figure 6.9. Temperature profile at 27.45μs illustrating the sensitivity of the solution to the collision cell size.

As mentioned in section 6.3.1, one potential disadvantage of time averaging is that the flow structures will be "smeared" as the flow field develops over the sampling interval. For this reason, the sampling interval must be kept as short as possible to ensure smearing is minimised. To investigate the effect of smearing, the shock thickness was measured for Mach 4 and 8 moving shocks. Here a propagating one-dimensional shock was set up in PDSC from equations (6-1) to (6-4), with the initial conditions being a Maxwell-Boltzmann distribution on both sides of the shock. The shock was allowed to propagate downstream for 30λ for the Mach 4 case and 50λ for the Mach 8 case, to allow the true particle velocity distribution and shock structure to establish before the thickness was measured. Figure 6.10 shows a comparison of the shock thickness δ measured using the current method with the experimental results and other data from the paper by Schmidt [16]. The results are normalized with the mean free path upstream of the shock wave (λ/δ). These results show the shock thicknesses obtained by unsteady sampling in PDSC are consistent with Schmidt's results. As long as the sampling period is constrained so that the majority of particles cannot migrate beyond the

sampling cell during this time, smearing is minimised and accurate shock structures are maintained.

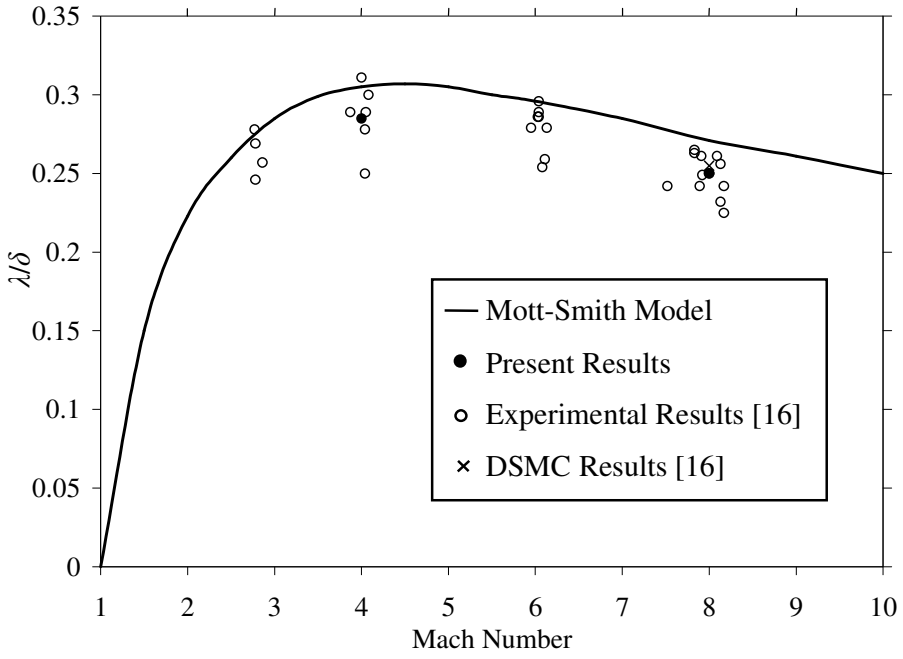

Figure 6.10. Normalized shock thickness predicted by PDSC compared to the data from reference [16].

The results of the shock tube validation study confirm that the unsteady sampling procedures have been implemented correctly in PDSC. The results produced by PDSC are very similar to those produced by the established DS2V code and compare well with the continuum solution. PDSC also predicts accurate shock thickness results. Furthermore, the time-averaging sampling method gives comparable results to the ensemble-averaging method and PDSC using ten processors is approximately ten times faster than the single-processor DS2V code.

6.4. Implementation of Transient Sub-Cells and Improved Collision Routines

6.4.1 Method

As mentioned in section 3.6.1, in order for the DSMC routine to be accurate, particles selected for collision must be close enough together for the collision to be realistic. As a consequence the sampling grid to which particles are indexed must contain cells with dimensions which are approximately $^1/_3 \sim 1$ times the local mean-free-path. This means that increasing flow field density results in an increase in the computational expense and memory

requirements because the simulations require a greater number of sampling cells and more simulated particles to ensure an adequate statistical sample within these cells. This is a particular problem for simulating processes like Pulsed Pressure Chemical Vapour Deposition (PP-CVD) which have regions of relatively high density and large gradients in macroscopic properties [17]. A potential method of overcoming this problem, whilst maintaining good collision quality, is to divide the sampling cells into sub-cells for the selection of collision partners. This means that the distance between collision partners is maintained at the dimensions of the sub-cells, whilst the resolution of the macroscopic sampling is at the dimensions of the sampling cells. Bird has also pointed out that sub-cells help maintain flow vorticity within the cells [15].

The implementation of sub-cells in DSMC allows the maintenance of good collision quality within the simulation, even for grids which are "under-resolved" (that is, if the sampling cells are bigger than the recommended setting of $^1/_3 \sim 1$ times the local mean free path). Running simulations with under-resolved sampling cells which employ sub-cells results in a reduction in the computational and memory requirements of the simulation, albeit at the cost of a reduction in the possible sampling resolution of the macroscopic properties, but without sacrificing simulation accuracy.

The methods used to for the implementation of sub-cells within the literature vary somewhat. Older versions of Bird's code [15] and Ivanov's SMILE code [18] employ a fixed number of sub-cells per sampling cell, however the latest version of DS2V code generates a transient grid to each cell at a time during the collision routine such that there is approximately one particle per sub-cell [19]. The use of virtual sub-cells, whereby the distances between the particle selected for collision and all other particles in the cell are simply calculated and the nearest particle chosen, was introduced in NASA's DAC code [20] and has since been included in DS2V.

Although the use of sub-cells in PDSC has been discussed in the past, sub-cells have not been implemented for a number of reasons, primarily because the division of unstructured sampling cells into unstructured sub-cells was considered complicated and likely to be computationally expensive. However, it was anticipated that accurately simulating PP-CVD, particularly around the jet inlet, would require very small sampling cells and hence

considerable computer memory overhead. For this reason, a computationally efficient form of implementing quadrilateral sub-cells on unstructured grids was designed and implemented.

In this scheme, the sampling cells are divided into sub-cells during the collision routine. Because the sub-cells only exist in one sampling cell at a time, and only during the collision routine, they can be considered "transient sub-cells" which will have negligible computer memory overhead. In every case, including when the sampling cells are unstructured these sub-cells are quadrilateral which reduces the complexity of sub-dividing the sampling cell and greatly facilitates particle indexing. The size of the sub-cells is indirectly controlled by the user, who inputs the desired number of particles per sub-cell, P. The program then determines the dimensions of the sub-cell array based on the number of particles with the cell, N_{parts}, as shown in table 6.2.

Table 6.2. Number of sub-cells in each sampling cell in PDSC sub-cells routine

	Structured	**Unstructured**
2D	$\sqrt{N_{parts}/P} \times \sqrt{N_{parts}/P}$	$\sqrt{N_{parts}/P} \times \sqrt{N_{parts}/P}$
3D	$\sqrt[3]{N_{parts}/P} \times \sqrt[3]{N_{parts}/P} \times \sqrt[3]{N_{parts}/P}$	$\sqrt[3]{N_{parts}/P} \times \sqrt[3]{N_{parts}/P} \times \sqrt[3]{N_{parts}/P}$

Note that in both cases $\sqrt{N_{parts}/P}$ and $\sqrt[3]{N_{parts}/P}$ are rounded down to the nearest whole number.

Figure 6.11 shows the way in which both structured and unstructured sampling cells are divided into sub-cells. As can be seen, in the unstructured case, there may be sub-cells which are entirely outside the boundary of the sampling cell, however this has no affect on the collision routine. In both cases, the concept is easily extended to three-dimensional sampling cells.

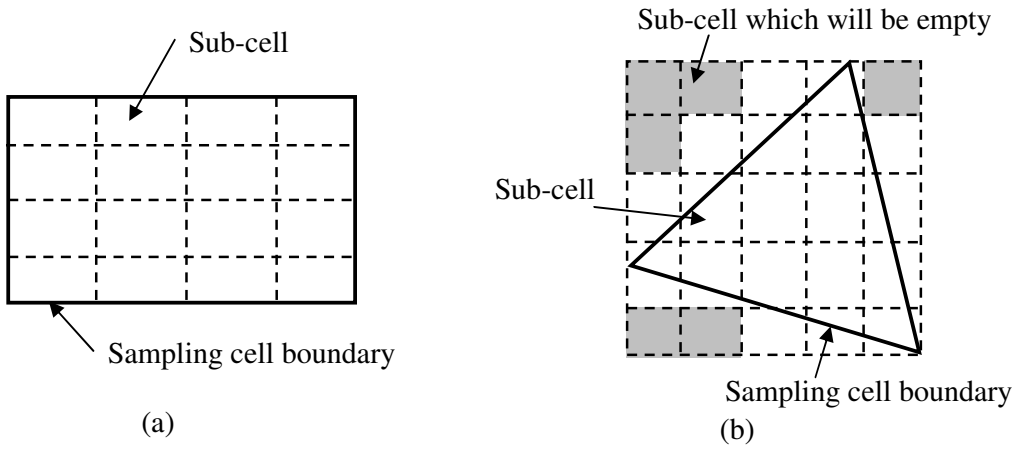

Figure 6.11. Division of a) structured and b) unstructured elements into sub-cells

During the collision routine, a particle is chosen at random from some point within the whole sampling cell. The sub-cell in which the particle lies is then determined and if another particle is in the same sub-cell then these particles are chosen for collision. If the first particle is alone within the sub-cell, then adjacent sub-cells are scanned for a collision partner. These sub-cell routines ensure nearest neighbour collisions, even within under-resolved sampling cells, with minimal computational and memory overhead.

Bird has also shown that preventing particles from colliding again their last collision partner, reduces the error in some variables such as heat transfer and shear stress by up to 5% [19]. The basis of this is that collisions between particles which just collided with each other is physically impossible, since the particle must be moving away from each other after the first collision. A minor modification was made to PDSC to prevent particles colliding with their last collision partner. This involved the creation of an array in which the last collision partner for every particle is stored and if the two particles are subsequently chosen for collision without having collided with any other particle, the collision is rejected.

Recently the virtual sub-cells concept discussed in section 3.6.2 has been implemented in PDSC. Virtual sub-cells are employed when the number of particles in a cell is relatively low; however the recent implementation of the concept in PDSC means that testing the procedure is beyond the scope of this thesis. All simulations in this thesis use transient adaptive sub-cells only.

6.4.2 Model Validation

6.4.2.1 Driven Cavity Flow

The first method used to further the use of transient sub-cells in PDSC was the simulation of steady driven cavity flow. This type of flow is frequently used as a benchmark test for CFD codes, however there have been few simulations focusing on driven cavity flows in the rarefied regime which are likely to become increasingly important in Micro-Electro-Mechanical (MEMS) systems. DSMC represents a possible method of simulating such devices [21], especially in the super-sonic regime, and the use of sub-cells to enforce nearest neighbour collisions will enhance these simulations. A complete account of this testing is given in the thesis by Hsien [22] and so will only be summarised briefly here.

Figure 6.12 shows the computational domain used in the study. The cavity is square (dimensions H x H) and bounded on all sides by diffuse walls at 300K. The upper wall is allowed to move at a Mach number of M (velocity u_p).

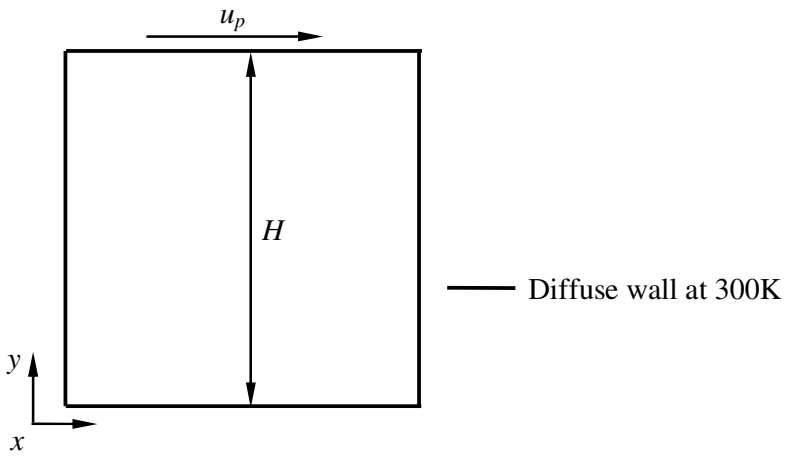

Figure 6.12. Computational domain for the steady driven cavity flow verification case.

In the thesis by Hsien [22], the upper wall is allowed to move at a Mach 1.1 – 1.4 and the Knudsen number of the flow is varied from 0.0033 to 10. The thesis presents a detailed investigation of the effect of Mach number and rarefaction on the driven cavity flow field. However, here only a benchmark study demonstrating the computational and memory reduction achieved through the use of transient sub-cells will be outlined.

In the benchmark test, M = 0.5 and Kn = 0.01. The test was conducted using subsonic conditions, because sub-sonic flows place a greater demand on DSMC in terms of statistical

uncertainties and therefore represent a more rigorous test. Two grids were used in the test. The first was a finer 400 x 400 grid with 25 particles per cell (4 million particles total), which satisfies the requirements for an accurate DSMC calculation without sub-cells in terms of sampling cell size and number of particles per cell. The second grid was chosen not to satisfy these requirements, this being a coarser 100 x 100 grid with 100 particles per cell (1 million particles total).

Figure 6.13 shows the profiles of the components of velocity, number density and temperature through the vertical centre-line of the cavity (x/H = 0.5). The profiles for both grids are shown to be consistent with each other within the expected statistical uncertainties of the results, with the coarser grid exhibiting less statistical scatter due to the greater number of particles per cell.

Figure 6.14 shows the merit of collision (*mcs/mfp*) ratio discussed in section 3.6.2 as a measure of the quality of the simulation for the two benchmark grids.

Figures 6.13 and 6.14 demonstrate the usefulness of sub-cells in a DSMC calculation. Figure 6.13 shows that the correct macroscopic properties are obtained while figure 6.14 shows that the collision quality, and thus the accuracy of the simulation, is superior to a simulation without sub-cells. The most remarkable thing about this result, is that the superior results obtaining using sub-cells were achieved using $1/16^{th}$ of the number of sampling cells and ¼ of the number of particles. The increase in computation cost in using sub-cells compared to the same grid and number of particles without sub-cells is approximately 15%. Thus the above result was achieved using a computational cost reduction of approximately three times.

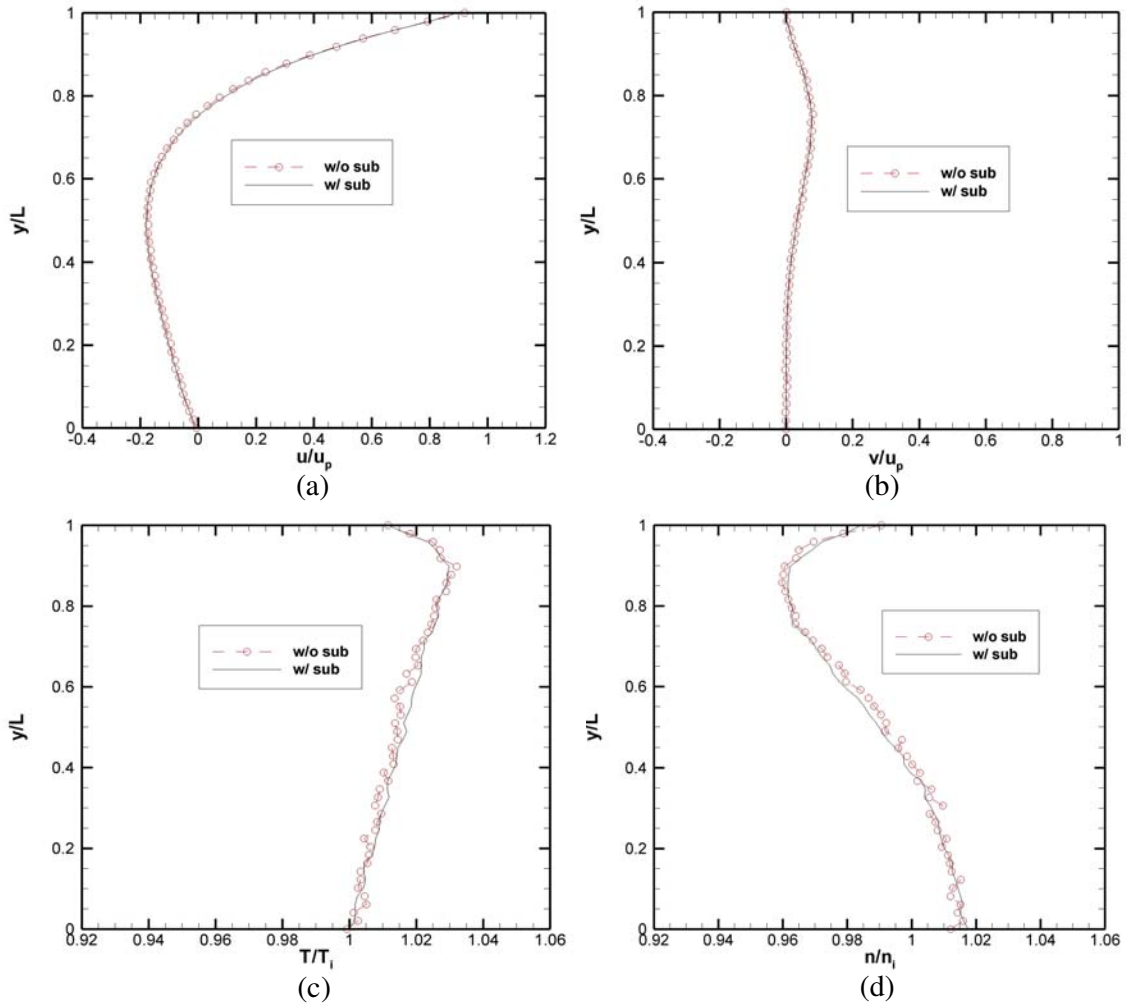

Figure 6.13. Profiles of properties along the vertical centre-line ($x/H = 0.5$) for steady driven cavity flow: a) x-velocity, b) y-velocity c) temperature and d) number density (figure reproduced with permission from thesis by Hsien [22]).

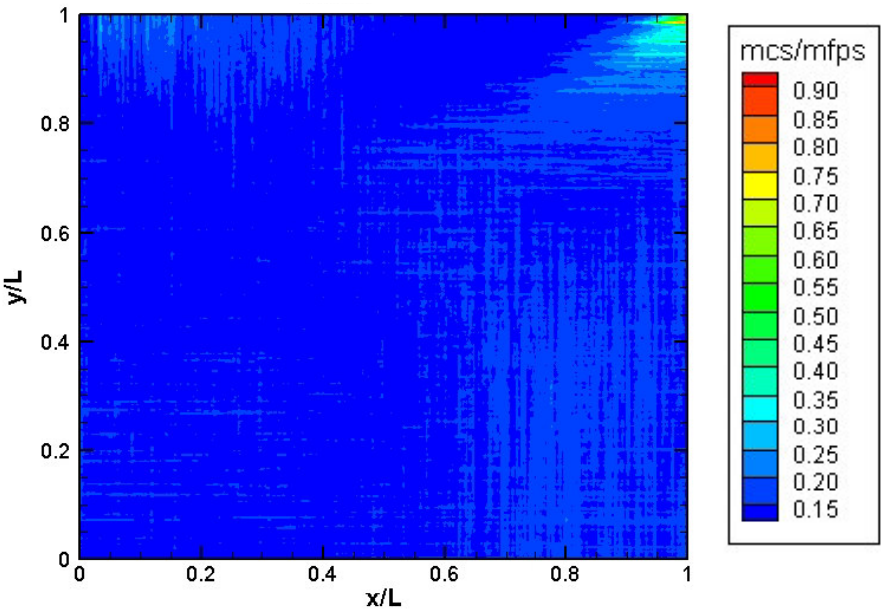

(a)

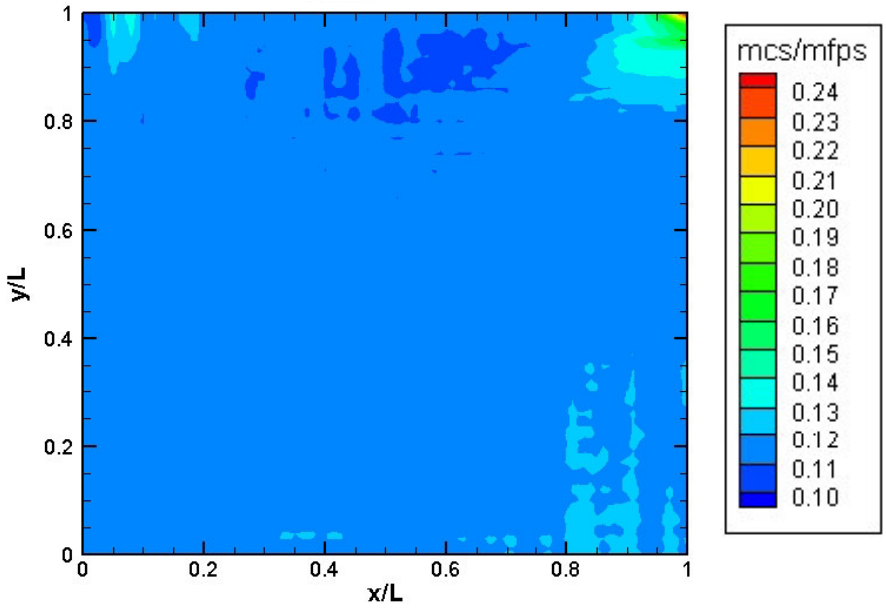

(b)

Figure 6.14. Merit of collision (*mcs/mfp* ratio) for driven cavity flow (Kn=0.01, M=0.5) for a) fine grid without sub-cells and b) coarse grid with sub-cells.

The results of this test indicate that the transient sub-cells can simultaneously increase the accuracy of a simulation and decrease the statistical scatter in the results while reducing the overall computational time of the simulations. Furthermore, this can be achieved on grids which are under-resolved in that the sampling cells are larger than the local mean free path.

6.4.2.2 Benchmark Test – Steady Hypersonic Flow over a Cylinder

A benchmark test for DSMC code recently adopted by Bird [23,24] is the Mach 10 hypersonic flow of argon at 200K over a 12 inch (0.3048m) circular cylinder with a thermally diffuse surface at 500K and a nominal free stream Knudsen number of 0.01 (actually the true value derived from VHS mean free path calculations is 0.0091). This case was first used by Lofthouse *et al.* [25] as a comparison between a Navier-Stokes solver and the MONACO DSMC code.

Bird has compared the results for the cylinder drag and peak surface heat transfer for his own single processor DS2V code and a number of other DSMC codes including Boyd's MONACO, Ivanov's SMILE, NASA's DAC and his own obsolete DS2G code. Using the results, he demonstrates that the use of sophisticated DSMC procedures such as nearest neighbour collisions, cell adaptation and variable time steps, can produce accurate engineering results with a fraction of the computational time of DSMC codes not employing these procedures. Furthermore, Bird points out that generally the computational costs of DSMC are severely overstated, primarily because the proponents of other solvers compare their results to DSMC code which does not employ sophisticated procedures. Indeed, Bird notes that his own DS2V code can reproduce equivalent results to the CFD code used in the study by Lofthouse *et al.* using 56% of the computational time [24]! The results from the DSMC solvers benchmarked by Bird are shown in table 6.3. It should be noted that DS2V uses 2º surface sampling intervals which are separate from the sampling cell grid at the surface. The effect of these will be further discussed below.

Table 6.3. Comparative results for the benchmark test of hypersonic flow over a 2D circular cylinder for various DSMC codes

Code	**Simulated Particles**	**Total Cells**	**Computation Time [hrs]**	**Drag [N]**	**Peak Heat Transfer [W/m^2]**
MONACO	26.8 million	34,770	1872*	40.00	39,319
DS2G	2.9 million	129,600 (sub-cells)	20 (3 GHz)	39.95	38,300
SMILE	24 million	4 million (collision cells)	--	39.76	39,000
DAC	1.3 million	--	15 (3GHz)	39.71	38,500
DS2V	330,000	41,000 (collision cells)	10 (3 Ghz)	39.76	38,400

*Simulated on a parallel system. This figure is the number of CPU hours

In order to benchmark PDSC against the other contemporary DSMC codes, PDSC was used to simulate the case. The geometry used in the simulation is shown in figure 6.15. The simulation conditions are the same as stated above and ten 1.73 GHz processors were used. A number of cases were run with varying numbers of particles, sampling times and structured sampling cells to assess the effect of these parameters on the results.

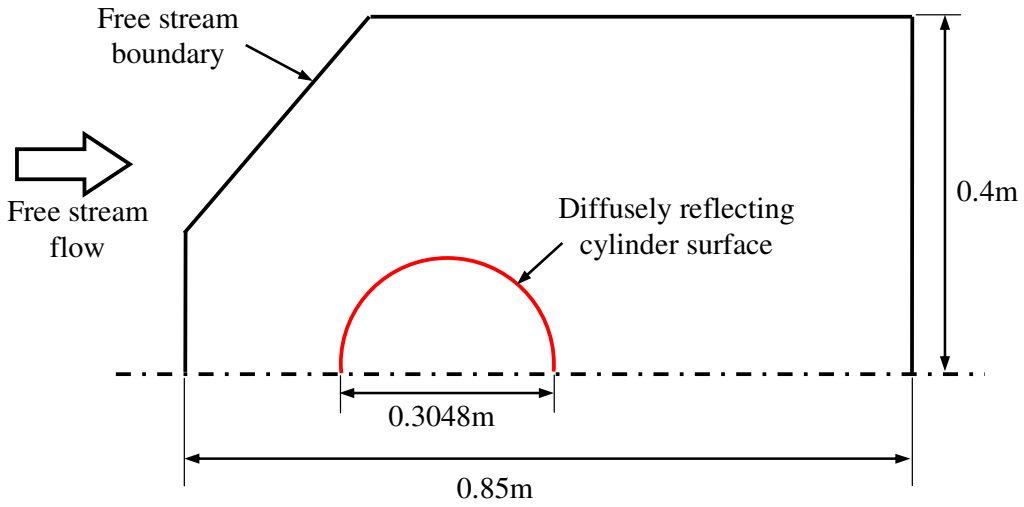

Figure 6.15. Geometry used in simulation of hypersonic flow over a 2D cylinder (not to scale. Note that only primary dimensions are shown for clarity)

Tables 6.4 and 6.5 summarise the results achieved using the various PDSC test cases. In every case, a spatial variable time step scheme was used with the transient stage (prior to sampling) of approximately 8,000 time steps. The quoted time includes both the transient and sampling stages. It should also be noted that only every second time step was sampled (e.g. a sampling period of 7,000 time steps indicates that there were 3,500 time steps included in the sample).

Table 6.4. Results using PDSC for the benchmark test of hypersonic flow over a 2D cylinder (5,082,964 simulated particles)

Sampling Period [Time Steps]	**Total Drag [N]**	**Peak Heat Flux [W/m^2]**	**Max Surface Sample Size***	**Simulation Time [s]†**
1,000	38.84	40,009	183,709	15,011
2,500	38.83	39,593	452,767	17,513
4,000	38.82	39,379	723,152	20,014
7,000	38.81	39,164	1,264,151	25,018

*The maximum sample size is calculated over a 2º surface interval, thus allowing a direct comparison with the results carried out by Bird.

†Quoted simulation time is the total real time on ten 1.73 GHz CPUs, not the number of CPU seconds.

Table 6.5. Results using PDSC for the benchmark test of hypersonic flow over a 2D cylinder (509,401 simulated particles)

Sampling Period [Time Steps]	Total Drag [N]	Peak Heat Flux [W/m^2]	Max Surface Sample Size*	Simulation Time [s]†
1,000	39.33	41,793	18,366	808
2,500	39.34	40,354	45,319	942
4,000	39.33	40,669	72,374	1,077
7,000	39.32	40,270	126,394	1,346

*The maximum sample size is calculated over a 2º surface interval, thus allowing a direct comparison with the results carried out by Bird

†Quoted simulation time is the total real time on ten 1.73 GHz CPUs, not the number of CPU seconds.

From the above tables it can be seen that the peak heat flux decreases with increasing sampling period and number of particles. Additionally, the total drag decreases with number of simulated particles. None of the results in tables 6.3, 6.4 or 6.5 can be regarded as the definitive solution, since there is no equivalent experimental data with which to compare the results. Additionally, it is difficult to make direct comparisons between the PDSC results and the results from other DSMC codes since little is known about the sampling procedures in these codes. However, it is reasonable to expect that the simulations employing a greater number of simulated particles with a greater total sample (i.e. increased sampling period) would give more accurate results.

The maximum sample sized used in Bird's study is approximately 44,000 particles over a 2º sampling interval [26]. This means the most appropriate comparison with Bird's result in table 6.3 is the PDSC result utilising 509,401 particles and a 2,500 time step sampling period. The computational time for this result is 942s (0.26hrs) which compares favourably with Bird's result (considering the difference in number of processors and processor speed).

The merit of collision (*mcs/mfp* ratio) was also maintained at below unity for most regions of the flow (including the rarefied wake region behind the cylinder); however there were some cells near the stagnation point which were under-resolved due to the high flow density in this region. These resulted in a merit of collision of slightly above one, however future simulations are planned which utilise adaptive mesh refinement which will overcome this problem.

As mentioned previously, Bird's DS2V code utilises 2º sampling intervals which a separate from the surface grid, unlike PDSC which uses the surface grid to obtain surface data. DS2V

effectively smoothes the data over a number of surface sampling cells which has the positive effect of reducing the statistical scatter in the surface results. However, the negative effect of this procedure is to reduce the peak heat flux, which would normally occur at the stagnation point, by averaging the heat flux over a relatively large area, a point which Bird conceded in reference [24].

To illustrate the effect of this smoothing process, the PDSC data for the 509,401 particles and a 2,500 time step sampling period case was post-processed across 2º surface intervals. Figures 6.16 and 6.17 show the raw and post-processed data respectively for the surface heat flux. The result was a reduction in the peak heat flux from 40,354 W/m^2 in the original data to 38,871 W/m^2, which compares closely to Bird's value of 38,400 W/m^2.

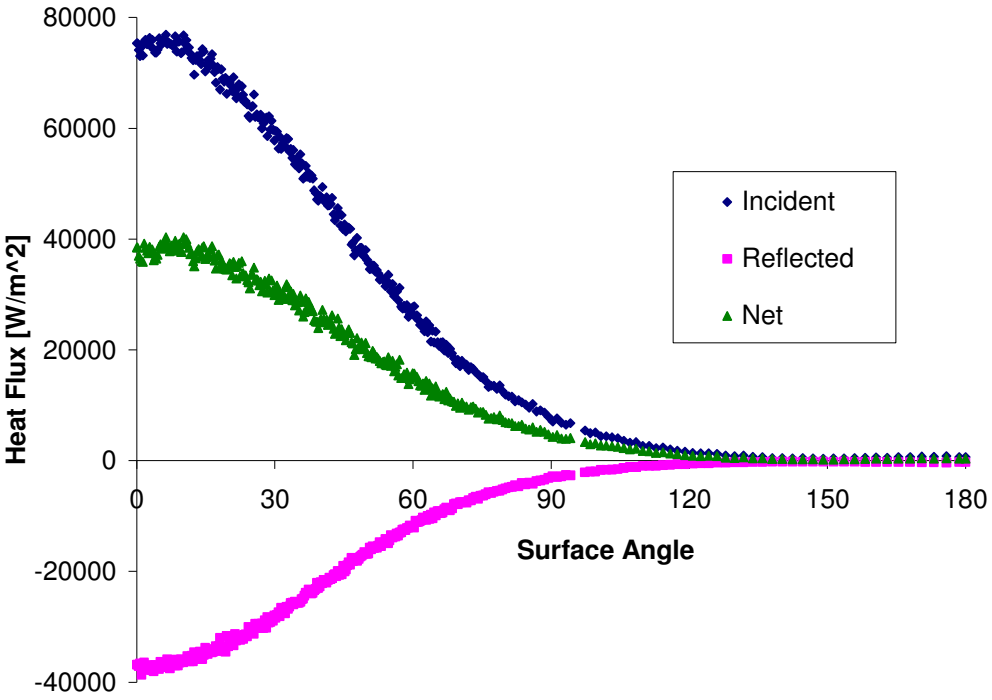

Figure 6.16. Raw heat flux components for hypersonic flow over a circular cylinder predicted by PDSC.

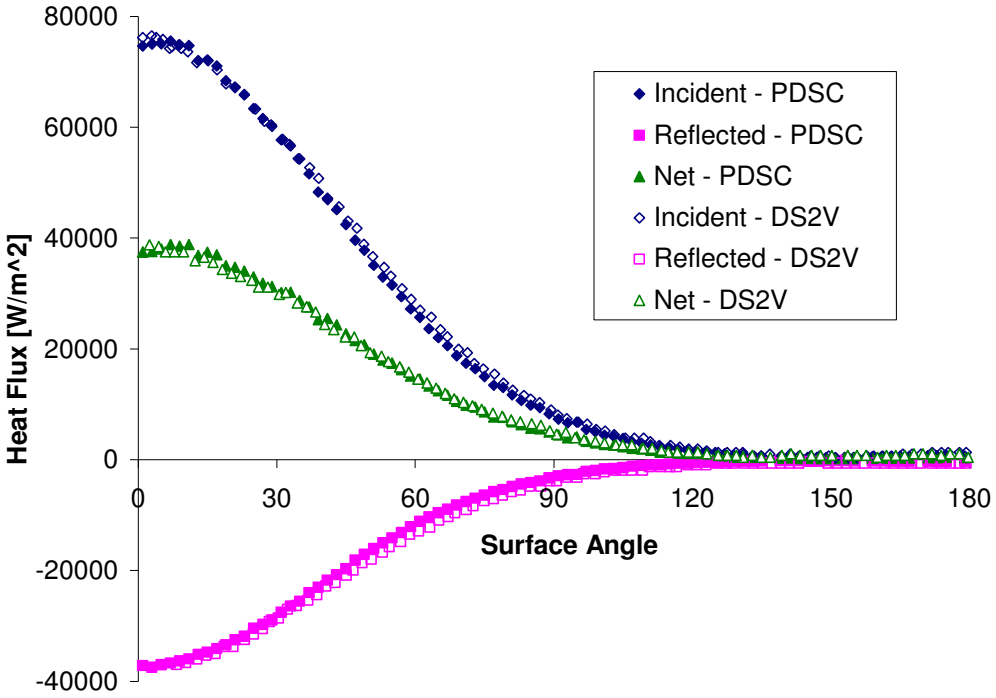

Figure 6.17. Heat flux components for hypersonic flow over a circular cylinder smoothed over 2º surface intervals as predicted by PDSC and DS2V.

Overall, PDSC compares favourably with other DSMC codes in terms of computational time and accuracy. PDSC was able to produce similar results with a similar magnitude of statistical scatter and similar computational times as Bird's DS2V code. More details of this study can be found in the manuscript by Tseng *et al.* [27].

6.5 The DSMC Rapid Ensemble Averaging Method (DREAM) Post-Processor

6.5.1 Method

Despite the efficient implementation of unsteady sampling procedures on parallel computers, simulating denser flows in reasonable computational times requires a compromise on the statistical scatter in the results. This is because reducing the statistical scatter significantly in time-averaged data necessitates a very large number of simulation particles with consequent large computational times. Other researchers have attempted to use data smoothing to prepare their results for presentation [28], however ultimately this removes data which may have physical significance.

In order to overcome this problem, a technique was developed whereby the data at a particular point in the flow was improved by re-running the PDSC algorithm over a small period immediately prior to that sampling point. The technique, called the DSMC Rapid Ensemble Averaging Method (DREAM), is outlined in figure 6.18.

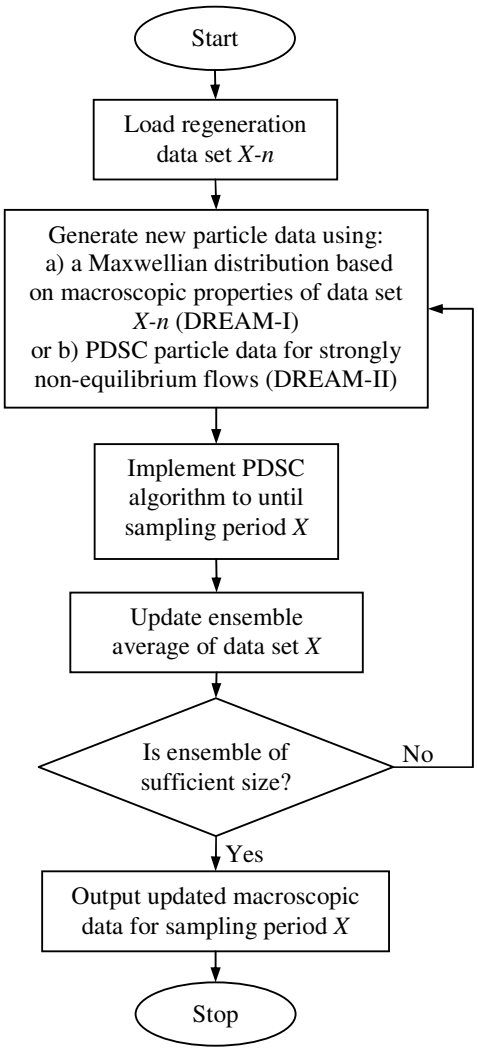

Figure 6.18. Simplified flow chart of the post-processing technique for unsteady DSMC sampling, called the DSMC Rapid Ensemble Averaging Method (DREAM).

Here we select a raw data set *X-n* produced by PDSC *n* sampling intervals prior to the sampling interval of interest *X*. For near-continuum flow (for example, shocks of less than approximately Mach 2) new particle data is generated from the macroscopic properties in data set *X-n* by assuming a Maxwellian distribution of velocities based on the three components of temperature T_x, T_y and T_z (this version of the code is called DREAM-I). The DREAM-I method has the advantage of easier implementation and requires no additional input/output

during the initial PDSC run, however for strongly non-equilibrium flows it may be unable to recover the correct particle velocity distribution at the sampling point. Thus, for strongly non equilibrium flows (i.e. higher Mach number shocks), the particle data is regenerated from the instantaneous particle data which can be outputted by PDSC in the original run, thus preserving the true phase-space data (DREAM-II). The standard PDSC algorithm is then used to simulate forward in time until the sampling period of interest X is reached. The time steps close to the sampling point are time-averaged in the same way as in PDSC and this process is repeated a number of times, thus building up a combination of ensemble- and time-averaged data without having to simulate from zero flow time for each run. This process decreases the statistical scatter in the results by adding to the number of particles in the sample, rather than by some artificial smoothing process. Because only a short period of the flow is processed in this way, the scheme has significant memory and computational advantages over ensemble-averaging and results in a greater number of sampling particles than the time-averaging scheme.

For DREAM to be accurate there must be a suitably large number of time steps between the particle regeneration and the sampling data sets so that 1) the velocity distribution can "relax" sufficiently quickly towards the true distribution in any non-Maxwellian regions and 2) so that the macroscopic properties at the regeneration data set will not overly constrain the data at the sampling time step (i.e. to ensure that particles can move out of their original cells before being re-sampled).

For stronger non-equilibrium flows, DREAM-II reloads the original PDSC phase-space data. This allows the particle data to be regenerated using the true velocity distribution in non-equilibrium regions. However DREAM-II does have a disadvantage in terms of storing the output particle data sets during the original PDSC run. Fortunately, due to the low cost of hard-drive storage, the process is not overly expensive even though particle data must be outputted from PDSC during every sampling period if the regions for post-processing by DREAM are not known *a priori*.

6.5.2. DREAM Validation and Operating Parameters

To test the DREAM-I scheme for improving the statistical scatter in the results, it was necessary investigate the validity of assuming a Maxwellian velocity distribution at every point in the flow when regenerating the particle data n sampling intervals prior to the output

time for near-equilibrium (i.e. low shock Mach number) flows. To do this, the particle velocity distribution in the shock structure of the DREAM-processed data was compared to that in the raw data generated by PDSC.

Figure 6.19 shows the velocity distributions in the normal shock region at 76.9μs for the shock tube case given above. Both the distributions from the raw PDSC data and from those processed by DREAM-I are given, along with the curve for a Maxwellian distribution at the same temperature. Particle velocity v has been normalized by the macroscopic temperature T and macroscopic velocity v_m as $(v\text{-}v_m)(m/2kT)^{1/2}$. The parameter $N\Delta tW/\lambda_2$ represents the number of mean-free-paths which an average particle will traverse in the N time steps of length Δt between regeneration and sampling, where W is the shock propagation velocity and λ_2 is the equilibrium mean free path immediately upstream of the shock.

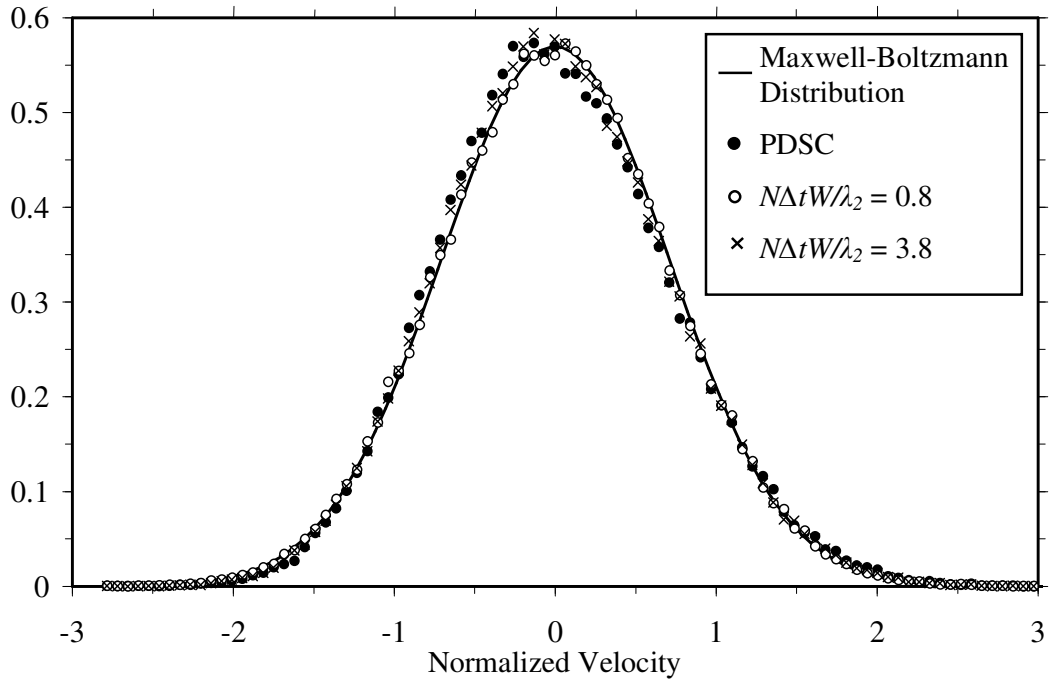

Figure 6.19. Particle velocity distributions in the normal shock structure as produced by PDSC and DREAM with different values of $N\Delta tW/\lambda_2$.

The peak in the velocity distribution in the PDSC raw data is shifted to the left of the Maxwellian distribution, indicating the shock is sufficiently strong to be non-equilibrium. For the assumption of an initial Maxwellian distribution in DREAM-I to be valid, DREAM-I must reproduce the same particle velocity distribution profile as unsteady PDSC, rather than a

Maxwellian distribution, thus indicating that the flow has relaxed towards an accurate distribution. When the particles have traveled less than one mean free path been regeneration and sampling, the distribution remains close to the Maxwellian. However, after approximately four mean free paths ($N\Delta tW/\lambda_2$=3.8), the particles have relaxed towards a similar distribution to that obtained by unsteady PDSC. This indicates that the assumption of a Maxwell-Boltzmann distribution in the regeneration step of DREAM-I is reasonably valid for Mach number flows below approximately Mach 2, providing the particles in the non-equilibrium regions are allowed to travel approximately four mean free paths between the regeneration and sampling time steps.

Figure 6.20 shows the temperature profile in the shock tube at 76.9μs as predicted by PDSC and after processing by DREAM-I with ten ensembled runs. Note temperature represents one of the macroscopic properties which has the highest statistical uncertainty in DSMC simulation. DREAM-I maintains the correct profile, while significantly reducing the statistical scatter in the results.

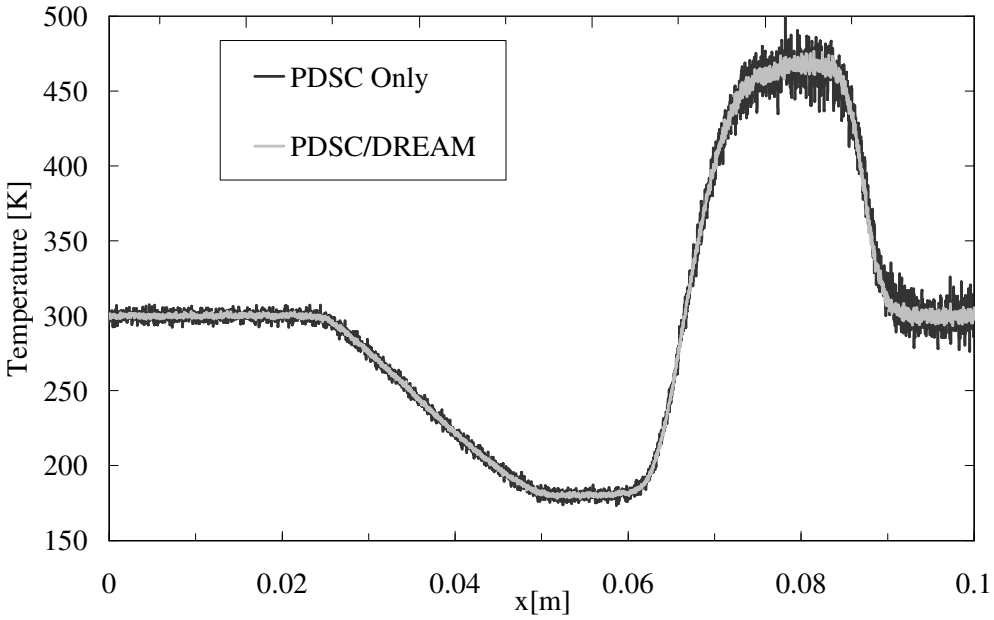

Figure 6.20. Comparison of shock tube temperature profiles at 76.9μs as predicted by PDSC and after processing by DREAM (ten ensembled samples).

A quantitative measure in the reduction in statistical scatter obtained by DREAM-I can be determined by comparing the standard deviation of macroscopic properties in the region of undisturbed flow. This represents the minimum reduction in statistical scatter, since the

undisturbed flow is stationary and will therefore be the most scattered data in the simulation domain. Figure 6.21 shows the reduction in density scatter after DREAM-I processing with different numbers of ensemble runs and different starting points, compared to the original PDSC data. Here the number N of time steps Δt between regeneration and output are normalized with the velocity v_∞ and mean free path λ_∞ in the dense region of the flow. The scatter is normalized with the scatter in the unprocessed data.

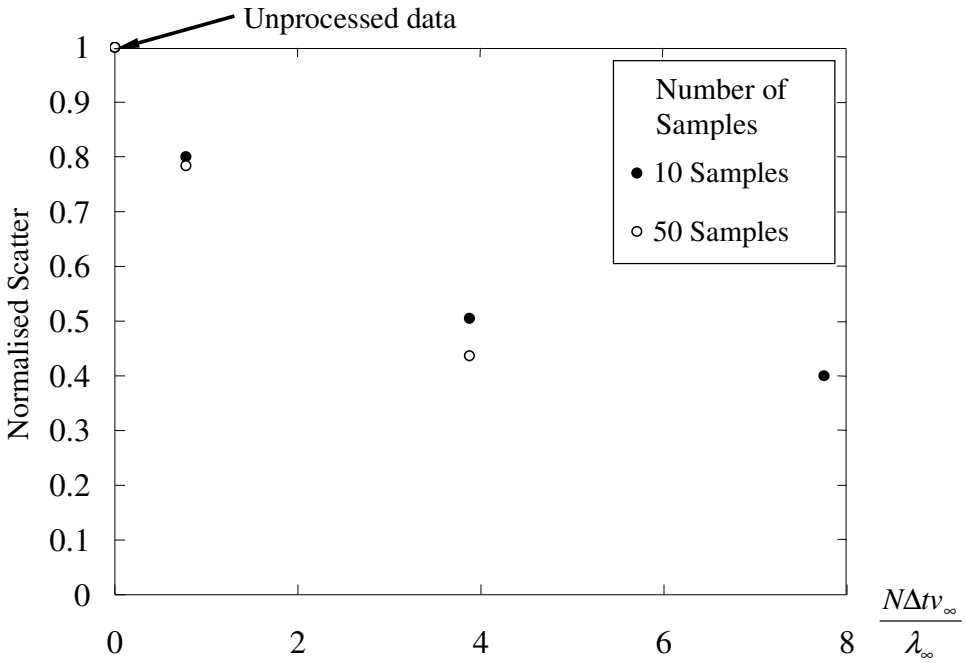

Figure 6.21. Reduction in the statistical scatter of PDSC results following processing with DREAM for different numbers of ensembled runs.

Figure 6.21 allows the appropriate number of ensemble runs and regeneration data set to be determined. It shows that it is necessary to start sufficiently far from the output time step of interest to ensure good reduction in statistical scatter in the results. Regenerating the particle data at a time step too close to the output time results in a poor reduction in scatter, because the particles do not move far enough away from their regeneration positions, effectively constraining the final solution to be too close to the macroscopic properties of the regeneration data. Using a greater number of time steps and more ensemble runs results in a further reduction in scatter, however it is interesting to note that reduction in statistical scatter remains almost the same or only slightly different at larger $N\Delta tW/\lambda_2$ (=7.8) for both the ten and fifty ensembled runs. Thus, using larger number of ensembled runs with larger $N\Delta tW/\lambda_2$ is a case of diminishing returns and it should be noted that DREAM processing time is

directly proportional to both the number of time steps and the number of ensembles in the sample.

Figure 6.22 shows the velocity distributions in a Mach 4 shock obtained using the assumption of a Maxwellian distribution (DREAM-I) in the regeneration data set. The data generated using DREAM-I (44,195 sampled particles) is compared to a separate "high resolution" PDSC run with a large number of particles (62,824 sampled particles). Although the velocity distribution has relaxed somewhat by $N\Delta tW/\lambda_2 = 9$, there is still a considerable discrepancy in the peak of the distribution. For "engineering" type simulations, the use of the Maxwellian distribution assumption in higher Mach number flows may be justified; however when the correct particle velocity distribution profile is required in non-equilibrium regions, the use of particle data obtained from the original PDSC run is necessary. Figure 13b shows the velocity distributions obtained in the Mach 4 shock using the original PDSC particle data method (DREAM-II) for $N\Delta tW/\lambda_2 = 4.5$ (44,195 sampling particles), showing a much greater agreement with the velocity distribution from the high resolution PDSC run. The velocity distribution in the cell of interest from the original PDSC run, which contains 2,076 sampling particles, is also shown. This run was used to generate the input phase-space data for DREAM-II and thus illustrates a major advantage of the method: initially PDSC can be run with a low number of simulated particles and DREAM-II can still obtain an accurate particle velocity profile, despite the scatter in the original data.

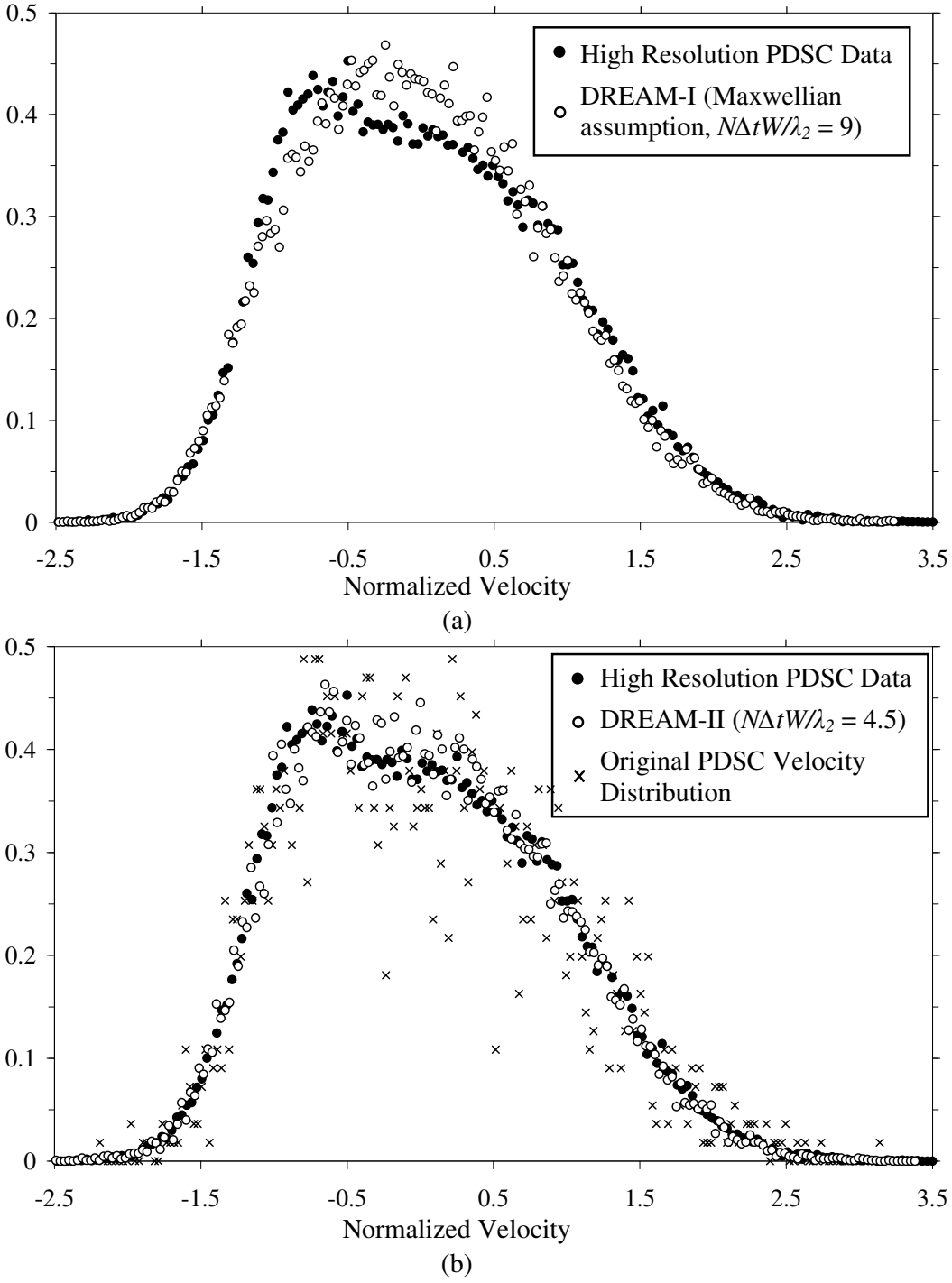

Figure 6.22. Particle velocity distributions in the normal shock structure for a Mach 4 shock as produced by PDSC and a) assuming a Maxwellian distribution (DREAM-I) and b) using the original phase space data (DREAM-II).

Figure 6.23 shows the particle velocity distribution obtained for a Mach 8 shock using DREAM-II which again demonstrates the ability of this method to obtain the correct particle velocity distribution in the shock. Here the high resolution PDSC data has 49,387 sampled particles and the DREAM-II result has 104,407 particles.

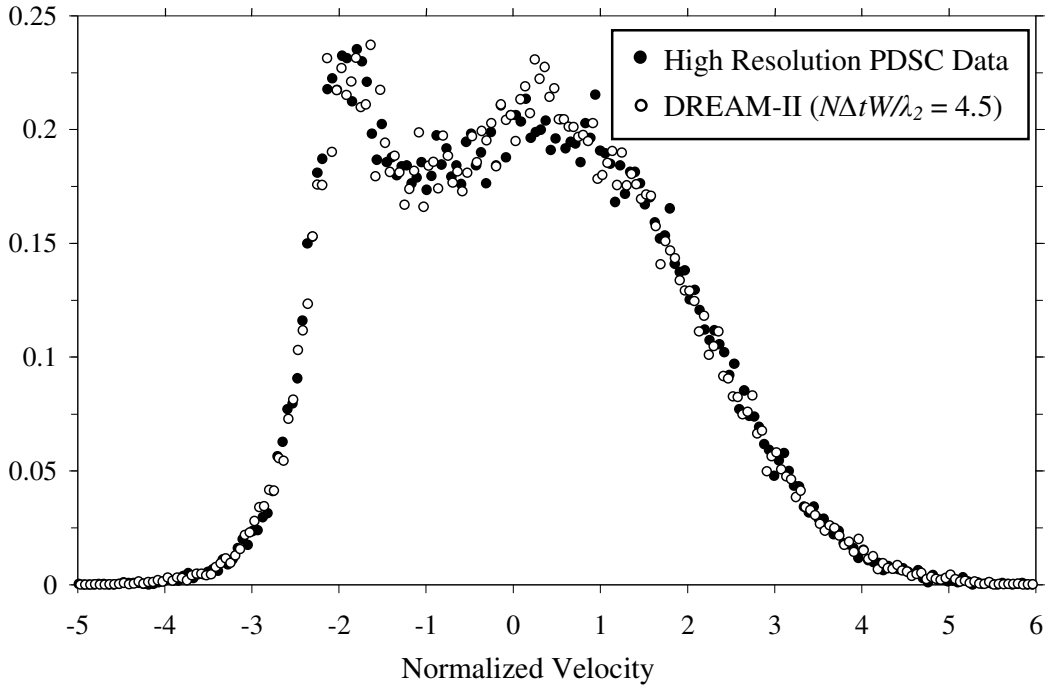

Figure 6.23. Particle velocity distributions in the normal shock structure for a Mach 8 shock as produced by PDSC and using the original phase space data (DREAM-II).

A rule of thumb for selecting an appropriate regeneration data set is that the parameter $N\Delta tv_\infty/\lambda_\infty$ should be about four or greater where a Maxwellian is assumed for lower Mach number flows (i.e. Mach < 2) in DREAM-I. This allows the particle velocities to relax to the correct distribution while ensuring good reduction in the scatter of the macroscopic data while not incurring excessive computational expense. Where the full phase-space data is used for higher Mach number flows in DREAM-II, $N\Delta tv_\infty/\lambda_\infty$ should also be set to about four to prevent constraining the macroscopic results to be close to the macroscopic data at the time of regeneration. Using approximately ten ensembles in the sample results in good reduction in statistical scatter while maintaining acceptable processing times.

6.6 Unsteady PDSC Applications

6.6.1 Introduction

The development of unsteady sampling routines for PDSC, the implementation of transient adaptive sub-cells and the DREAM post-processing code extends the capabilities of DSMC to the analysis of near-continuum time-dependent flows, which have hitherto been too computationally expensive to simulate. To provide further validation and to illustrate the potential of the code a number of test cases were simulated. These include unsteady Couette flow, the interaction of shocks with two-dimensional wedges and the development of unsteady vortices behind blunt bodies.

6.6.2 Unsteady Couette Flow

The first method used to further validate both the unsteady sampling techniques in PDSC and DREAM was the simulation of the development of Couette flow. A complete account of this testing is given in the thesis by Hung [29] and so will only be summarised briefly here.

The computational domain for the simulation is shown in figure 6.24. Here argon gas is initially at rest between two parallel diffuse plates at the same uniform temperature as the gas, in this case 300K. At time t=0 the upper plate begins moving instantaneously at speed U_∞=96.6 m/s. These conditions correspond to a Mach 0.3 flow with a Knudsen number of 0.02, based on the initial mean free path and the distance between the walls. Although this problem is one-dimensional, a 1m x 1m, 100 x 100 cell two-dimensional grid was used for validation since the code is two-dimensional. This grid spacing was chosen to be half of the mean free path in the undisturbed gas. The simulation time step was set at 3.11×10^{-5}s ($\Delta t/t_c = 0.62$, where t_c is the mean collision time of the stationary equilibrium gas) and TVTS was not used.

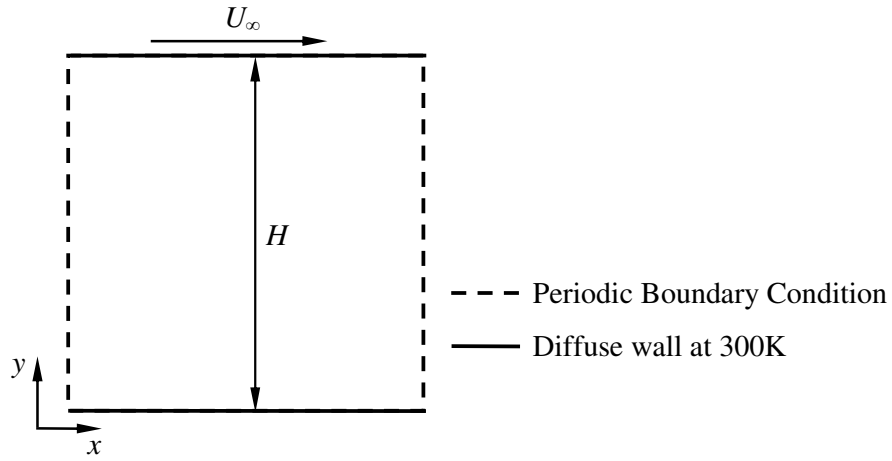

Figure 6.24. Computational domain for the developing Couette flow verification case.

A continuum solution for the velocity at the vertical position y and time t can be obtained from the incompressible Navier-Stokes equations [30]:

$$\frac{U(y,t)}{U_\infty} = \sum_{n=0}^{\infty} erfc[2n\eta_1 + \eta] + \sum_{n=0}^{\infty} erfc[2(n+1)\eta_1 - \eta] \tag{6-9}$$

where $\eta = y/2\sqrt{\nu t}$, $\eta_1 = H/2\sqrt{\nu t}$, *erfc* is the complementary error function and ν is the kinematic viscosity.

Figure 6.25 shows a comparison of the velocity profile from the raw PDSC data and the data after processing by DREAM as the flow reaches steady state, illustrating the reduction in statistical scatter achieved by using DREAM. Without DREAM the level of velocity slip at the walls cannot be determined due to the statistical scatter; however after processing the amount of slip is clearly discernable.

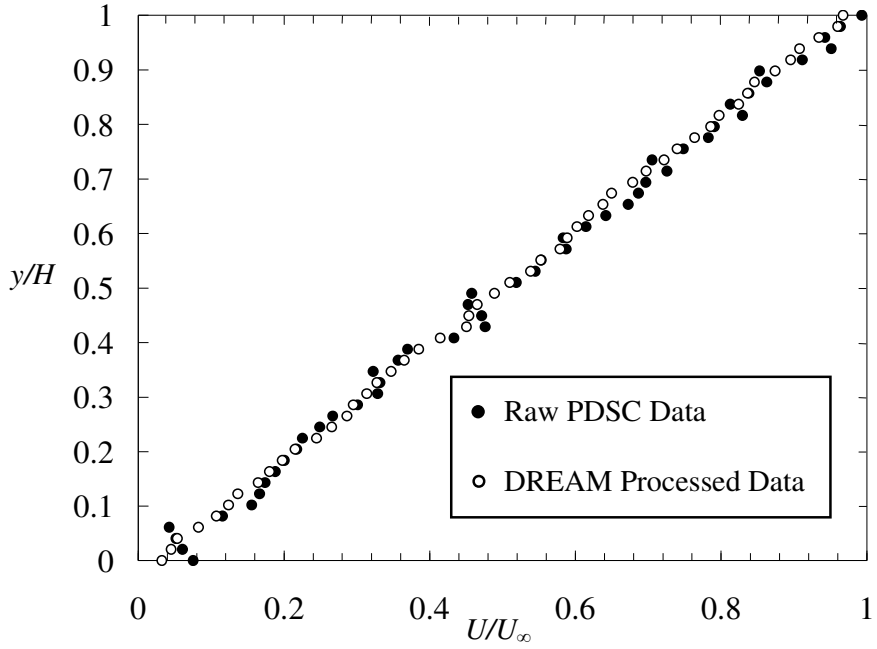

Figure 6.25. Comparison of raw PDSC data and data processed by DREAM as the Couette flow reaches steady state ($T = 72$).

Figure 6.26 shows the velocity profiles for a number of flow times as the Couette flow developed. All data has been processed by DREAM-I and is compared to the continuum solution given by equation (6-9). In all cases time has been normalised such that $T = tU_\infty/H$. This figure shows that the PDSC/DREAM-I solution lags the incompressible continuum solution. This is because of compressible effects and because the high level of rarefaction effectively results in slip between gas particles and the walls. The PDSC/DREAM solution also exhibits the expected phenomenon of velocity slip at the walls.

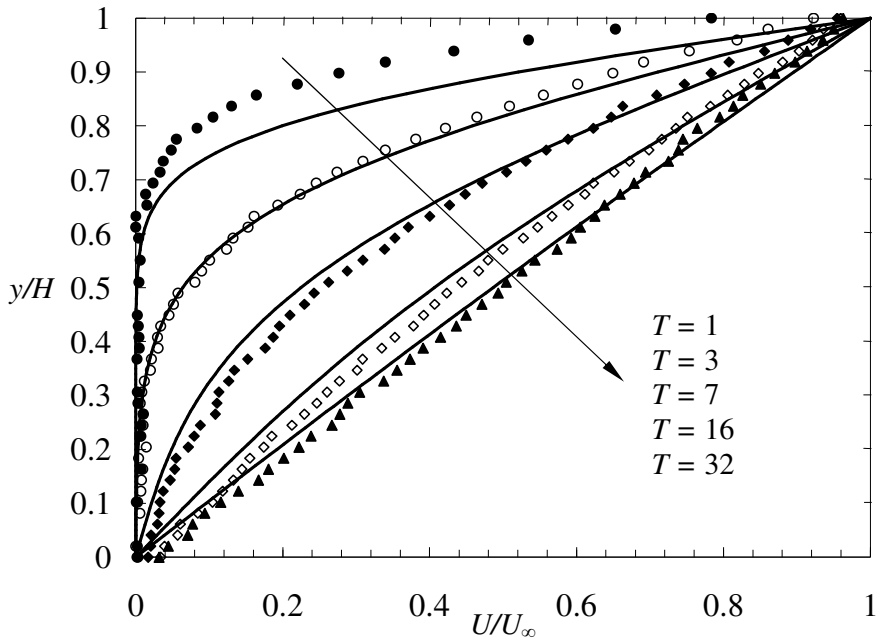

Figure 6.26. Comparison of Couette flow development predicted by unsteady PDSC/DREAM (symbols) with the exact incompressible Navier-Stokes solution (lines). Note all times are normalized as $T = tU_\infty/H$.

6.6.3 Shock Impingement on 2D Wedges

6.6.3.1 Shock Wave Reflection Over 25º Wedge

The impingement of planar shock waves over wedges is a frequently studied problem for all levels of rarefaction. Experimental studies of relatively rarefied flows have been carried out by Walenta [31,32] and comparable simulations using both DSMC and BGK solvers have been carried out by Xu *et al.* [33,34]. At the continuum level, the impingement of a planar Mach 2 shock of ideal air over a 46º wedge is frequently used as a bench mark test for advanced numerical schemes in gas dynamics. A number of experimental and simulation results from various researchers are given in the paper by Takayama and Jiang [35].

The test case was chosen to correspond to one of the experimental conditions of Walenta [32] and subsequently investigated using a BGK scheme by Xu and Honma [34]. The computational domain is shown in figure 6.27. Here a 25º wedge was simulated with a shock Mach number of 2.75 and VHS krypton as the molecular model. The Knudsen number based on width of the wedge normal to the flow and the high density flow to the left of the shock is 0.0019. For completeness, the flow conditions were calculated using the methods in section 6.3.2 and are $p_1 = 0.82$Pa, $p_2 / p_1 = 9.2$, $T_1 =$ 300K, $T_2 / T_1 =$ 3.21 and $u_2 = 398.7$ m/s.

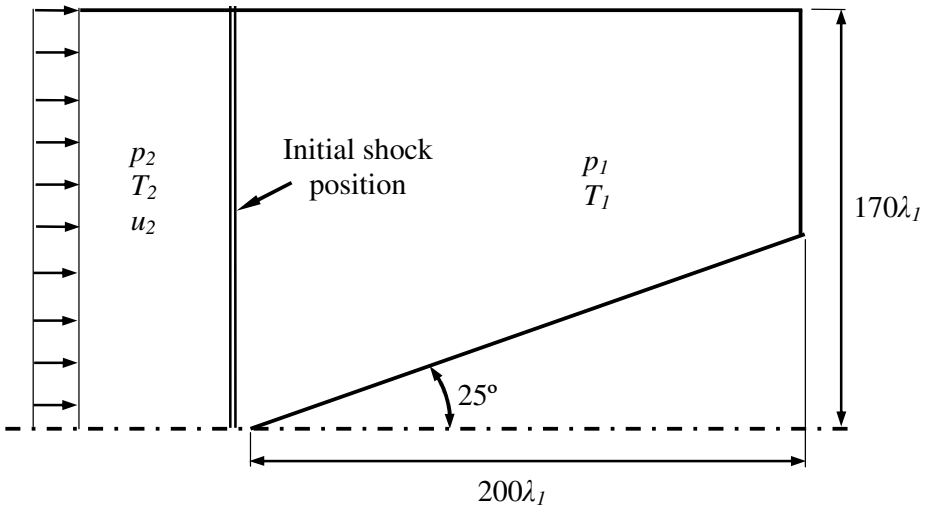

Figure 6.27. Computational domain for shock impingement on a 25º wedge.

The computational domain was divided into 77,899 unstructured sampling cells which were in turn divided into transient adaptive quadrilateral sub-cells which enabled nearest-neighbour collisions to be enforced. All domain boundaries were set as specular walls, except for the left hand inlet boundary which was set to the same conditions as behind the shock. A basic time step of $3\text{x}10^{-8}$s ($\Delta t/t_c = 0.0085$) was used with TVTS allowing the time step to increase by a factor of ten outside the sampling region. The number of particles in the domain peaked at approximately 7.2 million at the end of the simulation at which the shock reached a point $175\lambda_1$ from the leading edge of the wedge. The simulation time was 1.36 hours of simulation time on a 20-processor cluster similar to that described in section 3.1. A similar run without TVTS required 19.2 hours of simulation time. Post-processing of each data set using DREAM resulted in a reduction in the standard deviation of the density in the undisturbed region of flow from 20% in the original data to 9.6% in the processed data.

Figure 6.28 shows a comparison between the raw data from PDSC and the data processed by DREAM as the shock reaches approximately $175\lambda_1$ from the leading edge. Here the contours have been normalised by the densities in the undisturbed region ρ_1 and behind the shock ρ_2. In both cases, the reflected cylindrical shock, Mach stem and slip layer which form the triple point are clearly visible, however the structure is much better resolved in the DREAM processed data. In this figure, a density contour of $\frac{\rho-\rho_1}{\rho_2-\rho_1}=1.2$ from the equivalent case

simulated by Xu and Honma [34] is also given, which shows good qualitative agreement with the present results.

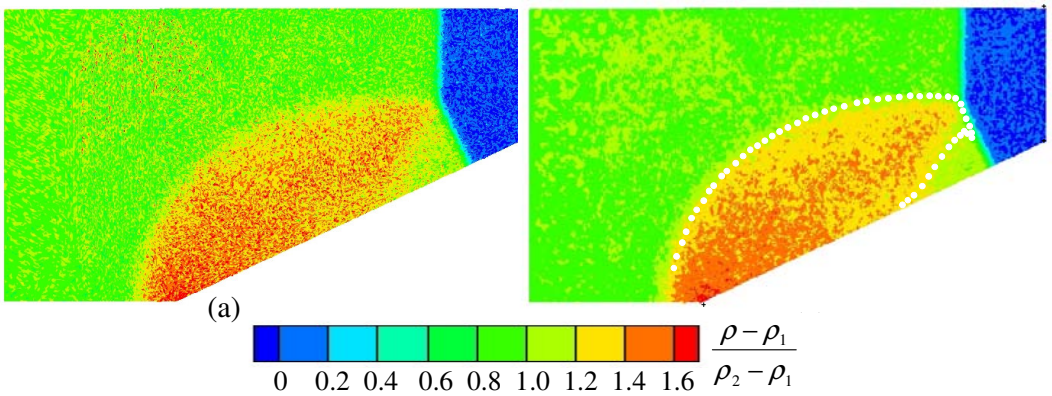

Figure 6.28. Comparison of (a) raw PDSC data and (b) data processed by DREAM for the impingement of a shock on a 25° wedge (Kn = 0.0019) at t = 900μs. The white markers show the $\frac{\rho-\rho_1}{\rho_2-\rho_1}=1.2$ contour from the equivalent numerical simulation by Xu and Honma [34].

Figure 6.29 shows the density contours at a further two points in the flow: when the shock reaches approximately $40\lambda_1$ and $110\lambda_1$ respectively. In both cases the data has been processed by DREAM. Again, in each case the resolution of the flow structure is greatly enhanced by using DREAM.

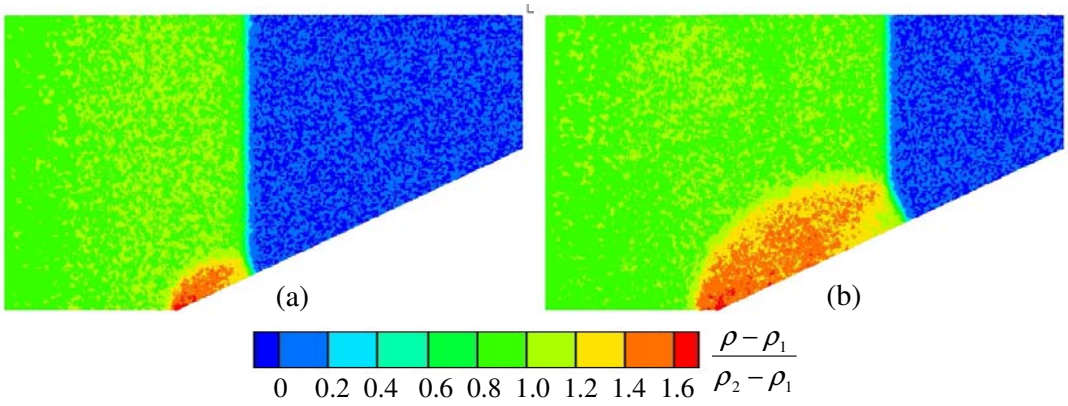

Figure 6.29. The impingement of a shock on a 25° wedge when the shock reaches approximately (a) $40\lambda_1$ (t = 280μs) and (b) $110\lambda_1$ (t = 600μs) from the leading edge of the wedge (Kn=0.0019). All data are processed by DREAM.

Figure 6.30 shows a comparison of the normalized density profile between the experimental data by Walenta [32], the BGK simulation by Xu and Honma [34] and the data from the present simulation at a point approximately $17.5\lambda_1$ behind the leading edge when the shock reaches $40\lambda_1$. Both the simulated profiles agree qualitatively, as they both use specular walls, however they differ from the experimental data due to the different wall conditions in the experiment. The PDSC/DREAM solution appears to exhibit higher density for $y/\lambda_1 < 10$ than the BGK solution.

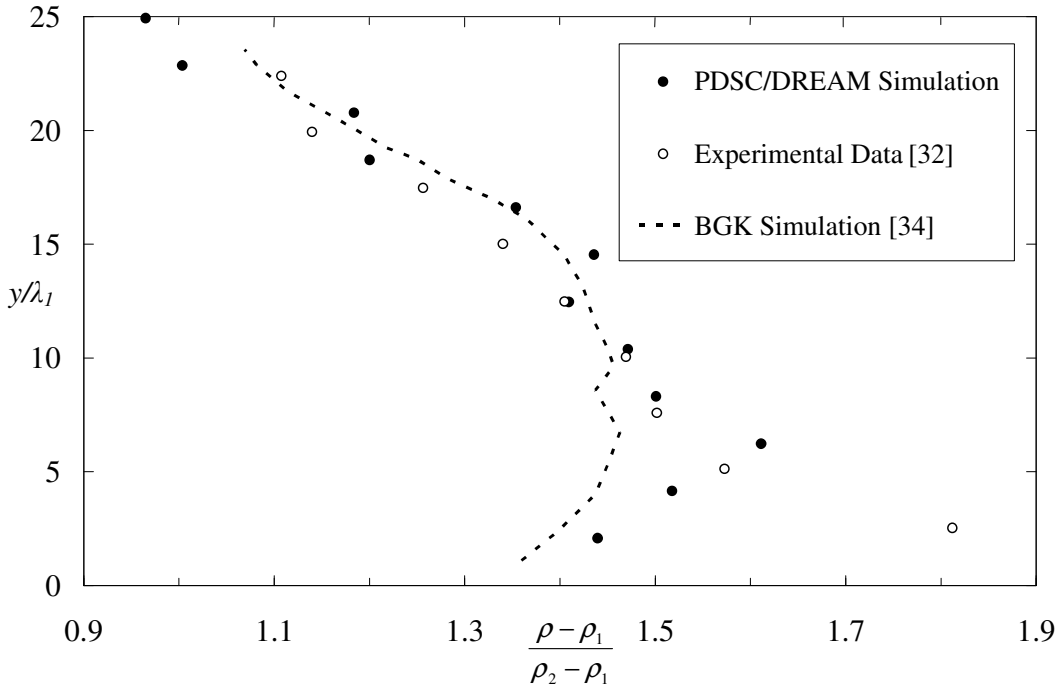

Figure 6.30. Comparison between the density distribution from experimental and simulation data at approximately $17.5\lambda_1$ from the leading edge of the 25° wedge when the incident shock reaches $40\lambda_1$.

6.6.3.2 Development of a Shock Wave Structure Passing a Wedge in a Channel

A further test problem used as a demonstration is the impingement of a planar Mach 1.3 shock over a two dimensional wedge in a channel. This problem was first studied in the classic experiment by Schardin who used high speed cinematography to study the flow [36]. The impingement of the shock on the wedge results in a complex evolution of interacting shock and vortex structures. Numerous authors have also studied similar problems using partial differential equation methods. For example, Huang [37] used a Navier-Stokes solver, and Sivier *et al.* [38] and Chang and Chang [39] used an Euler equation solver. The present

simulation was developed as a point of comparison, however it should be noted that the present conditions are more rarefied than any of the cases mentioned above.

The computational domain for the problem is shown in figure 6.31. Here the channel wall and wedge surfaces were implemented as specular walls, and the inlet boundary was set to the same conditions as the behind the moving shock. Argon gas was used as the working gas, and the Knudsen number based on the width of wedge normal to the flow and the high density flow to the left of the shock was 0.012. For completeness the flow conditions are: p_1 = 10Pa, T_1 = 300K, p_2/p_1 = 1.8625, T_2/T_1 = 1.2922 and u_2 = 128.5 m/s, with these values being determined by the same method as in section 6.3.2.

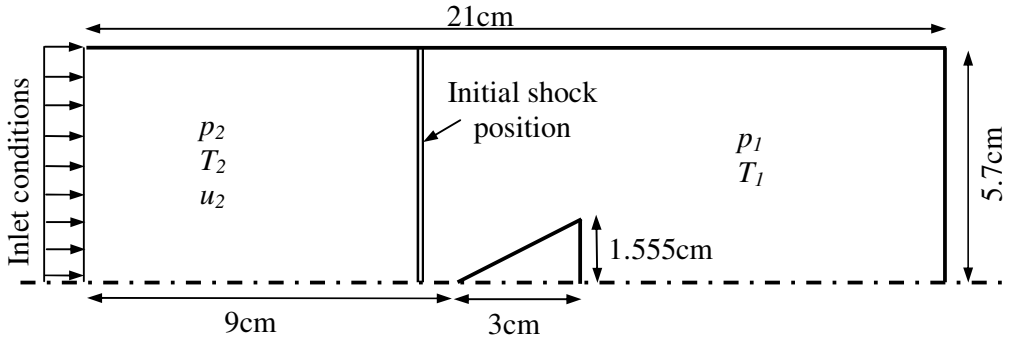

Figure 6.31. Computational domain for the shock structure passing over a wedge in a channel.

The computational domain was divided into 147,011 unstructured elements, with the element size in the region of the wedge being approximately equal to the equilibrium mean free path to the left of the shock. A sampling time step of $2\text{x}10^{-8}$s ($\Delta t/t_c$ = 0.049) was set such that no particle could traverse more than approximately one third of the mean free path over the sampling period, which consisted of 50 time steps. The TVTS scheme was employed, enabling the time step to be increased by a factor of ten when sampling was not occurring. The number of particles within the simulation domain peaked at approximately 21 million, and the total simulation required was approximately 3.5 hours of computational time on a 10-processor cluster with similar specifications as the cluster mentioned in section 6.3.2 (a run without TVTS required approximately 24 hours). The data sets at the points of interest generated by PDSC were then post-processed using DREAM to improve the statistical accuracy of the simulations. In each case the solution was approached from 500 time steps before the point of interest and 10 ensembles were used. This procedure was found to reduce the standard deviation of the density in the undisturbed region of flow from 9.27% in the

original data to 2.82% in the processed data and resulted in better resolution of the flow structure.

Figure 6.32 shows a series of density contours at different times as the shock passes over the wedge. The results reveal some very interesting flow field features, which are qualitatively consistent with the experimental and numerical results of the other authors mentioned above, although exhibit greater levels of rarefaction. As the incident shock passes over the wedge, the reflected cylindrical shock and Mach stem become clearly visible. At the end of the wedge, the Mach stem diffracts around the corner forming a further cylindrical shock and an expansion fan which moves in the opposite direction. The vortex structure formed behind the wedge then begins to move downstream. The cylindrical shocks from the upper and lower corner of the wedge cross each other (or, in the case of the simulation, reflect from the line of symmetry), which can be faintly seen in the figure. As the reflected shock from the front of the wedge grows larger, it reflects from the channel wall and then interacts with the shock structure below it.

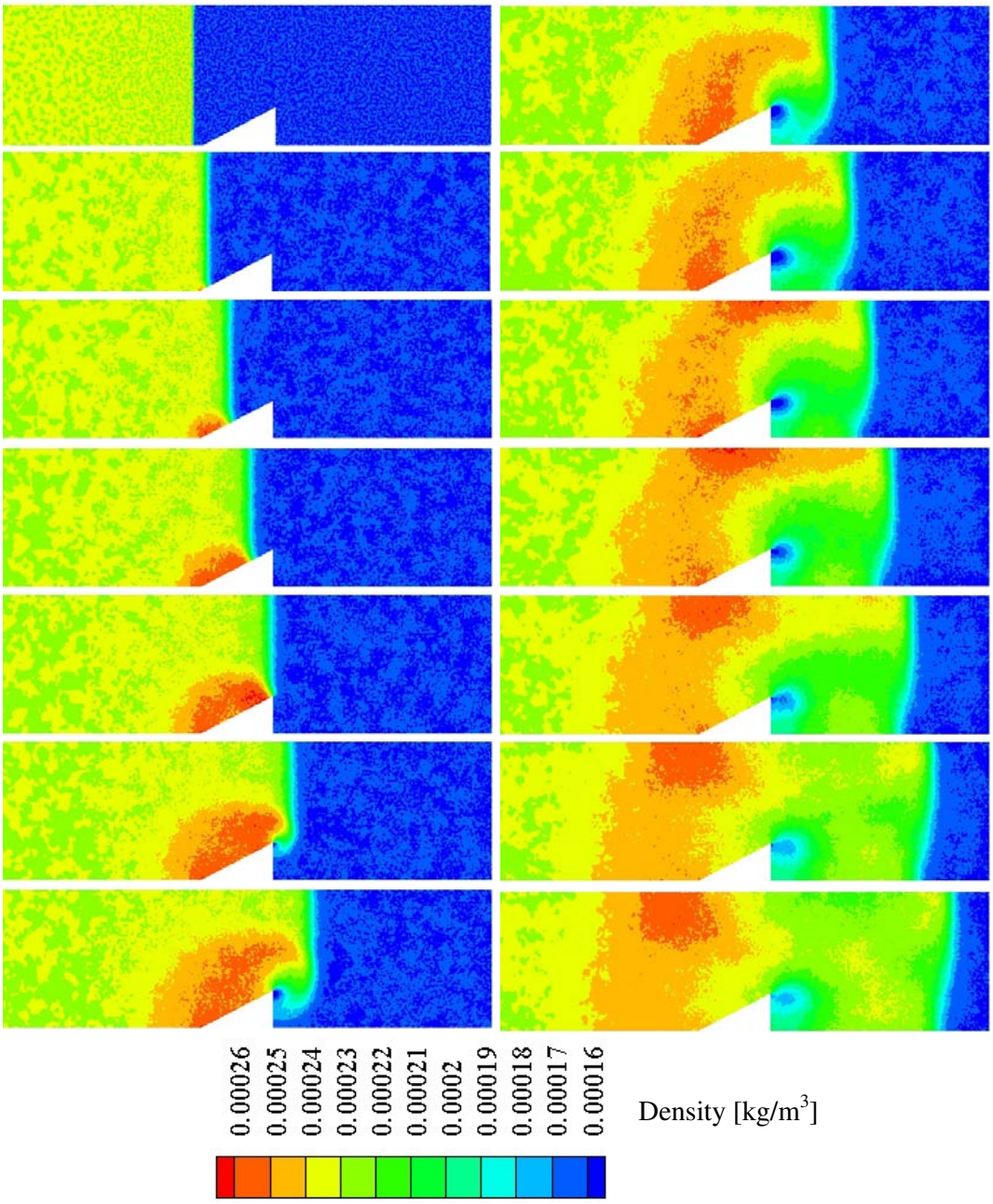

Figure 6.32. Contours of density [kg/m^3] for shock impingement on a wedge in a channel after processing by DREAM (Kn = 0.012). Each image is separated by 20μs

6.6.4 Vortex Shedding

At the time of writing, a limited amount of work had been completed on studying the unsteady vortex shedding behind blunt bodies in rarefied sub-sonic flows using PDSC. Previous DSMC studies by Bird [40] and Talbot-Stern and Auld [41] of vortex shedding behind flat plates normal to the flow had difficulty in obtaining the correct vortex shedding

frequency. This is probably because nearest neighbour collision were not guaranteed in the simulations resulting in vorticity not being preserved beyond the sampling cell level which would have consequences for the correct prediction of vortex shedding.

Initial studies using PDSC showed that the use of sub-cells had an effect on vortex shedding frequency. A study of Mach 0.6 flow over a 2D circular cylinder at Kn = 0.00833 and Re = 80, gave a Strouhal number, St ≈ 0.153. This compares very closely to the experimental results of Norberg [42].

The vortex shedding studies are ongoing and it is intended to publish the results in a paper currently under preparation [27], however the initial results indicate that PDSC is an excellent tool for predicting this phenomenon at a rarefied level.

References

[1] J.-S. Wu and Y.-Y. Lian, Parallel three-dimensional direct simulation Monte Carlo method and its applications, *Comput. Fluid* 32(8), 1133-1160 (2003).

[2] J.-S. Wu, K.-C. Tseng and F.Y. Wu, Parallel three-dimensional DSMC method using mesh refinement and variable time-step scheme, *Comput. Phys. Comm.* 162, 166-187 (2004).

[3] J.-S. Wu and K.-C. Tseng, Parallel DSMC method using dynamic domain decomposition, *Int. J. Numer. Meth. Eng.* 63, 37-76 (2005).

[4] J.-S. Wu, S.-Y. Chou, U.-M. Lee, Y.-L. Shao, and Y.-Y. Lian, Parallel DSMC simulation of a single under-expanded free orifice jet from transition to near-continuum regime, *J. Fluid Eng.* 127, 1161-1170 (2005).

[5] J.-S. Wu, W.-J. Hsiao, Y.-Y. Lian and K.-C. Tseng, Assessment of conservative weighting scheme in simulating chemical vapour deposition with trace species, *Int. J. Numer. Meth.* 43, 93-114 (2003).

[6] K.-C. Tseng, J.-S. Wu and I. Boyd, Simulations of Re-Entry Vehicles by Using DSMC with Chemical-Reaction Module, AIAA-2006-8084, in Proc. 14th AIAA/AHI Space Planes and Hypersonic Systems and Technologies Conf., Canberra, Australia, (2006).

[7] J.-S. Wu, F. Lee and S.-C. Wong, Pressure Boundary Treatment in Micromechanical Devices using the Direct Simulation Monte Carlo Method, *JSME Int. J., Ser. B.* 44(3), 439-450 (2001).

[8] D.M. Nicho and J.H. Salz, Dynamic Remapping of Parallel Computations with Varying Resource Demands, *IEEE Trans. Comput.* 39(9), 1073-1087 (1988).

[9] D.J. Auld, Direct molecular simulation (DSMC) of shock tube flow, in Proc. First European Computational Fluid Dynamics Conference, Brussels, Belgium (1992).

[10] J.D. Anderson, Modern Compressible Flow: With Historical Perspective (McGraw-Hill, New York, 1990).

[11] A. Ferri, Fundamental Data Obtained from Shock-Tube Experiments (Pergamon Press, New York, 1961).

[12] A.G. Gaydon and I.R. Hurle, The Shock Tube in High-Temperature Chemical Physics (Reinhold Publishing, New York, 1963).

[13] R. Roveda, D.B. Goldstein and P.L. Varghese, Hybrid Euler/Direct Simulation Monte Carlo Calculation of Unsteady Slit Flow, *J. Spacecraft Rockets* 37(6), 753-760 (2000).

[14] M.R. Smith, On the True direction Equilibrium Flux Method and its applications, PhD Thesis, University of Queensland (2008 – under examination).

[15] G.A. Bird, Molecular Gas Dynamics and the Direct Simulation of Gas Flows (Clarendon Press, Oxford, 1994).

[16] B. Schmidt, Electron beam density measurements in shock waves in argon, *J. Fluid Mech.*, 39(2), 361-373 (1969).

[17] H.M. Cave, S.P. Krumdieck and M.C. Jermy, Development of a model for high precursor conversion efficiency pulsed-pressure chemical vapor deposition (PP-CVD) processing, *Chem. Eng. J.* 135, 120-128 (2008).

[18] M. Ivanov, G. Markelov, S. Taylor and J. Watts, Parallel DSMC strategies for 3D computations, in Proc. of Parallel CFD'96, Capri, Italy (1996).

[19] G.A. Bird, The DS2V Program User's Guide, G.A.B. Consulting Pty Ltd (2005).

[20] G.J. LeBeau, K.A. Jacikas and F.E. Lumpkin, Virtual sub-cells for the Direct Simulation Monte Carlo Method, 41st AIAA Aerospace Sciences Meeting & Exhibit, Reno (NV) (2003).

[21] G.E. Karniadakis and A. Beskok, Micro flows: fundamentals and simulation (Springer, New York, 2002).

[22] S.-F. Hsien, Parallel Monte Carlo Simulation of Supersonic Driven-Cavity Flow from Free-molecular to Near-continuum Regime, ME Thesis, National Chiao-Tung University (2007).

[23] G.A. Bird, Sophisticated Versus Simple DSMC, in Proc. of 25th International Symposium on Rarefied Gas Dynamics, St. Petersburg, Russia (2006).

[24] G.A. Bird, “Sophisticated DSMC”, Lecture notes from the short course at the DSMC07 meeting, Santa Fe, New Mexico (2007).

[25] A.J. Lofthouse, I.D. Boyd and M.J. Wright, Effects of Continuum Breakdown on Hypersonic Aerothermodynamics, AIAA Paper 2006-993 (2006).

[26] Personal correspondence with Prof. G.A. Bird (12 July 2007).

[27] K.-C. Tseng, H.M. Cave, J.-S. Wu, J.-C. Huang, Y.-Y Lian, M.C. Jermy and S.P. Krumdieck, Simulations of Two-Dimensional Vortex Streets with the Direct Simulation Monte Carlo Method, *Phys. Fluids* (in preparation, 2008).

[28] D. Q. Xu, H. Honma and T. Abe, DSMC approach to nonstationary Mach reflection of strong incoming shock waves using a smoothing technique, *Shock Waves* 3(1), 67-72 (1993).

[29] W.-C. Hung, Preliminary Simulation of Instantaneously Started Supersonic Driven Cavity Flows in the Rarefied Gas Regimes Using the Parallel Direct Simulation Monte Carlo Method, ME Thesis, National Chiao-Tung University (2007).

[30] H. Schlichting and K Gersten, Boundary-Layer Theory (Springer-Verlag, New York, 2003).

[31] Z.A. Walenta, Microscopic structure of the Mach-type reflection of the shock wave, *Arch. Mech. Warszawa* 32(5), 819-825 (1980).

[32] Z.A. Walenta, Formulation of the Mach type reflection of shock waves, *Arch. Mech. Warszawa* 35(2), 187-201 (1983).

[33] D. Q. Xu, H. Honma and T. Abe, DSMC approach to nonstationary Mach reflection of strong incoming shock waves using a smoothing technique, *Shock Waves* 3(1), 67-72 (1993).

[34] D. Q. Xu and H. Honma, Numerical simulation for nonstationary Mach reflection of a shock wave: A kinetic-model approach, *Shock Waves* 1(1), 43-49 (1991).

[35] K. Takayama and Z. Jiang, Shock wave reflection over wedges: a benchmark test for CFD and experiments, *Shock Waves* 7(4), 191-203 (1997).

[36] H. Schardin, High frequency cinematography in the shock tube, *J. Photographic Sci.* 5, 19-26 (1957).

[37] J.C. Huang, A study of instantaneous starting cylinder and shock impinging over wedge flow, in Proc. 10th National Computational Fluid Dynamics Conference, Hua-Lien, Taiwan, August 2003 (in Chinese).

[38] S. Sivier, E. Loth, J. Baum and R. Löhner, Vorticity produced by shock wave diffraction, *Shock Waves* 2(1), 31-41 (1992).

[39] S.-M. Chang and K.-S. Chang, On the shock-vortex interaction in Schardin's problem, *Shock Waves* 10(5), 333-343 (2000).

[40] G. Bird, Knudsen and Mach number effects on the development of wake instabilities, AIAA Paper 1998-785 (1998).

[41] J. Talbot-Stern and D.J. Auld, Direct Simulation (Monte Carlo) of two dimensional vortex streets, AIAA/ASME Joint Thermophysics and Heat Transfer Conference, 7th, Albuquerque (NM) (1998).

[42] C. Norberg, Fluctuating lift on a circular cylinder: review and new measurements, *J. Fluid. Struct.* 17(1), 57-96 (2003).

7. PP-CVD Flow Field Simulations

7.1. Introduction

In chapter 5 basic DSMC simulations were performed to demonstrate the mechanisms leading to high precursor conversion efficiency and deposition uniformity observed in experimental PP-CVD reactors. This preliminary investigation enabled an understanding behind the physical mechanisms of PP-CVD to be developed; however supply pressures and injection times were limited to several orders of magnitude below those used in the experimental reactors.

The investigations of chapter 5 revealed that a critical part of the PP-CVD process is the injection phase and the period immediately after closing the inlet orifice when the jet structure disperses, since this is what leads to the high flow field uniformity required at the start of the pump-down phase. During the pump-down phase, the precursor simply diffuses to the surface since convective effects are negligible due to the relatively slow rate of pump-down compared to the rate of diffusion.

In order to simulate reactors with more realistic supply pressures, unsteady sampling procedures and improved collision routines were developed for an existing parallelised DSMC code (PDSC), as discussed in chapter 6. These procedures have been demonstrated as being capable of simulating unsteady flows in the near continuum regime with high accuracy and acceptable run times. Additionally, a post-processing methodology was developed to reduce the statistical scatter in the results at temporal points of interest.

In this chapter, PDSC will be used to simulate the carrier gas flow field in experimental PP-CVD reactor geometries at realistic supply pressures. A Navier-Stokes solution is used to reduce the computational expense of the simulations in the region surrounding the nozzle and this approach is shown to be justified as this region reaches steady state rapidly after the initiation of the injection phase. The results show that parallel DSMC code can be used to simulate PP-CVD reactors when sufficient computational resources are available.

7.2. Justification for a Hybrid Approach: Navier-Stokes Nozzle Simulations

In experimental PP-CVD reactors, the supply pressure is of the same order as atmospheric pressure, or higher. This ensures that a large quantity of precursor is delivered rapidly to the reactor volume during the injection process. For a typical PP-CVD reactor, the Knudsen number near the inlet orifice will be on the order of 10^{-4} or lower, for which continuum flow can be expected, and which would make simulation of the region near the orifice using pure DSMC very computationally expensive.

The concept of using a Navier-Stokes simulation to provide the inlet boundary conditions to the DSMC simulation to reduce the computational expense near the nozzle is illustrated in figure 7.1 (the contours of density shown in this figure are from the case I PDSC simulations described later in this chapter). Navier-Stokes simulations by T.-H. Lin (National Chiao Tung University) of typical PP-CVD reactors inlet orifices show that the flow in this region rapidly becomes choked and steady (details will be published in Lin's masters thesis). Thus the flow properties along the boundary of the Navier-Stokes region provide the inlet conditions to the DSMC simulation by assuming a Maxwell-Boltzmann distribution of particle velocities.

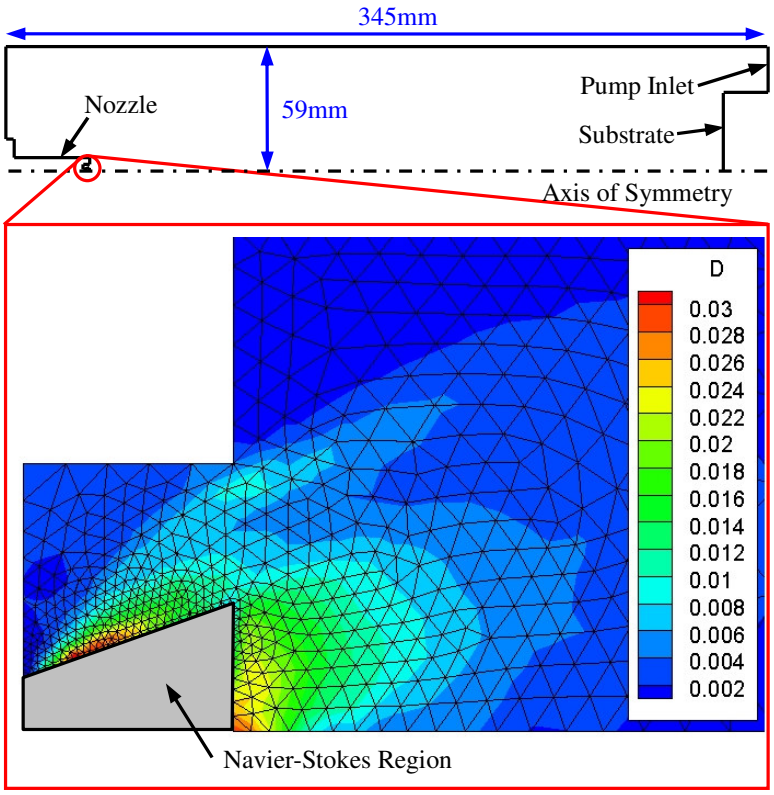

Figure 7.1. PP-CVD reactor geometry illustrating the concept of using a Navier-Stokes region to reduce the computational expense of simulations near the nozzle.

Figure 7.2 shows the contours of density and axial component of velocity computed from Lin's Navier-Stokes simulations for a helium supply pressure of 1atm (equivalent to case II in section 7.3 below) and an initial reactor pressure of 10Pa, at 10μs and 20μs after the initiation of the injection phase. From the figure, it can be seen that the flow contours near the nozzle become steady after, conservatively, 10μs. Because the flow is choked in this region, the downstream conditions have no influence on the flow near the nozzle so these contours remain unchanged throughout the injection phase. Figure 7.2 illustrates another interesting problem of modelling the flow using partial differential equation based solvers, which is the discontinuity at the nozzle lip. This region also would present a challenge to a pure DSMC method, since the rapid change of density would necessitate a corresponding rapid change in cell size.

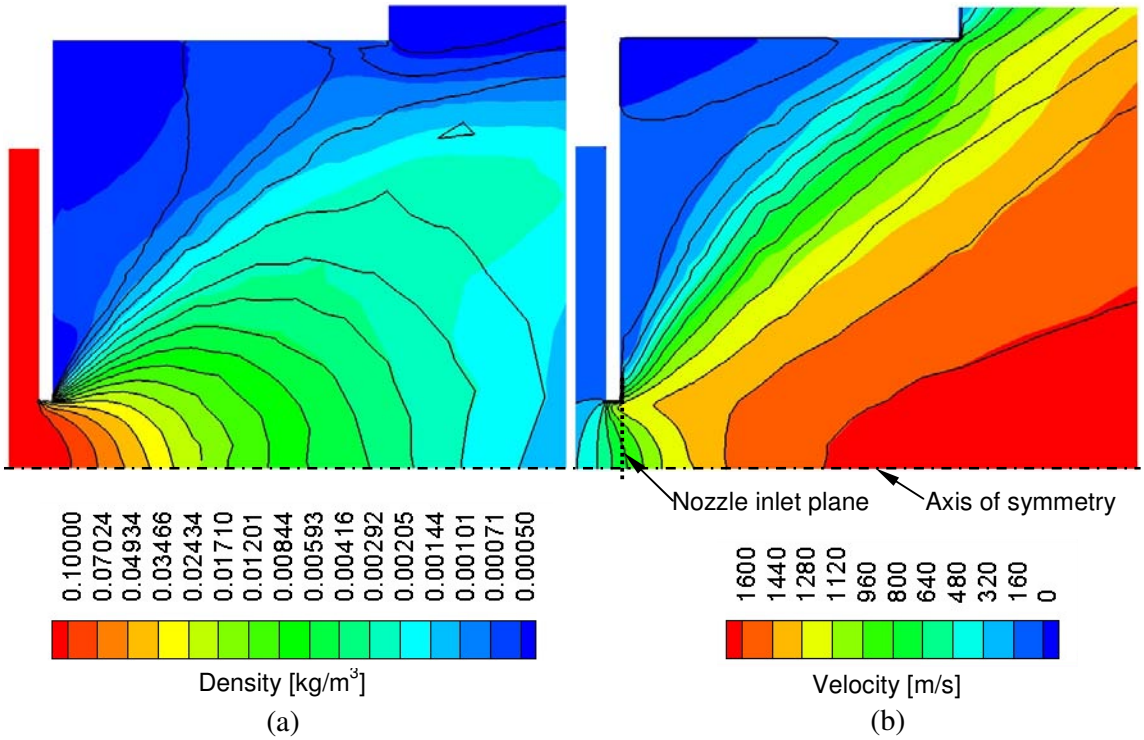

Figure 7.2. Contours of a) density and b) axial velocity at 10μs (filled contours) and 20μs (black lines) generated by Navier-Stokes simulations illustrating the rapid development of steady choked flow near the PP-CVD reactor inlet nozzle.

The use of an inlet boundary condition generated from a Navier-Stokes solution is a compromise; however it is justified by the massive reduction in computational expense which can be achieved avoiding the use of pure DSMC methods in this region.

7.3. Method

The initial transient of the PP-CVD injection phase was simulated using the unsteady axisymmetric PDSC code described in chapter 6. Two cases were run using a single-component supply gas (VHS helium), the simulation conditions for which are described in table 7.1. Case I was run primarily to verify the method at pressures approximately one order of magnitude lower than normal reactor conditions, whereas case II was run at realistic pressures as a test of PDSC's capabilities. In both cases TVTS was used and DREAM was not utilised.

Table 7.1. Simulation conditions for PP-CVD flow field simulations

	CASE I	**CASE II**
Supply Pressure, P	10 kPa (0.1 atm)	100 kPa (1 atm)
Pulse Range, $P_{min} \rightarrow P_{max}$	1 Pa → 100 Pa	10 Pa → 1000 Pa
Injection Time, t_i	0.1s	0.1s
Sampling Cells	16,516 (614 unstructured)	74,903 (1,090 unstructured)
Basic simulation time step, Δt	1×10^{-9} s	
Simulation Particles	Maintained at ~ 1×10^6 to ~ 2×10^6	
Wall Temperature, T_W	300 K (diffuse)	
Supply Temperature, T_S	293 K	
Substrate Temperature, T_{sub}	800 K (diffusely reflecting, non-absorbing)	
Inlet Orifice Diameter, d_i	1 mm	
PDSC Parameters	Sub-cells: transient adaptive on, TVTS: on, Dynamic domain decomposition: on	
Sampling Details	Time average of 100 adjacent time steps	
Processors	Cluster of 24 processors	

The reactor dimensions used in the simulations are equivalent to the design used in the naphthalene sublimation experiments described in section 2.3.5, and are shown below in figure 7.3.

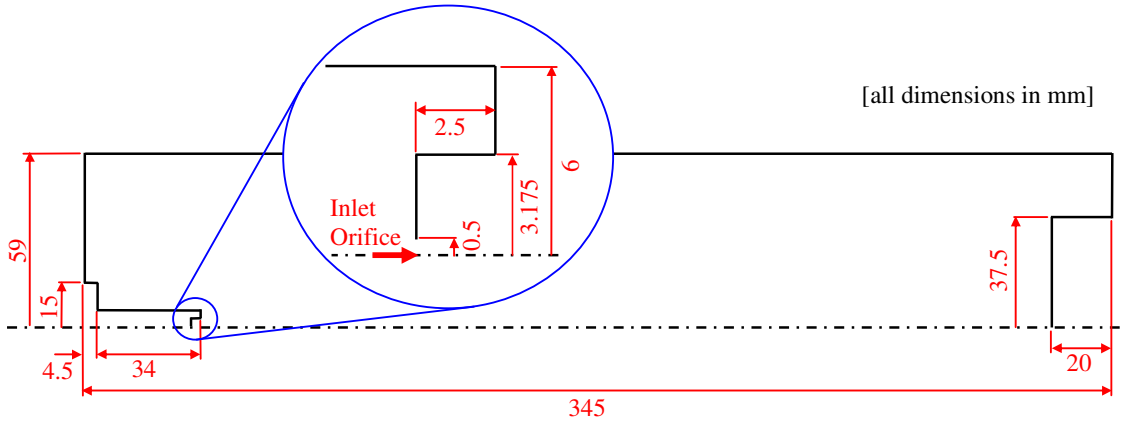

Figure 7.3. Schematic of reactor dimensions used in PP-CVD flow field simulations.

7.4. Results

7.4.1 Case I – 0.1 atm Supply Pressure

As mentioned above, the 0.1 atm supply pressure case was used as an initial verification of PDSC for simulating PP-CVD reactor flow at approximately one-tenth of typical experimental reactor pressures. Figure 7.4 shows the grid used in the simulation, in particular the detail near the orifice showing the Navier-Stokes region boundary.

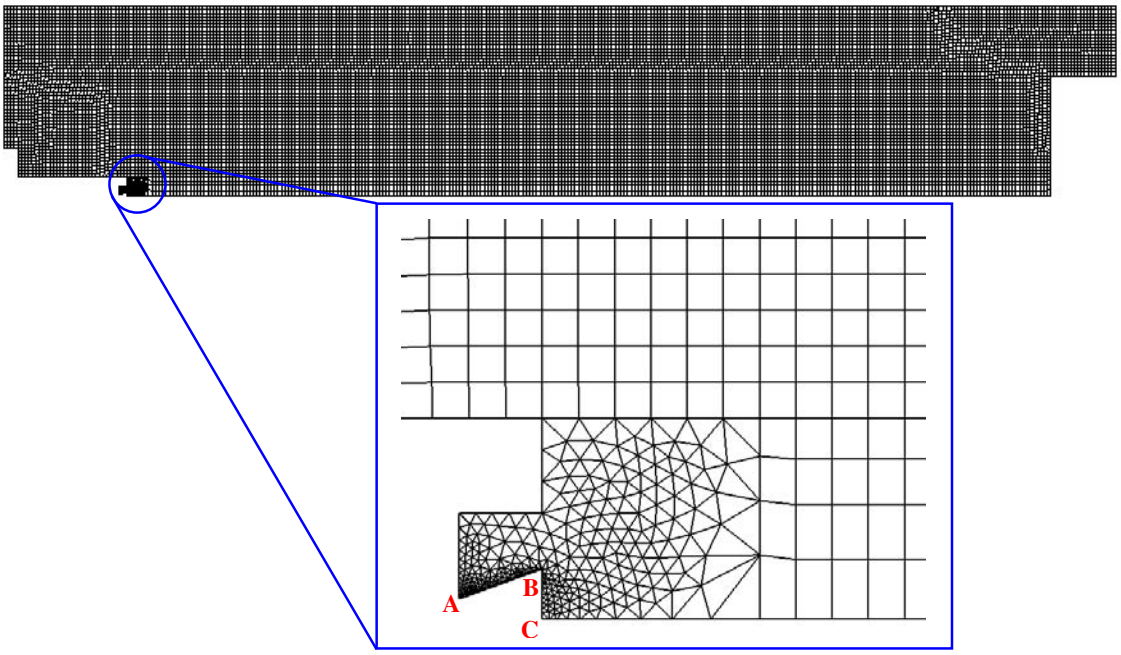

Figure 7.4. Simulation grid for PP-CVD flow field case I, including detail view of domain near the inlet orifice.

The profiles of number density, temperature and macroscopic velocity components along lines AB and BC were determined from the Navier-Stokes solution and used as the input parameters to the PDSC simulation. Because the reactor pressure, and hence the number of particles in the reactor, increases as the simulation progresses, the particle weighting was changed periodically to maintain the number of particles at a computationally manageable level.

Figure 7.5 shows contours of axial velocity, radial velocity and temperature as the flow field develops during the first 2.0 ms of flow.

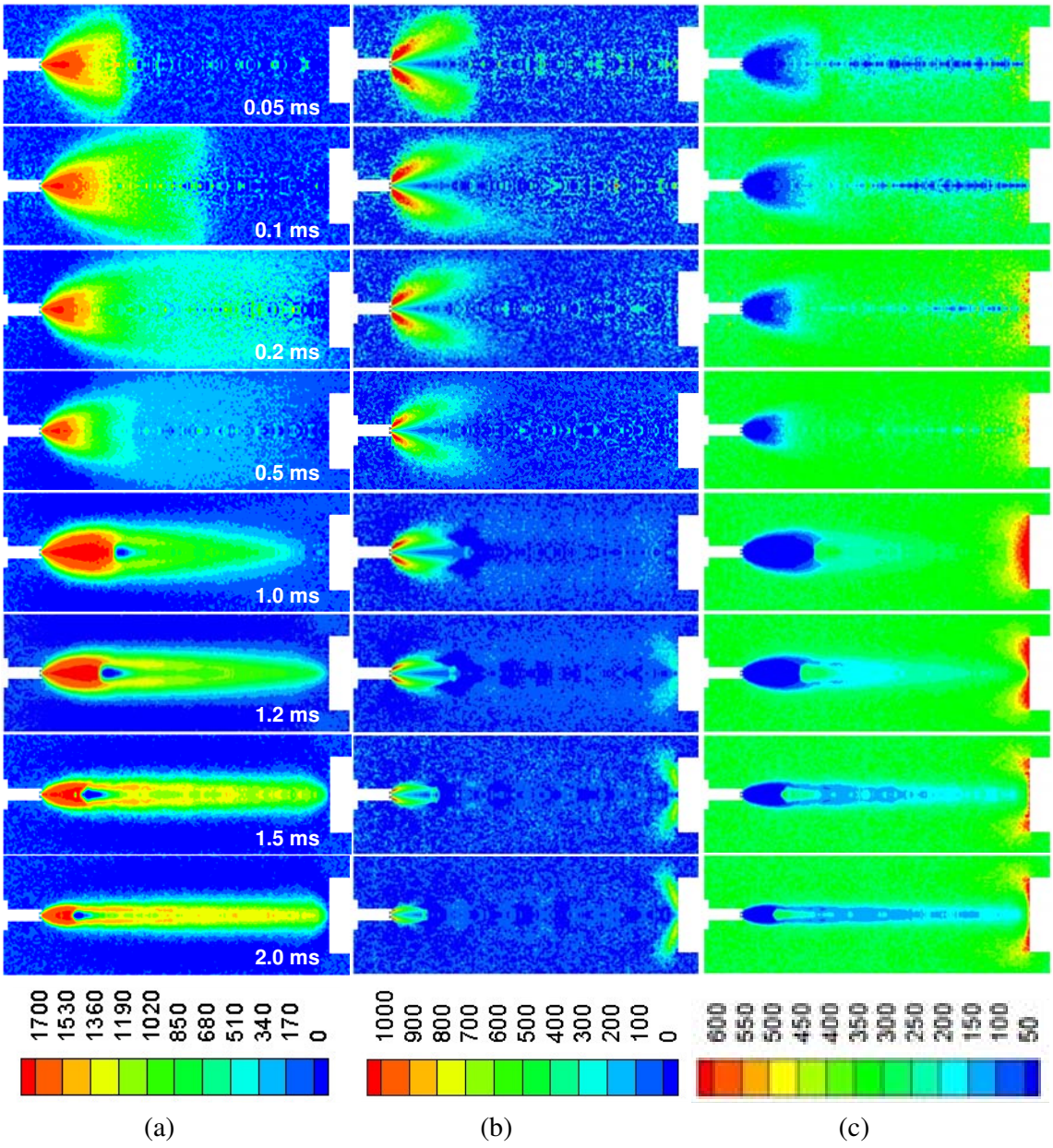

Figure 7.5. Contours of a) axial (x-component) velocity [m/s], b) radial (y-component) velocity [m/s] and c) total gas temperature [K] at various flow times for PP-CVD flow field case I.

Figure 7.6 shows the contours of density using a sliding density scale during the first 2.0ms of flow.

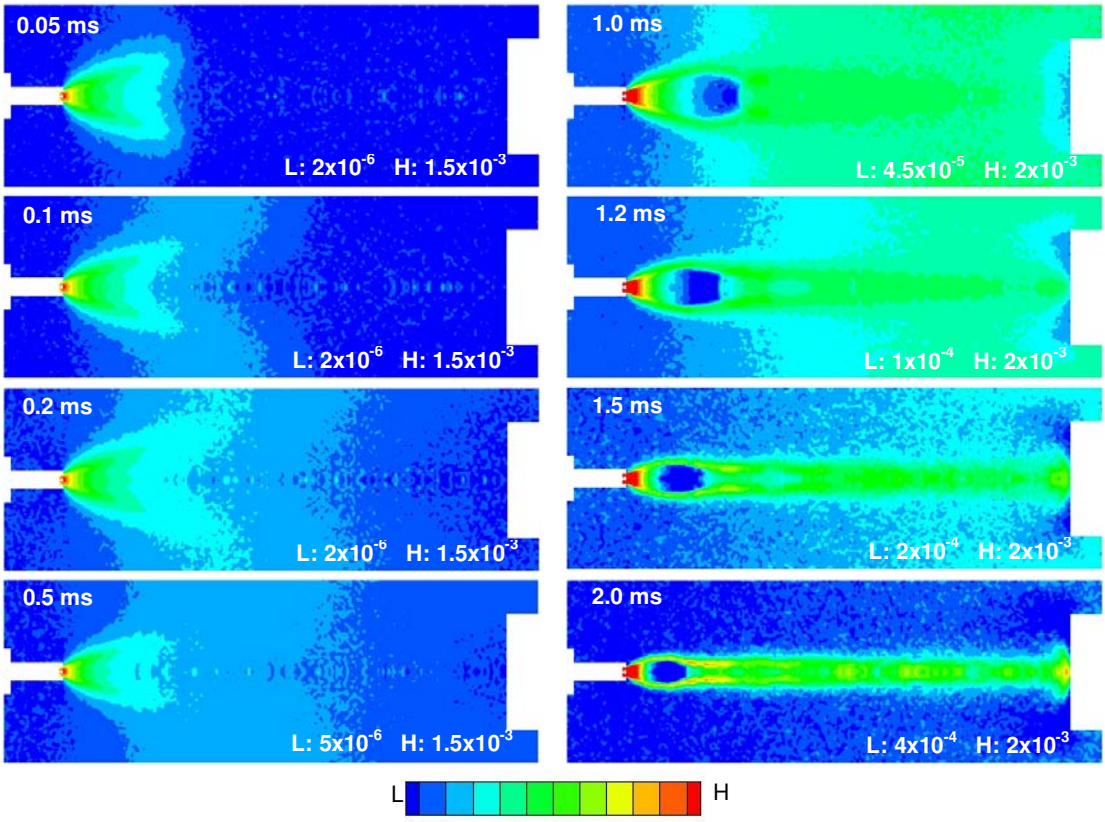

Figure 7.6. Contours of density [kg/m^3] for the PP-CVD flow field case I. Note that the scale is exponential and varies between plots. The values on the figures give the range of density contours in that figure.

The collapse of the jet after the inlet valve closes was also investigated during this simulation, although this occurred after a much shorter injection time, and consequently at a lower reactor pressure, than would normally be the case. Figure 7.7 shows contours of axial velocity as the jet structure collapses.

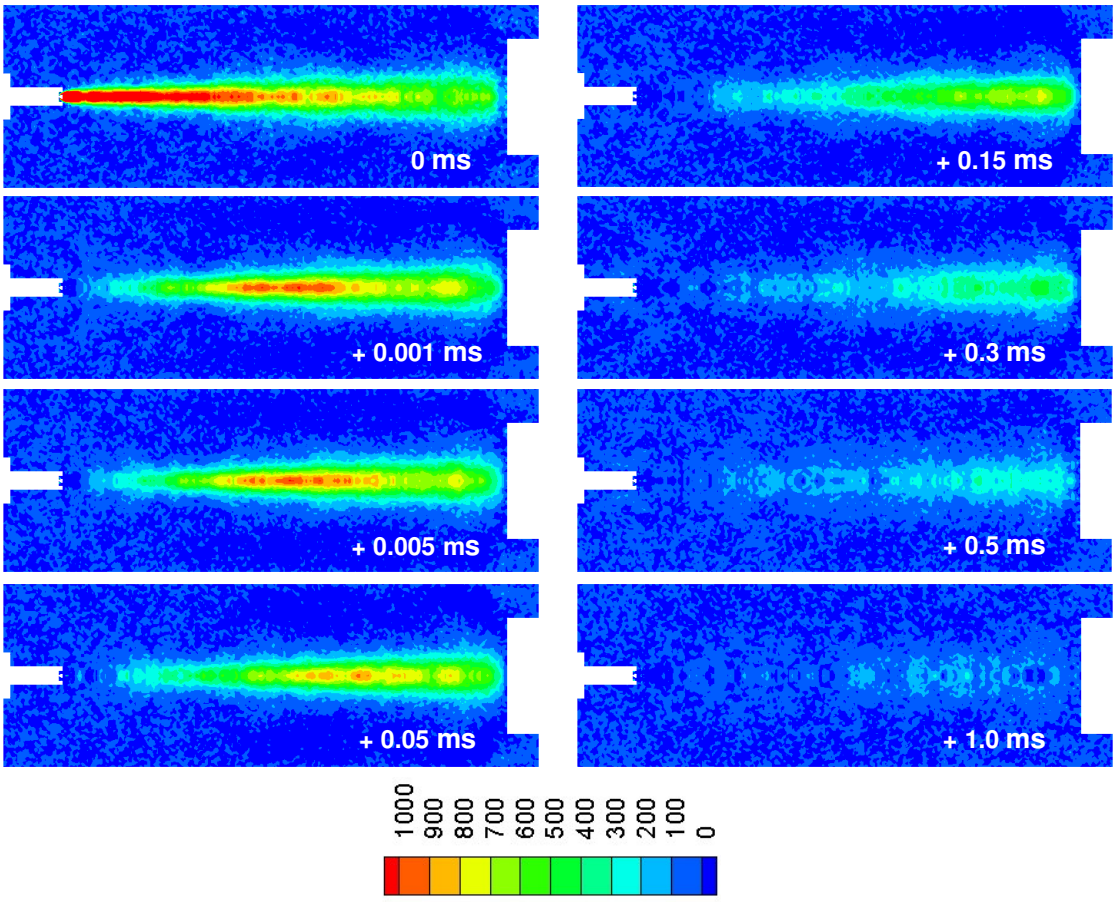

Figure 7.7. Contours of axial velocity after the inlet orifice closes (at 20ms) for case I.

7.4.2 Case II – 1 atm Supply Pressure

As mentioned above, the 1 atm supply pressure case was used as a test of PDSC's capability to simulate PP-CVD reactors at typical experimental reactor pressures. At such high pressures, the computational expense of the simulations is also high, but the full flow phenomena during the initial injection transient will be captured.

Figure 7.8 shows the grid detail near the orifice showing the Navier-Stokes region boundary. The full grid is not shown as the cells are too small to be resolved in the image.

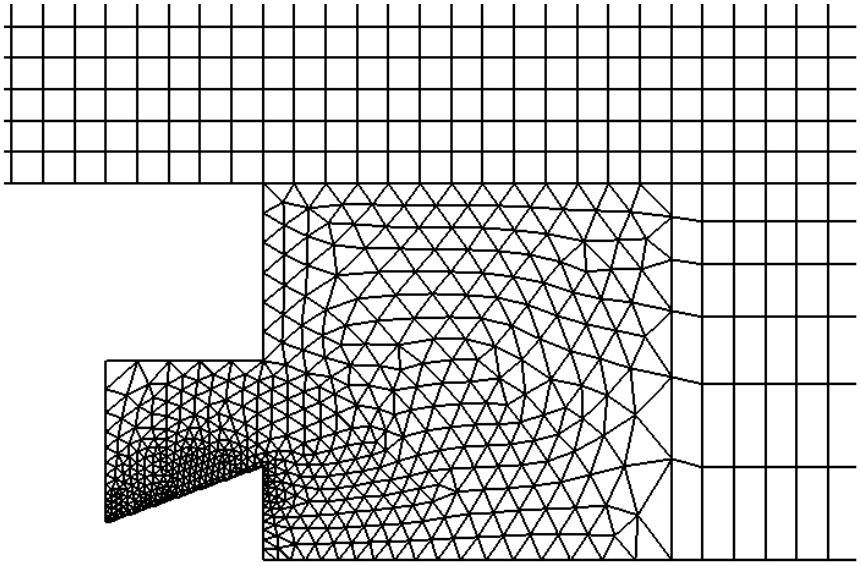

Figure 7.8. Simulation grid detail near the inlet orifice for PP-CVD flow field case II.

The inlet parameters for the PDSC simulation were determined in the same way as for case I above.

Figure 7.9 shows contours of axial velocity, radial velocity and temperature as the flow field develops during the first 4.0ms of the injection phase.

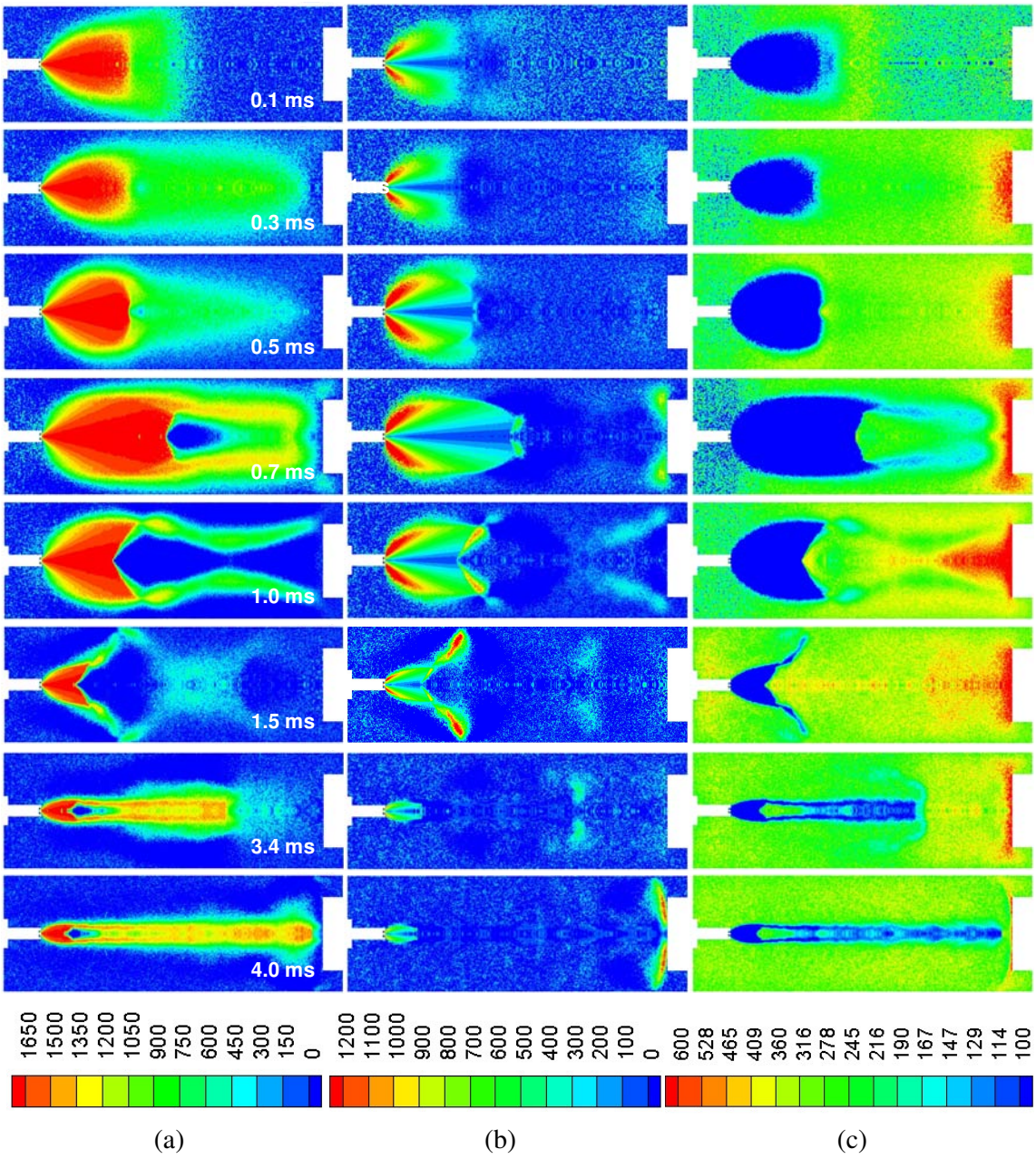

Figure 7.9. Contours of a) axial (x-component) velocity [m/s], b) radial (y-component) velocity [m/s] and c) total gas temperature [K] at various flow times for PP-CVD flow field case II.

Figure 7.10 shows a close up view of the contours of radial velocity near the nozzle inlet, showing the double expansion fans forming from the inlet orifice and the nozzle lip and figure 7.11 shows the contours of density using a sliding density scale during the first 4.0ms of flow.

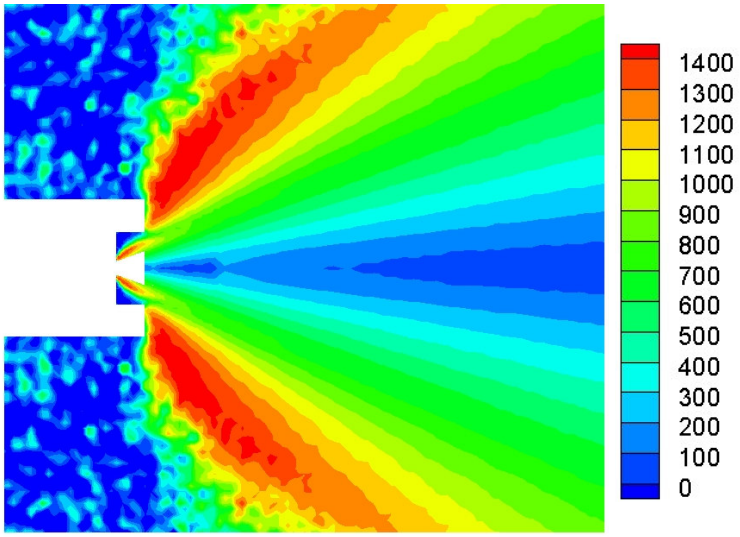

Figure 7.10. Contours of radial velocity [m/s] near the PP-CVD inlet nozzle at 1.0ms showing the double expansion fan formed at the orifice and nozzle lip.

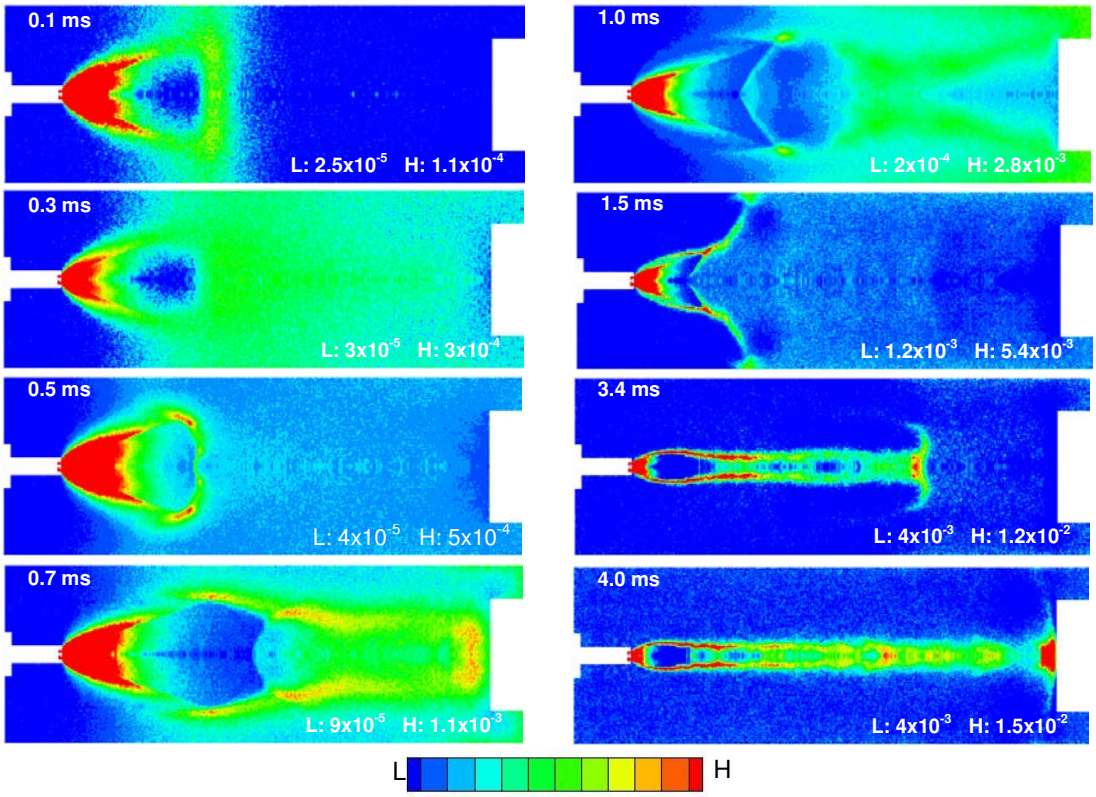

Figure 7.11. Contours of density [kg/m^3] for the PP-CVD flow field case II. Note that the scale is linear and varies between plots. The values on the figures give the range of density contours in that figure.

7.5. Discussion

Figures 7.5 and 7.6 show that the flow field in the PP-CVD reactor during the injection phase expands rapidly, and then contracts to form a quasi-steady under-expanded jet structure (with similar features to that illustrated in figure 4.1) by approximately 1.5ms. This is only a small fraction of a typical injection time which means that the jet structure is quasi-steady during the majority of the injection phase. From the CVD perspective, this quasi-steady jet is undesirable since it will result in a boundary layer on the substrate in this reactor configuration. However, as discussed in section 5.5, the operating principle of PP-CVD is that the precursor is delivered into the reactor as rapidly as possible during the injection phase, and then diffuses to the surface during the pump-down phase. The majority of the actual deposition process occurs during the pump-down phase, so deposition non-uniformity incurred during the injection phase is negligible.

Figure 7.7 shows that the collapse of the jet occurs rapidly after the inlet orifice is closed, and results in a uniform flow field soon after the jet shuts down, as suggested in section 5.4.2. Where the jet is shut down at higher reactor pressures, this collapse will occur even more rapidly due to the higher background pressure and corresponding reduced size of the jet.

In the higher supply pressure case (figures 7.9 and 7.11) the gas is less rarefied, even though the supply pressure to initial reactor pressure is the same, and the shock structure is more pronounced. The initial expansion is very rapid, and a shock propagates along the length of the reactor, reflecting from the substrate at approximately 0.3ms. After approximately 0.5ms the features of an under-expanded jet become distinguishable including the Mach disc and barrel shock, however the shock reflection from the reactor walls and from the substrate disrupts this structure. Some interesting features include dual barrel shocks formed by the expansion fan from the orifice and the lip of the orifice holder shown in figure 7.10, and the vortex structure visible at 1.5 ms. As the expansion continues, the highly transient structure begins to die down and a quasi-steady under-expanded jet begins to form. As the pressure in the reactor rises this jet begins to contract, and this contraction is expected to continue until the jet shuts off and collapses.

For both case I and case II, the operating principle remains the same: a rapid injection followed by a relatively slow pump-down results in high uniformity and precursor conversion efficiency. The simulations suggest that non-uniformity during the injection phase can be

minimised by adopting designs in which the jet does not impinge directly on the substrate. PDSC is an ideal tool to optimise these designs. Equally, the impingement of shock structures on the substrate may also be undesirable, however because jet and shock impingement occur during only a small fraction of the process cycle time, the effect on the overall process is likely to be negligible. They key design rule for the injection phase, is to deliver as much precursor as possible to the reactor volume, as rapidly as possible and *preferably* avoid impingement of the inlet jet on the substrate.

Figures 7.5 to 7.7 and 7.9 to 7.11 demonstrate some of the problems inherent in using DSMC throughout the whole flow field. There is a large amount of scatter in the stationary regions of the flow where the macroscopic velocity of the flow is a small fraction of the thermal velocities. This is a particular problem in the stagnant area above the nozzle where the density remains low for a considerable period, resulting in a small number of sampling particles per cell. Potential methods for overcoming these difficulties are discussed in chapter 9. The scatter also tends to be high near the axis of symmetry, however this effect was reduced by increasing the size of the sampling cells in the radial direction near the axis (see figures 7.4 and 7.8) and by employing radial weighting factors.

7.6. Conclusion

The simulations in this chapter represent the first attempt to simulate a PP-CVD flow field at realistic reactor pressures during the injection phase. They illustrate that parallelised DSMC is a feasible method for the simulation of PP-CVD and that much about the reactor flow field can be learned from simulations using this technique.

The computational expense of the simulations remains high, although it is well within the range of most PC cluster systems. The simulations in this chapter were primarily limited by difficulties in exporting the existing PDSC code to larger cluster systems, and high user demand on the available clusters.

The simulations also suggest that the specific details of the injection phase are actually relatively unimportant in PP-CVD reactor design. As long as the reactant is delivered to the reactor volume as rapidly as possible, and that a relatively uniform distribution of precursor

can be achieved following the injection phase, deposition uniformity and reactor efficiency will remain high during the pump-down phase.

Despite the above conclusion, PDSC remains a powerful analysis tool for the design of PP-CVD systems. Ensuring that the conditions of precursor uniformity can be met after the injection phase is important, and identifying important flow features (such as the double expansion fan in the reactor design simulated in this chapter) will enable system designs to be improved and optimised.

8. Future Work I: Advanced Modelling Techniques

8.1. Introduction

This thesis has concentrated on developing accurate methods of modelling the flow in PP-CVD reactors. The basic model presented in chapter 5 provided a good understanding of the mechanisms behind PP-CVD reactor efficiency and deposition uniformity; however was unable to simulate realistic reactor conditions. The development of unsteady parallel DSMC (PDSC) techniques in chapter 6 enabled the simulation of realistic reactor conditions for the first time (chapter 7); however the computational expense of the simulations remained large. Nevertheless, the technique enabled a substantial amount of data to be acquired about the injection phase and provided further valuable insights into PP-CVD.

Ultimately, the modelling of PP-CVD reactors should be as fast and efficient as possible, whilst providing sufficient data for improving and developing reactor designs for specific applications. While PDSC is clearly capable of modelling realistic PP-CVD, it requires computing power *presently* beyond the range of the normal user. Any reduction in computational expense that can be achieved, whether it is to be by continued improvements to PDSC or by some other method, will reduce the time, effort and, ultimately, cost in further developing the PP-CVD process.

In this chapter the continued development of PDSC and alternative methods for modelling the PP-CVD process are outlined, their advantages and disadvantages are presented and a route for future modelling work is proposed.

8.2. PDSC Development

8.2.1. Introduction

The DSMC method represents an excellent way of modelling flows in the rarefied to near-continuum regime. It is a method based on a phenomenological approach and, as such, has remained the benchmark method for modelling these types of flows for a number of decades. It has the significant advantage over methods based on differential equations that it suffers from no *numerical* error and phenomenological models for chemical reactions, wall interactions and gas collision dynamics can be incorporated readily into the basic algorithm.

The method does however have disadvantages. Unsteady flows, especially at near-continuum conditions, remain a significant challenge. Although the method is inherently unsteady, providing the balance between low statistical scatter in the results and acceptable computational times is very difficult. This is compounded by the presence of low speed regions within the flow, as occurs within PP-CVD, where the scatter is high since the thermal velocities exceed the macroscopic velocities.

DSMC has always suffered from the stigma of being perceived by some as a computationally expensive scheme. In fact, DSMC requires similar amounts of computation as CFD-type solvers for many flow problems, with superior accuracy in many cases [1]. The continued increase in computational power will bring increasing numbers of problems within the reach of DSMC for users with standard computing resources and will, with continued development, remain a valuable engineering and research tool.

Several potential developments in DSMC and PDSC have come about during the course of this research, and these are discussed below.

8.2.2. Virtual Mesh Refinement

As mentioned in section 6.2, PDSC includes a function to iteratively refine the sampling cells based on some criteria, such as local cell Knudsen number. The development of transient adaptive sub-cells discussed in section 6.4, led to the development of the concept of virtual mesh refinement first proposed by Wu *et al.* [2].

In virtual mesh refinement, the sampling cells themselves are not refined, but when an individual cell's resolution is insufficient a sub-grid of sampling cells is overlaid on the cell in the same way as is employed in transient adaptive sub-cells. These "sub-sampling cells" are stored in an array associated with the original sampling cell. The normal computational procedures are carried out on these sub-sampling cells, including nearest neighbour collision routines. During the sampling of macroscopic flow properties, the properties of the individual cells are weighted depending on the distance of their centroids to the centroid of the original sampling cell. Thus, the sampled resolution of the macroscopic flow properties remains unchanged, however the accuracy of the sampled macroscopic properties is increased.

The details of the scheme have yet to be finalised. At the time of writing this concept was under development as part of a M.E. thesis by C.-C. Su at the National Chiao Tung University in Hsinchu, Taiwan. Additionally, a 1D steady shock case and a Mach 5.73 flow over a flat nosed cylinder (equivalent to the case in reference [3]) had been successfully simulated using the technique.

8.2.3. Other Developments

PDSC is under a constant regime of iterative improvement. These tend to be minor adjustments to the procedures to improve the efficiency and reduce the computational expense of simulations. Additionally the DREAM post-processing procedure has considerable scope for improvement and is constantly being upgraded.

At the time of writing, no major developments were planned to the DSMC algorithms in PDSC, however a number of modules were planned to increase the utility of PDSC which do not specifically involve DSMC methods. These are discussed in the following sections.

8.3. Hybrid Methods

8.3.1. Introduction

Hybrid methods were briefly outlined in section 3.6.4. The basic concept is to reduce the computational expense of simulations, by using DSMC only in regions where it is required (i.e. in regions of continuum breakdown) and using a less computationally expensive continuum solver elsewhere, especially in regions of high density, collision-dominated flow. The method necessitates the use of a method to identify when to switch between the DSMC and continuum solver, and a number of breakdown parameters have been proposed as discussed in section 4.1.2.

In chapter 7 a simple hybrid method was used to reduce the computational expense of the dense flow near the PP-CVD inlet orifice. Here a single one-way coupling was used, with the Navier-Stokes solution for the whole flow field being solved first and this solution serving as an inlet boundary condition to the PDSC simulation. However, there are large regions of the PP-CVD flow field in which continuum breakdown will not have occurred, such as outside the core of the under-expanded jet, and it is appropriate to use a continuum solver in these regions if a reduction of computational expense can be achieved by doing so.

There are numerous choices for the continuum solver. Most examples in the literature use partial differential equation based Navier-Stokes [5,6] or Euler solvers [7,8], however several particle based Euler solvers have been proposed [9,10]. An alternative method is to use numerical solvers in both the continuum and kinetic regions, an example being the Unified Flow Solver being developed by Kolobov *et al.* [11,12] however, as discussed in section 4.2, none of these methods is presently mature enough to model PP-CVD.

In this section, several routes for the development of hybrid methods for PP-CVD are discussed. Additionally, a new hybrid scheme based on the Quiet DSMC scheme for Euler flow developed by Albright *et al.* [13] and Peter [14] is proposed.

8.3.2. Navier-Stokes or Euler/DSMC

PDSC already includes a hybrid Navier-Stokes solver for the continuum regime which is described in the paper by Wu and Lian [15] and Wu *et al.* [6]. This hybrid scheme couples the standard PDSC solver with the parallel UNIC-UNS scheme developed by Chen *et al.* [16] and includes full parallelisation, hybrid two-/three-dimensional meshes and a variety of turbulence models and boundary conditions.

Some of the advantages of using such a hybrid scheme (aside from the ability to simulate the flow accurately in both the continuum and rarefied regimes) are that *ad hoc* schemes are not required for adequate capture of shocks, variable particle weighting can be used in different DSMC regions to reduce the statistical scatter in the results (which can also help reduce the noise in the boundary conditions between the DSMC and Navier-Stokes solutions, which is otherwise a major handicap) and loose but accurate coupling can be achieved between the solvers.

Coupling between the schemes is achieved by first solving the entire flow field using the Navier-Stokes solver. A continuum breakdown parameter is then used to conservatively assess the boundary between the solvers at S(I), as shown in figure 8.1. Conventionally, the scheme used was the maximum value of Wang and Boyd's breakdown parameter (equation 4-2) based on gradients of temperature, density or velocity, or in the case of diatomic gases, a thermal non-equilibrium parameter which detects the separation of the rotational and kinetic temperatures [6], however these parameters tend to result in the boundary layer being selected in the DSMC region, which results in unnecessary computational expense. More recent work

suggests that the use of equation 4-2 based on gradients of pressure alleviates this problem by excluding the boundary layer from the DSMC domain [2].

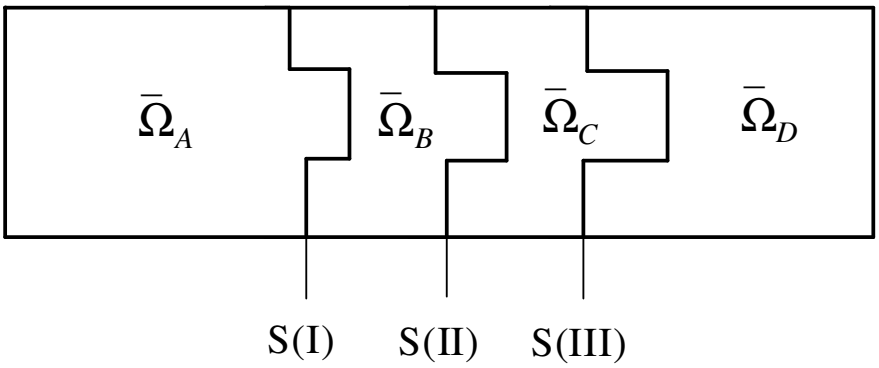

Figure 8.1. Definition of solution boundaries for hybrid Navier-Stokes/DSMC solver

Following the initial definition of the domain boundary, PDSC is used to solve the flow field in the region identified as the DSMC domain, plus a number of cells into the continuum domain $\overline{\Omega}_A \cup \overline{\Omega}_B \cup \overline{\Omega}_C$, using a Maxwell-Boltzmann distribution of particle velocities at the boundary with the Navier-Stokes solution, S(III). This results in additional computational expense but is justified on the grounds that this approach is conservative and that DSMC is valid in both domains anyway. The Navier-Stokes domain is then used to re-solve the whole region originally identified as being in continuum $\overline{\Omega}_B \cup \overline{\Omega}_C \cup \overline{\Omega}_D$ using a Dirichlet boundary condition at the interface based on samples from the PDSC solution, S(I). Finally, an intermediate boundary S(II), between S(I) and S(III), is created with PDSC updating the solution in $\overline{\Omega}_A \cup \overline{\Omega}_B$ and UNIC-UFS providing the solution in $\overline{\Omega}_C \cup \overline{\Omega}_D$.

The current work on the hybrid UNIC-UFS/PDSC solver is primarily based around reducing the computational cost of the procedure. An example of the way this is being achieved is to apply a convergence criterion to the continuum solution to determine when to stop updating the solution, rather than a fixed number of time steps as per the DSMC solution.

The use of the hybrid solver discussed above to investigate the PP-CVD flow field is a possibility; however before this can be done an unsteady version of the code must be developed which is not necessarily an easy task. The merit of carrying out this modification is still being debated, primarily because the computational expense of the simulations is likely

to remain high since the Navier-Stokes solution would need to be recalculated and would need to re-converge at frequent intervals (probably more frequently than just at the output intervals). It seems likely that one of the particle-only hybrid methods mentioned below will be more efficient for unsteady flow.

The use of some kind of particle-only Euler method in the continuum region, such as the one proposed by Macrossan [9] which was discussed in section 3.6.4, has several potential advantages. Primarily, coupling between the DSMC and Euler solvers is greatly simplified. The particles simply transfer between cells at the boundary between the solvers, and the method of updating particle velocities switches from the DSMC collision mechanism to Pullin's less computationally expensive Equilibrium Particle Simulation Method (EPSM) [10] in the Euler region. The disadvantage of such a scheme is that it is still subject to statistical scatter and the number of particles in the continuum cells is still relatively large. In section 8.3.3 a method is proposed with the potential to overcome these difficulties.

8.3.3. Quiet DSMC/DSMC

Quiet DSMC (QDSMC) was first proposed as an Euler solver by Albright *et al.* [17] and is more fully described and developed in further papers by Albright *et al.* [13,18,19] and the paper by Peter [14]. Instead of using random numbers within the algorithm to build up a stochastic representation as in DSMC, or by sampling randomly from a known distribution as in Macrossan's method, QDSMC uses a deterministic process whereby particles are repeatedly created, moved and then destroyed. The method used for the creation of particles utilises a Gauss-Hermite quadrature to replace the random number terms deterministically. The method enables the particle distribution function to be determined *with no statistical scatter* using only a small number of simulated particles. This has advantages over a pure DSMC algorithm which requires a very large number of sampled particles to obtain a smooth velocity distribution function.

To understand how QDSMC works, it is best to use the illustrative example given by Allbright *et al.* [17]. Here the hydrodynamics example from Pullin [10] is invoked, whereby the particle movements and their velocities over a time step *dt* are given by (here using a one dimensional case only):

$$x(t+dt) = x(t) + vdt \tag{8-1}$$

$$v(t+dt) = v(t) + \sqrt{2\sigma_v^2 dt}\,N(0,1) \tag{8-2}$$

where $\sigma_v^2(x(t), t)$ is the local velocity variance at time t and $N(0,1)$ is a random variable.

The procedure starts at some initial time t by creating n particles on i spatial grid points x_i (for the one-dimensional case) according to an initial velocity distribution function $f(x_i,t)$ with each particle carrying a mass $f(x_i,t)/n$. Each particle is then moved and its velocity updated according to equations (8-1) and (8-2) by utilising a random variable $N(0,1)$. The particles are then weighted back onto the grid to give the new distribution function $f(x_i,t+\Delta t)$.

The procedure discussed above works well and it forms the basis of several other similar schemes, however it requires a large number of particles in the sampling cells to give an adequate reduction in statistical noise. QDSMC solves this problem by replacing the random variable $N(0,1)$ with the weights w_j and abscissas q_j (i.e. the Gauss-Hermite parameters) of a Gaussian quadrature approximation. This can be achieved since $N(0,1)$ represents a normal distribution with a probability density function given by:

$$p(x) = \frac{e^{-x^2/2}}{\sqrt{2\pi}} \tag{8-3}$$

The Gaussian quadrature approximation, which becomes exact when the function $f(x)$ is a linear combination of the $2J-1$ polynomials $x^0, x^1, \ldots, x^{2J-1}$, for equation (8-3) is:

$$\int_{-\infty}^{\infty} \frac{e^{-x^2/2} f(x) dx}{\sqrt{2\pi}} = \sum_{j=1}^{J} w_j f(q_j) \tag{8-4}$$

Hence, equation (8-4) can be applied to equation (8-2) to give:

$$v(t+dt) = v(t) + \sqrt{2\sigma_v^2 dt}\,q_i \tag{8-5}$$

The application of Gauss-Hermite parameters provides the "quiet start" (i.e. low statistical noise) to the simulation by generating new particles in each cell via the moments stored on the grid points. The particles are then advanced, and the new moments of quantities carried by the particles are accumulated on the grid, the old particles are destroyed, and the process repeats.

The method is not limited to the simple example of equations (8-1), (8-2) and (8-3): it can be applied to other systems and this has been done for plasmas [13,17], Coulomb collisions [19] and, importantly for PP-CVD, to particle-based Eulerian methods [13]. The method allows results to be obtained with low statistical scatter using very few particles per cell and has been shown to provide excellent results for a number of examples, including strong shocks. The references listed above should be consulted for more details.

The possibility of coupling QDSMC with DSMC is very promising indeed since it allows both a reduction in the computational expense of simulating collisions *and* a reduction in the number of particles required per cell. This idea is likely to result in a significant reduction in computational expense for simulating the continuum regions in the flow field, while leaving DSMC to deal with the non-continuum regions. The major advantage is that a strictly particle-based method is maintained. Coupling isn't quite as straightforward as Macrossan's method (where only the collision algorithm needs to be changed) since particles leaving the DSMC region must be represented by a smaller number of particles in the QDSMC region, and vice versa. However, the coupling could be provided relatively easily by buffer cells supplying particles to the DSMC region generated from a Maxwell-Boltzmann distribution obtained from the QDSMC moments, and by a "quiet start" to the QDSMC region from the DSMC macroscopic flow properties.

8.4. Conservation Element/Solution Element (CESE) Based Methods

8.4.1. Introduction

The Conservation Element/Solution Element (CESE) method is a new frame work for solving conservation laws in continuum mechanics developed by Chang and To in 1991 [20]. Rather than an extension or modification of any other traditional numerical method (i.e. finite element, finite volume or finite difference method), the CESE method has been developed entirely from fundamentals. The use of the CESE method in the fields of computational fluid dynamics, aero-acoustics and electro-magnetics has begun to gain traction, despite some opposition from supporters of more traditional schemes.

There exist a wide array of traditional computational fluid dynamics (CFD) solvers which are usually developed for specific problems and then extended to other situations, using *ad hoc* methods, where they are often unsuitable. The motivation for developing the CESE method

was the desire to construct a much more general scheme, based on fundamental physics in a logical numerical framework.

The key features of the CESE method are that the modelling is based on the original integral form of the conservation equations, rather than a differential form. To achieve this space-time is treated as a single entity and conservation of global and local fluxes of mass, momentum and energy within this domain are enforced, as opposed to traditional methods which only enforce spatial flux. Because no dimensional splitting is required, the CESE method is a genuine multi-dimensional (space *and* time) approach to the solution of conservation equations.

One difficulty in time accurate computation is that a fine balance must be achieved to maintain stability and accuracy, since numerical dissipation increases computational stability but reduces the solution's accuracy. A key requirement in the development of the CESE method was to develop a non-dissipative core scheme and to add controlled dissipation to stabilise the system.

Recent discussions have indicated that the CESE method could be used as a solution method for the Model Boltzmann Equations (MBEs). The proposed method is potentially ideal for the simulation of PP-CVD, in that it deals with an unsteady problem at the kinetic level, and has no inherent difficulties dealing with a large range in flow velocities. An impressive example of the ability to deal with such a wide range in velocities was presented by Yen [21], who used CESE to solve the Navier-Stokes equation for the startup and shutdown of a rocket diffuser system, and was able to capture a velocity range from approximately zero to Mach 8 without requiring a Riemann solver or flux-splitting.

In this section the basic features and methodology of the CESE method are briefly outlined, including its advantages over other numerical schemes. The use of CESE as a Model Boltzmann Equation (MBE) solver is then proposed.

8.4.2. CESE Method

In 1992 Chang pointed out that the origin of numerical diffusion in traditional schemes is that these schemes are not invariant under a space-time inversion [22]. That is, marching the

solution obtained using a traditional scheme back in space-time does not obtain the original conditions (i.e. time integration cannot be carried out reversibly).

The exact solution to a partial differential equation at any time must be completely determined by the initial state, the solution at a point must have a finite domain of dependence at that point at an earlier time and the solution must not dissipate with time. These requirements dictate the solver must be a two-level, explicit, non-dissipative scheme. No traditional methods meet these requirements.

In the CESE a-scheme space-time mesh points are staggered to form a two-level, explicit scheme which is invariant under space-time inversion. As shown for the 1D case in figure 8.2, each cross-shaped solution element (SE) is also associated with two rectangular conservation elements (CEs).

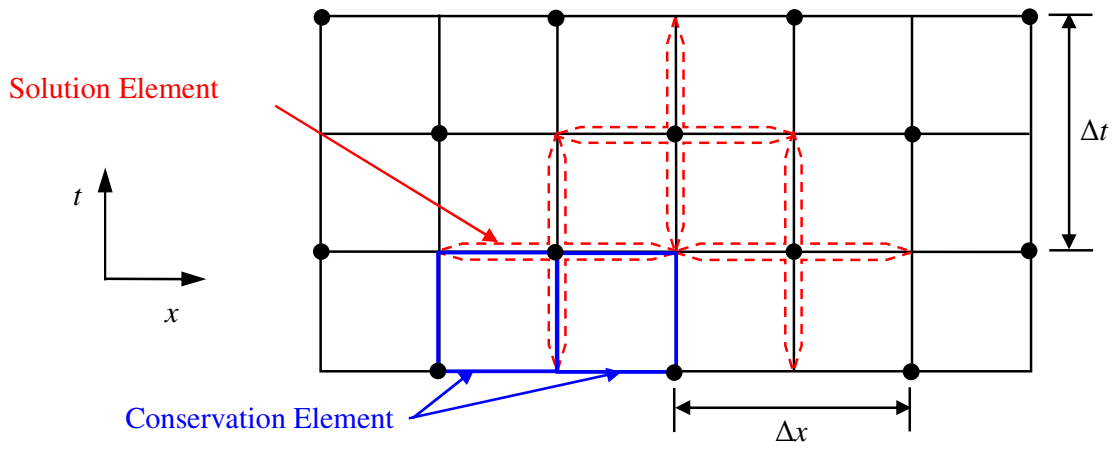

Figure 8.2. One dimensional conservation element-solution element (CESE) grid

As can be seen from figure 8.2, the CEs over which conservation of space-time fluxes are enforced do not overlap and so, since the fluxes between the individual CE faces are uniquely defined, these fluxes are conserved both locally *and* globally. Each face of a CE belongs unambiguously to one SE which utilise a simple approximation for the space-time equations. The CE/SE scheme thus fulfils the requirement of a two-level, explicit, non-dissipative scheme.

More details of the various CE/SE schemes can be found in references [20,23-27].

8.4.3. Model Boltzmann Equation (MBE) Solver Using CESE

Equations (3-20) and (3-21) represent the Model Boltzmann Equations (MBEs) which are ideally suited for solution by the CESE method. As mentioned in section 3.5, MBEs have been solved using finite-difference schemes, however these schemes are prone to the same problems which encumber traditional Navier-Stokes solvers.

The CESE method is ideally suited for solving the MBEs since the MBEs are already cast into the form required for the CESE a-scheme [27] with the collision term acting as a source term in the equations. Since CESE treats space-time in a unified manner, the technique is ideal for building the kind of unsteady schemes necessary for simulating processes such as PP-CVD.

Development of a CESE solver for the MBEs has already begun at National Chiao Tung University in Hsinchu, Taiwan.

8.5. Conclusions

In this section, a wide variety of potential simulation methods for PP-CVD were presented, many of which are novel techniques which will be useful for applications other than PP-CVD modelling. Probably no single method will be suitable for all PP-CVD reactor configurations and it is likely that the best approach is to develop a number of these methods and select the appropriate one for a particular reactor design.

Reactors which operate at lower pressures will generally need non-continuum solvers and so the development of PDSC and MBE based solvers is appropriate for these designs. At somewhat higher pressures, hybrid methods will allow the computational expense of non-continuum solvers to be reduced. Some reactors will require only continuum solvers: indeed recent work by T.-H Lin, a master's degree student at the National Chaio-Tung University in Taiwan, indicates that Navier-Stokes solvers with appropriate shock capturing techniques may provide adequate engineering results for reactors with higher operating pressures (i.e. reactor pressure greater than approximately 1000Pa). However, the development of CESE Navier-Stokes solvers will provide a more accurate and robust method for carrying out these simulations than traditional CFD schemes.

In the author's opinion, the best compromise method which will allow a wide range of PP-CVD reactor configurations to be modelled is a hybrid particle-only method such as a hybrid DSMC-QDSMC code. Such a method is able to cover a wide range of non-continuum to continuum flows, without the problem of the complicated coupling procedures of hybrid DSMC-Navier-Stokes solvers.

A number of modelling problems for PP-CVD have yet to be addressed. For example, many PP-CVD reactors operate using a liquid metal-organic precursor introduced into the reactor via an ultrasonic nozzle. Although the operating principal of these reactors – a rapid unsteady expansion of precursor, followed by a relatively long pump-down period – remains the same, an evaporating droplet model needs to be incorporated into the reactor simulation method. A further problem arising from complex metal-organic precursors is the need to derive collision parameters for particle-based models, and the quantum chemistry method developed by Wu and Hsu [28] may be appropriate for this. These issues will be discussed in greater depth in chapter 10.

PP-CVD has already provided the motivation for the development of unsteady parallel-DSMC methods and is at least partially responsible for inspiring the initiation of the development of the other novel flow modelling methods mention in this chapter. These methods will undoubtedly be useful in many other applications and their continued development is extremely worthwhile.

References

[1] G.A. Bird, "Sophisticated DSMC", Lecture notes from the short course at the DSMC07 meeting, Santa Fe, New Mexico (2007).

[2] J.-S. Wu, K.-C. Tseng, H.M. Cave, Y.-Y. Lian, J.-P. Yu, Y.-S. Chen, M.C. Jermy and S.P. Krumdieck, Developing a General-Purpose Parallelized Direct Simulation Monte Carlo Code (PDSC) Using Unstructured Grid: A Progress Report, presentation at DSMC: Theory, Methods and Application, Sante Fe, New Mexico (2007).

[3] G.A. Bird, Molecular Gas Dynamics and the Direct Simulation of Gas Flows (Clarendon Press, Oxford, 1994).

[4] Q. Sun, I.D. Boyd, and G.V. Candler, A hybrid continuum/particle approach for modelling subsonic rarefied gas flows. *J. Comput. Phys.* 194, 256-277 (2004).

[5] C.R. Duttweiler, D. Baganoff, W.J.A Feiereisen, Hybrid Navier-Stokes/Particle Method for Simulating Rarefied Flow, American Physical Society Division of Fluid Dynamics Meeting (1997).

[6] J.-S. Wu, Y.-Y. Lian, G. Cheng, R.P. Koomullil and K.-C. Tseng, Development and verification of a coupled DSMC-NS scheme using unstructured mesh, *J. Comp. Phys.* 219(2), 579-607 (2006).

[7] H.S. Wijesinghe, R.D. Hornung, A.L. Garcia and N.G. Hadjiconstantiou, Three-dimensional hybrid continuum-atomistic simulations for multiscale hydrodynamics, *J. Fluids Eng*. 126(5), 768-777 (2004).

[8] R. Roveda, D.B. Goldstein and P.L. Varghese, Hybrid Euler/Direct Simulation Monte Carlo Calculation of Unsteady Slit Flow, *J. Spacecraft Rockets* 37(6), 753-760 (2000).

[9] M.N. Macrossan (2001) A Particle-Only Hybrid Method for Near-Continuum Flows, in Proc. of 22nd International Symposium on Rarefied Gas Dynamics, 388-395, Sydney, Australia (2001).

[10] D.I. Pullin, Direct simulation methods for compressible ideal gas flow, *J. Comput. Phys.* 34, 231-144 (1980).

[11] V.I. Kolobov, S.A. Bayyuk, R.R. Arslanbekov, V.V. Aristov, A.A. Frolova and S.A. Zabelok, Construction of a unified continuum/kinetic solver for aerodynamic problems, *J. Spacecraft Rockets* 42(4), 598-606 (2005).

[12] V. Aristov and V. Kolobov, Lecture notes from the Workshop on Direct Boltzmann Equation Solver and Its Applications, Hsinchu, Taiwan (2007).

[13] B. J. Albright, D.S. Lemons, M.E. Jones, and D. Winske, Quiet direct simulation of Eulerian fluids, *Physical Review E* 65, 1-4 (2002).

[14] W. Peter, Quiet direct simulation Monte-Carlo with random timesteps, *J. Comp. Phys.* 221, 1-8 (2007).

[15] J.-S. Wu and Y.-Y. Lian, Parallel three-dimensional direct simulation Monte Carlo method and its applications, *Comput. Fluid* 32(8), 1133-1160 (2003).

[16] UNIC-UNS User's Manual, Engineering Sciences Incorporated, Huntsville (AL) (2000).

[17] B.J. Albright, M.E. Jones, D.S. Lemons and D. Winske, Kinetic plasma modeling with Quiet Monte Carlo Direct Simulation, in Proc. of The Sixth International School/Symposium for Space Plasma Simulations, Garching, Germany (2001).

[18] B.J. Albright, W. Daughton, D.S. Lemons, D. Winske, and M.E. Jones, Quiet direct simulation of plasmas, *Phys. Plasma* 9(5), 1898-1904 (2002).

[19] B.J. Albright, D. Winske, D.S. Lemons, W. Daughton, and M.E. Jones, Quiet Direct Simulation of Coulomb Collisions, *IEEE Trans. Plasma Sci.* 31(1), 19-24 (2003).

[20] S.-C. Chang and W.-M. To, A New Numerical Framework for Solving Conservation Laws – The Method of Space-Time Conservation Element and Solution Element, NASA Technical Memorandum 104495 (1991).

[21] J. Yen, Transient Simulations of a Rocket-Diffuser System Using CESE Method, Presentation at 1st Taiwan-USA Workshop on CESE Method, Hsinchu, Taiwan (2007).

[22] S.-C. Chang, On an Origin of Numerical Diffusion: Violation of Invariance Under Space-Time Inversion, NASA Technical Memorandum 105776 (1992).

[23] S.-C. Chang, New Developments in the Method of Space-Time Conservation Element and Solution Element – Applications to the Euler and Navier-Stokes Equations, NASA Technical Memorandum 106226 (1993).

[24] S.-C. Chang, X.-Y. Wang and C.-Y. Chow, New Developments in the Method of Space-Time Conservation Element and Solution Element – Applications to Two-Dimensional Time-Marching Problems, NASA Technical Memorandum 106758 (1993).

[25] S.-C. Chang, X.-Y. Wang, C.-Y. Chow and A. Himansu, The Method of Space-Time Conservation Element and Solution Element – Development of a New Implicit Solver, NASA Technical Memorandum 106897 (1995).

[26] S.-C. Chang, X.-Y. Wang and C.-Y. Chow, The Method of Space-Time Conservation Element and Solution Element – A New High–Resolution and Genuinely Multidimensional Paradigm for Solving Conservation Laws I. The Two Dimensional Time Marching Schemes, NASA Technical Memorandum 208843 (1998).

[27] S.-C. Chang, The Space-Time Conservation Element and Solution Element Method – Motivating Ideas, Basic Schemes and It's Recent Developments, In Proc. of 14th National Computational Fluid Dynamics Conference, Nantou County, Taiwan (2007).

[28] J.-S. Wu and Y.-L. Hsu, Derivation of Variable Soft Sphere Model Parameters in Direct-Simulation Monte Carlo Method Using Quantum Chemistry Computation, *Jpn. J. Appl. Phys.* 42, 7574-7575 (2003).

9. Future Work II: PP-CVD Development

9.1. Introduction

This thesis has concentrated primarily on the development of methods for modelling the flow field in existing experimental PP-CVD reactors and in developing an understanding of the physical mechanisms leading to the observed operating characteristics of these reactors. The modelling tools which have been developed and proposed have been designed to be flexible enough to assist in the design of future PP-CVD reactor development.

After a continued period of experimental and theoretical development of the PP-CVD concept, facilitated by numerical simulation, it is likely that future design configurations will be dictated primarily by industrial requirements. In this chapter, the future work required to develop the PP-CVD concept to the point of commercialisation will be presented and several possible concepts for alternative PP-CVD designs will be outlined.

9.2. Reactor Development

To date, PP-CVD reactor design has focussed on flexible experimental systems capable of depositing a variety of materials on primarily planar substrates. In these systems, substrate throughput or system automation has not been a consideration, and the reactor design has primarily been driven by flexibility, cost minimisation and the availability of appropriate components. Nevertheless, and perhaps remarkably, these basic systems have been capable of producing a wide variety of materials with widely varying operating conditions, and have enabled a good deal to be learnt about the process operating parameters.

With the development of simulation tools for the process, and the increased theoretical and experimental knowledge gained from the early designs, the time has been reached for which the next generation of experimental reactors can be developed. These reactors will be developed to overcome some of the problems suffered with the early designs and will provide the first step to development for full industrial commercialisation for specific applications.

Some of the technical difficulties encountered with the early designs are illustrated in figure 9.1 and include problems with leaking around the vacuum seals, problems with heater design

(specifically uniform substrate heating and heater failure under the pulsed flow regime), time-consuming substrate loading procedures and jet impingement on the substrate (in the case of direct liquid injection reactors, the problem was droplets forming on the ultrasonic nozzle and dripping onto the substrate which is positioned directly below the nozzle).

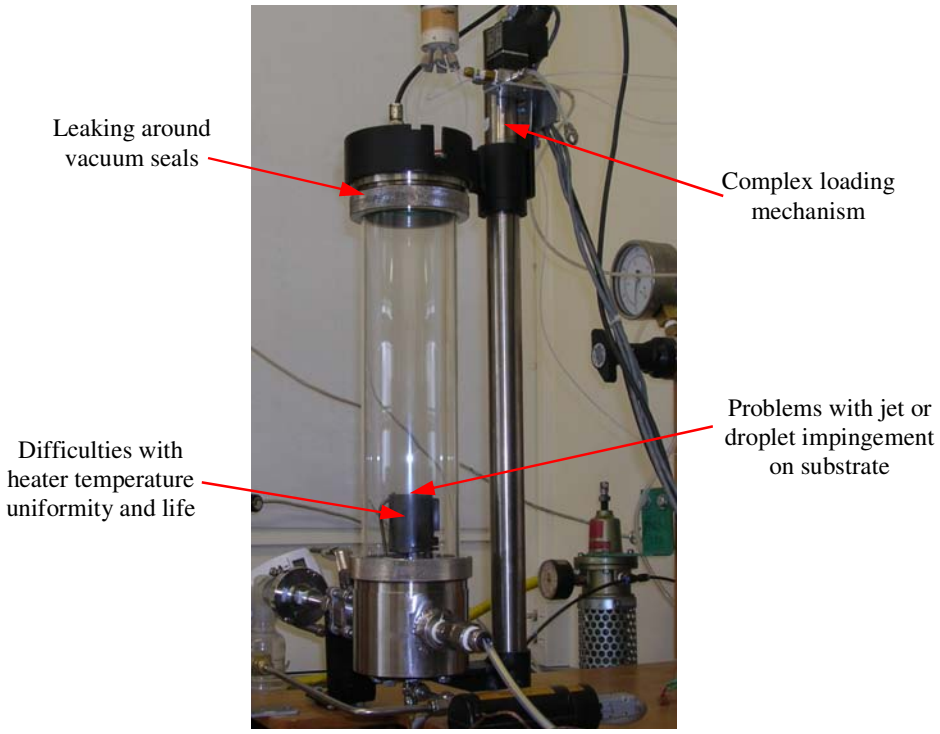

Figure 9.1. Basic PP-CVD reactor design technical difficulties.

A number of concepts for improving the experimental reactor design have been proposed by Dr. Susan Krumdieck, and these are illustrated in figure 9.2. Here the reactor is more compact with the inlet nozzle positioned below and behind the heater. This prevents jet/droplet impingement on the substrate. The nozzle diameter is increased, enabling the required amount of precursor to be delivered into the reactor more rapidly. The loading and sealing difficulties are overcome by using a hinged lid, which means only a single surface needs to be sealed. The assembly is made from stainless steel with a single quartz window for observation and possibly so the substrate can be heated externally by an ultra-violet heating lamp. The substrate heater is side mounted which more closely resembles the configuration of most robotic substrate loaders. Overall, the system is designed to preserve the low cost and flexibility of the initial designs, while overcoming the technical problems of the earlier designs.

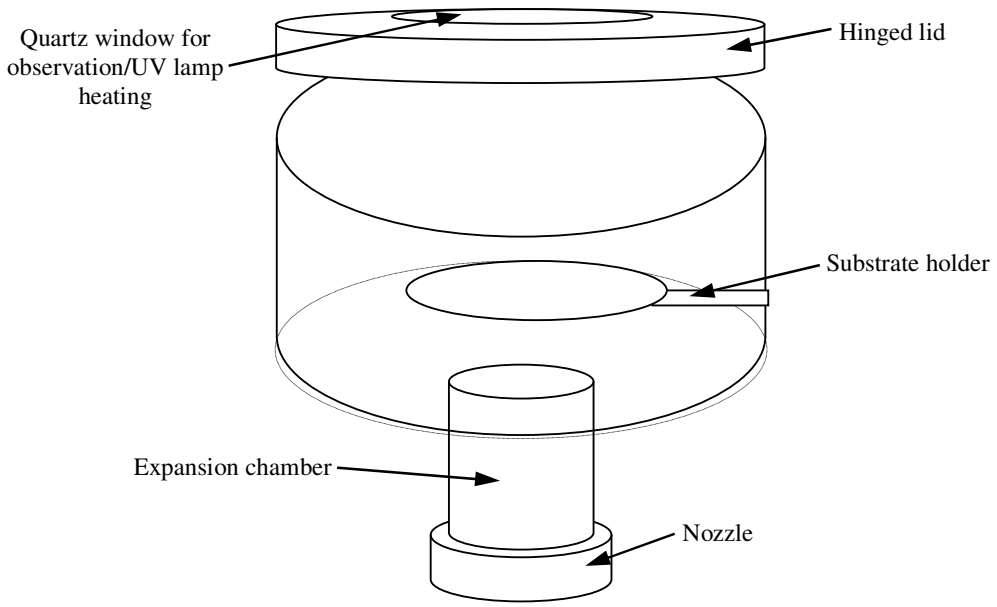

Figure 9.2. Concept sketch for new experimental reactor design [illustration courtesy of S.P. Krumdieck].

As mentioned above, ultimately the designs for specific industrial applications will be dictated by commercial requirements. These designs will be developed through a combination of design experience and modelling of the systems using the simulation tools developed and proposed in this thesis. The most important performance factors for a commercially viable CVD system are given by Krumdieck as film quality, uniformity and throughput [1]. PP-CVD has already shown itself capable of producing high quality, uniform films of a number of materials. In the experimental reactors, throughput is low despite a relatively high deposition rate, since only one substrate is in the reactor at once. Future designs require wafer stacking and automated loading systems to increase throughput.

Additional important factors for a viable CVD system include cost (including the capital cost of the equipment itself and running costs), maintenance factors (such as mean time between failures and utilisation factor), equipment footprint and process flexibility. The equipment cost of PP-CVD is not likely to be any higher than conventional CVD equipment. In fact, since the reactor designs are relatively simple (i.e. there is no requirement for complex wafer rotation mechanisms) and because only relatively low cost vacuum pumping equipment is necessary, the majority of the equipment cost is likely to be incurred in automating the wafer loading. It is highly likely that PP-CVD reactors can utilise the automation equipment (i.e.

substrate loading mechanisms) already in use for more conventional CVD designs. This will greatly facilitate the transition between experimental systems and systems for specific industrial applications. PP-CVD operating costs are also likely to be lower than conventional systems, since the precursor utilisation efficiency is high resulting in less precursor waste and precursor recovery/filtration systems can be greatly down-sized or eliminated altogether. Equipment footprint, which is another cost-related factor, is likely to be similar to conventional CVD equipment.

Maintenance requirements are also unlikely to exceed those of conventional systems. PP-CVD reactors have additional complexity in the precursor supply systems and this is likely to require extra maintenance, however the removal of the complex wafer rotation systems common to AP-CVD reactors counter-balance this to some extent.

PP-CVD reactors also have a significant advantage over many conventional CVD systems in that they are flexible manufacturing systems capable of depositing different kinds of materials on different substrates. It is conceivable that a PP-CVD reactor configured for depositing silicon from gaseous silane could be reconfigured in a short amount of time to deposit titania from a liquid metal-organic precursor. This makes it attractive equipment for niche manufacturing with short production runs requiring flexible deposition technologies.

9.3. Reactor Modelling: The Next Step

The numerical methods which will be used to facilitate the development of future PP-CVD reactors have been outlined in detail in chapter 8. In this section, the short term plan for reactor modelling will be outlined.

The first problem which must be adequately addressed is the simulation of reactors involving realistic deposition processes (for example, multiple reactive species). The best starting point is the simulation of the simple diamond deposition reactor discussed in section 2.3.2, as this enables the simulation of an existing deposition system with simple reactor geometry.

Most papers in the literature concerning the deposition of diamond films focus on the physics and chemistry of the actual surface deposition process (e.g. reference [2]), however to accurately simulate the flow field, accurate data on the flow field chemistry is required.

Despite the presence of only two species in the supply gas (H_2 and CH_4) the actual number of species likely to be present in the reactor is much higher, due to a large number of possible dissociation and recombination reactions between species in the flow. For example, Mankelevich *et al.* [3] list 37 reversible reactions involving 15 species, including several large molecules with DSMC collision parameters which do not appear to be readily available in the literature (i.e. C_2H_4 and C_2H_6). Thus, the first step to in simulating such a system is the determination of these parameters using the quantum method outlined by Wu and Hsu [4].

As mentioned in section 3.6.2, weighting factors are necessary in multi-species simulations where the concentration of one species is very low. Without these factors, to obtain accurate statistical sampling for the macroscopic properties of the low concentration species, a very large number of particles would be required. This greatly increases the computational expense and this is particularly undesirable for an unsteady simulation. The use of a weighting scheme enables approximately the same number of particles of both species to be simulated, thus facilitating accurate statistical sampling. In this case, the each simulated particle for the lower concentration species represents a smaller number of real particles than the simulated particles for the higher concentration species.

The species weighting method used in PDSC is the conservative weighting scheme developed by Boyd [5] and used by Wu *et al.* in the simulation of a silane CVD reactor [6]. In early species dependent weighting schemes, the momentum and energy are not conserved within each collision and this induces a random walk in the results which may exceed the reduction of scatter achieved by employing the scheme in the first place [7]. In the scheme developed by Boyd [5], this problem is overcome in elegant and simple manner. As shown in figure 9.3, when a particle of the abundant species (1) having mass m_1, velocity components u_{1i} and weighting W_1 is selected for collision with a particle of the trace species (2) having mass m_2, velocity components u_{2i} and weighting W_2, the abundant particle is split into two particles with a weight W_2 and a weight W_1-W_2. The collision is then calculated using the two particles having weight W_2 and then the particles from the split abundant molecule are recombined, thus conserving the linear momentum throughout the collision.

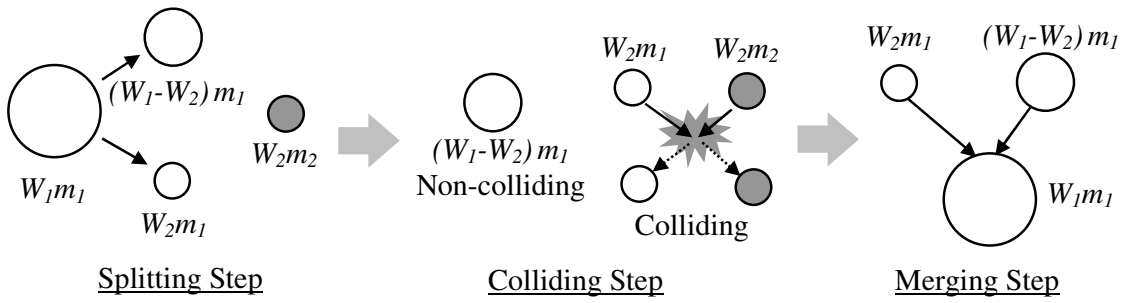

Figure 9.3. Schematic representation of the conservative weighting scheme (CWS)

Setting the steps from figure 9.3 in terms of equations for momentum, the initial momentum of the system in each direction P_i is:

$$P_i = W_1 m_1 u_{1i} + W_2 m_2 u_{2i} = W_1\left[(1-\phi)m_1 u_{1i} + \phi\left(m_1 u_{1i} + m_2 u_{2i}\right)\right] \quad \text{where} \quad \phi = \frac{W_2}{W_1} \tag{9-1}$$

During the colliding step, the momentum is conserved and the final velocity of the particle of the trace species u_{2i}' and the post-collision velocity of the colliding part of the abundant species u_{1i}' can be given by:

$$P_i = W_1\left[(1-\phi)m_1 u_{1i} + \phi\left(m_1 u_{1i}' + m_2 u_{2i}'\right)\right] \tag{9-2}$$

In the merging step, the final velocity of the merged abundant species particle can be obtained by:

$$P_i = W_1 m_1 u_{1i}'' + W_2 m_2 u_{2i}' \quad \text{thus} \quad u_{1i}'' = (1-\phi)u_{1i} + \phi u_1' \tag{9-3}$$

Unfortunately, energy is lost during the process described in figure 9.3 since, considering the three components of velocity, the difference in pre- and post- collision total energies is:

$$\begin{aligned} \Delta E = E' - E &= W_1 \frac{1}{2} m_1 \left[\left(u_{1x}' - u_{1x}\right)^2 + \left(u_{1y}' - u_{1y}\right)^2 + \left(u_{1z}' - u_{1z}\right)^2\right] \\ &= W_1 \frac{1}{2} m_1 \phi(1-\phi)\left[\left(u_{1x} - u_{1x}'\right)^2 + \left(u_{1y} - u_{1y}'\right)^2 + \left(u_{1z} - u_{1z}'\right)^2\right] \end{aligned} \tag{9-4}$$

However, as can be seen from equation (9-4) the amount of energy lost ΔE is proportional to the weighting ratio ϕ which is always very small, thus energy is almost conserved within these collisions. Boyd [5] has proposed a remedy to this situation by adding the lost energy in the system to a subsequent collision between two non-trace species particles in the same cell, thus

ensuring energy is effectively conserved. Extension of the scheme for collisions which include reaction chemistry is given in the paper by Wu *et al.* [6].

The use of the CWS and the determination of the collision parameters of all the species in a diamond deposition reactor will enable the simulation of these reactors. These simulations are proposed as the next logical step for the development of the PP-CVD process.

9.4. Experimental Flow Field Visualisation

As mentioned in section 2.3.5, experimental visualisation of the PP-CVD flow field is extremely challenging and standard techniques such as smoke visualisation and Schlieren imaging are virtually impossible under the highly unsteady conditions which occur during the period of initial expansion in the injection phase. As discussed, a naphthalene sublimation technique has been developed for experimental work; however this technique cannot provide visualisation of the flow field itself, and only gives an indirect indication as to what might be happening.

The simulation tools in this thesis have been extensively tested and validated for a number of test cases utilising experimental and numerical data in the literature. These tests give confidence that the simulations of PP-CVD are producing an accurate representation of the flow field; however validation against experimental flow field data from the actual reactors is desirable.

One possible method for flow field visualisation is particle imaging velocimetry (PIV). PIV is an optical technique for flow visualisation in which the flow field is "seeded" with particles. These particles scatter the light from a laser sheet used to illuminate the flow. A high speed digital camera is then used to take two closely spaced images of the flow. These images are post-processed using computer software to provide displacement vectors for the particles within the flow and thus to build up a visualisation of the flow field [8].

There are two primary technical difficulties to overcome for PIV visualisation of the highly unsteady flow field in PP-CVD. Firstly, the rapid expansion of the flow field means that to obtain images during the initial expansion period, the PIV images must be very closely spaced. The second difficulty concerns the seeding of the flow. The seeding particles must be light

and small enough to follow the flow field and also must not "shatter" when undergoing the rapid expansion. One method of producing particles for PIV is to use a Laskin type seeder which produces relatively uniform sized particles of approximately 1-2μm from liquids (in this case olive oil) [9,10]. For PP-CVD flow field visualisation, six Laskin nozzles were constructed in a paint tin, as shown in figure 9.4. Each nozzle can be turned on or off independently thus allowing variation in the rate at which droplets are produced. This device was found to be suitable for seeding the flow in the chamber prior to injection; however is unsuitable for seeding the inlet gas since the particles are too large and are likely to shatter during the sudden expansion between the inlet orifice and the reactor chamber. New porous particles with low inertia and high aerodynamic drag are becoming available and these may be suitable for this purpose. As such, the use of PIV as a possible visualisation technique for PP-CVD will continue to be investigated during future work.

(a) (b) (c)

Figure 9.4. Laskin seeder designed for PIV visualisation of the PP-CVD flow field. a) External view, b) nozzle configuration and c) nozzle detail.

Several other potential methods for investigating the flow field have been discussed and alternative methods will continue to be sought. One possible method recently proposed by Assoc. Prof. Susan Krumdieck to measure the extent of the jet during the injection phase is to introduce a hot wire into the reactor. As the jet passes over the wire, the rate of heat lose from the wire can be detected and the change in density of the flow field inferred.

9.5. Ultrasonic Injection PP-CVD Modelling

In section 1.3, the two types of PP-CVD reactor configuration were mentioned: the gas-injection and the liquid-injection configurations. In this thesis, the focus has been exclusively on the gas injection configuration; however in future work the modelling techniques need to be extended to include the liquid-injection configurations, since these are important in metal-organic PP-CVD and have been used in the majority of deposition experiments to date (see section 2.3.2).

In the liquid-injection PP-CVD reactors, the liquid precursor is delivered directly into the reactor volume via an ultrasonic nozzle. This ultrasonic nozzle produces droplets of approximately 18μm median diameter [11] and these rapidly evaporate within the reactor. To incorporate a droplet model into the existing or proposed simulation methods, firstly a thorough investigation into the mechanisms of droplet evaporation for the different precursor/solvent combinations is required. A number of droplet evaporation models exist for conventional CFD solvers such as Fluent, and adaptation of these models to a PDE based solver such as an MBE solver should be relatively straight forward. Incorporation of a droplet model in a particle-based simulation is likely to prove more challenging. Numerous examples of molecular dynamics simulations of droplet evaporation can be found in the literature (e.g. reference [12]), however no work utilising DSMC could be found.

Modelling the complex metal-organic precursors used in ultrasonic injection PP-CVD with particle-based methods is also a challenge. These molecules are typically very large with multiple degrees of freedom, and data for their collision parameters is not available. Consequently, these values need to be determined experimentally or by the quantum mechanics based method proposed by Wu and Hsu [6]. As a first step, a sensitivity test on the parameters of the Larsen-Borgnakke collision model will be conducted to determine whether the collision parameters for complex metal-organic precursors need to be determined precisely.

Beyond droplet modelling and determining the collision parameters for metal-organic precursors and their solvents, there is no additional complexity envisaged in modelling ultrasonic injection PP-CVD reactors and the existing and proposed modelling techniques should be able to be used.

9.6. Plasma-Enhanced PP-CVD

Plasma-enhanced CVD systems are widely used in the manufacture of thin films where the avoidance of high substrate temperatures is required [13]. The primary application is in the semiconductor industry where deposition is required on wafers which already contain temperature sensitive materials. In these systems, the energy required for initiating the deposition reaction is not obtained by heating the substrate, but rather from a plasma.

Plasmas are ionised gases which are usually produced by AC or DC discharge between two electrodes. In deposition systems, the percentage of ionised particles in the plasma remains low (typically not more than 10%). The free electrons within the plasma have very high energies (equivalent to tens of thousands of Kelvins in temperature) because their small size means they are unable to exchange their energy efficiently with the neutral species in the plasma, which remain at approximately ambient temperature. These highly energetic electrons provide energy to initiate the deposition reaction(s).

The idea of building a plasma-enhanced PP-CVD reactor is an intriguing one and has the potential to further extend the utility of the PP-CVD process to deposition on temperature-sensitive substrates. Because PP-CVD is an unsteady process, unlike conventional plasma-enhanced CVD reactors, maintaining a stable plasma throughout the process is likely to be the major challenge. Initial development of the process is likely to be entirely experimental; however in the future appropriate modelling techniques will need to be reviewed and investigated.

9.7. Conclusions

In this section, some of the considerations for the future development of the PP-CVD process have been outlined and a new possibility, for plasma-enhanced PP-CVD systems, has been proposed.

Clearly the PP-CVD process has significant potential and, although a great deal of progress has been made, further work is required before the system can be developed for specific industrial applications. The aim of future work will be to continue to develop PP-CVD towards this goal, utilising the simulation tools developed and proposed within this thesis.

References

[1] S. Krumdieck, "Chapter 2. CVD Reactors and Delivery Systems Technology", to appear in: Chemical Vapour Deposition: Precursors and Processes, Eds: A. Jones and M. L. Hitchman (Royal Society of Chemistry Publishing, Cambridge, 2008).

[2] P.W. May, Diamond thin films: a 21st-century material, *Phil. Trans. R. Soc. Lond. A* 356 (2000), 473-495.

[3] Y.A. Mankelevich, A.T. Rakhimov and N.V. Suetin, Two-dimensional simulation of a hot filament chemical vapor deposition reactor, *Diam. Relat. Mater.* 5, 888-894 (1996).

[4] J.-S. Wu and Y.-L. Hsu, Derivation of Variable Soft Sphere Model Parameters in Direct-Simulation Monte Carlo Method Using Quantum Chemistry Computation, *Jpn. J. Appl. Phys.* 42, 7574-7575 (2003).

[5] I.D. Boyd, Conservative species weighting scheme for the direct simulation Monte Carlo method, *J. Thermophys. Heat Tran.* 10(4), 579-585 (1996).

[6] J.-S. Wu, W.-J. Hsiao, Y.-Y. Lian and K.-C. Tseng, Assessment of conservative weighting scheme in simulating chemical vapour deposition with trace species, *Int. J. Numer. Meth.* 43, 93-114 (2003).

[7] G.A. Bird, Molecular Gas Dynamics and the Direct Simulation of Gas Flows (Clarendon Press, Oxford, 1994).

[8] M. Raffel, C.E. Willert and J. Kompenhans, Particle image velocimetry: a practical guide (Springer, New York, 1998).

[9] W.H. Echols and J.A. Young, Studies of Portable Air-Operated Aerosol Generators, U.S. Naval Research Laboratory Report NRL5929 (1963).

[10] A. Melling, Tracer particles and seeding for particle image velocimetry, *Meas. Sci. Technol.* 8, 1406–1416 (1997).

[11] "Nozzle Data Sheet, Nozzle Model 8700-120", Sono-Tek Inc., Milton (NY) (1999).

[12] T.L. Kaltz, L.N. Long, M. M. Micci and J.K. Little, Supercritical Vaporization of Liquid Oxygen Droplets Using Molecular Dynamics, *Combust. Sci. Tech.* 136(1), 279-301 (1998).

[13] D.L. Smith, Thin-film Deposition: Principles and Practice (McGraw-Hill, New York, 1995).